

DYNAMICS IN THE HILL PROBLEM
WITH APPLICATIONS TO SPACECRAFT MANEUVERS

by

Benjamin F. Villac

A dissertation submitted in partial fulfillment
of the requirements for the degree of
Doctor of Philosophy
(Aerospace Engineering)
in The University of Michigan
2003

Doctoral committee:

Associate Professor Daniel J. Scheeres, Chairman
Professor Anthony M. Bloch
Professor Pierre T. Kabamba
Professor Harris N. McClamroch
Professor Ralf J. Spatzier

© Benjamin F. Villac 2003
All Rights Reserved

To my mother, Marie-Chantal

ACKNOWLEDGEMENTS

I would like to thank the members of the doctoral committee for accepting to be part of the committee, and as inspirational persons and teachers. Special thanks are due to my advisor, Daniel J. Scheeres without whom this dissertation would not have seen birth.

I am also grateful to the Europa Orbiter design team for inviting me to spend two months at the Jet Propulsion Laboratory during the summer of 2001, and supporting me during the first two years of my research work and to the Rackham School of Graduate Studies who supported me during the final year.

Finally, I would like to thank my mother, Marie-Chantal Abribat, for her constant moral support and I dedicate this dissertation to her.

TABLE OF CONTENTS

Dedication	ii
Acknowledgements	iii
List of Figures	viii
List of Tables	ix
List of Appendices	x
Chapter I. Introduction	1
1. Overview of the results obtained	3
2. Overview of the dissertation	4
Chapter II. The Three body, Restricted and Hill problems	6
1. The Three body problem	7
2. The restricted approximation	11
3. The Hill approximation	16
4. The orbiter case: The restricted Hill problem	24
Chapter III. Dynamics of the Hill problem	30
1. First properties	31
2. The Jacobi constant and the energy manifold	36
3. Orbital elements and Delaunay variables	46
4. Dynamics close to the primary	54

5.	Dynamics far from the primary	63
Chapter	IV. Periapsis Poincaré maps	69
1.	Periapsis Poincaré maps	71
2.	Picard's method of successive approximations	80
3.	First step in Hill's problem.	85
4.	Applications	92
Chapter	V. Third body driven plane changes	102
1.	Classic vs. third body driven transfers	103
2.	Fuel unconstrained problem	112
3.	Design problem and optimality	121
Chapter	VI. Escape, capture and transit	134
1.	Periapsis Poincaré map for escape, capture and transit	136
2.	Application to escape and capture maneuvers	151
Chapter	VII. Future directions	162
1.	Summary of the results obtained	162
2.	Possible future research directions.	164
Appendices		167
Bibliography		181

LIST OF FIGURES

Figure

II.1. Jacobi coordinates	10
II.2. Geometry of the restricted problem	15
II.3. Geometry of the Hill problem	22
II.4. Geometry of the Hill problem in the case of an orbiter	26
III.1. A few Lyapunov periodic orbits around L_1 and L_2	34
III.2. Zero velocity surfaces for $J = -2.2$	41
III.3. Zero velocity surfaces for $J = Jc$	42
III.4. Zero velocity surfaces for $J = -2.1$	43
III.5. Zero velocity surfaces for $J = -3^{1/3}$	45
III.6. Polar orbit around Europa	59
III.7. Equatorial orbit around Europa	60
III.8. Representation of the motion on a low altitude, circular orbit	61
IV.1. Radius, eccentricity and inclination for a sample polar orbit.	69
IV.2. Concept of a Poincaré map	71
IV.3. Limiting curves between periapsis and apoapsis in the planar Hill problem.	76
IV.4. Integral $p^{7/2}I_2^{-4}$	87
IV.5. Integral $p^{7/2}(I_2^{-4} - I)$	87
IV.6. Integral $p^{7/2}I_0^{-4}$	88
IV.7. Integral $p^{7/2}(I_0^{-4} - I)$	88

IV.8. Integral $p^{7/2} I_{-2}^{-4}$	89
IV.9. Integral $p^{7/2} (I_{-2}^{-4} - I)$	89
IV.10. $\Delta r_p/r_p$, $a = 6123 \text{ km}$, $e = 0.6839$, $i = 30 \text{ deg}$	94
IV.11. Δi , $a = 6123 \text{ km}$, $e = 0.6839$, $i = 30 \text{ deg}$	94
IV.12. $\frac{\Delta r_p}{r_p}$, $a = 6123 \text{ km}$, $e = 0.6839$, $i = 60 \text{ deg}$	95
IV.13. Δi , $a = 6123 \text{ km}$, $e = 0.6839$, $i = 60 \text{ deg}$	95
IV.14. $\frac{\Delta r_p}{r_p}$, $a = 6123 \text{ km}$, $e = 0.6839$, $i = 90 \text{ deg}$	96
IV.15. Δi , $a = 6123 \text{ km}$, $e = 0.6839$, $i = 90 \text{ deg}$	96
IV.16. $\frac{\Delta r_p}{r_p}$, $a = 6123 \text{ km}$, $e = 0.6839$, $i = 120 \text{ deg}$	97
IV.17. Δi , $a = 6123 \text{ km}$, $e = 0.6839$, $i = 120 \text{ deg}$	97
IV.18. $\frac{\Delta r_p}{r_p}$, $a = 6123 \text{ km}$, $e = 0.6839$, $i = 150 \text{ deg}$	98
IV.19. Δi , $a = 6123 \text{ km}$, $e = 0.6839$, $i = 150 \text{ deg}$	98
V.1. Geometry of bi-elliptic plane changes	104
V.2. Geometry of 3 rd body driven plane changes	105
V.3. Example of periapsis Poincaré maps.	109
V.4. A geometric view of third body driven plane changes	110
V.5. Series of 3 rd body driven plane changes for the Europa case	111
V.6. $\Delta r_p = 0$ lines for $r_p = 0.08$, $r_a = 0.6$ and $i = 90^\circ$	114
V.7. Extrema values of plane change as a function of inclination (1)	116
V.8. Extrema values of plane change as a function of inclination (2)	117
V.9. Extrema values of plane change as a function of inclination (3)	117
V.10. Extrema values of plane change as a function of apoapsis radius	118
V.11. Extrema values of plane change as a function of periapsis radius	120
V.12. $\Delta r_p = 0$ line for $r_p = 0.003$, $r_a = 0.5$ and $i = 90^\circ$	124
V.13. Local-Global extrema on individual zero lines	125
V.14. Range of possible third body driven plane changes	126
V.15. Limiting curve for the existence of $+180^\circ$ plane changes.	127

V.16. A bound on the domain of optimality of one impulse maneuvers	129
V.17. Analytic estimate of the limit of optimality	131
V.18. Analytic upper bound for the cost of 3^{rd} body driven plane changes.	132
VI.1. Stable and unstable direction of the libration points dynamics	138
VI.2. Geometry of the Poincaré map	142
VI.3. Example of a 2D Poincaré map for $J = -2.16$	144
VI.4. Series of Poincaré maps (Σ_2^a) at several values of the Jacobi constant . . .	145
VI.5. Poincaré maps for escape and capture (case of Europa $J = -2.16$)	147
VI.6. Extrema of radius and longitude of periapsis on Σ_2^a as a function of J . .	149
VI.7. Extrema of eccentricity and inclination on Σ_2^a as a function of J	150
VI.8. ΔV as computed along the stable manifold associated with L_2	152
VI.9. Strategies to escape.	154
VI.10. Optimal ΔV and longitude of periapsis for escape	156
VI.11. Envelopes of the projections of a few Poincaré maps	160
VI.12. Projection of a Poincaré map onto the $(r, \Delta V)$ space	160

LIST OF TABLES

Table

III.1. Parameters for the dynamics close to Mercury, the Earth, Europa, Titan and Triton	62
IV.1. Constraints on periapsis and apoapsis in the Hill problem.	74
IV.2. Comparison between DPTRAJ and analytical results.	91
VI.1. Minimum ΔV to escape the surface of some planetary satellites	158
B.1. Length and time scales of the solar system planetary satellites	173
C.1. Roots of the reduced cubic equation defining \mathcal{Z}	177

LIST OF APPENDICES

Appendix

A.	Symplectic transformations	167
B.	Scaling to planetary satellites	172
C.	Reduced cubic equations	174
D.	Changes in elements	178
E.	Numerical integration	180

CHAPTER I

INTRODUCTION

Access to space is expensive and every extra kilogram of propellant comes at the detriment of a kilogram of scientific equipment. Thus, since the early days of spaceflight, mission designers have tried to use the natural space environment to reduce the costs of orbital transfers. For example, the Voyager spacecraft, which was designed to explore the outer part of the solar system in the late 1970's, used 1210 kg of solid propellant for its entire mission. Yet, had the spacecraft not used fly-bys of Jupiter and the other giant planets, it could not have traveled further than Jupiter. It has now reached the edge of the solar system and is the farthest man-made object from the Earth.

Even though fly-bys are really the expression of third body effects, the analysis of these maneuvers are performed using a two body model and the third body effect is accounted for by a change in the state of the spacecraft before and after encounter.

Third body dynamics present however, many more realms of motion that can be used to achieve challenging scientific goals within the limited budgets of present day missions. These dynamics are intrinsically non-Keplerian, and thus cannot be analyzed in the two body framework. As an example, the Genesis mission which aims at elucidating the origin of the solar system by collecting solar wind particles close to the Earth-Sun libration points, used the dynamics associated with heteroclinic connections between Lyapunov orbits in the restricted three body problem to achieve a total ΔV budget of less than 100 m/s for the entire mission [23].

Along these lines, this dissertation explores the use of non-Keplerian, natural dynamics

associated with the presence of a third body to effect classical orbital maneuver objectives. It has been motivated to a large extent by the Europa Orbiter mission whose goal is to determine whether an ocean exists under the surface ice crust of the Jovian moon Europa, which could shelter the existence of possible extraterrestrial life. The orbital environment of this satellite cannot be analyzed by a two body model because of the strong perturbations coming from Jupiter. For instance, these perturbations result in instabilities of high-inclination, low altitude circular orbits, and they can cause a spacecraft to impact the satellite over a period of a few weeks.

While many studies have taken the restricted three body problem as the underlying framework, many interesting transfers can be analyzed using the Hill problem. Originally derived by G.W.Hill [18] at the end of the nineteenth century to investigate the motion of the Moon, this model, described as “luminous” by Henrard [17], presents the non-negligible advantage of simplicity while accurately representing the nonlinear dynamics of interest. Hence, this slight shift in modeling allows us to investigate a range of physical situations while significantly simplifying the equations of motion.

This dissertation investigates the nonlinear dynamics of this problem while emphasizing their application to spacecraft orbital maneuvers.

After the derivation of the model by Hill, early work focused on the determination of the families of periodic orbits in this problem. An account of these results and their extension to other families can be found in [12]. Another focus at the beginning of the century was the derivation of precise Lunar ephemerides by Brown that could be computed fast enough to be useful*. Brown developed his Lunar theory based on Hill’s problem, and it was used until the 1960’s. After this early research, the Hill problem did not attract attention until Hénon[12], Petit [16], Chavineau [6] and others revived the subject by using Hill’s problem in connection with planetary ring and asteroid dynamics. Today, the Hill problem has attracted a broad audience for representing a simple model of a non-

*There were no computers at that time!

integrable system, and it is applied in both dynamical astronomy and astrodynamics. It has been used to analyze chaotic scattering [16, 17], the destruction of KAM tori [36], star cluster dynamics [34], motion in Earth-Moon-Sun system [30], motion about comets and asteroids [33] and system of families of periodic orbits [14].

1. Overview of the results obtained

The results obtained in this work are based on a central idea of orbital dynamics, that is, the reduction of dynamics to a discrete map associated with periapsis passages (closest approach to the primary). More precisely, the changes in orbital elements from periapsis to periapsis passage define a Poincaré map which allows us to study natural physical phenomena of importance, such as impact with the primary. The Poincaré map is well suited for the analyses of spacecraft maneuvers since many maneuvers are performed at periapsis. This point of view, while implicit in a two body framework, has not been applied, as yet, to the three body type models.

Approximations of one iteration of this periapsis map can be obtained using Picard's method of successive approximations. The application of this method to the Hill problem results in first order estimates of the changes in orbital elements over one orbit, which allow us to draw a qualitative picture of the dynamics. For example, the sign of the changes are shown to follow a “quadrant rule”, generalizing results already obtained in the planar problem. These estimates also indicate the possibility of controlling the dynamics of an orbiter[†] via the orientation of the trajectories with respect to the disturbing body and, thus, using these dynamics for orbital control purposes.

An analysis of plane change maneuvers has been performed along these lines, showing that the resulting transfers, which can be thought of as classical bi-elliptic plane changes with the apoapsis maneuvers suppressed by the use of the 3rd body forces, can provide a significant improvement over classical approaches for a wide range of initial conditions.

[†]That is a spacecraft orbiting a primary (planet or planetary satellite) and perturbed by a large distant body (Sun or giant planet, respectively).

Notably, a reversal of the direction of motion of a spacecraft in the equatorial plane uses 70% less fuel than a conventional one impulse maneuver.

Also, using the periapsis Poincaré map idea, an investigation of escape, capture and transit in the Hill problem is presented. It is shown, in particular, that the set of first periapsis passages of escaping and capture trajectories lie in a small region in the vicinity of the primary, characterized by the extrema of radius, longitude of periapsis and inclination. Also, these results lead to a simple classification of planetary satellites of the solar system that indicate the possibility or impossibility of low energy capture maneuvers in these environments. Finally, these results are applied to the problem of single impulse, direct escape from low altitude, circular orbits, yielding an optimal escape criterion in the planar case and a practical escape approach in the three dimensional case. This approach allows us to realize over $130m/s$ of ΔV savings[‡] in the case of an Europa orbiter, as compared to a classic parabolic plane change maneuver.

These investigations also bring some insight into the dynamics of the Hill problem. In particular, the existence of limiting curves that partition the position space into exclusive periapsis or apoapsis regions is shown. The “quadrant rule” which indicates the regions of increase or decrease in angular momentum magnitude in the planar case is extended to the spatial problem, and the large control authority of the longitude of the ascending node and the argument of periapsis is established. These properties may have potential applications to a wider realm than spaceflight mechanics, such as the analyses of the accretion properties of planetary satellites or the stellar escape rate in star clusters dynamics.

2. Overview of the dissertation

This dissertation begins by deriving the Hill problem from the full three body problem in Chapter II, showing that, while the orbiter case can be derived from the restricted three

[‡]The cost of impulsive maneuvers can be expressed in terms of mass, but this measure is very dependent on the technology used (type of rocket engine). Thus, it is customary in astrodynamics to express the effects of impulsive maneuvers in terms of the magnitude of the change in velocity they produce, known as ΔV . When comparing different methods or costs, the savings realized are expressed in terms of ΔV , as well.

body model, the Hill problem remains a valid approximation to three body dynamics in the more general case of two small masses perturbed by a larger one, no matter the ratio of the two small masses. To bring this out, we use symplectic scaling to shed some light into the relationship between the different models.

This technique is also used as a tool to investigate the limiting case dynamics (close to and far from the primary) in Chapter III, where other general results in the Hill problem are also presented.

Chapter IV defines the periapsis Poincaré map and its approximation using Picard's method of successive approximations. A qualitative picture of the orbital dynamics is thus obtained and presented. From this, two applications developed in the sequel are suggested.

Chapter V is concerned with the application of third body forces to effect plane changes. A new class of plane change maneuvers is defined. This class of maneuvers allow performance of large plane changes at reduced cost, using only two impulsive maneuvers. Comparison with the classical approach is treated and optimal results are given.

Chapter VI looks at the limitations of the approximations obtained by analyzing escape, capture and transit trajectories in the Hill problem. Applications to the one impulse, optimal escape and capture problems are treated.

The dissertation concludes with thoughts on possible future research directions in Chapter VII.

CHAPTER II

THE THREE BODY, RESTRICTED AND HILL PROBLEMS

The three body problem describes the motion of three point mass particles under their mutual gravitational interactions. This classical problem represents a large range of astronomical situations. The motion of the Moon around the Earth as perturbed by the Sun, or the motion of a comet as perturbed by the Sun and Jupiter are examples of such situations.

As investigators realized that a general solution of the problem was not possible*, simplifications were made to the problem. These simplifications were generally justified by physical reasoning, arguing on the order of magnitude of certain terms in the equations of motion. For example, it is rather obvious that the mass of the Sun or of Jupiter are much larger than the mass of a comet, therefore implying very little effect of the gravitational attraction of the comet on the motions of Jupiter and the Sun. This leads directly to the equations of the restricted problem. Similarly, the sum of the mass of the Earth and Moon is much smaller than the mass of the Sun, and a change of variables leads to a formulation as the Hill problem.

A rigorous mathematical way to define these limiting processes is given via the Hamiltonian formalism and symplectic scaling techniques. The restricted and Hill approximations represent the first term in the expansion of the Hamiltonian of the three body problem when a symplectic scaling (i.e., canonical transformation) is introduced. Perturbation techniques can then be used to prove the existence of families of periodic orbits or the

*Indeed, Poincaré proved that the three body problem is non-integrable.

existence of KAM tori, thus implying regions of bounded motion (in the planar case).

This chapter derives the restricted and Hill problems from the full three body problem using the above methodology, showing that, even though G.W.Hill derived the equations that now bear his name from the restricted three body model, these equations have greater generality. This was not realized until the 1980's, when Hénon and Petit [15] gave a derivation of this model in the full three body problem framework and Meyer and Schmidt [27] used a symplectic scaling technique to prove that most periodic orbits in the Hill problem can be continued analytically to the full three body problem.

Another aim of this chapter is to clarify the relationship between the normalized models and the physical systems where quantities are measured in a given dimensional system (e.g., the SI units). One of the interesting properties of the Hill model is its dimensionless and parameterless form when suitable length and time scales are introduced.

1. The Three body problem

The aim of this section is to present the Hamiltonian of the three body problem as the starting point of the subsequent sections. The Jacobi coordinates in a rotating frame are introduced since they allow a first reduction of the problem and are the natural setting for the development of the restricted and Hill approximations.

1.1. Equations of motion

Denoting m_i and \mathbf{R}_i , $i = 1, 2, 3$, the masses and position of the three particles considered in an inertial frame, the application of Newton's second law of motion and Newton's law of gravitation directly lead to the following equations:

$$\ddot{\mathbf{R}}_1 = -Gm_2 \frac{\mathbf{R}_1 - \mathbf{R}_2}{|\mathbf{R}_1 - \mathbf{R}_2|^3} - Gm_3 \frac{\mathbf{R}_1 - \mathbf{R}_3}{|\mathbf{R}_1 - \mathbf{R}_3|^3} \quad (\text{II.1})$$

$$\ddot{\mathbf{R}}_2 = -Gm_1 \frac{\mathbf{R}_2 - \mathbf{R}_1}{|\mathbf{R}_2 - \mathbf{R}_1|^3} - Gm_3 \frac{\mathbf{R}_2 - \mathbf{R}_3}{|\mathbf{R}_2 - \mathbf{R}_3|^3} \quad (\text{II.2})$$

$$\ddot{\mathbf{R}}_3 = -Gm_1 \frac{\mathbf{R}_3 - \mathbf{R}_1}{|\mathbf{R}_3 - \mathbf{R}_1|^3} - Gm_2 \frac{\mathbf{R}_3 - \mathbf{R}_2}{|\mathbf{R}_3 - \mathbf{R}_2|^3} \quad (\text{II.3})$$

where G represents the universal gravitational constant.

We can immediately see that, as $m_3 \rightarrow 0$, the first two equations reduce to a two body problem, leaving the third equation describing the motion of a massless particle in the gravitational field of two point mass particles. This is the restricted problem as formulated in inertial space.

Similarly, as $m_1, m_2 \rightarrow 0$, the first two equations describe two uncoupled Keplerian problems; this was the basis of Lunar theories before the work of Hill. A subtler scaling is needed to take into account the coupling between the small masses.

1.2. Hamiltonian formalism and Jacobi coordinates

The Hamiltonian formalism is now introduced to investigate these limiting processes. We rewrite the above differential equations as:

$$\begin{aligned}\dot{\mathbf{R}}_i &= \frac{\partial \mathcal{H}}{\partial \mathbf{S}_i} & i = 1, 2, 3 \\ \dot{\mathbf{S}}_i &= -\frac{\partial \mathcal{H}}{\partial \mathbf{R}_i}\end{aligned}$$

where $\mathbf{S}_i = m_i \dot{\mathbf{R}}_i$ is the conjugate momentum of the position \mathbf{R}_i of the i^{th} particle in the inertial frame and the Hamiltonian \mathcal{H} is given by:

$$\mathcal{H} = \sum_{i=1}^3 \frac{|\mathbf{S}_i|^2}{2m_i} - \sum_{1 \leq i < j \leq 3} \frac{Gm_i m_j}{|\mathbf{R}_i - \mathbf{R}_j|} \quad (\text{II.4})$$

These equations admit the ten general integrals of motion present in the N -body problem, namely, the energy, the position of the center of mass, the linear and angular momenta. A change of coordinates can be used to eliminate the barycenter and linear momentum integrals. These coordinates, the Jacobi coordinates, are useful for deriving the restricted and Hill model in the case of three bodies.

The first step in defining these coordinates is to transform the initial Hamiltonian (II.4) into a rotating coordinate system with angular velocity $\boldsymbol{\omega} = (\omega_1, \omega_2, \omega_3)^\dagger$. That is, we

[†]It is generally convenient to take $\omega_1 = \omega_2 = 0$, but this is not required at this stage.

make the following symplectic change of coordinates:

$$\begin{aligned}\mathbf{Q}_i &= \exp(\boldsymbol{\Omega}t)\mathbf{R}_i \\ \mathbf{P}_i &= \exp(\boldsymbol{\Omega}t)\mathbf{S}_i\end{aligned}$$

where

$$\boldsymbol{\Omega} = \begin{bmatrix} 0 & \omega_3 & -\omega_2 \\ -\omega_3 & 0 & \omega_1 \\ \omega_2 & -\omega_1 & 0 \end{bmatrix} \quad (\text{II.5})$$

so that $\boldsymbol{\omega} \times \mathbf{R} = -\boldsymbol{\Omega}\mathbf{R}$ for any vector \mathbf{R} .

Under this change of coordinates, the above Hamiltonian transforms to[‡]:

$$\mathcal{H} = \sum_{i=1}^3 \left\{ \frac{|\mathbf{P}_i|^2}{2m_i} - \mathbf{Q}_i^T \boldsymbol{\Omega} \mathbf{P}_i \right\} - \sum_{1 \leq i < j \leq 3} \frac{Gm_i m_j}{|\mathbf{Q}_i - \mathbf{Q}_j|}$$

Then one can define the Jacobi coordinates as:

$$\begin{aligned}\mathbf{u}_0 &= \{m_1 \mathbf{Q}_1 + m_2 \mathbf{Q}_2 + m_3 \mathbf{Q}_3\} (m_1 + m_2 + m_3)^{-1} \\ \mathbf{u}_1 &= \mathbf{Q}_1 - \mathbf{Q}_2 \\ \mathbf{u}_2 &= \mathbf{Q}_3 - \{m_1 \mathbf{Q}_1 + m_2 \mathbf{Q}_2\} (m_1 + m_2)^{-1}\end{aligned}$$

That is, the first vector, \mathbf{u}_0 , represents the position of the center of mass of the three particles, the second vector, \mathbf{u}_1 , represents the relative position of the second particle relative to the first one, and the last vector, \mathbf{u}_3 , corresponds to the position of the third particle relative to the center of mass of the first two particles. Figure II.1 illustrates this situation.

This point transformation can be made symplectic (see Appendix A) by defining:

$$\begin{aligned}\mathbf{v}_0 &= \mathbf{P}_1 + \mathbf{P}_2 + \mathbf{P}_3 \\ \mathbf{v}_1 &= \{m_1 \mathbf{P}_2 - m_2 \mathbf{P}_1\} (m_1 + m_2)^{-1} \\ \mathbf{v}_2 &= \{(m_1 + m_2) \mathbf{P}_3 - m_3 (\mathbf{P}_1 + \mathbf{P}_2)\} (m_1 + m_2 + m_3)^{-1}\end{aligned}$$

[‡]See Meyer and Hall [26] or Arnold [3] for further details on time dependent canonical transformations.

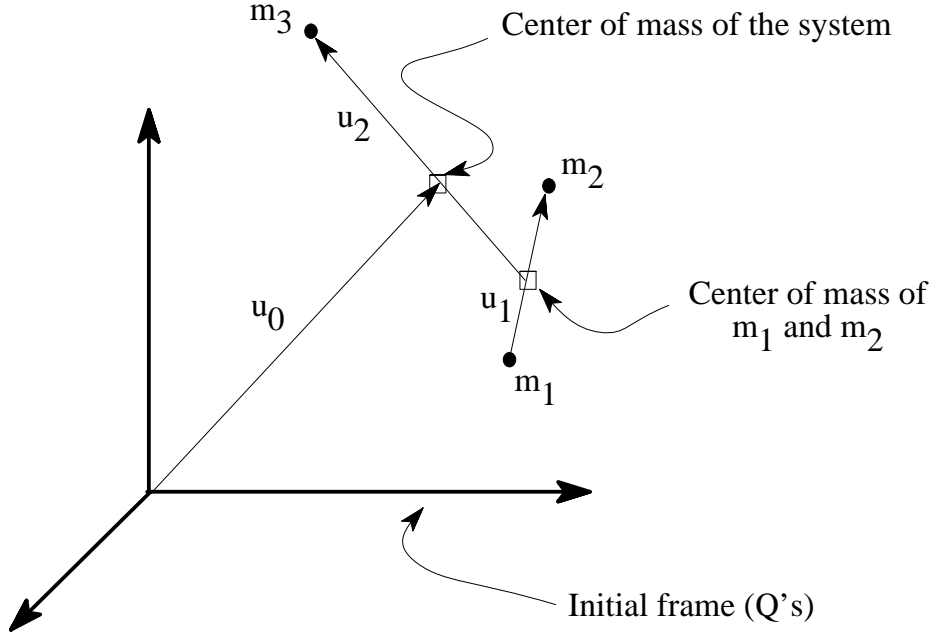


Figure II.1: Jacobi coordinates

Then, the Hamiltonian reduces to

$$\mathcal{H} = \sum_{i=0}^2 \left\{ \frac{|\mathbf{v}_i|^2}{2M_i} - \mathbf{u}_i^T \boldsymbol{\Omega} \mathbf{v}_i \right\} - \frac{Gm_1m_2}{|\mathbf{u}_1|} - \frac{Gm_2m_3}{|\mathbf{u}_2 - \nu_1 \mathbf{u}_1|} - \frac{Gm_1m_3}{|\mathbf{u}_2 + \nu_2 \mathbf{u}_1|} \quad (\text{II.6})$$

where

$$\begin{aligned} M_0 &= m_1 + m_2 + m_3 \\ M_1 &= \frac{m_1 m_2}{m_1 + m_2} \quad \text{and} \quad \nu_1 = \frac{m_1}{m_1 + m_2} \\ M_2 &= \frac{m_3(m_1 + m_2)}{m_1 + m_2 + m_3} \quad \nu_2 = \frac{m_2}{m_1 + m_2} \end{aligned}$$

Now the vectors \mathbf{u}_0 and \mathbf{v}_0 that represent the position and momentum of the center of mass, are independent of the other variables in the Hamiltonian (they don't appear in the potential term) and one can reduce the Hamiltonian by setting $\mathbf{u}_0 = 0$ and $\mathbf{v}_0 = 0$. This corresponds to choosing the center of the frame at the center of mass of the system.

We are now ready to develop the different scalings that lead to the restricted and Hill approximations.

2. The restricted approximation

The restricted three body problem describes the dynamics of a small mass attracted by two point masses revolving around each other in a Keplerian circular orbit. This model has found many applications in both astronomy and astrodynamics. It is indeed the simplest model of the main perturbation of an object in interplanetary space (e.g., comet, Jupiter, Sun system) or even for Earth orbiters for high enough altitudes [28].

2.1. Derivation

To derive this model from the Hamiltonian of the full three body problem (II.6), let the mass of the third particle be denoted by ϵ^2 . The Hamiltonian (II.6) is rewritten as:

$$\mathcal{H} = \mathcal{H}_{Kepler} + \tilde{\mathcal{H}} \quad (\text{II.7})$$

where

$$\mathcal{H}_{Kepler} = \frac{|\mathbf{v}_1|^2}{2M_1} - \mathbf{u}_1^T \boldsymbol{\Omega} \mathbf{v}_1 - \frac{Gm_1m_2}{|\mathbf{u}_1|} \quad (\text{II.8})$$

and

$$\tilde{\mathcal{H}} = \left(1 + \frac{\epsilon^2}{m_1 + m_2}\right) \frac{|\mathbf{v}_2|^2}{2m_3\epsilon} - \mathbf{u}_2^T \boldsymbol{\Omega} \mathbf{v}_2 - \epsilon^2 \frac{Gm_2}{|\mathbf{u}_2 - \nu_1 \mathbf{u}_1|} - \epsilon^2 \frac{Gm_1}{|\mathbf{u}_2 + \nu_2 \mathbf{u}_1|}$$

The Hamiltonian \mathcal{H}_{Kepler} represents a Kepler problem and depends only on \mathbf{u}_1 and \mathbf{v}_1 . Since the third mass is assumed to be small, it is physically legitimate to expect that this particle will have very little effect on the motion of the first two masses. Therefore a change of variable of the form $\mathbf{u}_1 = \mathbf{u}(t) - \epsilon \boldsymbol{\xi}$ and $\mathbf{v}_1 = \mathbf{v}(t) - \epsilon \boldsymbol{\eta}$ where $(\mathbf{u}(t), \mathbf{v}(t))$ represents a solution of the Hamiltonian (II.8) seems reasonable. We want however to keep the autonomous nature of the system, and therefore, $(\mathbf{u}(t), \mathbf{v}(t))$ is chosen to be a relative equilibrium (i.e., critical point) of the Kepler problem. These relative equilibria correspond to circular orbits with mean motion equal to the angular velocity of the frame.

That is, we perform the following change of variable on $(\mathbf{u}_1, \mathbf{v}_1)$:

$$\mathbf{u}_1 = \mathbf{a} - \epsilon \boldsymbol{\xi} \quad (\text{II.9})$$

$$\mathbf{v}_1 = -M_1 \Omega \mathbf{a} - \epsilon \boldsymbol{\eta} \quad (\text{II.10})$$

where \mathbf{a} is orthogonal to $\boldsymbol{\omega}$ and satisfies the relation[§] (see Appendix A):

$$\omega^2 = \frac{G(m_1 + m_2)}{a^3} \quad (\text{II.11})$$

Then, one can develop \mathcal{H}_{Kepler} around this nominal circular orbit by using Taylor's expansion theorem:

$$\mathcal{H}_{Kepler} = \mathcal{H}_{Kepler}(\mathbf{a}, -M_1 \Omega \mathbf{a}) + \frac{\epsilon^2}{2} (\boldsymbol{\xi}, \boldsymbol{\eta})^T \mathbf{S}(\boldsymbol{\xi}, \boldsymbol{\eta}) + \mathcal{O}(\epsilon^3)$$

where the constant term $\mathcal{H}_{Kepler}(\mathbf{a}, -M_1 \Omega \mathbf{a})$ can be set to zero without loss of generality since the addition of a constant in a Hamiltonian does not change the equations of motion. \mathbf{S} represents the Hessian of \mathcal{H}_{Kepler} evaluated at the critical point $(\mathbf{a}, -M_1 \Omega \mathbf{a})$ and is equal to:

$$\mathbf{S} = \begin{bmatrix} \omega^2 \left(\mathbf{I} - 3 \frac{\mathbf{a}\mathbf{a}^T}{a^2} \right) & -\Omega \\ \Omega & \frac{\mathbf{I}}{M_1} \end{bmatrix} \quad (\text{II.12})$$

where \mathbf{I} represents the 3×3 identity matrix.

That is, the term $\frac{1}{2}(\boldsymbol{\xi}, \boldsymbol{\eta})^T \mathbf{S}(\boldsymbol{\xi}, \boldsymbol{\eta})$ represents the linearized motion of the two particles around a nominal circular orbit. This is the Clohessy-Wiltshire equations in Hamiltonian form. These equations also appear in the derivation of the Hill problem (see next section) and in the analysis of the motion far from the primary in the Hill approximation, as we will see in the next Chapter. These equations will be studied in more detail at that point.

Returning to the Hamiltonian (II.7), one can complete the transformation (II.9)-(II.10) into a canonical transformation with multiplier ϵ^{-2} by setting:

$$\mathbf{u}_2 = \mathbf{q}$$

$$\mathbf{v}_2 = \epsilon^2 \mathbf{p}$$

[§]recall that vectors are represented by bold letters and the corresponding unbold letters represent their norm. Here, $\omega = |\boldsymbol{\omega}|$ and $a = |\mathbf{a}|$.

Then, the Hamiltonian (II.7) transforms into:

$$\frac{\mathcal{H}}{\epsilon^2} = \mathcal{H}_R + \frac{1}{2}(\xi, \eta)^T S(\xi, \eta) + \mathcal{O}(\epsilon) \quad (\text{II.13})$$

where

$$\mathcal{H}_R = \frac{|\mathbf{p}|^2}{2} - \mathbf{q}^T \Omega \mathbf{p} - \frac{Gm_2}{|\mathbf{q} - \nu_1 \mathbf{a}|} - \frac{Gm_1}{|\mathbf{q} + \nu_2 \mathbf{a}|} \quad (\text{II.14})$$

represents the Hamiltonian of the restricted problem. It only depends on \mathbf{q} and \mathbf{p} .

Thus we see that an appropriate scaling allows us to rewrite the full three body problem as the restricted problem plus a linear motion around a reference circular orbit, to the first order in ϵ (i.e., $\sqrt{m_3}$). That is, the motion of the primaries and the small mass particle decouple to first order and one can study the motion of the small mass particle assuming the primaries are fixed in the rotating coordinate system, i.e., ξ and η are taken equal to zero.

Note that the above scaling does not change the length, mass and time scales with which the original three body problem was formulated. The scaling only affects the \mathbf{p} variable in the Hamiltonian of the restricted problem, but this scaling correspond to dividing by m_3 , which is a consequence of the uncoupling (to the first order) between the (ξ, η) and (\mathbf{q}, \mathbf{p}) variables. Indeed, the equation of motion for particle \mathbf{R}_i in Newtonian form does not depend the mass m_i (see equations (II.1)-(II.3)). When the Hamiltonian decouples, this independence appears directly in the Hamiltonian, in a similar fashion to that in the Kepler problem (see Appendix A).

2.2. Normalization

In most studies of the restricted problem, the equations are written in a normalized form where only one parameter, generally denoted μ , remains in the equations. This allows us, for example, to perform numerical computation for a given value of μ and then apply the results to any physical system which scales to this normalized model with this particular value of μ .

To obtain this normalized form of the equations and the dependence of μ on the physical parameters, we change the length and time scale by using the following symplectic transformation with multiplier $\alpha\beta$:

$$\begin{aligned}\mathbf{q} &= \alpha \tilde{\mathbf{q}} \\ \mathbf{p} &= \beta \tilde{\mathbf{p}} \\ t &= \gamma \tau\end{aligned}$$

where α , β and γ need be chosen to simplify the Hamiltonian H_R .

Scaling of the time variable simply results in multiplying the Hamiltonian by the given factor, here γ , so that the above scaling results in:

$$\mathcal{H}_R = \frac{\gamma\beta}{\alpha} \frac{|\tilde{\mathbf{p}}|^2}{2} - \gamma\omega \tilde{\mathbf{q}}^T \tilde{\Omega} \tilde{\mathbf{p}} - \frac{\gamma}{\alpha^2\beta} \frac{Gm_2}{|\tilde{\mathbf{q}} - \nu_1 \mathbf{a}/\alpha|} - \frac{\gamma}{\alpha^2\beta} \frac{Gm_1}{|\tilde{\mathbf{q}} + \nu_2 \mathbf{a}/\alpha|}$$

where $\tilde{\Omega}$ has been obtained from the normalized vector $\frac{\omega}{\omega}$.

Thus, we see that setting $\alpha = a$, $\beta = (a\omega)^{-1}$ and $\gamma = \omega^{-1}$, results in nondimensionalizing the Hamiltonian. Recall indeed that $\omega^2 = G(m_1 + m_2)a^{-3}$, $\nu_1 = m_1(m_1 + m_2)^{-1}$ and $\nu_2 = m_2(m_1 + m_2)^{-1}$.

Moreover, denoting $\mu = \nu_1$, we have $\nu_2 = 1 - \mu$, and we obtain the normalized Hamiltonian of the restricted problem written in vector form as:

$$\mathcal{H}_R = \frac{|\tilde{\mathbf{p}}|^2}{2} - \tilde{\mathbf{q}}^T \tilde{\Omega} \tilde{\mathbf{p}} - \frac{1 - \mu}{|\tilde{\mathbf{q}} - \mu \tilde{\mathbf{a}}|} - \frac{\mu}{|\tilde{\mathbf{q}} + (1 - \mu) \tilde{\mathbf{a}}|}$$

where $\tilde{\mathbf{a}} = \mathbf{a}/a$. The resulting equations of motion are given by:

$$\ddot{\tilde{\mathbf{q}}} - 2\tilde{\omega} \times \dot{\tilde{\mathbf{q}}} + \tilde{\omega} \times (\tilde{\omega} \times \tilde{\mathbf{q}}) = -(1 - \mu) \frac{\tilde{\mathbf{q}} - \mu \tilde{\mathbf{a}}}{|\tilde{\mathbf{q}} - \mu \tilde{\mathbf{a}}|^3} - \mu \frac{\tilde{\mathbf{q}} + (1 - \mu) \tilde{\mathbf{a}}}{|\tilde{\mathbf{q}} + (1 - \mu) \tilde{\mathbf{a}}|^3}$$

To express this Hamiltonian in Cartesian coordinates, it is standard to let $\omega = (0, 0, \omega)$ and $\tilde{\mathbf{a}} = (1, 0, 0)$, so that the z -axis is chosen along the angular momentum of the primaries and the primaries lie on the x -axis. The y -axis is chosen to complete the orthonormal frame (see Figure II.2).

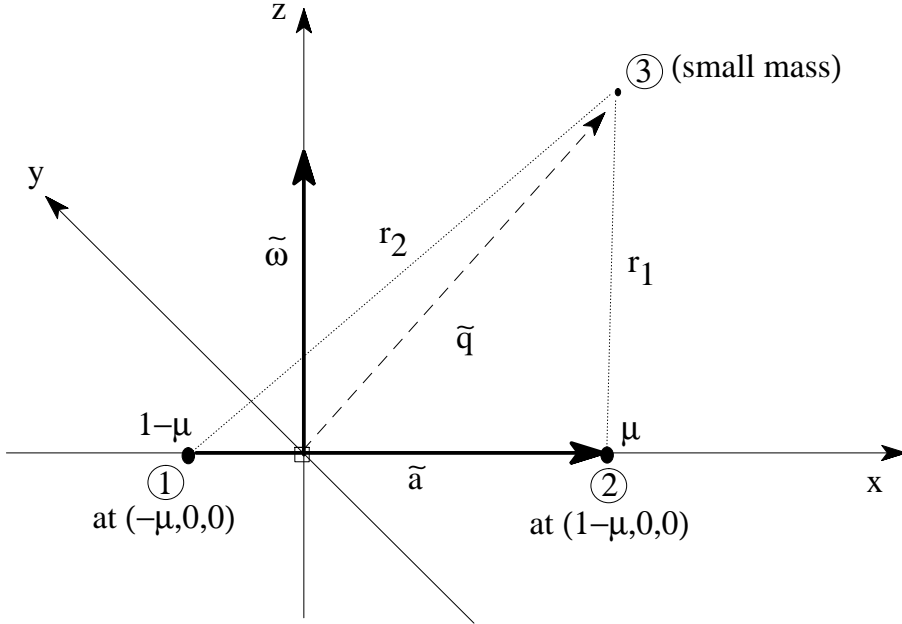


Figure II.2: Geometry of the restricted problem

Then, denoting (x, y, z) and (p_x, p_y, p_z) the components of \tilde{q} and \tilde{p} respectively, the Hamiltonian \mathcal{H}_R can now be expressed in the more conventional form as:

$$\mathcal{H}_R = \frac{1}{2} \left\{ (p_x + y)^2 + (p_y - x)^2 + p_z^2 - (x^2 + y^2) \right\} - \frac{\mu}{r_1} - \frac{1-\mu}{r_2}$$

where $r_1 = \sqrt{(x - 1 + \mu)^2 + y^2 + z^2}$ and $r_2 = \sqrt{(x - \mu)^2 + y^2 + z^2}$ represent the distance of the third mass from the primaries (m_1 and m_2 respectively).

Then, the equations of motion become:

$$\begin{aligned}\ddot{x} - 2\dot{y} - x &= -\mu \frac{(x - 1 + \mu)}{r_1^3} - (1 - \mu) \frac{(x - \mu)}{r_2^3} \\ \ddot{y} + 2\dot{x} - y &= -\mu \frac{y}{r_1^3} - (1 - \mu) \frac{y}{r_2^3} \\ \ddot{z} &= -\mu \frac{z}{r_1^3} - (1 - \mu) \frac{z}{r_2^3}\end{aligned}$$

Hence, we see that any physical situation can be scaled to this normalized form of the equations by choosing the length and time scales, l and τ respectively, as:

$$l = a \quad \text{and} \quad \tau = \frac{1}{\omega}$$

The only dimensionless parameter remaining in the equation, μ , is given by:

$$\mu = \frac{m_1}{m_1 + m_2}$$

2.3. Comments

A more classical derivation of the restricted problem than that presented here can be found in the treatise on the subject by Szebehely [37]. The above derivation was inspired by Meyer [24, 25] and Meyer and Schmidt [27], even though the scaling used is not exactly the same since the emphasis here was to make explicit the normalization process and the length and time scales.

However, we should note that from the expression of the Hamiltonian derived in (II.13), a further reduction of the Clohessy-Wiltshire part of the Hamiltonian results in the following theorem, as a direct application of a standard perturbation theorem on Hamiltonian systems (see [24] for the full details):

Any non-degenerate periodic solution of the classical restricted problem whose period is not a multiple of 2π can be continued into the full three body problem.*

Also, we should note that the restricted problem is still of current research interest as attested by the monographs of Hénon on families of periodic orbits [13], the papers on homoclinic phenomena [22], or the studies on transport phenomena in the solar system [21]. One of the main ingredients in this last subject only involves the dynamics close to one of the primaries, and it can be analyzed using the Hill problem, as we shall see in Chapter VI.

3. The Hill approximation

The Hill approximation can be used when two of the masses are close together and small when compared to the third one. Hence, it is a complementary approach to the restricted

*i.e., with multiplicity of the characteristic multiplier +1 exactly equal to 2.

case, even though the Hill approximation has traditionally been considered to be a special case of the restricted problem and is often used in such a restricted sense. This special case will be considered in the next section.

The general case is derived in this section using the same techniques as in the previous section. In its full generality, the Hill problem has several applications in dynamical astronomy, in particular in the exploration of planetary ring dynamics and binary encounters.

3.1. Derivation

As in the restricted problem, the derivation of the Hill problem from the full three body problem results in splitting the Hamiltonian (II.6) into the linearized motion about a circular orbit and the Hamiltonian of the Hill problem to the first order in a small parameter related to the smallness assumptions made on the masses and their mutual separations.

In the restricted problem, the third mass has been assumed small as compared to the two others, thus it was physically reasonable to assume that the two remaining masses were moving approximately on a Keplerian circular orbit.

Similarly, in the Hill approximation, we assume that the first two masses are small compared to the third one (i.e., we assume m_1 and m_2 are small as compared to m_3) and that the two small masses are close together as compared to their separation from the third mass. Therefore, it seems physically reasonable to expect that the center of mass of the two small masses will move on an approximate Keplerian orbit around m_3 , that is the variables $(\mathbf{u}_2, \mathbf{v}_2)$ should appear in the Hamiltonian (II.6) as the Hamiltonian of a Kepler problem to the zeroth order.

Since the terms in (II.6) that depends on $1/|\mathbf{u}_2|$ are the last two terms, we can expand them by using a Legendre polynomials. Recall indeed that for any vector \mathbf{u} and \mathbf{v} such that $|\mathbf{v}| < |\mathbf{u}|$,

$$\frac{1}{|\mathbf{u} - \mathbf{v}|} = \frac{1}{|\mathbf{u}|} \sum_{n=0}^{\infty} \left(\frac{|\mathbf{v}|}{|\mathbf{u}|} \right)^n P_n(\cos \theta)$$

where $\cos \theta$ represent the cosine of the angle between the vectors \mathbf{u} and \mathbf{v} and P_n repre-

sents the Legendre polynomial of degree n . These polynomials are given by the following relations:

$$\begin{aligned} P_n(x) &= \frac{(-1)^n}{2^n n!} \cdot \frac{d^n}{dx^n} [(1 - x^2)^n] \\ P_0(x) &= 1 \end{aligned}$$

so that, $P_1(x) = x$ and $P_2(x) = \frac{1}{2}(3x^2 - 1)$.

Now it is clear that the term $\Delta = \frac{Gm_2 m_3}{|\mathbf{u}_2 - \nu_1 \mathbf{u}_1|} + \frac{Gm_1 m_3}{|\mathbf{u}_2 + \nu_2 \mathbf{u}_1|}$ can be expanded as:

$$\Delta = \frac{Gm_3}{|\mathbf{u}_2|} \sum_{n=0}^{\infty} b_n \left(\frac{|\mathbf{u}_1|}{|\mathbf{u}_2|} \right)^n P_n(\cos \theta) \quad (\text{II.15})$$

where $b_n = m_1(-\nu_1)^n + m_2\nu_0^n$ and $\cos \theta$ represents the cosine of the angle between the vectors \mathbf{u}_1 and \mathbf{u}_2 .

Since $b_0 = m_1 + m_2$ and $b_1 = 0$, we see that the Hamiltonian (II.7) can be rewritten as:

$$\mathcal{H} = \mathcal{H}_{Kepler} + \tilde{\mathcal{H}} \quad (\text{II.16})$$

where

$$\mathcal{H}_{Kepler} = \frac{|\mathbf{v}_2|^2}{2M_2} - \mathbf{u}_2^T \boldsymbol{\Omega} \mathbf{v}_2 - \frac{Gm_3(m_1 + m_2)}{|\mathbf{u}_2|} \quad (\text{II.17})$$

and

$$\tilde{\mathcal{H}} = \frac{|\mathbf{v}_1|^2}{2M_1} - \mathbf{u}_1^T \boldsymbol{\Omega} \mathbf{v}_1 - \frac{Gm_1 m_1}{|\mathbf{u}_1|} - \sum_{n=2}^{\infty} b_n \left(\frac{|\mathbf{u}_1|}{|\mathbf{u}_2|} \right)^n P_n(\cos \theta)$$

We are now ready to apply the scaling that will introduce a small parameter: let ϵ represent the ratio $\frac{m_1+m_2}{m_3}$, so that a small value of ϵ accounts for the smallness of the first two masses as compared to the third one. Then, in order to take into account the first order effects of this last large mass on the motion of m_1 and m_2 , we have to scale this effect relative to this small parameter. More precisely, we want to scale the distance u_2 such that the phase space region where the gravitational attraction of m_1 and m_2 on each other and

on m_3 are of the same order. That is, the smaller is ϵ , the farther the third mass must be as compared to the separation of m_1 and m_2 . In such a situation, the combined effect of m_1 and m_2 on m_3 is equivalent (to the first order in ϵ) to the effect of a particle of mass $m_1 + m_2$ that would be located at the center of mass of m_1 and m_2 . That is, m_3 follows an approximate two body motion, as appears in \mathcal{H}_{Kepler} , and a change of variable similar to (II.9) and (II.10) for the variables $(\mathbf{u}_2, \mathbf{v}_2)$ is appropriate.

The following change of variables:

$$\begin{aligned}\mathbf{u}_2 &= \epsilon^{-1/3} \mathbf{a} - \boldsymbol{\xi} \\ \mathbf{v}_2 &= -\epsilon^{1/3} M_2 \boldsymbol{\Omega} \mathbf{a} - \boldsymbol{\eta}\end{aligned}$$

results in writing (II.17) as[¶]:

$$\mathcal{H}_{Kepler} = \frac{1}{2} (\boldsymbol{\xi}, \boldsymbol{\eta})^T \mathbf{S}(\boldsymbol{\xi}, \boldsymbol{\eta}) + \mathcal{O}(\epsilon^{2/3})$$

where, as previously, the constant term $\mathcal{H}_{Kepler}(\epsilon^{-1/3} \mathbf{a}, -\epsilon^{-1/3} M_2 \boldsymbol{\Omega} \mathbf{a})$ has been set to zero without loss of generality. The matrix \mathbf{S} is given by the same formula as in the case of the restricted problem (formula (II.12)) but with M_1 replaced by M_2 and ω^2 satisfying the relation:

$$\omega^2 = \epsilon \frac{G(m_1 + m_2 + m_3)}{a^3}$$

Completing the above transformation by the identity transformation for the variables $(\mathbf{u}_1, \mathbf{v}_1)$, i.e.:

$$\mathbf{u}_1 = \mathbf{q}$$

$$\mathbf{v}_1 = \mathbf{p}$$

one obtains a symplectic transformation of the original full three body problem.

Using the relations:

[¶]See Appendix A for further details.

$$\epsilon \frac{Gm_3}{a^3} = \omega^2 (1 + \mathcal{O}(\epsilon)) \quad \text{and} \quad \frac{1}{|\boldsymbol{u}_2|^3} = \frac{\epsilon}{a^3} (1 + \mathcal{O}(\epsilon^{1/3}))$$

and substituting the above symplectic transformation into the Hamiltonian (II.16), one obtains the following splitting of the Hamiltonian:

$$\mathcal{H} = \frac{1}{2}(\boldsymbol{\xi}, \boldsymbol{\eta})^T \boldsymbol{S}(\boldsymbol{\xi}, \boldsymbol{\eta}) + \mathcal{H}_H + \mathcal{O}(\epsilon^{1/3}) \quad (\text{II.18})$$

where

$$\mathcal{H}_H = \frac{|\boldsymbol{p}|^2}{2M_1} - \boldsymbol{q}^T \boldsymbol{\Omega} \boldsymbol{p} - \frac{Gm_1 m_2}{|\boldsymbol{q}|} - \omega^2 M_1 |\boldsymbol{q}|^2 P_2(\cos \theta)$$

\mathcal{H}_H , the Hamiltonian of the Hill problem in natural units, can be rewritten in a more classical form by noting that $P_2(x) = \frac{1}{2}(3x^2 - 1)$ and $\cos \theta = \frac{\boldsymbol{q}^T \boldsymbol{a}}{|\boldsymbol{q}| \cdot |\boldsymbol{a}|}$. Then, the last term in \mathcal{H}_H is rewritten as:

$$|\boldsymbol{q}|^2 P_2(\cos \theta) = \frac{1}{2} \left\{ 3 \left(\frac{\boldsymbol{q}^T \boldsymbol{a}}{|\boldsymbol{a}|} \right)^2 - |\boldsymbol{q}|^2 \right\}$$

and the Hamiltonian \mathcal{H}_H reads:

$$\mathcal{H}_H = \frac{|\boldsymbol{p}|^2}{2M_1} - \boldsymbol{q}^T \boldsymbol{\Omega} \boldsymbol{p} - \frac{Gm_1 m_2}{|\boldsymbol{q}|} - \frac{\omega^2 M_1}{2} \left\{ 3 \left(\frac{\boldsymbol{q}^T \boldsymbol{a}}{|\boldsymbol{a}|} \right)^2 - |\boldsymbol{q}|^2 \right\} \quad (\text{II.19})$$

Note that the exponent 1/3 in the above scaling has been chosen so that the next term in the Legendre expansion (II.15) is small while letting $|\boldsymbol{q}|$ be measured in natural units. More precisely, let \boldsymbol{b} represent the radius of the nominal circular orbit (i.e., $\boldsymbol{b} = \epsilon^{-1/3} \boldsymbol{a}$ in the above scaling). The third term in (II.15) is proportional to $\omega^2 \frac{|\boldsymbol{q}|^3}{|\boldsymbol{b}|} P_3(\cos \theta)$ and imposing this term to be of the order ϵ results in $|\boldsymbol{q}| \sim \epsilon^{1/3} |\boldsymbol{b}|$. But, in order to keep $|\boldsymbol{q}|$ in natural units ($\mathcal{O}(1)$ in ϵ), we must scale \boldsymbol{b} by $\epsilon^{-1/3}$.

Physically, this reasoning tells us that the Hill approximation is accurate as long as the distance between the small masses is within $\epsilon^{1/3}$ of the mean distance to the perturbing body, where $\epsilon = (m_1 + m_2)/m_3$ is determined by the relative values of the masses. The length a thus represents a characteristic length of the Hill approximation. For example, the ratio ϵ in the case of the Earth, Moon, Sun system is $\sim 3 \times 10^{-6}$ and the ratio of the

Earth-Moon distance to the characteristic length a is ~ 0.1789 . Thus, the Hill problem is a good approximation to analyze the relative motion of the Earth and Moon as perturbed by the Sun.

As for the restricted problem, we see that an appropriate scaling allows us to separate the Hamiltonian of the three body problem, so that the motion of the two particles m_1 and m_2 decouples from the motion of the distant, large mass m_3 . That is, to study the motion of the masses m_1 and m_2 , one can assume the perturbing mass to be fixed in the rotating frame (in the direction indicated by the vector \mathbf{a} from the center of mass of the two small particles) and that its only effect is a linear perturbation (quadratic term in the Hamiltonian) of a Keplerian problem in rotating coordinates. In fact, the need to formulate the problem in a rotating frame is entirely due to the effect of this large mass.

Note that classically, the above scaling is described by saying that the perturbing mass is at infinity and with an infinite mass. This accounts for the relations between the quantities \mathbf{q} , \mathbf{a} , ω and m_3 when ϵ is taken to be zero in the above development. Of course, the transformation obtained with such a value for ϵ is not symplectic!

3.2. Normalization

As for the restricted problem, the Hill problem can be normalized by selecting proper length and time scales. Unlike the restricted problem, however, the normalized form of Hill's equations are parameterless, which allows us to scale any physical system modeled by Hill's equations into a unique “canonical” system.

We proceed similarly to the normalization of the restricted problem by introducing a symplectic change of variable and time with free parameters α , β and γ :

$$\begin{aligned}\mathbf{q} &= \alpha \tilde{\mathbf{q}} & \text{and} & \quad t = \gamma \tau \\ \mathbf{p} &= \beta \tilde{\mathbf{p}}\end{aligned}$$

Then the Hamiltonian (II.19) becomes:

$$\mathcal{H}_H = \frac{\gamma \beta}{\alpha} \frac{|\tilde{\mathbf{p}}|^2}{2M_1} - \gamma \omega \tilde{\mathbf{q}}^T \tilde{\boldsymbol{\Omega}} \tilde{\mathbf{p}} - \frac{\gamma}{\alpha^2 \beta} \frac{G m_1 m_2}{|\tilde{\mathbf{q}}|} - \frac{\gamma \alpha \omega^2}{\beta} \frac{M_1}{2} (3(\tilde{\mathbf{a}} \cdot \tilde{\mathbf{q}})^2 - |\tilde{\mathbf{q}}|^2)$$

where, as previously, tilde letters represent normalized quantities: $\tilde{\mathbf{a}} = \mathbf{a}/a$ and $\tilde{\Omega}$ is obtain using (II.5) and $\tilde{\omega} = \omega/\omega$.

Thus, we can see that choosing $\alpha = (G(m_1 + m_2)/\omega^2)^{1/3}$, $\beta = \omega M_1 \alpha$ and $\gamma = \omega^{-1}$, the Hamiltonian of the Hill problem normalizes to:

$$H_H = \frac{|\tilde{\mathbf{p}}|^2}{2} - \tilde{\mathbf{q}}^T \tilde{\Omega} \tilde{\mathbf{p}} - \frac{1}{|\tilde{\mathbf{q}}|} - \frac{1}{2} (3(\tilde{\mathbf{a}}^T \tilde{\mathbf{q}})^2 - |\tilde{\mathbf{q}}|^2)$$

No parameters remain in this Hamiltonian and the equations of motion can be written in vector form as:

$$\ddot{\tilde{\mathbf{q}}} + 2\tilde{\omega} \times \tilde{\mathbf{q}} + \tilde{\omega} \times (\tilde{\omega} \times \tilde{\mathbf{q}}) = -\frac{\tilde{\mathbf{q}}}{|\tilde{\mathbf{q}}|^3} - \tilde{\mathbf{q}} + 3(\tilde{\mathbf{a}}^T \tilde{\mathbf{q}})\tilde{\mathbf{a}}$$

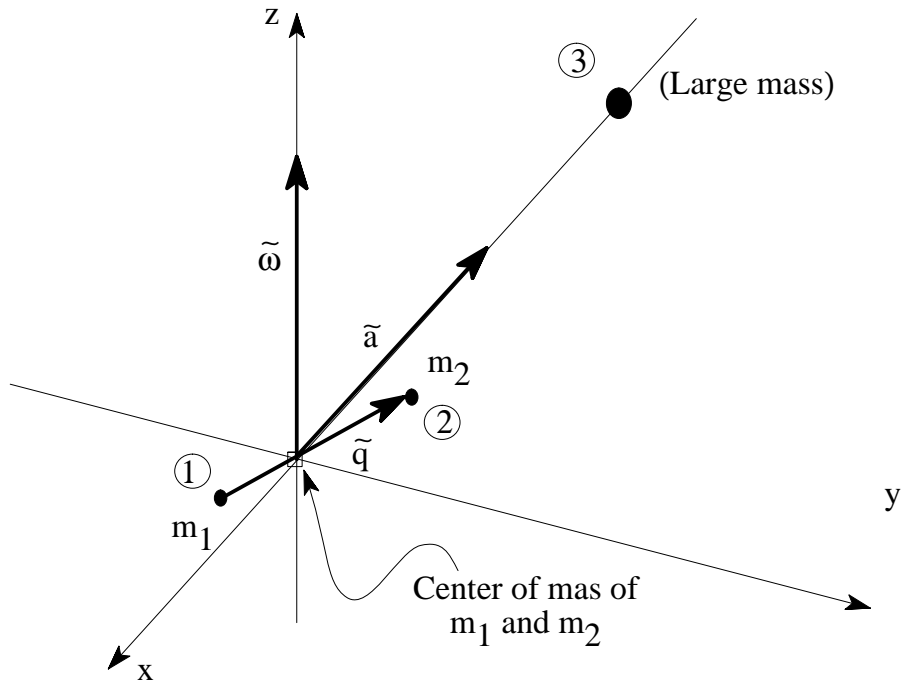


Figure II.3: Geometry of the Hill problem

Choosing the axes of the frame in a similar way as in the restricted problem, as shown on Figure II.3 (ω along the z -axis and a along the x -axis), one can rewrite the Hamiltonian of the Hill problem as:

$$\mathcal{H}_H = \frac{(p_x + y)^2 + (p_y - x)^2 + p_z^2}{2} - \frac{1}{r} - \frac{1}{2} (3x^2 - z^2)$$

where $r = \sqrt{x^2 + y^2 + z^2}$.

Then, the equations of motion can be rewritten in a standard form as:

$$\ddot{x} - 2\dot{y} = -\frac{x}{r^3} + 3x \quad (\text{II.20})$$

$$\ddot{y} + 2\dot{x} = -\frac{y}{r^3} \quad (\text{II.21})$$

$$\ddot{z} = -\frac{z}{r^3} - z \quad (\text{II.22})$$

That is, this canonical form of the equations has been obtained by setting the length and time scales l and τ , respectively, to be:

$$\begin{aligned} l &= \left(\frac{G(m_1 + m_2)}{\omega^2} \right)^{1/3} \\ \tau &= \frac{1}{\omega} \end{aligned}$$

3.3. Comments

In the derivation of the Hill problem in natural units, a preliminary symplectic scaling of the momenta $v_1 \rightarrow M_1 v_1$ and $v_2 \rightarrow M_1 v_2$ allows us to write the Hamiltonian of the Hill problem (II.19) without the dependence on M_1 :

$$\mathcal{H}_H = \frac{|\mathbf{p}|^2}{2} - \mathbf{q}^T \boldsymbol{\Omega} \mathbf{p} - \frac{G(m_1 + m_2)}{|\mathbf{q}|} - \omega^2 |\mathbf{q}|^2 P_2(\cos \theta) \quad (\text{II.23})$$

This reflects the fact that the scaling allows us to decouple the motion of the third particle, and as a result the relative position of the first two masses depends only on the total mass $m_1 + m_2$ of the system (\mathbf{q} indeed represents the relative position of m_1 and m_2), in a similar manner as for the Kepler problem. This scaling does not affect the units of length, time and mass.

Another derivation of the Hill problem from the full three body problem can be found in Hénon and Petit [15]. The above derivation has been inspired by the papers of Meyer on symplectic scaling and periodic orbits [24, 25] and Meyer and Schmidt [27]. The scaling adopted here differs from that used in [27], however, since, as for the restricted problem, our aim was to keep the natural units of length and time throughout to make explicit the

relationship between the normalized equations and the physical systems modeled by these equations. We should note, however, that a further reduction of the Clohessy-Wiltshire part of the Hamiltonian (II.18) results in an analogous theorem to the one quoted for the restricted problem (see [27] for the full details):

Any non-degenerate periodic solution of Hill's equations whose period is not a multiple of 2π can be continued into the full three body problem.

Besides the study of families of periodic orbits [12], the Hill problem has been investigated by several researchers who studied chaotic scattering [17, 12] and the destruction of KAM tori [36]. It is interesting to note, indeed, that a linear perturbation of an integrable problem may result in a non-integrable one.

4. The orbiter case: The restricted Hill problem

When the the mass m_2 is small compared to m_1 in the above Hill problem, one can further expand the Hamiltonian (II.23) so that the center of the frame is located at the center of mass of the first body, m_1 , and the resulting problem becomes independent of the small mass m_2 (to the first order in this small parameter). This further approximation is the same as the one performed in the restricted two body problem (see appendix A) where a spacecraft moving around the Earth is analyzed with an “inertial” frame fixed at the center of the Earth.

The restricted Hill problem can represent the motion of an orbiter around a planet or planetary satellite as perturbed by the Sun or a massive planet respectively.

4.1. The restricted Hill problem

We start from the Hill problem as defined by (II.23). Note that, in this problem, the center of the frame is at the center of mass of m_1 and m_2 . Now, assuming the second mass small as compared to the first one, we let $\epsilon = \frac{m_2}{m_1}$ and the Hamiltonian \mathcal{H}_H is rewritten as:

$$\mathcal{H}_H = \mathcal{H}_{HR} + \mathcal{O}(\epsilon)$$

where

$$\mathcal{H}_{HR} = \frac{|\mathbf{p}|^2}{2} - \mathbf{q}^T \Omega \mathbf{p} - \frac{Gm_1}{|\mathbf{q}|} - \frac{\omega^2}{2} \left\{ 3 \left(\frac{\mathbf{q}^T \mathbf{a}}{a} \right)^2 - |\mathbf{q}|^2 \right\} \quad (\text{II.24})$$

This Hamiltonian \mathcal{H}_{HR} is formally the same as \mathcal{H}_H with the mass $m_1 + m_2$ replaced by the mass m_1 , and, upon applying the normalization:

$$\begin{aligned} \mathbf{q} &= \left(\frac{Gm_1}{\omega^2} \right)^{1/3} \tilde{\mathbf{q}} \\ \mathbf{p} &= \omega m_2 \left(\frac{Gm_1}{\omega^2} \right)^{1/3} \tilde{\mathbf{p}} \\ t &= \frac{\tau}{\omega} \end{aligned}$$

the restricted Hill problem transforms into the same normalized form of the equations as the Hill problem (II.20)-(II.22).

Note here, however, that the Kepler part of the Hamiltonian \mathcal{H}_{HR} corresponds to a restricted two body problem with center of mass m_1 fixed at the origin of the rotating frame. This is indeed the case since, in this approximation, $\frac{m_1 Q_1 + m_2 Q_2}{m_1 + m_2} = Q_1 + \mathcal{O}(\epsilon)$, so that $u_2 = Q_3 - Q_1 + \mathcal{O}(\epsilon)$ is defined relative to the center of mass of the first body m_1 . Figure II.4 illustrates this situation.

4.2. Scaling to planetary satellites

The Hamiltonian \mathcal{H}_{HR} is independent of the mass of the spacecraft, m_2 , and only depends on the properties of the central planet/planetary satellite, m_1 . These properties are the gravitational parameter, $\mu = Gm_1$, and the orbital angular velocity, ω , around the large, perturbing mass. The parameter μ governs the two body effects of the motion while ω governs the third body effects. Setting $\omega = 0$ reduces the Hamiltonian \mathcal{H}_{HR} to a restricted two body problem.

Expressed in natural units, the equations of motions of the spacecraft are:

$$\ddot{x} - 2\omega \dot{y} = -\frac{\mu}{r^3}x + 3\omega^2 x$$

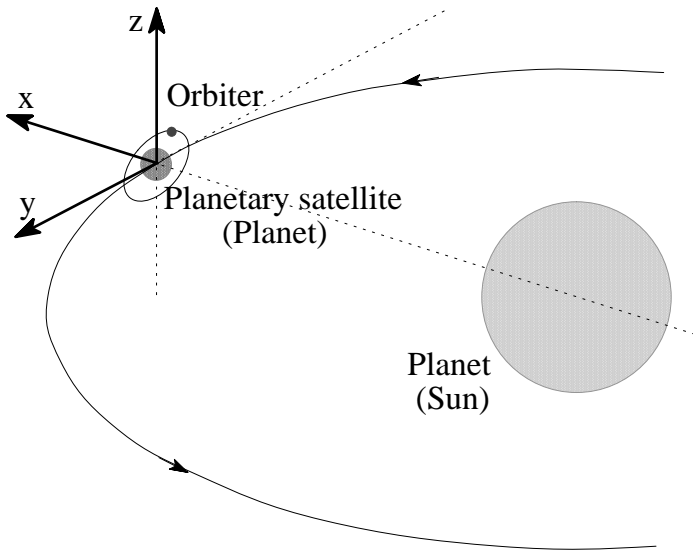


Figure II.4: Geometry of the Hill problem in the case of an orbiter

$$\begin{aligned}\ddot{y} + 2\omega \dot{x} &= -\frac{\mu}{r^3}y \\ \ddot{z} &= -\frac{\mu}{r^3}z - \omega^2 z\end{aligned}$$

where $r = \sqrt{x^2 + y^2 + z^2}$ is the distance of the spacecraft from the center of the attracting body m_1 .

Now, setting the length and time scales respectively as:

$$l = \left(\frac{\mu}{\omega^2}\right)^{1/3} \quad \text{and} \quad \tau = \frac{1}{\omega}$$

one obtains the normalized equations (II.20)-(II.22). This normalization is formally equivalent to setting $\omega = 1$ and $\mu = 1$ in the above equations.

The point here is that l and τ only depend on the planet/planetary satellite and, thus, determine the dynamical properties of its orbital environment. Any computation performed on the normalized model is scalable to a particular physical situation by multiplying length and time by l and τ , respectively. Table 1 gives the length and time scale for most of the planetary satellites of the solar system whose mass, orbital period and radius are known^{||},

^{||}The last column of this table will be explained in Chapter VI.

allowing one to scale the subsequent computations to any particular physical system modeled by the Hill equations. In the remainder of this dissertation, computations will be performed in the non-dimensional setting, with some scaled results given for the sake of illustration.

Finally, we should note that these scalings depend both on the physical parameters of the primaries as well as their orbital characteristics (mean motion ω). Therefore, planetary satellites of rather different mass and radius may have the same normalized radius, as is approximately the case for Io (Jupiter), Dione (Saturn) and Ariel (Uranus) (see Table 1). Similarly, planetary satellites with similar physical radii can have very different dynamical properties, and thus a large difference in their normalized radius, as for example with the Jupiter satellites Amalthea and Himalia. As we will see in the next chapter, low altitude, stable circular orbits around Himalia are possible while their existence is doubtful for the case of Amalthea.

4.3. From the restricted to the Hill problem

The restricted Hill problem has been derived from the Hill problem by assuming that the second mass was small as compared to the first one. The same situation can occur in the restricted three body problem, thus leading to the same problem.

This subsection indicates how to derive the restricted Hill problem from the restricted three body problem in order to complete the description of the relationship between the Hill and the restricted problems. Moreover, this point of view was the original one adopted by Hill in his “Researches in the Lunar theory”*** [18]. Starting from the Hamiltonian of the restricted problem (II.14) and applying the following symplectic change of variables:

$$\mathbf{q} = \mathbf{u} + \nu_1 \mathbf{a}$$

$$\mathbf{p} = \mathbf{v} - \Omega \mathbf{a}$$

***Though he did not use the Hamiltonian formalism.

one obtains the following Hamiltonian:

$$\mathcal{H}_R = \frac{|\mathbf{v}|^2}{2} - \mathbf{u}^T \Omega \mathbf{v} - \frac{Gm_2}{|\mathbf{u}|} + \left\{ \mathbf{u}^T \Omega \Omega \mathbf{a} - \frac{Gm_1}{|\mathbf{u} + \mathbf{a}|} \right\}$$

where the constant term $(\nu_1 - \frac{1}{2}) \mathbf{a}^T \Omega \Omega \mathbf{a}$ has been removed from the Hamiltonian since it does not change the equations of motion.

Then, one can expand the term $\frac{Gm_1}{|\mathbf{u} + \mathbf{a}|}$ in a similar way as for the derivation of the Hill problem:

$$\frac{Gm_1}{|\mathbf{u} + \mathbf{a}|} = \frac{Gm_1}{a} - \mathbf{u}^T \left(\frac{Gm_1}{a^3} \mathbf{a} \right) + \frac{Gm_1}{a^3} |\mathbf{u}|^2 P_2(\cos \theta) + \frac{Gm_1}{a^3} \mathcal{O} \left(\frac{|\mathbf{u}|^3}{a} \right)$$

where, as previously, P_2 represents the Legendre polynomial of degree 2 and $\cos \theta$ is the cosine of the angle between the vectors \mathbf{u} and \mathbf{a} .

Letting $\epsilon = \frac{m_2}{m_1}$, the relations between \mathbf{a} and $\omega^{\dagger\dagger}$ can be written as:

$$\omega^2 = \frac{Gm_1}{a^3} + \mathcal{O}(\epsilon) \quad \text{and} \quad \Omega \Omega \mathbf{a} = -\frac{Gm_1}{a^3} \mathbf{a} + \mathcal{O}(\epsilon)$$

so that:

$$\mathbf{u}^T \left(\frac{Gm_1}{|\mathbf{a}|^3} \mathbf{a} \right) = -\mathbf{u}^T \Omega \Omega \mathbf{a} + \mathcal{O}(\epsilon)$$

and, upon removing the constant terms, one obtains the following Hamiltonian:

$$\mathcal{H}_R = \frac{|\mathbf{v}|^2}{2} - \mathbf{u}^T \Omega \mathbf{v} - \frac{Gm_2}{|\mathbf{u}|} - \omega^2 |\mathbf{u}|^2 P_2(\cos \theta) + \mathcal{O} \left(\epsilon, \frac{|\mathbf{u}|^3}{a} \right)$$

As for the Hill problem, we can let $\mathbf{a} = \epsilon^{-1/3} \mathbf{b}$ (where $|\mathbf{b}|$ is assumed to be of the same order as $|\mathbf{u}|^3$, consistent with the assumption that the disturbing body is far from the primary m_2), so that the above Hamiltonian reduces to the Hamiltonian of the restricted Hill problem to the first order in $\epsilon^{1/3}$. (Note that the notation is different from the restricted Hill problem as given by (II.24). Here, the disturbing body is m_1 and the spacecraft is represented by m_3 and the characteristic length is given by $|\mathbf{b}|$).

^{††}See equations (II.11) and Appendix A.

4.4. Comments

The terminology “restricted Hill problem” is not used in standard practice and no distinction is generally made between the Hill problem and its restricted form. These models are indeed represented by the same sets of equations, even though the length scales are slightly different. This situation is, in fact, the same as for the two body problem (see Appendix A) and thus the common usage will be used in the remainder of this dissertation.

As we have seen in this section, the Hill and restricted problems are not incompatible and the orbiter case represents a physical situation that can be modeled by either of these models. However, as indicated in the introduction, the Hill problem has the non-negligible advantage of simplicity.

These two models can also be obtained for the four body problem where the restricted and Hill approximations can be used in conjunction to model the motion of a spacecraft in the Earth-Moon environment, as perturbed by the Sun [30].

CHAPTER III

DYNAMICS OF THE HILL PROBLEM

This chapter presents some features of the dynamics in the Hill problem that are used in the subsequent chapters. The results are presented in the normalized form of the Hill problem, as given by equations (II.20)-(II.22).

The first section presents the basic properties of Hill's equations, such as the invariance of the equatorial plane, the equilibrium solutions and the symmetries present in this problem. This last property is especially useful in numerical investigations since it generally reduces (by at least a factor of four) the regions of phase space to be analyzed.

The second section investigates the implications of the Hamiltonian nature of the Hill problem, by presenting the basic topology and geometry of the energy manifold. The key points consist of the existence of a minimum threshold in the value of the Hamiltonian before escape becomes possible, and a maximum value of energy for which all transit trajectories will have a closest approach to the primary (i.e., periapsis passage).

The third section presents the reformulation of the Hill problem in terms of orbital elements. This formulation will be used in the following chapters. Orbital elements represent the most commonly used set of variables in celestial mechanics and astrodynamics and many properties are easily expressed in terms of them. In particular, all the results obtained in terms of orbital elements can be compared to a two body model, where these elements are constants of the motion. This section also presents the Delaunay variables, which can be thought of as a canonical representation of the elements.

While the nonlinear dynamics of interest to us are on the order of the length and time

scale of the Hill problem, dynamics close to and far from the primary are given attention as they contain some of the features needed in the orbit transfers considered later. Also, these dynamics represent a link between two commonly used models in spacecraft trajectory analyses, the Kepler and restricted three body problems.

In particular, the investigation of dynamics close to the primary, presented in Section 4, allows us to establish the existence of stable, low altitude, circular orbits. Motion of a spacecraft can then be approximated by a Keplerian circular orbit when close to the primary, for relatively short time spans. The presentation uses both a symplectic technique, allowing us to reduce the Hamiltonian of the Hill problem into a Kepler problem to the first order in a small parameter and to prove the existence of KAM tori, and an averaging approach.

Finally, a brief analysis of motion far from the primary is performed using the Clohessy-Wiltshire equations. These dynamics are related to the restricted problem in the case of an orbiter. These dynamics can be considered as an outer layer between the Hill and the restricted problem and can be used to patch the results obtained from the escape problem to a restricted model.

Note that this chapter is not exhaustive and only presents the properties that are relevant for the subsequent results. Many topics of interest in the Hill problem are not mentioned in this chapter.

1. First properties

Recall that the normalized Hill problem is given by the equations:

$$\ddot{x} - 2\dot{y} = -\frac{x}{r^3} + 3x \quad (\text{III.1})$$

$$\ddot{y} + 2\dot{x} = -\frac{y}{r^3} \quad (\text{III.2})$$

$$\ddot{z} = -\frac{z}{r^3} - z \quad (\text{III.3})$$

where $r = \sqrt{x^2 + y^2 + z^2}$ is the magnitude of the relative position vector between the small masses. The rotating frame in which these equations are formulated has been presented in Figure II.4 for the case of an orbiter.

Looking at these equations, we see that the only out-of-plane force acting on the particle is proportional to its altitude over the equatorial plane (i.e. the (x, y) -plane). Thus, if at any given instant one has $z = 0$ and $\dot{z} = 0$, the particle will remain in the equatorial plane for all times. That is, the equatorial plane is invariant under the flow and one can consider the Hill problem to be restricted in this plane, as was done in the original paper by Hill [18]. As we will see subsequently, the dynamics in the planar case and in the spatial problem are somewhat different, and generally easier in the planar problem. However, both cases are of interest and we will consider both of them in the sequel.

1.1. Libration points

The next, almost obvious, property of the Hill problem is the existence of equilibrium solutions. These can be determined by setting all the derivatives to zero in the above equations and solving for the remaining variables, or by computing the critical points of the Hamiltonian (II.20).

These equilibrium solutions are located on the x -axis at $x = \pm (\frac{1}{3})^{1/3}$. The point with negative abscissa is generally denoted L_1 and the one with positive abscissa is denoted L_2 . We will denote $x_c = (\frac{1}{3})^{1/3}$ in the sequel. These solutions are called the libration points because of the existence of periodic and quasi-periodic orbits in their vicinity.

Indeed, the linearized equations around these points are given by:

$$\frac{d}{dt} \begin{bmatrix} \mathbf{q} \\ \dot{\mathbf{q}} \end{bmatrix} = \begin{bmatrix} \mathbf{O} & \mathbf{I} \\ \mathbf{A}_1 & \mathbf{A}_2 \end{bmatrix} \begin{bmatrix} \mathbf{q} \\ \dot{\mathbf{q}} \end{bmatrix}$$

where \mathbf{O} and \mathbf{I} are, respectively, the 3×3 zero and identity matrices and \mathbf{A}_1 and \mathbf{A}_2 are given, respectively, by:

$$\mathbf{A}_1 = \begin{bmatrix} 9 & 0 & 0 \\ 0 & -3 & 0 \\ 0 & 0 & -4 \end{bmatrix} \quad \text{and} \quad \mathbf{A}_2 = \begin{bmatrix} 0 & -2 & 0 \\ 2 & 0 & 0 \\ 0 & 0 & 0 \end{bmatrix}$$

The eigenvalues of these linearized equations are given by:

$$\begin{aligned}\lambda_1^\pm &= \pm\sqrt{2\sqrt{7}+1} \\ \lambda_2^\pm &= \pm i\sqrt{2\sqrt{7}-1} \\ \lambda_3^\pm &= \pm 2i\end{aligned}$$

The first four eigenvalues, λ_1^\pm and λ_2^\pm , correspond to the planar dynamics while the eigenvalues λ_3^\pm represent the out-of-plane dynamics. Note that in the linearization, these dynamics are decoupled. The out-of-plane dynamics consist only of periodic motions while the in-plane dynamics consist of unstable periodic orbits with two dimensional stable and unstable manifolds.

A generalization of a classical theorem of Lyapunov due to Moser [29] allows us to extend this picture to the nonlinear system (equations (III.1)-(III.3)). More precisely, the dynamics of the nonlinear equations in the planar case consist of a family of periodic orbits (that is a two dimensional manifold in phase space) starting at the libration points with two dimensional stable and unstable manifolds for each periodic orbit. These periodic orbits are generally referred to as Lyapunov orbits. In the spatial problem, there is a center manifold of dimension 4 that includes the Lyapunov orbits and tori of quasi-periodic orbits. These orbits are unstable and two dimensional stable and unstable manifolds are associated with them.

Figure III.1 shows an example of Lyapunov orbits at L_1 and L_2 . These dynamics will be investigated further in Chapter VI.

Finally, note that, L_1 and L_2 are also present in the restricted three body problem. As compared to the Hill problem, these points are not symmetric about the origin and their abscissa are given by (modulo the shift of origin and the scaling presented in the previous chapter):

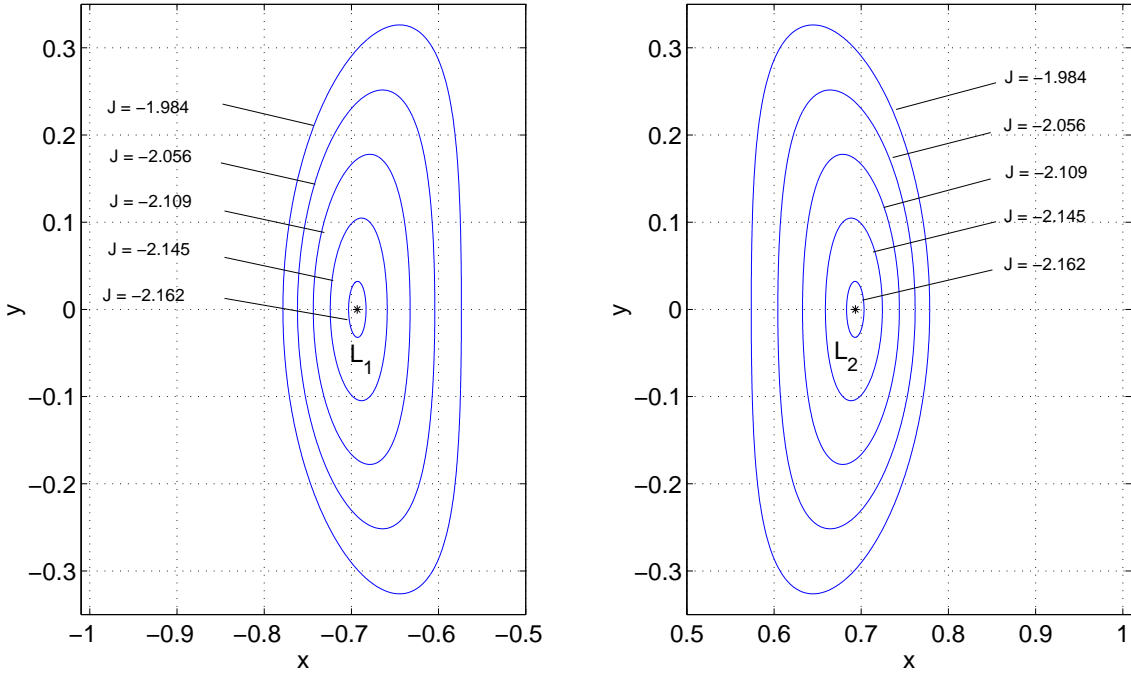


Figure III.1: A few Lyapunov periodic orbits around L_1 and L_2 .

$$x_{L_1} = -\left(\frac{1}{3}\right)^{1/3} - \frac{1}{3}\left(\frac{\mu}{3}\right)^{1/3} + \frac{1}{9}\left(\frac{\mu}{3}\right)^{2/3} + \dots \quad \text{and} \quad x_{L_2} = \left(\frac{1}{3}\right)^{1/3} + \frac{1}{3}\left(\frac{\mu}{3}\right)^{1/3} + \frac{1}{9}\left(\frac{\mu}{3}\right)^{2/3} + \dots$$

In the limiting case of the orbiter problem, with $\mu \rightarrow 0$, we obtain the values of the Hill problem . The “almost symmetries” (the dynamics close to L_1 and L_2 are almost isometric) present in the restricted problem are fully realized in the limiting case (L_1 and L_2 are symmetric with respect to the origin). However, the limiting process destroys the additional equilibrium solutions of the restricted problem (L_3 and the equilateral points L_4 and L_5).

1.2. Discrete symmetries

As we have seen for the case of the libration points L_1 and L_2 , the Hill model takes advantage of “almost symmetries” present in the restricted three body problem for small μ by turning them into exact symmetries.

More precisely, if $(x, y, z, \dot{x}, \dot{y}, \dot{z}, t)$ denotes a solution of the equations of motion, then

the trajectories obtained by applying the following transformations are also valid solutions:

$$\begin{aligned}(x, y, z, \dot{x}, \dot{y}, \dot{z}, t) &\xrightarrow{S_1} (-x, y, z, \dot{x}, -\dot{y}, -\dot{z}, -t) \\(x, y, z, \dot{x}, \dot{y}, \dot{z}, t) &\xrightarrow{S_2} (x, -y, z, -\dot{x}, \dot{y}, -\dot{z}, -t) \\(x, y, z, \dot{x}, \dot{y}, \dot{z}, t) &\xrightarrow{S_3} (x, y, -z, \dot{x}, \dot{y}, -\dot{z}, t)\end{aligned}$$

The compositions of these three symmetries yield other symmetries, notably the compositions of (1),(2) and (1),(2),(3) yield:

$$\begin{aligned}(x, y, z, \dot{x}, \dot{y}, \dot{z}, t) &\xrightarrow{S_4} (-x, -y, z, -\dot{x}, -\dot{y}, \dot{z}, t) \\(x, y, z, \dot{x}, \dot{y}, \dot{z}, t) &\xrightarrow{S_5} (-x, -y, -z, -\dot{x}, -\dot{y}, -\dot{z}, t)\end{aligned}$$

This last symmetry is a pure symmetry about the origin which results in the symmetry of L_1 and L_2 . More generally, all the dynamics that are present in the vicinity of L_1 are also present in the vicinity of L_2 , and the corresponding trajectories are symmetric about the origin. This is the case for the Lyapunov orbits, as is clearly apparent on Figure III.1, and for the stable/unstable manifolds of these periodic orbits. In other words, if $P(\mathcal{X})$ is a property of a trajectory close to L_2 , then $S_5(P(\mathcal{X}))$ will be the corresponding property of the symmetric trajectory in the vicinity of L_1 . This will apply to the case of escaping trajectories as discussed in Chapter VI, where the one-to-one correspondence between L_1 and L_2 will allow us to restrict the analysis to L_2 -escaping trajectories.

From S_3 , we see that the same is true for reflections about the (x, y) -plane, allowing us, in the case of escaping trajectories, to restrict the computations to trajectories having a positive z -coordinate. This will be used to simplify the computation of the Poincaré maps.

The symmetries S_1 and S_2 involve a reflection in time, and applied to the case of the dynamics close to the libration points, we see that the stable and unstable manifolds are symmetric about the (x, z) -plane. Again, this can be seen on Figure III.1. In the case of escaping trajectories, applying S_1 and S_3 results in capture trajectories, and the analysis performed in Chapter VI will directly apply to this class of trajectories. Further discussion of these cases will be considered then.

Thus, we see that the many symmetries present in the Hill problem can significantly simplify the computation and analysis for preliminary studies, and allows us to see the similarities between several classes of trajectories which are otherwise different in the setting of the restricted three body problem.

2. The Jacobi constant and the energy manifold

We have seen in the previous chapter that the Hill problem can be written in normalized form as a Hamiltonian system with Hamiltonian given by:

$$\mathcal{H}_H = \frac{|\mathbf{p}|^2}{2} - \mathbf{q}^T \boldsymbol{\Omega} \mathbf{p} - \frac{1}{|\mathbf{q}|} - \frac{1}{2} \{ 3(\mathbf{q}^T \mathbf{a})^2 - |\mathbf{q}|^2 \} \quad (\text{III.4})$$

(tildes have been removed, as compared to equation (II.20), for notational convenience).

Since this Hamiltonian is independent of time, it is conserved along the flow defined by the equations of motion. This integral of motion, written in position/velocity form, is known as the Jacobi constant* and is denoted J .

$$J(\mathbf{q}, \dot{\mathbf{q}}) = \frac{|\dot{\mathbf{q}}|}{2} - \frac{1}{|\mathbf{q}|} - \frac{1}{2} \{ 3(\mathbf{q}^T \mathbf{a})^2 + |\boldsymbol{\Omega} \mathbf{q}|^2 - |\mathbf{q}|^2 \}$$

Written in Cartesian coordinates, this integral takes the form:

$$J = \frac{v^2}{2} - \frac{1}{r} - \frac{1}{2} (3x^2 - z^2) \quad (\text{III.5})$$

where $v = |\dot{\mathbf{q}}| = \sqrt{\dot{x}^2 + \dot{y}^2 + \dot{z}^2}$ represents the speed of the spacecraft in the rotating frame and $r = |\mathbf{q}| = \sqrt{x^2 + y^2 + z^2}$ represents its distance from the center of the primary.

2.1. The energy manifold and zero velocity surfaces

The existence of this integral of motion has an immediate consequence. At a fixed value of J , motion is constrained to lie on the energy manifold \mathcal{E} , which is five dimensional in the spatial problem and three dimensional in the planar problem. The manifold \mathcal{E} can be

*This name is sometimes given in the literature to the quantity $-2\mathcal{H}_H$. Note that $\mathbf{p} = \dot{\mathbf{q}} - \boldsymbol{\Omega} \mathbf{q}$.

expressed in position/velocity form as:

$$\mathcal{E}(C) = \{(\mathbf{q}, \dot{\mathbf{q}}) \mid J(\mathbf{q}, \dot{\mathbf{q}}) = C\}$$

Notably, the projection of \mathcal{E} onto position space, called the Hill region, can have a bounded component, thus implying bounded regions of motion. This region is denoted \mathcal{H} :

$$\mathcal{H}(C) = \{\mathbf{q} \mid \exists \dot{\mathbf{q}} : J(\mathbf{q}, \dot{\mathbf{q}}) = C\}$$

In order to investigate the topology and geometry of these regions, let us first remark that the boundaries of \mathcal{E} and \mathcal{H} are the same and correspond to the surfaces of zero velocity, \mathcal{Z} , defined by setting $v = 0$ in the definition of J .

$$\mathcal{Z}(J) = \left\{ \mathbf{q} \mid J + \frac{1}{|\mathbf{q}|} + \frac{1}{2} (3(\mathbf{q}^T \mathbf{a})^2 + |\Omega \mathbf{q}|^2 - |\mathbf{q}|^2) = 0 \right\}$$

Away from these surfaces, the pre-image of a point under the natural projection of \mathcal{E} over \mathcal{H} is a two-sphere representing all possible directions of the velocity vector at that position. Indeed, the dependence of J on $\dot{\mathbf{q}}$ is only through its magnitude, v , so that for a given value of the Jacobi constant and a given position, the magnitude of the velocity vector is fixed.

Thus we see that the topology of the energy manifold and Hill regions are really determined by the surfaces of zero velocity. The topology of these surfaces change at the critical points of the Jacobi constant when v is set to zero:

$$\nabla_{\mathbf{q}} J = \begin{bmatrix} -\frac{x}{r^3} + 3x \\ -\frac{y}{r^3} \\ -\frac{z}{r^3} - z \end{bmatrix}$$

Thus, we see that $\nabla_{\mathbf{q}} J = 0$ for $x = \pm (\frac{1}{3})^{1/3}$, $y = z = 0$, that is the first singularity in the zero velocity surfaces occurs at the libration points L_1 and L_2 . These critical points occur for a value of J equal to $J_c = -\frac{3}{2}(3)^{1/3}$ and it can be checked that they are non-degenerate with index two. In the compact case, Morse theory indicates that the topology

of the surface for $J < J_c$ and $J > J_c$ differs by a two-cell. In our case, the surfaces are non-compact but, as we see below, a similar situation occurs. More precisely, for $J < J_c$, \mathcal{Z} has three different connected components, one of which (the closest to the primary) is bounded. For $J > J_c$, the two unbounded components connect with the bounded one by forming two “throats” that allow particles to move from the inner side of the primary’s orbit to its outer side. The subsection below investigates this change in more detail.

The second singularity of the zero velocity surface is obtained when $x = z = 0$ and $y \rightarrow \infty$. As we see below, this case does indeed correspond to a change in the topology of the surfaces, even though the singularity is degenerate. In this case, $J = 0$ and the zero velocity surfaces detach from the (x, y) -plane.

2.2. A closer look at the zero velocity surfaces

In order to obtain a more precise picture of these zero velocity surfaces, it is convenient to rewrite the defining relation in spherical coordinates, as defined by:

$$\begin{aligned} x &= r \cos \phi \cos \lambda \\ y &= r \sin \phi \cos \lambda \\ z &= r \sin \lambda \end{aligned}$$

so that $|\mathbf{q}| = r$, ϕ is the longitude ($0 \leq \phi < 2\pi$) and λ is the latitude ($-\pi \leq \lambda \leq \pi$).

Then the relation $J + \frac{1}{|\mathbf{q}|} + \frac{1}{2} (3(\mathbf{q}^T \mathbf{a})^2 + |\boldsymbol{\Omega} \mathbf{q}|^2 - |\mathbf{q}|^2) = 0$ is rewritten as (after multiplication by $2|\mathbf{q}|$):

$$g(\phi, \lambda)r^3 + 2Jr + 2 = 0 \quad (\text{III.6})$$

where $g(\phi, \lambda) = 3 \cos^2 \phi \cos^2 \lambda - \sin^2 \lambda = \frac{1}{r^2} (3x^2 - z^2)$. This equation is a reduced cubic equation in r and an explicit solution is available through the use of Cardan’s formulas (see Appendix C).

Note that $g(\phi, \lambda) = 0$ on the planes $z = \pm \sqrt{3}x$. From equation (III.6), we deduce that the zero velocity surfaces will intersect these planes at a fixed distance $r = -\frac{1}{J}$ from the

origin. These intersections will only exist for $J < 0$. The projection of these intersections on the (x, y) -plane corresponds to ellipses of semi-major axis equal to $\frac{1}{|J|}$ along the y -axis and semi-minor axis equal to $\frac{1}{2|J|}$ along the x -axis.

When $J \geq 0$ the zero velocity surfaces do not intersect these planes, nor do they restrict motion in the equatorial plane (i.e., the (x, y) -plane). Indeed, the discriminant of the reduced cubic (III.6) is:

$$D = -\frac{4 \times 27}{g^2(\phi, \lambda)} \left\{ 1 + \frac{1}{g(\phi, \lambda)} \left(\frac{2J}{3} \right)^3 \right\}$$

so that $D < 0$ when $g(\phi, \lambda) > 0$. This implies the existence of a single real root of the equation, but Descartes' rule (see Appendix C) indicates that this root is negative (i.e., there is no solution since r represents a distance and is, by definition, positive). Thus, there is no component of the zero velocity surface in the region $g(\phi, \lambda) > 0$ when $J \geq 0$.

Now, from the definition of $g(\phi, \lambda)$, it is clear that $-1 \leq g(\phi, \lambda) \leq 3$, with $g(\phi, \lambda) = -1$ on the z -axis and $g(\phi, \lambda) = 3$ on the x -axis. Thus, this short discussion shows that for $J \geq 0$, the zero velocity surfaces do not cross the equatorial plane and only restrict the out-of plane motion.

Since the applications where the zero velocity surfaces enter into play (chapter VI) only involve low energies ($J < 0$), the remainder of this discussion will focus on this case. Appendix C contains further material on the case $J \geq 0$.

When $J < 0$ and $g(\phi, \lambda) < 0$ (polar region), it is clear that $D < 0$ and, by Descartes' rule, the only real solution of (III.6) is positive. Hence, in the polar region, the zero velocity surfaces intersect the radial lines at only one point. This solution tends to $r = -\frac{1}{J}$ as $g(\phi, \lambda) \rightarrow 0^-$.

For $g(\phi, \lambda) > 0$, three cases have to be considered:

- When $J < J_c$, $D > 0$ and Descartes' rule can be used to show that there are exactly two distinct positive solutions of (III.6) for each ϕ and λ . By examining these solutions (see Appendix C), one can see that the smallest solution connects to

the polar cap at $r = -\frac{1}{J}$ on the planes $g(\phi, \lambda) = 0$, and the other solution to $+\infty$ as $g(\phi, \lambda) \rightarrow 0^+$. Hence, for $J < J_c$, the zero velocity surfaces have one bounded component near the primary and two unbounded components further apart. Motion in the bounded component is, *per force*, bounded, and particles close to the primary cannot escape. Figure III.2 gives a graphical representation of this case.

- When $J = J_c$, the discussion of the above case ($J < J_c$) holds except on the x -axis where $g(\phi, \lambda) = 3$. At this location, $D = 0$ and the two distinct real positive roots collapse into a single, real, positive root so that the three component of \mathcal{Z} touch at the libration points. Note that this case is the only value of J for which \mathcal{Z} (and hence \mathcal{E} and \mathcal{H}) is not a manifold since the points of contact at the libration points represent two singularities of the surface. Figure III.3 illustrates this situation.
- When $J_c < J < 0$, the zero velocity surface opens up from L_1 and L_2 as can be seen in Figure III.4. This can also be shown from the defining equation (III.6). Indeed, in this case, $\left(\frac{2|J|}{3}\right)^3 < 3$ and, in the region $g(\phi, \lambda) > \left(\frac{2|J|}{3}\right)^3$, $D < 0$. The only real root can be checked to be negative, so that no part of \mathcal{Z} closes the regions near the libration points. When $g(\phi, \lambda) = \left(\frac{2|J|}{3}\right)^3$, $D = 0$ and the only real positive root is the double root. For $g(\phi, \lambda) < \left(\frac{2|J|}{3}\right)^3$, we again found two distinct positive real roots, the smallest of which connects with the polar cap at $r = -\frac{1}{J}$ when $g(\phi, \lambda) = 0$, while the other root tends to $+\infty$. Thus, when $J_c < J < 0$, \mathcal{Z} has two holes close to the libration points and transit through these openings is now possible. Some particles from the vicinity of the primary can escape, even though bounded motion can still exist, as we will see in section 5.

We finish this discussion with a few more points that will be needed in chapter VI. First, note that while the openings start at the libration points L_1 and L_2 , the boundaries, as defined by $D = 0$ in the above discussion, lie on spheres whose radii increase with J . More precisely, $D = 0$ for $g(\phi, \lambda) = \left(\frac{2|J|}{3}\right)^3$. Then, one can notice that a solution r of

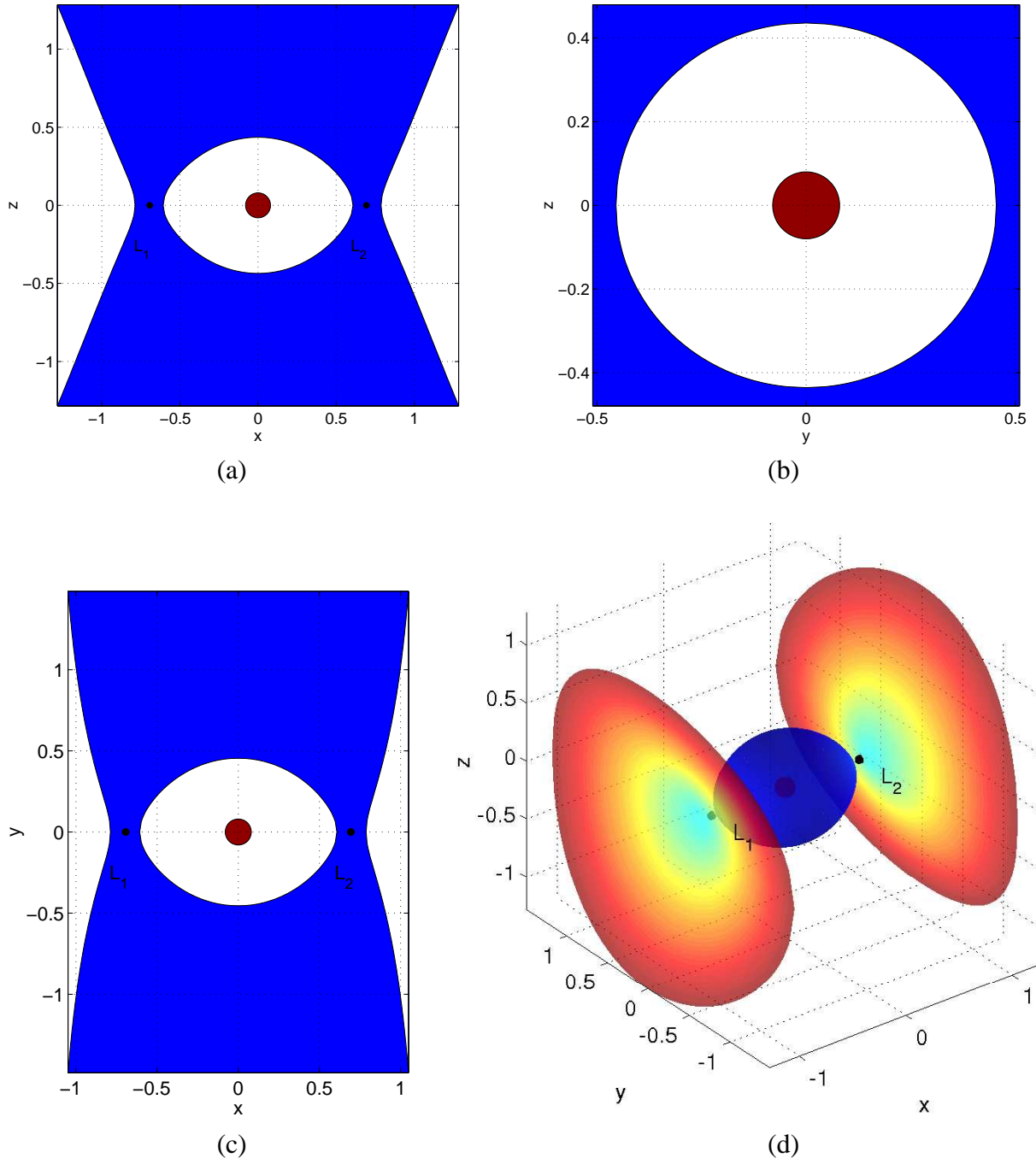


Figure III.2: Zero velocity surfaces for $J = -2.2$. (a) (x, z) -projection. (b) (y, z) -projection. (c) (x, y) -projection. (d) Spatial representation. The blue regions represent the forbidden regions of motion at the given value of Jacobi constant. The surface of Europa (normalized radius of 0.08) is also represented.

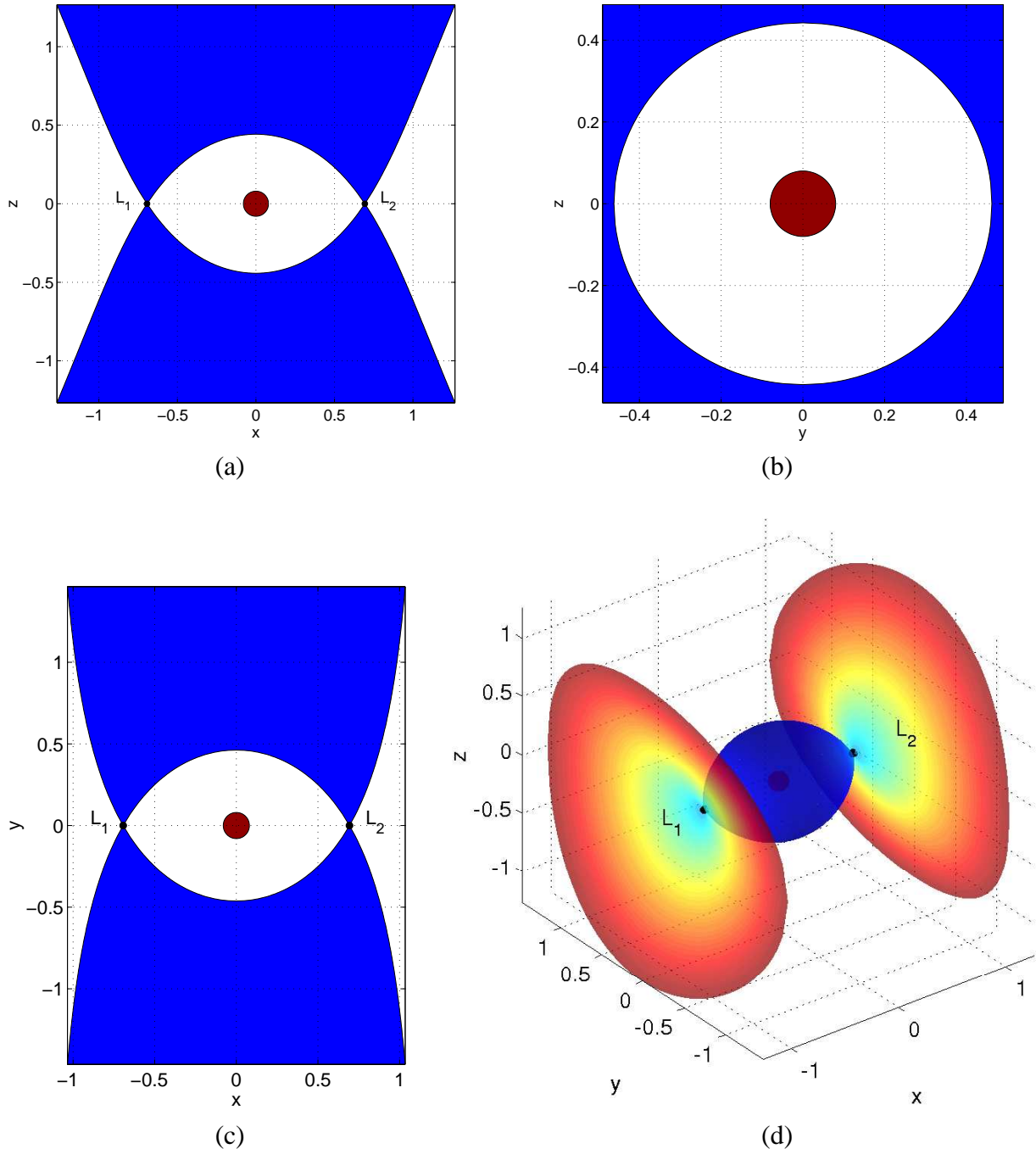


Figure III.3: Zero velocity surfaces for $J = J_c$. (a) (x, z) -projection. (b) (y, z) -projection. (c) (x, y) -projection. (d) Spatial representation. The blue regions represent the forbidden regions of motion at the given value of Jacobi constant. The surface of Europa (normalized radius of 0.08) is also represented.

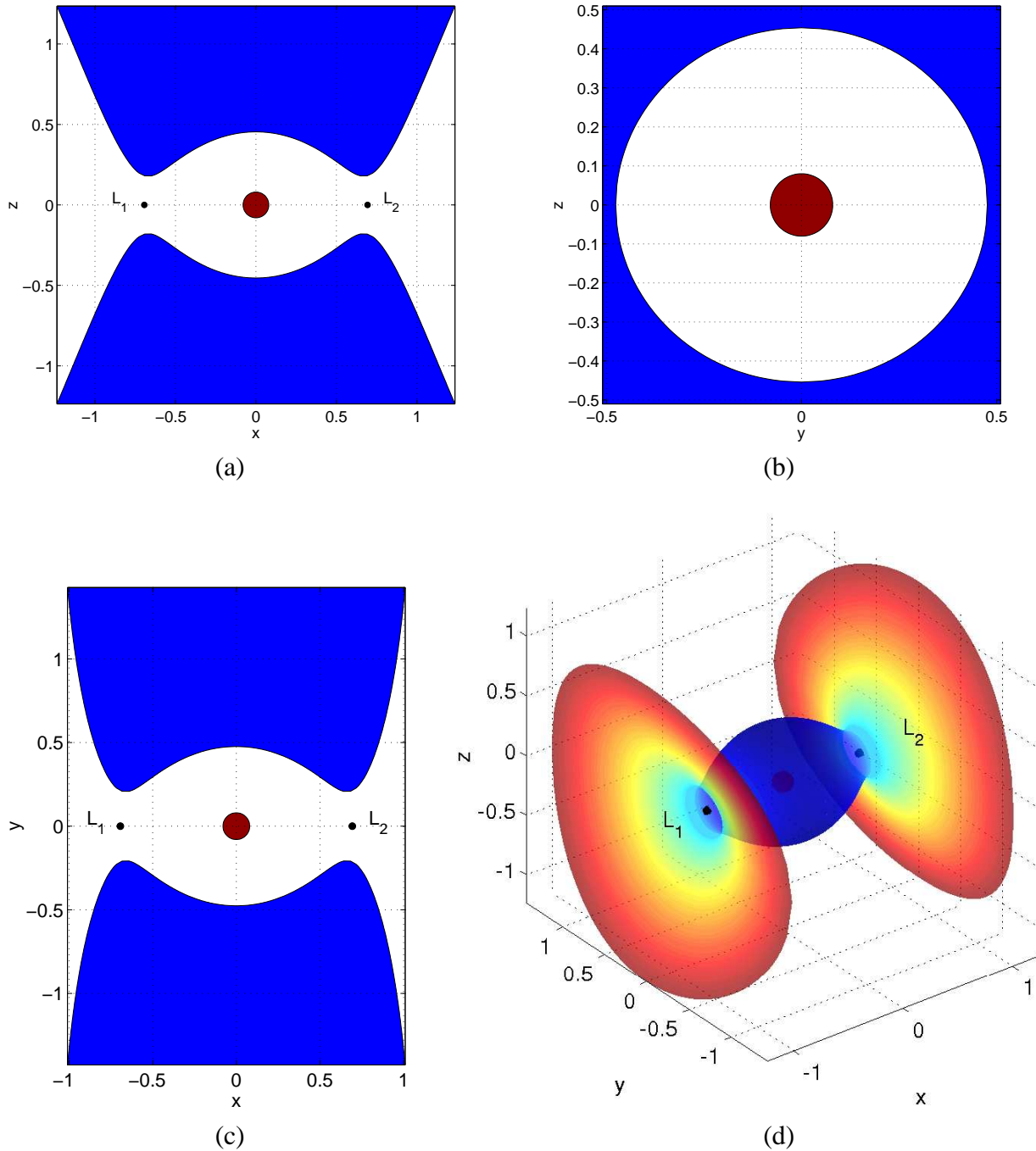


Figure III.4: Zero velocity surfaces for $J = -2.1$. (a) (x, z) -projection. (b) (y, z) -projection. (c) (x, y) -projection. (d) Spatial representation. The blue regions represent the forbidden regions of motion at the given value of Jacobi constant. The surface of Europa (normalized radius of 0.08) is also represented.

(III.6) depends on ϕ and λ only through the function g , so that, at constant g , r is constant. In the case $D = 0$, one can check that $r = \sqrt{\frac{2|J|}{3g(\phi,\lambda)}} = \frac{3}{2|J|}$, that is, the openings, as defined by tangency with the radial line, correspond to the intersection of the zero velocity surface with a sphere of radius $r = \frac{3}{2|J|}$ that increases with J (since we only consider the case $J < 0$).

However, one can also define the openings as the minimum area sections of the throats. Since the zero velocity surfaces start from the x -axis and is symmetric about the (x, y) and (x, z) plane, these minimum area sections are delimited by the points of \mathcal{Z} at which the distance from the x -axis is minimal. This distance, $\delta_{(x)} = y^2 + z^2$, can be obtained from the definition of J (equation (III.5)) as:

$$\delta_{(x)}^2 = \frac{4}{(3x^2 - z^2 + 2J)^2} - x^2 \quad (\text{III.7})$$

Upon computing $\frac{\partial\delta}{\partial x}$, one can check that the minimum is reached at:

$$\begin{aligned} x_{min} &= \sqrt{z^2 - 2(J + 3^{1/3})} & \text{for } J < -3^{1/3} \\ x_{min} &= 0 & \text{for } J \geq -3^{1/3} \end{aligned}$$

Then, $\delta_{min} = 3^{-1/3} - x_{min}$ and one can compute r_{min} to be exactly x_c . That is, while the openings as defined by tangency with the radial lines lie on spheres whose radii, $r = \frac{3}{2|J|} > x_c$, increase with J , the minimum area sections lie on a fixed sphere with radius x_c , independent of J .

Further computations of derivatives (see Appendix C) allow us to show that the minimum distance of the zero velocity surfaces from the origin (tangent spheres) are reached at the poles for the spatial problem and on the y -axis in the planar problem at $r = -\frac{1}{J}$. This last value is always greater than the radius obtained at the poles. Moreover, since $\frac{1}{|J|} < x_c$ for $J < -3^{1/3}$, we see that every transit trajectory (i.e., a trajectory crossing the planes $x = x_c$ and $x = -x_c$) must have a point of closest approach from the primary inside the region bounded by the planes $x = \pm x_c$ (i.e., the existence of a periapsis passage as defined by $\dot{r} = 0$ and $\ddot{r} > 0$ is guaranteed). Figure III.5 illustrates the geometry of the zero velocity surface for the critical value $-3^{1/3}$ of J .

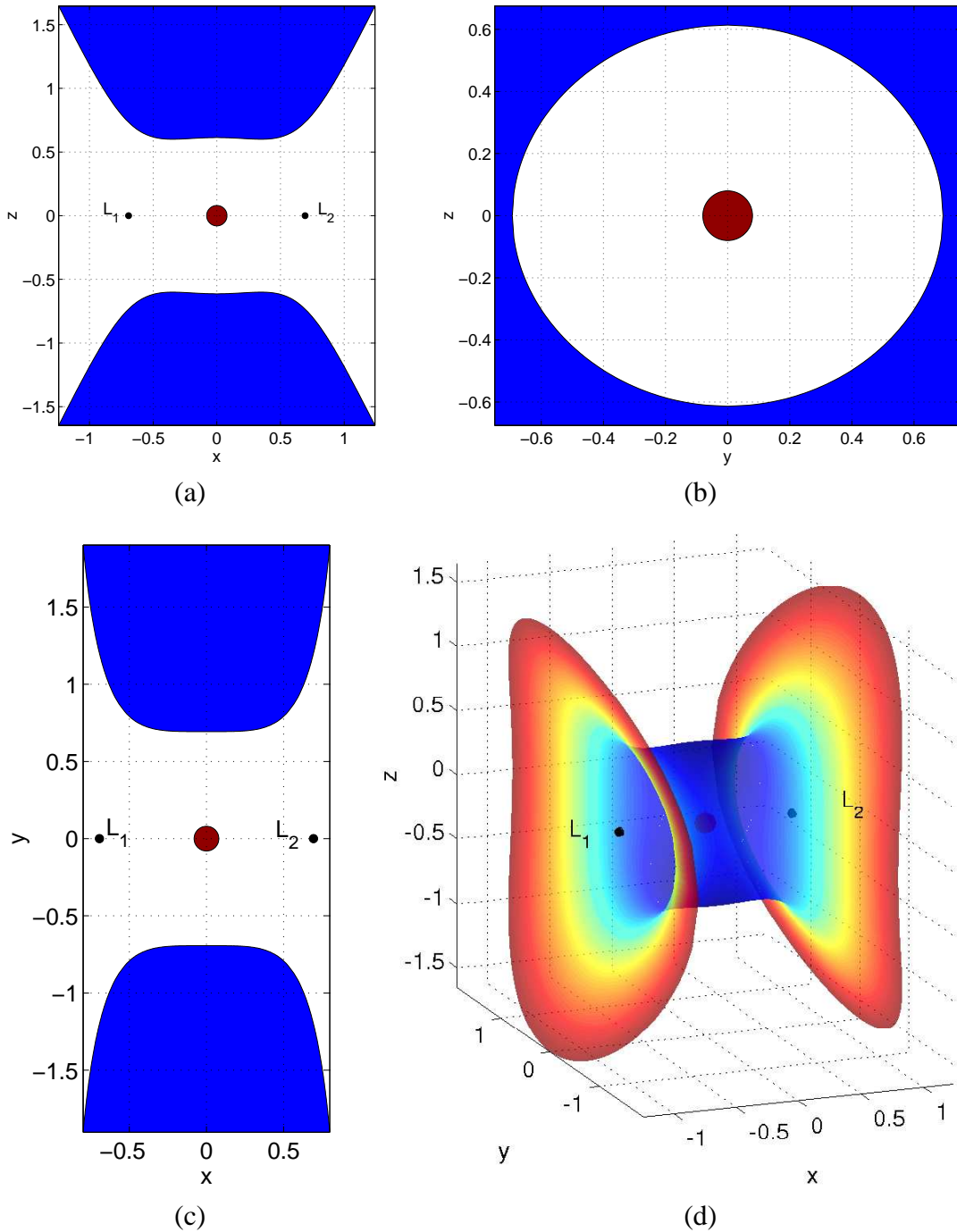


Figure III.5: Zero velocity surfaces for $J = -3^{1/3}$. (a) (x, z) -projection. (b) (y, z) -projection. (c) (x, y) -projection. (d) Spatial representation. The blue regions represent the forbidden regions of motion at the given value of Jacobi constant. The surface of Europa (normalized radius of 0.08) is also represented.

Finally, we should like to note that in the same way as δ has been derived from the definition of the Jacobi integral (III.5), we readily obtain that r satisfies:

$$r = \frac{-2}{3x^2 - z^2 + 2J} \quad (\text{III.8})$$

thus showing that the zero velocity surfaces are asymptotic to the surfaces $z = \pm\sqrt{3x^2 + 2J}$.

3. Orbital elements and Delaunay variables

Orbital elements are ubiquitous in both celestial mechanics and astrodynamics. They represent a convenient and geometric way of parameterizing the state of a point mass particle, and much useful information can be easily extracted from them.

This subsection recalls the definition of the orbital elements while emphasizing a slight modification that is well suited for problems formulated in a rotating frame, as is the case with the Hill problem.

3.1. Orbital elements

The Kepler problem is completely integrable and the path of any particle consists of a conic section whose nature depends on the value of the energy (ellipses, parabolas or hyperbolas for negative, zero or positive energies, respectively). Even though the orbital elements are defined for all regimes of motion, we are mainly interested in motion presenting several periapsis passages, so our focus will be on the elliptical case.

The shape of the ellipse in the orbital plane is either described by the semi-major axis, a , and the eccentricity, e , or the periapsis and apoapsis radii, r_p and r_a , respectively. These quantities are related via $r_p = a(1 - e)$ and $r_a = a(1 + e)$. Then, motion on the ellipse is described by an angular coordinate that is related to the time, as for example the true anomaly, f , the eccentric anomaly, E , or the mean anomaly, M . These quantities are related to each other via:

$$\tan(E/2) = \sqrt{\frac{1-e}{1+e}} \tan(f/2)$$

$$M = E - e \sin E$$

This last equation is Kepler's equation and cannot be solved algebraically. The mean anomaly is then related to time via $M = n(t - t_0)$ where $n = a^{-3/2}$ [†] is the mean motion and t_0 represents the time of periapsis passage.

Then in order to complete the description of the state of a particle, one must determine the position of the ellipse in space, through, for example, the use of three Euler angles (the 3 – 1 – 3 sequence from an initial Cartesian frame) known as the longitude of the ascending node, Ω , the inclination, i , and the argument of periapsis, ω .

Note that, even though orbital elements are very useful, they are not well defined for zero eccentricity and zero inclination (ω and Ω are not well defined in these cases). Other sets of elements have been devised for these cases, but we will not use them in this work.

The relation between the Cartesian coordinates of an inertial frame and the orbital elements can be expressed as:

$$\begin{bmatrix} x \\ y \\ z \end{bmatrix} = \mathbf{R}_{(i,\omega,\Omega)} \begin{bmatrix} r \cos f \\ r \sin f \\ 0 \end{bmatrix} ; \quad \begin{bmatrix} \dot{x} \\ \dot{y} \\ \dot{z} \end{bmatrix} = \mathbf{R}_{(i,\omega,\Omega)} \frac{na}{\sqrt{1-e^2}} \begin{bmatrix} -\sin f \\ e + \cos f \\ 0 \end{bmatrix} \quad (\text{III.9})$$

where $\mathbf{R}_{(i,\omega,\Omega)} = \mathbf{R}_3(-\Omega)\mathbf{R}_1(-i)\mathbf{R}_3(-\omega)$ is the direction cosines matrix of the ellipse in space[‡] and r , the magnitude of the position vector, satisfies $r = \frac{a(1-e^2)}{1+e\cos f}$.

The definition of the orbital elements given above allows us to easily express the motion of a point particle in a central gravitational field since, in this case, $(a, e, i, \omega, \Omega)$ are constants of motion.

Now, when the field is no longer central, the orbital elements vary as a function of time, but can still be used as a parameterization of the phase space and often represent a convenient system of coordinates (even though they are not canonical). Lagrange proposed an easy way to obtain the differential equation governing these variations. The resulting equations are now known as the Lagrange planetary equations and can be expressed as:

$$\dot{\mathbf{s}} = \mathbf{B}^{-1} \nabla_{\mathbf{s}} \mathcal{F}$$

[†]Recall that we are in a non-dimensional setting where the gravitational parameter μ is equal to 1.

[‡] \mathbf{R}_3 and \mathbf{R}_1 represent the rotation matrices about the third and first axis respectively.

where $\mathbf{s} = (a, e, i, \omega, \Omega, M)$ represents the vector of orbital elements, \mathbf{B} represents a matrix whose elements are given by the Lagrange brackets ($[s_l, s_k] = \left(\frac{\partial \mathbf{x}}{\partial s_l} \right)^T \frac{\partial \dot{\mathbf{x}}}{\partial s_k} - \left(\frac{\partial \mathbf{x}}{\partial s_k} \right)^T \frac{\partial \dot{\mathbf{x}}}{\partial s_l}$ for any element s_l and s_k) and $\nabla_{\mathbf{s}} \mathcal{F}$ represents the gradient of the negative of the Hamiltonian (as expressed in an inertial frame, i.e., kinetic plus potential energy) with respect to the elements. It is customary to remove the Keplerian energy part of \mathcal{F} , i.e., $\frac{-1}{2a}$, and call the resulting function the disturbing function, denoted \mathcal{R} . Since only the equation governing the variations of the mean anomaly depends on $\frac{\partial \mathcal{F}}{\partial a}$, Lagrange's planetary equations can be expressed with \mathcal{R} in place of \mathcal{F} , except for the mean anomaly equation to which n has to be added.

3.2. Formulation in a rotating frame

Note that the above definition of the orbital elements are defined specifically relative to an inertial frame. However, as soon as the center of the frame is at the center of mass of the primary, any inertial frame can be used. In particular, when a problem is formulated in a rotating frame, as is the case for the Hill problem, one can define the elements at each instant of time in the inertial frame that is superimposed with the rotating frame at that instant. This is equivalent to defining the longitude of the ascending node relative to the x -axis of the rotating frame. Indeed, since at two different instants t_1 and t_2 the corresponding inertial frames only differ by a rotation around the z -axis with angle $N(t_2 - t_1)$ [§], the only difference in defining the elements in the two frames lies in the longitude of the ascending node which is shifted by $N(t_2 - t_1)$. Thus, setting an initial inertial frame that is superimposed with the rotating frame at the initial epoch $t = 0$, one obtains the relation:

$$\Omega = \Omega_0 - Nt$$

[§]We denote N the angular speed of the frame to make its dependence explicit and reserve the notation ω (that was used in Chapter II) only for the argument of periapsis so as to avoid any confusion. Note that in the normalized setting, $N = 1$.

where Ω represents the longitude of the ascending node in the rotating frame and Ω_0 is the longitude of the ascending node with respect to the given, initial inertial frame.

Now, to obtain the variations of the elements in the rotating frame, we can simply note that $\frac{d\Omega}{dt} = \frac{d\Omega_0}{dt} - N$ and $\frac{\partial \Xi}{\partial \Omega} = \frac{\partial \Xi}{\partial \Omega_0}$ for any function Ξ . Thus, the Lagrange brackets are the same in the inertial and rotating frame, and the Lagrange planetary equations for the rotating frame are simply obtained by adding N to the right hand side of the equations governing Ω_0 .

However, a more fundamental way to view this point is to realize that the derivation of Lagrange's planetary equations are valid for any set of $2n$ first order differential equations and any valid set of elements (i.e., a change of variables that must be one-to-one). The only difficulty being the computation of the brackets.

In particular, this derivation is very well suited for a canonical set of equations. Starting from $\dot{\mathbf{q}} = \frac{\partial \mathcal{H}}{\partial \mathbf{p}}$ and $\dot{\mathbf{p}} = -\frac{\partial \mathcal{H}}{\partial \mathbf{q}}$, one can express the left hand sides in terms of the elements \mathbf{s} :

$$\frac{\partial \mathbf{q}}{\partial \mathbf{s}} \cdot \frac{d\mathbf{s}}{dt} = \frac{\partial \mathcal{H}}{\partial \mathbf{p}} \quad (\text{III.10})$$

$$\frac{\partial \mathbf{p}}{\partial \mathbf{s}} \cdot \frac{d\mathbf{s}}{dt} = -\frac{\partial \mathcal{H}}{\partial \mathbf{q}} \quad (\text{III.11})$$

so that, multiplying (III.10) by $-\left(\frac{\partial \mathbf{p}}{\partial \mathbf{s}}\right)^T$ and (III.11) by $\left(\frac{\partial \mathbf{q}}{\partial \mathbf{s}}\right)^T$ and adding the results, one obtains:

$$\mathbf{B} \cdot \frac{d\mathbf{s}}{dt} = -\nabla_{\mathbf{s}} \mathcal{H}$$

where, as previously, \mathbf{B} has its components given by the Lagrange brackets:

$$[s_l, s_k] = \left(\frac{\partial \mathbf{q}}{\partial s_l} \right)^T \frac{\partial \mathbf{p}}{\partial s_k} - \left(\frac{\partial \mathbf{q}}{\partial s_k} \right)^T \frac{\partial \mathbf{p}}{\partial s_l} \quad (\text{III.12})$$

Upon inverting \mathbf{B} , one obtains the Lagrange planetary equations for any Hamiltonian system.

In the case of the Kepler problem in a rotating frame, $\mathcal{H} = \frac{|\mathbf{p}|^2}{2} - \mathbf{q}^T \boldsymbol{\Omega} \mathbf{p} - \frac{1}{|\mathbf{q}|}$ so that $\dot{\mathbf{q}} = \mathbf{p} + \boldsymbol{\Omega} \mathbf{q}$ and, thus, \mathbf{p} represents the velocity in inertial space. Then, from (III.12), it

is immediately clear that the brackets computed in the rotating frame are exactly equal to the brackets computed in the inertial frame, which are superimposed on the rotating frame for each given instant. Moreover, the Hamiltonian of the Kepler problem in a rotating frame is expressed as a Kepler problem in an inertial frame plus the disturbing function $\mathbf{q}^T \Omega \mathbf{p} = N|\mathbf{h}| \cos i$ where \mathbf{h} is the angular momentum (per unit mass) of the particle in inertial space. Thus we see that the Lagrange planetary equations for a problem formulated in a rotating frame are the same as the classical Lagrange planetary equations with the addition of a term \mathcal{R}_R , that depends on the angular momentum in the disturbing function.

In the case of the Hill problem, the disturbing function is (without the addition of \mathcal{R}_R):

$$\mathcal{R} = \frac{1}{2} (3x^2 - r^2)$$

so that, using the relations between Cartesian and orbital elements, one obtains:

$$\mathcal{R} = \frac{r^2}{2} \{ 3(\cos(\omega + f) \cos(\Omega) - \sin(\omega + f) \sin(\Omega) \cos(i))^2 - 1 \}$$

where Ω is defined with respect to the x -axis of the rotating frame.

3.3. The Delaunay variables

The orbital elements are very convenient for many purposes but are not canonical, and a canonical set of elements may thus be desirable when one wants to apply theorems that are formulated in a canonical framework, such as the existence of KAM tori. One such possible set of elements was derived by Delaunay and consists of complementing the elements M , ω and Ω by three variables, denoted L , G and H .

Noting that Hamilton's equations can be written as:

$$\dot{\mathbf{z}} = \mathbf{J} \nabla_{\mathbf{z}} \mathcal{H}$$

where $\mathbf{z} = (\mathbf{q}, \mathbf{p})$ and \mathbf{J} is the symplectic matrix[¶] and comparing them with the Lagrange planetary equations as expressed for a Hamiltonian system:

$$\dot{\mathbf{s}} = -\mathbf{B}^{-1} \nabla_{\mathbf{s}} \mathcal{H}$$

[¶] $\mathbf{J} = \begin{bmatrix} \mathbf{0} & \mathbf{I} \\ -\mathbf{I} & \mathbf{0} \end{bmatrix}$ where $\mathbf{0}$ and \mathbf{I} are, respectively, the $n \times n$ zero and identity matrices.

we see that the elements will be canonical if and only if $\mathbf{B} = \mathbf{J}$ (indeed, $\mathbf{J}^{-1} = -\mathbf{J}$).

This is equivalent to imposing normalized conditions for the brackets, as given by:

$$\begin{aligned}[M, L] &= 1 & [M, G] &= 0 & [M, H] &= 0 \\ [\omega, L] &= 0 & [\omega, G] &= 1 & [\omega, H] &= 0 \\ [\Omega, L] &= 0 & [\Omega, G] &= 0 & [\Omega, H] &= 1\end{aligned}$$

From the classical expression of the brackets in terms of $(a, e, i, \omega, \Omega, M)$, it is easy to check that L , G and H are given by (see [19] for example):

$$\begin{aligned}L &= na^2 \\ G &= na^2(1 - e^2) \\ H &= na^2(1 - e^2) \cos i\end{aligned}$$

The variable L is also expressed as $L = \sqrt{-2/C}$ where C denotes the Keplerian energy and the variables G and H represent, respectively, the magnitude of the angular momentum and the projection of the angular momentum on the z -axis. As for the Keplerian elements, the Delaunay variables are not well defined for circular orbits and motion in the equatorial plane. Other sets of canonical elements (e.g., the Poincaré elements) can be used in such cases.

We should note that this set of elements can also be obtained directly from another set of canonical variables (such as the Cartesian elements in inertial space) by using a generating function. However, since Kepler's equation is transcendental with respect to Cartesian coordinates, the expression of this generating function is not necessarily obvious (see [26] for example). The above derivation, while being simple, has the advantage of giving the explicit relation of the orbital elements with a canonical framework and to directly apply to the case where Ω is defined with respect to a rotating frame, the term $\mathbf{q}^T \boldsymbol{\Omega} \mathbf{p} = NH$ being directly included into the Hamiltonian.

As before, one can decompose the Hamiltonian as $\mathcal{H}_H = -\frac{1}{2L} + NH + \mathcal{R}$ where \mathcal{R} is independent of L (if the disturbing potential only depends on position) and the equations

governing the evolution of L , G , and H are obtained by taking the partial of \mathcal{R} with respect to M , ω and Ω respectively.

It should be noted that, away from the values $L \neq 0$, $G \neq 0$ and $L \neq G$ which corresponds to the singularity at the origin and the cases of values zero and one for the eccentricity^{||}, the Hamiltonian \mathcal{H}_H and the disturbing function \mathcal{R} are analytic in the Delaunay variables.

Finally we conclude this subsection by giving another set of canonical elements, closely related and derived from the Delaunay's variables. They simply consists of changing the conjugate variables (M, L) by the pair $(T = ML^3, C = -1/(2L^2))$. The variable T represents the difference between the time, t , and the time of periapsis passage, t_p . Since t and t_p always appear together in any disturbing function, the partial derivatives with respect to T and t are equal. Thus, it can be easily checked that the resulting transformation is canonical, and we obtain the following relations:

$$\begin{aligned}\dot{C} &= \frac{\partial \mathcal{R}}{\partial t} \\ \dot{G} &= \frac{\partial \mathcal{R}}{\partial \omega} \\ \dot{H} &= \frac{\partial \mathcal{R}}{\partial \Omega}\end{aligned}$$

This set of element may be preferable since the variable C has a direct physical meaning as the Keplerian energy. Note also that the Jacobi constant is simply expressed in these variables as:

$$J = C - NH - \mathcal{R}$$

This last expression will be used in the next chapter to derive approximate expressions of C given some estimates on G and H .

^{||}These results can be proven easily by using the standard Fourier series expansions of r , $\cos f$ and $\sin f$ as a function of the mean anomaly.

3.4. Symmetries

We finish this section by translating the symmetries already observed in Cartesian coordinates into orbital elements. This is required when one wishes to take advantage of the symmetries while working with orbital elements.

This translation can be directly obtained by using relations (III.9), noting that M , t and f vary in the same direction (a reversal of time corresponds to a reversal of mean and eccentric anomaly) and by explicitly computing $\mathbf{R}_{(i,\omega,\Omega)}$ in (III.9):

$$\mathbf{R}_{(i,\omega,\Omega)} = \begin{bmatrix} \cos \Omega \cos \omega - \sin \Omega \sin \omega \cos i & -\cos \Omega \sin \omega - \sin \Omega \cos \omega \cos i & \sin \Omega \sin i \\ \sin \Omega \cos \omega + \cos \Omega \sin \omega \cos i & -\sin \Omega \sin \omega + \cos \Omega \cos \omega \cos i & -\cos \Omega \sin i \\ \sin i \sin \omega & \sin i \cos \omega & \cos i \end{bmatrix}$$

Thus, one can immediately see that S_1 and S_2 are expressed in terms of orbital elements as:

$$\begin{aligned} (a, e, i, \omega, \Omega, M) &\xrightarrow{S_1} (a, e, i, \pi - \omega, -\Omega, -M) \\ (a, e, i, \omega, \Omega, M) &\xrightarrow{S_2} (a, e, i, \pi - \omega, \pi - \Omega, -M) \end{aligned}$$

The other symmetries only involve ω and Ω and can be expressed as:

$$\begin{aligned} (\omega, \Omega) &\xrightarrow{S_3} (\pi + \omega, \pi + \Omega) \\ (\omega, \Omega) &\xrightarrow{S_4} (\omega, \Omega - \pi) \\ (\omega, \Omega) &\xrightarrow{S_5} (\pi + \omega, \Omega) \end{aligned}$$

Since ω and Ω are defined modulo 2π , we see that the transformations:

$$\begin{cases} \omega \rightarrow \omega + m\pi \\ \Omega \rightarrow \Omega + n\pi \end{cases} \quad n, m \in \mathbb{Z}$$

leave the flow invariant.

This fact will be used in Chapter V, since we will reduce the dynamics to the (ω, Ω) -torus space, so that computations will only need to be performed on the intervals $[0, \pi]^2$ (instead of $[0, 2\pi]^2$).

4. Dynamics close to the primary

The length and time scales defined in Chapter II, l and τ , were used to transform Hill's problem into a normalized form. Besides this use, l and τ can be regarded as characteristic length and time scales that characterize non-Keplerian phenomena in the dynamics.

For instance, the libration points L_1 and L_2 are situated on the x -axis at a distance of $(1/3)^{1/3}l \simeq 0.69l$ from the center of mass and $2\pi\tau$ is the period of motion of the satellite (planet) around the massive planet (Sun). This would suggest that for small values of radius and short time scales (as compared to l and τ), the dynamics become close to Keplerian and motion is only slightly disturbed. This is in accordance with our physical intuition of a tightly bound trajectory (the disturbing planet is far away and its gravitational pull is small when compared to the primary).

This section describes two complementary approaches to describe this realm of motion: KAM tori and the averaging method.

4.1. Perturbation of the two body problem and KAM tori

The above physical intuition can be expressed by scaling the Hamiltonian of the Hill problem (III.4). This is achieved by performing the following symplectic change of variables and time:

$$\boldsymbol{q} = \epsilon^{2/3} \boldsymbol{\xi}$$

$$\boldsymbol{p} = \epsilon^{-1/3} \boldsymbol{\eta}$$

$$t = \epsilon\tau$$

so that, \mathcal{H}_H transforms to:

$$\mathcal{H}_H = \mathcal{H}_0 + \epsilon\mathcal{H}_1 + \epsilon^2\mathcal{H}_2$$

$$\text{where } \mathcal{H}_0 = \frac{|\boldsymbol{\eta}|^2}{2} - \frac{1}{|\boldsymbol{\xi}|}, \quad \mathcal{H}_1 = \boldsymbol{\xi}^T \boldsymbol{\Omega} \boldsymbol{\eta} \quad \text{and} \quad \mathcal{H}_2 = -\frac{1}{2} \{ 3(\boldsymbol{\xi}^T \boldsymbol{a})^2 - |\boldsymbol{\xi}|^2 \}.$$

This form of the Hamiltonian indicates that for motion close to the center of the frame, the flow is close to Keplerian for a time scale that is small compared to the period of rotation of the frame. Moreover, one can see that the main perturbation when close to the primary comes from the rotation of the frame, but, as was noticed in Chapter II, this effect is entirely due to the presence of a third body and cannot be, physically, dissociated from it. These results can in fact be strengthened by applying a theorem of Arnold [2] on the existence of KAM tori.

In order to apply this theorem, we first write \mathcal{H}_H in terms of Delaunay's variables:

$$\begin{aligned}\mathcal{H}_0 &= -\frac{1}{2L} \\ \mathcal{H}_1 &= H \\ \mathcal{H}_2 &= -\mathcal{R}\end{aligned}$$

As was noticed in the section on Delaunay's elements, the Hamiltonian \mathcal{H}_H is analytic in $(M, \omega, \Omega, L, G, H)$, when $L \neq 0$, $G \neq 0$ and $L \neq G$.

Then, a second canonical transformation is applied:

$$(M, \omega, \Omega, L, G, H) \rightarrow (\lambda, \alpha, \beta, L, A, B)$$

where

$$\begin{aligned}A &= \sqrt{L - G} & \lambda &= M + \omega + \Omega \\ B &= \sqrt{G - H} & \text{and} & \alpha = -2A(\omega + \Omega) \\ & & & \beta = -2B\Omega\end{aligned}$$

It can easily be checked that this transformation is canonical (the variables λ , α and β having been obtained by symplectic completion of the transformation $(L, G, H) \rightarrow (L, A, B)$).

Note that in this new set of variables, $G = L - A^2$ and $H = L - A^2 - B^2$, $M = \lambda + \frac{\alpha}{2A}$, $\omega = -\frac{\alpha}{2A} - \frac{\beta}{2B}$ and $\Omega = -\frac{\beta}{2B}$. Thus, \mathcal{H}_H remains analytic in the new variables if L , A and B are non-zero and $L \neq A^2$. Moreover, the variable λ remains an angle variable and \mathcal{H}_H is 2π periodic in λ .

Now a third canonical change of variable is applied to transform \mathcal{H}_H into the desired form of Arnold's theorem. This last transformation is a slight modification of a transformation generally associated with Poincaré's elements. It consists of:

$$(\lambda, \alpha, \beta, L, A, B) \rightarrow (\lambda, \xi_1, \xi_2, \eta_1, \eta_2)$$

where

$$\begin{aligned} \eta_1 &= \sqrt{2A - C_1} \cos \alpha & \text{and} & \eta_2 = \sqrt{2B - C_2} \cos \beta \\ \xi_1 &= \sqrt{2A - C_1} \sin \alpha & \xi_2 &= \sqrt{2B - C_2} \sin \beta \end{aligned}$$

The constants C_1 and C_2 are positive and arbitrary small.

Note that, in this new set of variables, \mathcal{H}_H is analytic in the following domain:

$$0 < L_{min} < L \quad (\text{III.13})$$

$$|\boldsymbol{\eta}| \leq R, \quad |\boldsymbol{\xi}| \leq R \quad (\text{III.14})$$

where $0 < R^2 < \sqrt{L_{min}} - \frac{C_1}{2}$.

The last inequalities (III.14) can also be expressed as:

$$\frac{C_1}{2} \leq A \leq R^2 - \frac{C_1}{2} \quad (\text{III.15})$$

$$\frac{C_2}{2} \leq B \leq R^2 - \frac{C_2}{2} \quad (\text{III.16})$$

showing that the constant C_2 restricts the inclination, so that the equatorial plane is not included in the above domain. This is not, however, a dynamical phenomena and is only a result of the initial choice of coordinates. The derivation is indeed valid for the planar problem if we restrict ourselves to the variables L and G .

Thus, in this new set of coordinates, the Hamiltonian \mathcal{H}_H is in the desired form to apply Arnold's theorem on the existence of KAM tori. Indeed, we have just seen that \mathcal{H}_H is analytic in the domain of phase space considered. Moreover, $\mathcal{H}_0 = -\frac{1}{2L^2}$ has a non-singular Hessian with respect to L and the conjugate variable of L is an angle variable. Finally, \mathcal{H}_1 is expressed as a non-singular quadratic form in $\tau_i = \eta_i^2 + \xi_i^2$ ($i = 1, 2$):

$$\mathcal{H}_1 = L - \frac{1}{4}(C_1^2 + C_2^2) + \frac{1}{2}(C_1 \tau_1 + C_2 \tau_2) - \frac{1}{4}(\tau_1^2 + \tau_2^2)$$

Thus, in the domain defined by inequalities (III.13)-(III.14), we have an invariant set foliated by invariant tori on which the flow is conditionally periodic. The complement of this set in the domain of phase space considered has very small measure (depending on the constants chosen) but form a dense set in the domain considered.

The invariant tori correspond to small perturbation of the motion on Keplerian orbits in a rotating frame. Thus, on these tori, the motion of a spacecraft can be well approximated by the nearby Keplerian motion. This motion corresponds to a linear increase in the mean anomaly and a constant rate of precession for the longitude of the ascending node.

This theorem does not give us, however, a bound on how far these results can be applied. Indeed, the existence of these tori depends on the constants in the above variables, and notably on the first symplectic scaling used. In particular, the region of phase space for which the KAM tori may exist may be well below the physical surface of the primary. In the planar case, this happens for example, as soon as the periapsis of the stable or unstable manifold associated with the libration points is below the surface [36].

The result obtained is, however, interesting since it shows some relations between the semi-major axis, the eccentricity and the inclination that affect the stability of the motion. Indeed, from the inequalities (III.15), (III.16) and the definition of A and B , we can see that:

- The larger the semi-major axis, the smaller the eccentricity. That is, stable, highly elliptic motion is destroyed more rapidly than circular motion as we move away from the center of the frame.
- The higher the inclination, the smaller the angular momentum. That is, circular orbits with given radius are more stable for low inclinations rather than for high inclinations, thus indicating the possible destabilizing effect of high inclinations.

Finally, we should note that the existence of KAM tori does not prove the stability of motion in the spatial problem (existence of Arnol'd diffusion), but it does prove the stability of motion for the planar problem in the region of phase space close to the origin.

4.2. Averaging

While the above discussion is rigorous, it does not provide us any idea on how far from the primary we can consider circular motion to be close to Keplerian**. Perturbation methods, while non-rigorous, give us such an estimate. This subsection briefly reviews the results obtained in [32].

When the mean motion of the spacecraft is large compared to the mean motion of the primary around the disturbing body, one can average over the mean anomaly of the spacecraft to obtain the secular variation of the elements describing its motion. Moreover, when one wants to consider time scales large compared to the period of revolution of the primary around the disturbing body, one can average the disturbing function of the previous averaging over the mean motion of the primary. The resulting disturbing function, given by

$$\overline{\overline{\mathcal{R}}} = \frac{1}{(2\pi)^2} \int_0^{2\pi} \int_0^{2\pi} \mathcal{R} dM d(Nt)$$

is independent of time and the Lagrange planetary equations for this disturbing function yield the secular variations of the orbital elements (except M) as a function of time, i.e., the variations that occur on a time scale much larger than $\frac{2\pi}{N}$.

The result of this double averaging are a zero change in semi-major axis and an integrable system for i , e and Ω if we restrict ourselves to the 1st order in eccentricity (i.e., orbits close to circular):

$$\begin{aligned} \frac{di}{dt} &= \mathcal{O}(e^2) \\ \frac{de}{dt} &= \frac{15}{8} \frac{N^2}{n} e \sin^2 i \sin 2\omega + \mathcal{O}(e^2) \\ \frac{d\omega}{dt} &= \frac{3}{8} \frac{N^2}{n} (4 - 5 \sin^2 i + 5 \sin^2 i \cos 2\omega) + \mathcal{O}(e^2) \end{aligned}$$

The resulting integration indicates two distinct realms of motion depending on the initial inclination.

**While the theorem uses averaging on \mathcal{H}_1 , the resulting small parameter given by the theorem is just guaranteed to exist, but no bound is given on its magnitude. We used an existence theorem.

For $30.23^\circ \leq i \leq 140.77^\circ$, the eccentricity increases exponentially as:

$$\begin{aligned} e &\sim \exp \lambda t \\ \lambda &\sim \left(\frac{3\sqrt{6}}{4} \right) \left(\frac{N}{n} \right) N \end{aligned}$$

and the argument of periapsis is shown to converge towards a fixed limit. Figure III.6 shows the eccentricity of an integrated trajectory for an initially polar, circular orbit, 400km above the surface of Europa. The integration time is 60 units of time which corresponds to 9.5 revolutions of Europa around Jupiter. Note that the short and long periodic terms, even though significant, remain small and below 0.005 for the eccentricity and below 1.5 degrees for the inclination.

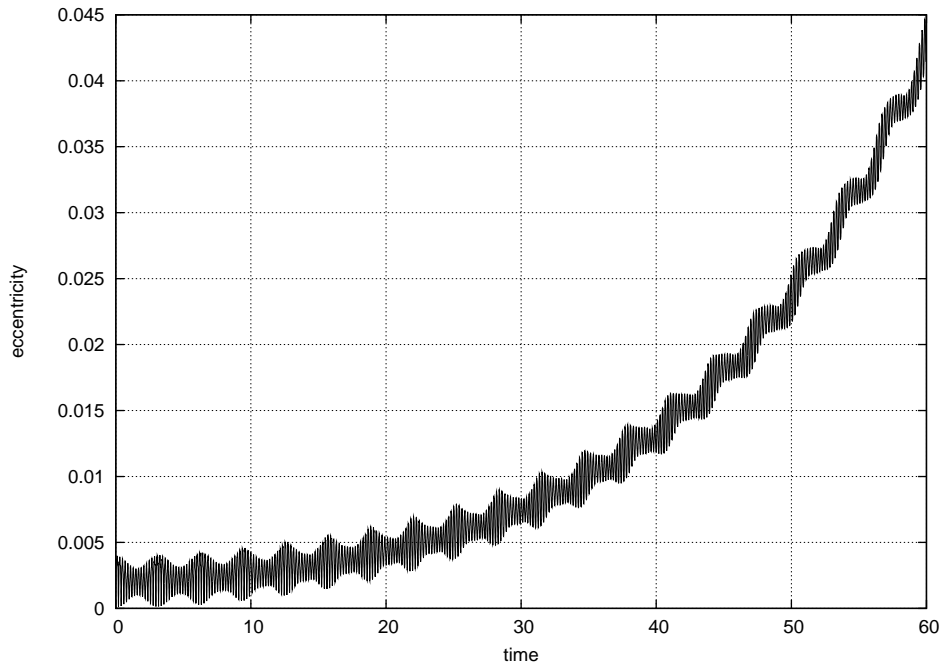


Figure III.6: Polar orbit around Europa

For $0 \leq i < 39.23^\circ$ and $140.77^\circ < i \leq 180^\circ$, the eccentricity is shown to oscillate secularly and the argument of periapsis to circulates indefinitely. Figure III.7 shows an initially equatorial, circular trajectory, 400 km above the surface of Europa, integrated for 60 units of time. Again the short and long periodic terms remain small.

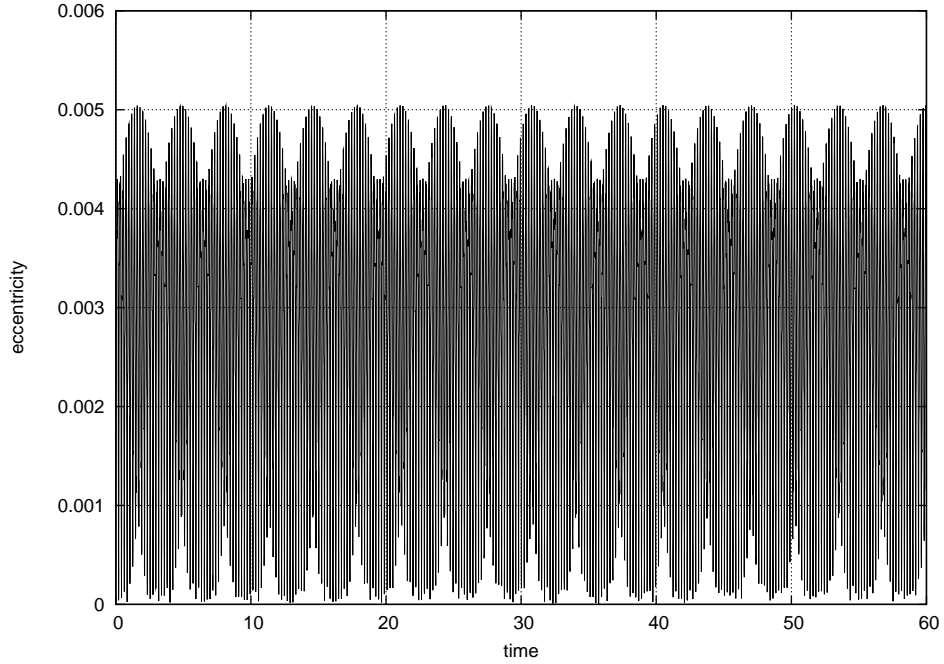


Figure III.7: Equatorial orbit around Europa

Note that the above theory, while approximate and taking into account only the secular variations of the elements, allows us to correctly predict the time of impact of a low orbiter in the case of Europa, as compared to precise numerical modeling ([32]).

Since the underlying assumption of this averaging method is $N \ll n$, we see that in the normalized setting, we have $n > 10$, so that the radii of the circular orbits for which the above averaging results apply must be less than $0.1^{2/3} \simeq 0.215$. Looking at the numerical values given in Appendix B, we can see that most planetary satellites in the solar system have their normalized radius below this bound. However, this is not true for the very small satellites (such as Phobos, Amalthea, Thebe, Adrastea and Metis). Moreover, these cases often correspond to non-spherical bodies, and the dynamics around them is closer to the dynamics around asteroids.

4.3. Motion of an orbiter close to the primary

The above discussions indicate that for low altitude ($r < 0.2$ and relatively short time spans, $t \sim 2\pi/N$), the motion of a spacecraft close to a circular orbit can be approximated by a Keplerian motion. This assumption is not rigorous but simplifies the computations and comparisons to be made in the subsequent chapters. Indeed, with this assumption, the classical orbital transfers (such as a change of plane of motion, an increase or decrease in the radius of a circular orbit) continue to make sense and the results obtained in the next chapters can be compared to the corresponding classical results.

Geometrically, this assumption consists of replacing slightly deformed tori by undeformed tori on which the equations of motion are simply linear:

$$M = M_0 + nt$$

$$\Omega = \Omega_0 - Nt$$

Figure III.8 illustrates this situation.

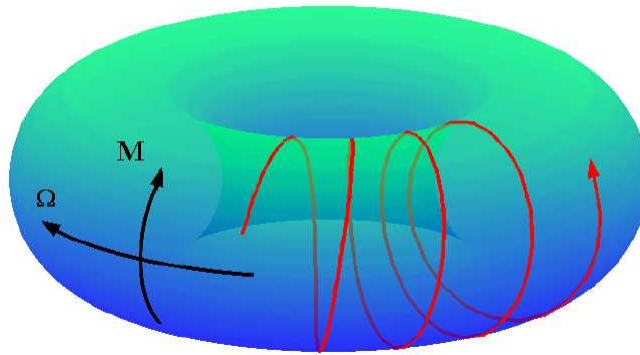


Figure III.8: Representation of the motion on a low altitude, circular orbit

Note that for near polar orbits, the instability indicated by the averaging method does not cause any trouble as long as the time span is short as compared to the instability characteristic time $\tau_s = 1/\lambda$. More precisely, the eccentricity of a near-circular orbit will grow by an order of magnitude after $\ln(10) \simeq 2.302\dots$ characteristic times. Table

III.1 gives the values of τ_s for a few satellite/planets in the solar system. For example, in the case of an Europa orbiter, an initial eccentricity of 0.001 will reach the value of 0.01 after 27 days, while the spacecraft would have performed ~ 75 revolutions around Europa (this corresponds to a decrease of $\sim 15 \text{ km}$ in the periapsis radius for the case of a 200 km altitude orbiter). In the case of a polar orbiter, this time span can clearly be used to perform a maneuver to transfer the spacecraft into a stable circular orbit to avoid impact with the satellite over long time spans.

Table III.1: Parameters for the dynamics close to Mercury, the Earth, Europa, Titan and Triton [32]

Primary	Char. instability time τ_S (days)	Mean motion ratio N/n	Positioning error on Ω (degree)
Mercury	> 30 years	0.00067	0.12
Earth	> 500 years	0.00016	0.029
Europa	13.66	0.0225	4.05
Titan	220.28	0.00627	1.12
Triton	31.20	0.0163	2.93

Another property of the motion (due to the assumption $N \ll n$) is that any given value of mean anomaly, M , and longitude of the ascending node, Ω , can be approximately reached by a spacecraft moving on a low altitude, circular orbit to within a certain error. Indeed, over one revolution, Ω will precess by $180\frac{N}{n} \text{ deg}$, which is small when the approximation $N \ll n$ is realized. This positional accuracy is indicated in the last column of Table III.1 for the few satellites/planets already considered.

Note that this positional accuracy improves over many orbits. In the idealized model of a Keplerian motion in a rotating frame, the motion being conditionally periodic for most initial conditions, the positional accuracy can be made arbitrarily small by waiting for sufficiently long times. This same situation also prevails on preserved KAM tori. These facts will be used in Chapter V, since M and Ω will be shown to control the changes in orbital elements that occur during a transfer trajectory.

Finally, we should note that the assumption made on the motion of a low altitude, circular orbit can be overcome by computing, for example, the short periodic variations of the elements^{††}, thus including the slight deformation of the tori into the picture. As long as these perturbations remain small, the large fuel savings obtained in the subsequent applications would only be slightly changed, but the possibility of performing them would, of course, not be changed.

5. Dynamics far from the primary

This section investigates the asymptotic form of the motion of a particle when far from the primary. This situation would occur, for example, after a particle escapes from the vicinity of the primary through a throat formed by the zero velocity surfaces when $J > J_c$. Also, in the case of an orbiter (i.e., in the framework of the restricted Hill problem), these asymptotic dynamics allow us to patch any escaping solution of the Hill problem onto an outer solution, corresponding to a two body motion around the disturbing body, to obtain an approximate solution of the restricted three body problem.

5.1. Equations of motion

Motion far from the primary can be obtained by scaling the Hamiltonian of the Hill's problem using the following symplectic change of variable:

$$\begin{aligned} \mathbf{q} &= \frac{\boldsymbol{\xi}}{\epsilon} \\ \mathbf{p} &= \frac{\boldsymbol{\eta}}{\epsilon} \end{aligned}$$

Under this transformation, \mathcal{H}_H is rewritten as:

$$\mathcal{H}_H = \frac{|\boldsymbol{\eta}|}{2} - \boldsymbol{\xi}^T \boldsymbol{\Omega} \boldsymbol{\eta} - \frac{1}{2} (3(\boldsymbol{\xi}^T \mathbf{a})^2 - |\boldsymbol{\xi}|^2) - \frac{\epsilon^2}{|\boldsymbol{\xi}|} \quad (\text{III.17})$$

^{††}or by direct numerical integration of the low altitude, initial orbits.

That is:

$$\mathcal{H}_H = \frac{1}{2} [\boldsymbol{\xi}^T \ \boldsymbol{\eta}^T] \mathbf{S} \begin{bmatrix} \boldsymbol{\xi} \\ \boldsymbol{\eta} \end{bmatrix} + \mathcal{O}(\epsilon)$$

where \mathbf{S} has the same expression as in Chapter II (the only difference being in the unit chosen):

$$\mathbf{S} = \begin{bmatrix} (\mathbf{I} - \mathbf{a}\mathbf{a}^T) & -\boldsymbol{\Omega} \\ \boldsymbol{\Omega} & \mathbf{I} \end{bmatrix}$$

Thus, when looking at motion far from the primary, the Hill's equations of motion reduce to the linearized motion about the circular orbit defined by the motion of the primary^{††} around the disturbing body. This is again the Clohessy-Wiltshire equations.

Note that this fact is physically reasonable since the Hill problem has been defined as describing the relative motion of two small masses whose center of mass follows an approximately circular orbit around a massive body. When the small masses are far from each other, their gravitational attraction is negligible and the particle are thus only moving under the influence of the massive body on a nearly circular orbit.

Note also that because of the scaling, “infinitely far” in Hill’s coordinates only corresponds to a relatively small displacement when looking at the order of length scale determined by the large disturbing body.

From (III.17), we immediately compute the equations of motion:

$$\ddot{\boldsymbol{\xi}} + 2\boldsymbol{\omega} \times \boldsymbol{\xi} + \boldsymbol{\omega} \times (\boldsymbol{\omega} \times \boldsymbol{\xi}) - 3(\boldsymbol{\xi}^T \mathbf{a})\mathbf{a} - \boldsymbol{\xi} = 0$$

or, expressed in components:

$$\left\{ \begin{array}{lcl} \ddot{x} - 2\dot{y} - 3x & = & 0 \\ \ddot{y} + 2\dot{x} & = & 0 \\ \ddot{z} + z & = & 0 \end{array} \right.$$

^{††}or the center of mass of the two small masses.

5.2. Brief discussion of the dynamics

The above equations (Clohessy-Wiltshire equations) are linear and time invariant and can thus be easily integrated. It turns out that the out-of-plane dynamics (z) are decoupled from the in-plane dynamics (x, y). The out-of-plane motion consists of an harmonic oscillator:

$$\begin{bmatrix} z(t) \\ \dot{z}(t) \end{bmatrix} = \begin{bmatrix} \cos Nt & \frac{\sin Nt}{N} \\ -N \sin Nt & \cos Nt \end{bmatrix} \begin{bmatrix} z(t_0) \\ \dot{z}(t_0) \end{bmatrix}$$

and the in-plane motion is given by the following linear transformation:

$$\begin{bmatrix} x(t) \\ y(t) \\ \dot{x}(t) \\ \dot{y}(t) \end{bmatrix} = \begin{bmatrix} 4 - 3 \cos Nt & 0 & \frac{\sin Nt}{N} & 2 \frac{1 - \cos Nt}{N} \\ 6(\sin Nt - Nt) & 1 & 2 \frac{\cos Nt - 1}{N} & 4 \frac{\sin Nt}{N} - 3t \\ 3N \sin Nt & 0 & \cos Nt & 2 \sin Nt \\ 6N(\cos Nt - 1) & 0 & -2 \sin Nt & 4 \cos Nt - 3 \end{bmatrix} \begin{bmatrix} x(t_0) \\ y(t_0) \\ \dot{x}(t_0) \\ \dot{y}(t_0) \end{bmatrix}$$

The in-plane motion consists of a linear drift along the y -axis when the initial conditions satisfy $2x_0 - \dot{y}_0 \neq 0$. In a larger framework, this motion corresponds to two particles moving on trajectories that differ in semi-major axis (difference in mean motion).

When $2x_0 - \dot{y}_0 = 0$, motion consists of elliptical motion centered at the center of the frame and with its semi-major axis along the y -axis twice as large as the semi-minor axis directed along the x -axis. This mode corresponds to two particles moving on trajectories differing by a small value in eccentricity.

In the general case, all these modes can exists simultaneously and the motion corresponds to a linear superimposition of the modes.

5.3. Matched asymptotic expansions

As we have seen in Chapter II, Hill's equations can be obtained from the restricted three body problem by letting a small parameter (gravitational parameter of the primary μ) tend to zero. This limiting process allowed us to simplify the equations of motion, and we obtained a set of equations that describes the dynamics well only when close to the primary.

Note also that, when performing this procedure, a simultaneous scaling that depends on this small parameter was also applied so that when $\mu \rightarrow 0$, the length scale also tends to zero. Equivalently, when looking at the dynamics from the point of view of the Hill's length scale, we let the length scale and the gravitational parameter of the disturbing, massive body tend to infinity.

Now, in the above derivation of the Clohessy-Wiltshire equations, we applied this inverse scaling (length scale goes to infinity) on the Hill problem. That is, overall we performed two opposite limiting processes, and one can wonder what happens if the order of the limits is reversed. As we will see below, this procedure leads to the same set of equations, the Clohessy-Wiltshire equations.

The procedure just outlined is typical of singularly perturbed problems where an approximate solution is constructed by matching two asymptotic solutions. Singularly perturbed problems generally consist of a set of differential equations depending on a small parameter in such a way that either the equations degenerate when the small parameter is set to zero or the small parameter multiplies a singularity of the equations. For example, this would occur if the highest derivative (either spatial or temporal) of the equations is multiplied by the small parameter:

$$\epsilon f'' + f' + 1 = 0 \quad \text{or} \quad \frac{D\mathbf{v}}{Dt} = -\nabla p - \frac{1}{\mathcal{R}_e} \Delta \mathbf{v}$$

as happens in fluids mechanics when the Reynolds number, \mathcal{R}_e , is large.

In our case, the small parameter multiplies a singularity of the equations corresponding to the center of the primary. Recall from Chapter II that the restricted problem, as formulated in the body centered frame and normalized, is expressed as:

$$\mathcal{H}_R = \frac{|\mathbf{v}|^2}{2} - \mathbf{u}^T \Omega \mathbf{v} - \frac{\mu}{|\mathbf{u}|} + (\mathbf{u}^T \mathbf{a})^2 - \frac{1-\mu}{|\mathbf{u} + \mathbf{a}|} \quad (\text{III.18})$$

If the small parameter is set to zero in the above equations, the equations simplify (with much information lost) to the point that all the boundary conditions of the problem cannot be satisfied: the no-slip condition cannot be satisfied in fluid mechanics and, in our case,

the primary is removed from the picture and the problem reduces to a Kepler problem expressed in a frame centered on a circular orbit.

$$\mathcal{H}_O = \frac{|\mathbf{v}|^2}{2} - \mathbf{u}^T \Omega \mathbf{v} + (\mathbf{u}^T \mathbf{a})^2 - \frac{1}{|\mathbf{u} + \mathbf{a}|} \quad (\text{III.19})$$

The solution of this simplified problem is referred to as the outer solution.

Even though this solution is accurate far from the singularity, it breaks down when one comes closer to it, and a boundary layer correction has to be found. The method to obtain such a solution is to scale the problem in such a way that the singularity is no longer multiplied by the small parameter. In the limit, we obtain the inner problem. In our case, we can apply the symplectic change of variable $\mathbf{u} = \mu^{1/3} \mathbf{q}$ and $\mathbf{v} = \mu^{1/3} \mathbf{p}$ on (III.18) and obtain the Hill problem:

$$\mathcal{H}_H = \frac{|\mathbf{p}|^2}{2} - \mathbf{q}^T \Omega \mathbf{p} - \frac{1}{|\mathbf{q}|} + \frac{|\mathbf{q}|^2}{|\mathbf{a}|^2} P_2(\cos \theta)$$

Then in order to obtain a globally valid solution of the original problem (the restricted three body problem), one can patch this inner solution to the outer one via an intermediary solution. The matched asymptotic expansion technique constructs this intermediary solution by equating the outer limit of the inner problem with the inner limit of the outer problem.

In our case, we just have seen that the outer limit of the inner problem consists of the Clohessy-Wiltshire equations. On the other hand, the inner limit of the outer problem can be obtained by using the canonical transformation $\mathbf{u} = \epsilon \xi$ and $\mathbf{v} = \epsilon \eta$ on the Hamiltonian \mathcal{H}_O (III.19). One can check that the result is again the Clohessy-Wiltshire equations (an expansion of $\frac{1}{|\epsilon \xi + \mathbf{a}|}$ has to be performed, similar to the derivation of the Hill problem).

Thus, an approximate solution of the restricted three body problem can be obtained as a solution of the Hill problem, patched onto a two body trajectory via matching the coefficient of integration using the Clohessy-Wiltshire equations. This technique can in fact be continued to higher order and was used extensively in astrodynamics in the 60's and

70's, when interplanetary trajectories were analyzed using patched conic approximations [5].

In our case, this shows that the escaping solutions to be obtained in chapter VI can be embedded into a more global framework (for the case of an orbiter) to analyze, for example, possible future impacts of the spacecraft with the primary (after one or multiple loops around the disturbing body). Matching between the regions near the libration points and infinity can also be performed by using series expansions, as given in a paper by Hénon and Petit [15].

CHAPTER IV

PERIAPSIS POINCARÉ MAPS

Figure IV.1 presents the radius, eccentricity and inclination of a particle placed, initially, on a polar, elliptical orbit ($e = 0.6$), $\sim 400 \text{ km}$ above the surface of Europa.

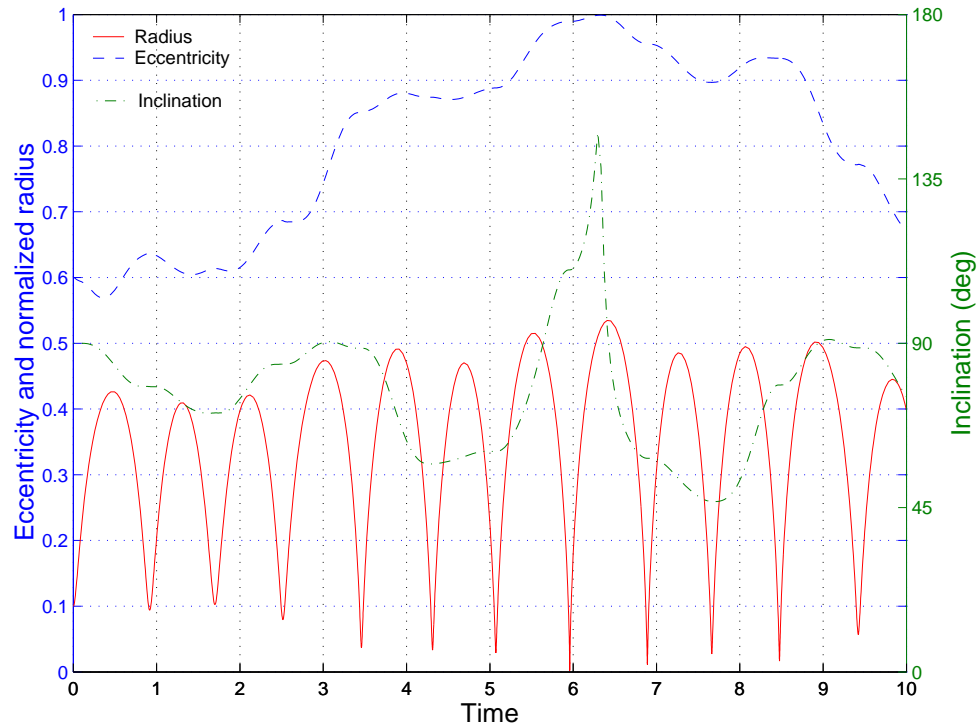


Figure IV.1: Radius, eccentricity and inclination for a sample polar orbit (initial conditions are: $a = 0.25$, $e = 0.6$, $i = 90^\circ$, $\omega = 0^\circ$, $\Omega = 0^\circ$, $M = 0^\circ$)

One can clearly see that both the eccentricity and the inclination are not constant and undergo very large changes from periapsis passage to periapsis passage. In the case presented, the trajectory would impact the surface of Europa after four revolutions around the

planetary satellite.

The aim of the chapter is to present a systematic way of analyzing these dynamics by considering them from periapsis passage to periapsis passage. Even though these periapsis maps can be computed numerically, estimates of the functional form of these maps may be preferable to obtain a global qualitative picture of these dynamics. An attempt to obtain such estimates is presented in this chapter via the use of Picard's method of successive approximations [41].

The first section defines the periapsis maps as Poincaré maps between surfaces of section defined by the periapsis condition. It is shown in particular that these maps are well defined (transversal to the flow) over an interesting range of initial conditions and they allow us to partition the position space into periapsis or apoapsis exclusive regions.

Section 2 reviews the process of Picard's method of successive approximations and investigates their use for the integration of Hamiltonian systems. It is shown in particular that each step of the process defines a symplectic map for a restricted class of Hamiltonian systems (which includes integrable problems) and a reduction process can be used to transform the process into an energy preserving one.

In section 3, the first step of the method is applied to the system of differential equations defining the Hill's problem, resulting in approximate expressions for the changes in energy and angular momentum over one orbit. A numerical check on the accuracy of these expressions is given, showing the validity to within 10% for a large range of initial conditions.

Finally, section 4 gives some qualitative results derived from the previous approximate expressions. Notably, the dependence on the initial conditions of the changes of the orbital elements over one orbit are discussed.

1. Periapsis Poincaré maps

A Poincaré map generally refers to the association of a discrete time system given an initial, more complicated, continuous time, dynamical system. It allows us to reduce the dimensionality of the system by at least one, and by two if there exists a first integral, as is the case in the Hill problem.

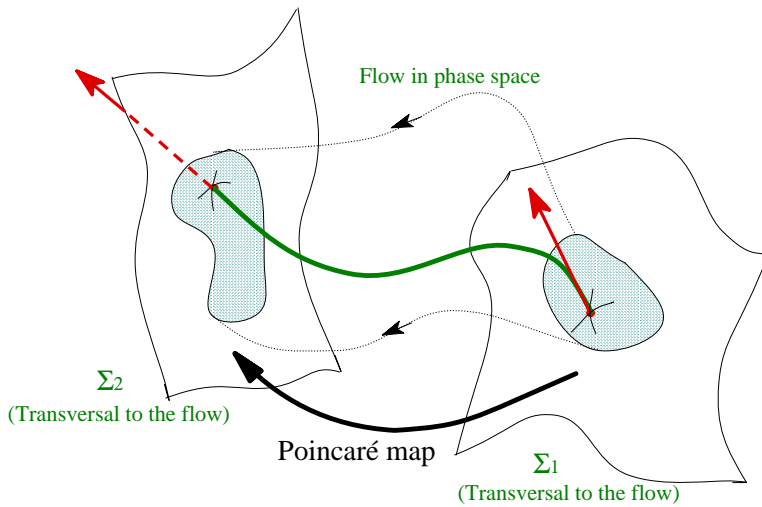


Figure IV.2: Concept of a Poincaré map

While generally applied to periodic orbits or to study the structure of flows near homoclinic/heteroclinic trajectories [42], the definition of a Poincaré map really requires only the choice of two surfaces of section transversal to the flow in phase space, and can be used in more general ways (see Figure IV.2 for a sketch of this situation). In our case, the surfaces of section are defined by a periapsis condition. The study of the Poincaré map is that of the discrete map from one surface of section to the next one.

1.1. Periapsis condition

Periapsis is defined as the point of closest approach from the central body. Thus, at these points, the magnitude of the radius vector achieves a minimum and the periapsis condition

can be formulated as*:

$$\begin{cases} \dot{r} = 0 \\ \ddot{r} > 0 \end{cases} \quad (\text{IV.1})$$

Expressed in terms of the position and velocity vectors, this definition is equivalent to:

$$\begin{cases} \mathbf{q}^T \dot{\mathbf{q}} = 0 \\ v^2 + \mathbf{q}^T \ddot{\mathbf{q}} > 0 \end{cases} \quad (\text{IV.2})$$

where $\ddot{\mathbf{q}}$ represents the acceleration of the particle in the rotating frame.

Thus we can see that periapsis is defined by a geometrical condition (\mathbf{q} orthogonal to $\dot{\mathbf{q}}$) plus a condition on the speed of the particle. In fact, the geometrical condition (apsis condition) projects onto the whole Hill region, \mathcal{H} , while the restriction imposed by the periapsis condition is more restrictive, as we will see in the next subsection. Note that when $v^2 + \mathbf{q} \cdot \ddot{\mathbf{q}} < 0$, the magnitude of the radius vector achieves a maximum. At such points, the particle is said to be at apoapsis.

Note that, even though $\dot{\mathbf{q}}$ and $\ddot{\mathbf{q}}$ are dependent on the frame, it can be easily checked that the notion of periapsis (or apoapsis) is independent of the frame. That is:

$$\begin{cases} (\mathbf{q}^T \dot{\mathbf{q}})_I = (\mathbf{q}^T \dot{\mathbf{q}})_R \\ (v^2 + \mathbf{q}^T \ddot{\mathbf{q}})_I = (v^2 + \mathbf{q}^T \ddot{\mathbf{q}})_R \end{cases} \quad (\text{IV.3})$$

where the subscripts I and R refer, respectively, to an inertial and a rotating frame centered at the center of mass of the attracting body.

The notion of periapsis (or apoapsis) does depend, however, on the force field considered. For example, the notion as defined in the Hill problem and the Kepler problem are not equivalent.

For the Kepler problem in a rotating frame, we have $\ddot{\mathbf{q}} = -2\boldsymbol{\omega} \times \dot{\mathbf{q}} - \boldsymbol{\omega} \times (\boldsymbol{\omega} \times \mathbf{q}) - \frac{\mathbf{q}}{|\mathbf{q}|^3}$, so that periapsis is achieved when \mathbf{q} and $\dot{\mathbf{q}}$ are orthogonal and $v^2 > \frac{1}{r} - 2\boldsymbol{\omega} \times (\mathbf{q} \times \dot{\mathbf{q}}) - |\boldsymbol{\omega} \times \mathbf{q}|^2$.

*Strictly speaking, one can also have $\ddot{r} = 0$ at periapsis but we will restrict ourselves to the definition given.

The acceleration in the Hill problem differs from that of the Kepler problem in a rotating frame by the term $-\mathbf{q} + 3(\mathbf{a}^T \mathbf{q})\mathbf{a}$. That is the periapsis condition is given by:

$$v^2 > \frac{1}{r} - 2\boldsymbol{\omega} \times (\mathbf{q} \times \dot{\mathbf{q}}) - |\boldsymbol{\omega} \times \mathbf{q}|^2 + |\mathbf{q}|^2 - 3(\mathbf{a}^T \mathbf{q})^2 \quad (\text{IV.4})$$

Thus, for $|\mathbf{q}|^2 - 3(\mathbf{a}^T \mathbf{q})^2 > 0$, a particle can be at periapsis in the Hill problem while being at apoapsis in the Kepler problem. For $|\mathbf{q}|^2 - 3(\mathbf{a}^T \mathbf{q})^2 < 0$, the situation is opposite, that is, a particle can be at apoapsis in the Hill problem while being at periapsis in the Kepler problem. Note that these cases can occur only for small eccentricities, i.e., nearly circular orbits.

Finally, one can notice that the notion of periapsis and apoapsis agree in both problems when $|\mathbf{q}|^2 - 3(\mathbf{a}^T \mathbf{q})^2 = 0$, which corresponds to a cone in position space with apex at the origin, axis given by the x -axis and with normal section corresponding to circles in the (y, z) coordinates. The first situation ($|\mathbf{q}|^2 - 3(\mathbf{a}^T \mathbf{q})^2 > 0$) occurs “outside” the cone while the other case ($|\mathbf{q}|^2 - 3(\mathbf{a}^T \mathbf{q})^2 < 0$) occurs “inside” the cone (i.e., the region containing the axis).

In the remainder, our focus will be on the case of the Hill problem and periapsis will thus be defined by (IV.4).

1.2. First consequences

An interesting fact in the Hill problem (this also holds for the restricted three body problem) is that the periapsis condition (resp. apoapsis condition) reduces to a condition independent of the velocity in the planar case. Indeed, one can use the Jacobi constant $J = \frac{1}{2}v^2 - \frac{1}{r} - \frac{1}{2}r^2g(\phi, \lambda)$ to express the speed of the particle in terms of its position and energy.

More precisely, in the planar case, $\boldsymbol{\omega} \times (\mathbf{q} \times \dot{\mathbf{q}}) = rv$ at any apsis in the direct case, while $\boldsymbol{\omega} \times (\mathbf{q} \times \dot{\mathbf{q}}) = -rv$ at any apsis in the retrograde case. Table IV.1 summarizes the implications of this formulation.

Table IV.1: Constraints on periapsis and apoapsis in the Hill problem.

	Direct case	Retrograde case
Periapsis	$2r^2v + f(r) > 0$	$f(r) - 2r^2v > 0$
Apoapsis	$2r^2v + f(r) < 0$	$f(r) - 2r^2v < 0$

The function $f(r)$ is obtained by expressing v^2 in the definition of $\dot{\mathbf{q}}$ in terms of position and the Jacobi constant.

$$f(r) = 2g(\phi, \lambda)r^3 + 2Jr + 1 \quad (\text{IV.5})$$

Note that the cases of direct apoapsis and retrograde periapsis are only possible if $f(r) < 0$ and $f(r) > 0$, respectively. Thus, in the region where $f(r) > 0$ (close to the center of the frame), a particle cannot be at direct apoapsis, while in the regions where $f(r) < 0$, a particle cannot be at a retrograde periapsis.

The equation $f(r) = 0$ is a cubic in r , very similar to the one defining the zero velocity surfaces, and can be solved explicitly. In fact, this equation *is* the equation defining \mathcal{Z} , modulo a scaling of the radius and the Jacobi constant. More precisely, letting $r = 4^{-1/3}\bar{r}$ and $J = \frac{1}{2}4^{1/3}\bar{J}$, equation (IV.5) transforms into (III.6). Thus, all the discussion performed in Chapter III for the case of the zero velocity surfaces applies, modulo the above scaling.

In particular, the surfaces $f(r) = 0$ determine a bounded region close to the primary where $f(r) > 0$ and no direct apoapsis is possible. Also, far from the primary (corresponding to the outer region in \mathcal{H}), we again have $f(r) > 0$ and no direct apoapsis is possible. This means that at a point where \mathbf{q} and $\dot{\mathbf{q}}$ are orthogonal and $\mathbf{q} \times \dot{\mathbf{q}}$ is along the positive z -axis, a particle will locally move away from the primary.

In fact, these regions connect when the surface opens at the value $\bar{J} = J_c$. In non-scaled units, this correspond to a value of Jacobi constant equal to $J = -\frac{3}{2}\left(\frac{3}{2}\right)^{1/3}$. At this value of J , all trajectories with $y = 0$ and $\dot{x} = 0$ will move away from the primary when $\dot{y} > 0$ on the positive x -axis and $\dot{y} < 0$ on the negative x -axis. For many trajectories, this will mean escape.

Similarly, outside the region $f(r) > 0$, the motion is constrained so that no retrograde periapsis is possible. It can be easily proven that such regions always exist for $J < 0$. In fact, all points on \mathcal{Z} corresponds to such a situation when $r < -\frac{3}{2J}$. Recall that this value of r correspond to the tangency of \mathcal{Z} with the radial lines when $J \geq J_c$ and lies in the region of forbidden motion for $J < J_c$. Thus, for $J < J_c$, all points on \mathcal{Z} in the inner region corresponds to apoapsis, while all points of \mathcal{Z} in the outer region correspond to periapsis. When $J \geq J_c$, the situation holds equally well, if the inner region is determined by $r < -\frac{3}{2J}$. In fact, this result shows that the outer component of $f(r) = 0$ meet \mathcal{Z} at $r = -\frac{3}{2J}$ and thus crosses the x -axis at r_c when $J = J_c$.

Finally, we should note that when $J < J_c$, the inner component of $f(r) = 0$ lies about midway between the origin and \mathcal{Z} and exactly midway on the y -axis, i.e., at $r = -\frac{1}{2J}$.

Figures IV.3 illustrates these situations in the 1st quadrant of the (x, y) plane (the other quadrants being obtained by symmetries).

The above discussion can, in fact, be strengthened by looking at the signs (and hence the roots) of the functions $f(r) - 2r^2v$ and $f(r) + 2r^2v$, where v is expressed in terms of position and the Jacobi constant. These functions involve square roots and the zeros cannot be solved explicitly. These zeros can, however, be easily computed numerically. In fact, these zeros are the roots of the 6th degree polynomial $w(r) = (f(r) - 2r^2v)(f(r) + 2r^2v)$:

$$w(r) = 4(g-1)r^3(gr^3 + 2Jr + 1) - 4r^3 + (2Jr + 1)^2 \quad (\text{IV.6})$$

The roots of $w(r)$ can be sorted according to the sign of $f(r)$ so as to make them correspond to the zeros of the above functions. Therefore, with the help of Table IV.1, one obtains the following diagram for the partitioning of a radial line (assuming the roots exist) between periapsis and apoapsis regions:

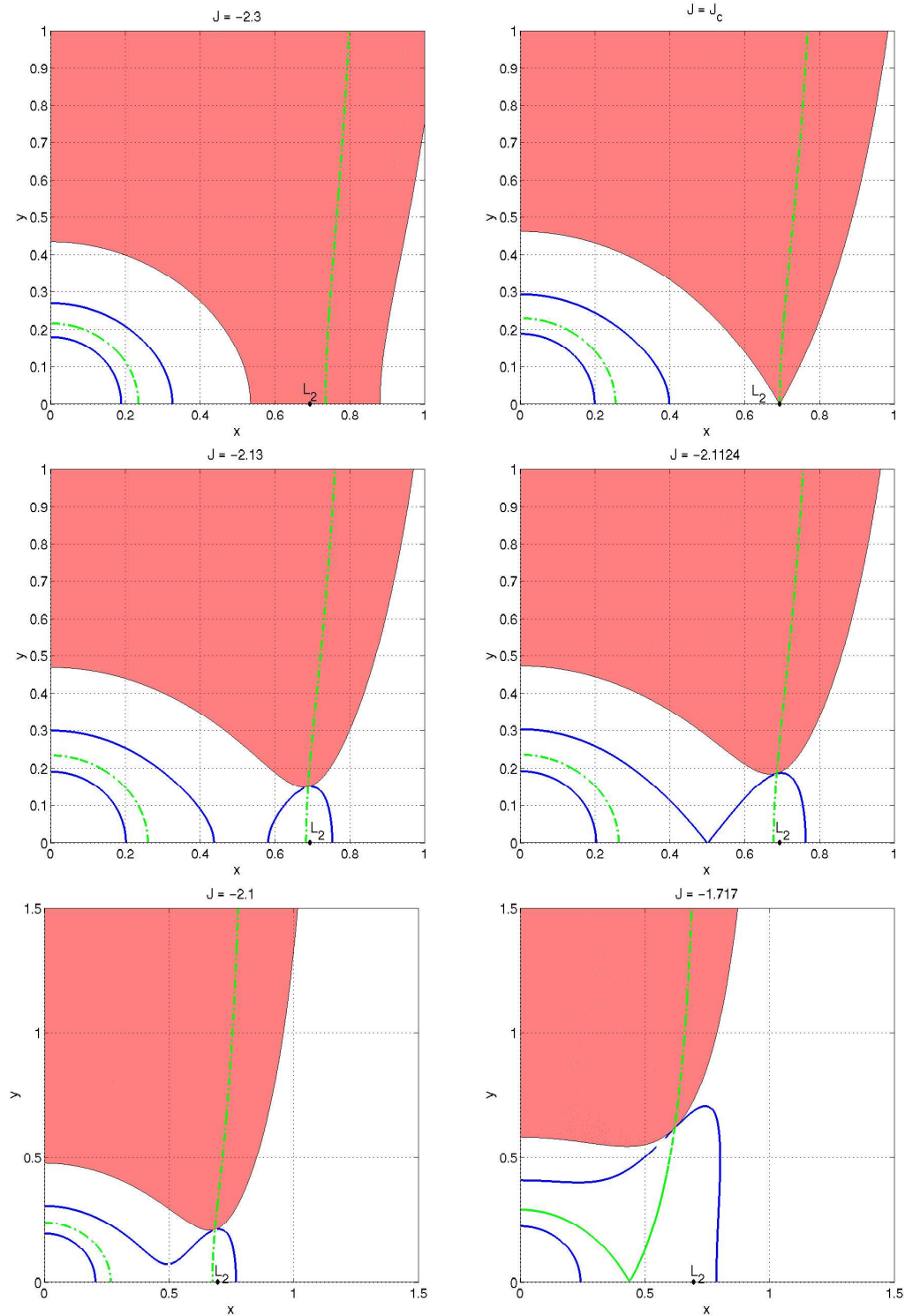
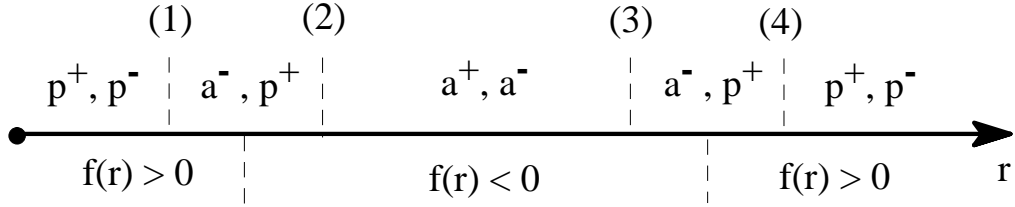


Figure IV.3: Limiting curves between periapsis and apoapsis in the planar Hill problem (solid line: $w(r) = 0$; dash-dot line: $f(r) = 0$).



where a^+ , a^- , p^+ and p^- denote, respectively, direct and retrograde apoapsis and periapsis, and the numbers (1) through (4) represent the roots of $w(r)$.

Thus, close to the primary, only periapses are possible and, close to the surface $f(r) = 0$, only retrograde apoapses and direct periapses are possible. More generally, looking at Figure IV.3 where the roots of $w(r)$ have been plotted (thick solid lines), one can obtain an idea of what these regions look like.

Further properties of the roots of $w(r)$ can be obtained by looking at w as a function of J . Indeed, $w(r)$ is a quadratic form in J , so that even though the roots of $w(r)$ cannot be solved a priori by radicals, one can solve for J as a function of r .

$$w(J) = 4r^2J^2 + 4r(1 + 2(g - 1)r^3)J + [1 + 4(g - 2)r^3 + 4g(g - 1)r^6] \quad (\text{IV.7})$$

The reduced discriminant of $w(J) = 0$ is $\Delta' = 16r^5[1 - (g - 1)r^3]$, so that, in particular, $\Delta' > 0$ as soon as $g \leq 1$ or $r < (g - 1)^{-1/3}$ when $g > 1$. Thus, for $g > 1$, $w(r) > 0$ for $r > (g - 1)^{-1/3}$ and only periapses are possible. The value of $r = (g - 1)^{-1/3}$ is actually reached for $J = -\frac{3}{2}(g - 1)^{1/3}$. In the particular case of the x -axis, the corresponding values of r and J are, respectively, $r = 2^{-1/3} \simeq 0.793$ and $J = -\frac{3}{2}2^{1/3} \simeq -1.889$.

From (IV.7), one can also see that for each value of r , there corresponds two values of J (J^+ and J^-) for which $w(J) = 0$. This fact allows us to show that the points at which the roots (2) and (3) in the previous diagram collapse (if they exist) also correspond to the points at which the roots (1) and (4) must collapse and the corresponding values of J are J^- and J^+ , respectively. Notably, $w(r) > 0$ for any value of r on a radial line defined by $g > 1$, when $J > -\frac{3}{4}[4(g - 1)]^{1/3} + \sqrt{\frac{3}{4}\frac{1}{[4(g - 1)]^{1/3}}}$. The last root on this radial line will occur when J equals this critical value, at a radius of $[4(g - 1)]^{-1/3}$. In the particular case

of the x -axis, these critical values of collapse and disappearance of roots are $r = 0.5$ and $J = -\frac{3}{2} - \frac{1}{2}\sqrt{\frac{3}{2}} \simeq -2.1124$ and $J = -\frac{3}{2} - \frac{1}{2}\sqrt{\frac{3}{2}} \simeq -0.8876$, respectively. This is in concordance with the plots shown on Figure IV.3.

Another interesting consequence of these results is that for low values of the Jacobi constant, the two inner roots of $w(r)$ lie on curves which are close to circular and the Hill's periodic orbits which are almost circular must, *per force*, lie close to these curves. Indeed, the periapsis of such an orbit must lie below the first curve in the direct case and its apoapsis must lie above it. Since the eccentricity is small at each point of these orbits, the two apses must be close together. The same situation holds true in the retrograde case with the 2nd curve. In fact, the situation is more general and remains true for any quasi-periodic, quasi-circular orbits. That is, the KAM tori corresponding to trajectories with small eccentricity in the rotating Kepler problem must lie close to these curves, when they exist, giving us a qualitative idea of their evolution as a function of J .

Finally, we should note that in the spatial problem, $2\boldsymbol{\omega}^T(\mathbf{q} \times \dot{\mathbf{q}}) = rv \cos \theta$ where θ represents the inclination as defined in the rotating frame. The above results apply to this case by replacing the direct and retrograde cases with θ below or above 90° . The limits between regions with only periapsis or apoapsis possible are independent of θ and are thus given by the roots of $w(r)$.

1.3. Transversality

As was noted in the introduction of the present section, Poincaré maps are defined by choosing some surface of section transversal to the flow. Transversality means that the flow generated by the differential equations under consideration crosses, locally, the surfaces of section from one side to the other. This requirement of transversality is indeed needed to avoid degeneracies, such as circular orbits in the Kepler problem for a periapsis Poincaré map.

In our case, the flow is generated by the vector field $\mathbf{X} = (\dot{\mathbf{q}}^T, \ddot{\mathbf{q}}^T)$ where $\ddot{\mathbf{q}}$ is given

by Hill equations:

$$\ddot{\mathbf{q}} = -2\boldsymbol{\omega} \times \dot{\mathbf{q}} - \boldsymbol{\omega} \times (\boldsymbol{\omega} \times \mathbf{q}) - \frac{\mathbf{q}}{|\mathbf{q}|} - \mathbf{q} + 3(\mathbf{a}^T \mathbf{q}) \quad (\text{IV.8})$$

The surfaces of section are first defined by the apsis condition, $\mathbf{q}^T \dot{\mathbf{q}} = 0$, so that the transversality condition requires that $\mathbf{X}^T \nabla(\mathbf{q}^T \dot{\mathbf{q}}) \neq 0$. That is:

$$v^2 + \mathbf{q}^T \ddot{\mathbf{q}} \neq 0 \quad (\text{IV.9})$$

Thus, in the case of a periapsis Poincaré map, transversality is automatically satisfied (with the definition we adopted). In fact, the same holds true for an apoapsis Poincaré map and one can define periapsis to apoapsis maps, as well.

Note that the cases where $\mathbf{X}^T \nabla(\mathbf{q}^T \dot{\mathbf{q}}) = 0$ are exactly given by the roots of $w(r)$, as discussed in the previous subsection. Away from these roots, periapsis and apoapsis are well defined.

By looking at the dynamics via Poincaré maps, the dimensionality of the initial system is reduced by one. Moreover, one can also restrict the map to lie in a given energy manifold to remove one additional dimension. Thus, in the spatial Hill problem , we obtain 4-dimensional maps, while in the planar problem, one obtains a 2-dimensional map. As we have seen in the previous subsection, these maps can be parameterized by the position and the inclination in the rotating frame. The position can either be defined via Cartesian coordinates or by using spherical coordinates.

We should note that other restrictions of the maps are possible and will be used in the subsequent sections and chapters. Indeed, one can consider a restricted region of phase space (as defined, for example, by some fixed value of a set of orbital elements) and look at their image under the maps. As compared to the more classical usage of Poincaré maps, we will study the one-time iterate of the maps to obtain numerical conditions on the existence of certain transfers, rather than analyzing the asymptotic behavior of these maps.

In the realm of the same idea, note that the periapsis Poincaré maps, as defined above, are not canonical (which is preferable for theoretical investigations), but can be slightly

changed so as to become canonical. Indeed, in the region of phase space where the notion of periapsis between the Hill and Kepler problems agree, one can define periapsis as the points where the mean anomaly, M , is zero (modulo 2π). Then, a canonical map can be obtained from Delaunay's variables by considering the surface of section defined by the condition $M = 0$ [2π] and restricting the flow to the energy manifold by computing L from the expression of the Jacobi constant. A similar map can be defined with the modified set of Delaunay's variable (see previous chapter). Even though the numerical applications which are presented in chapter V and VI do not use these formulations, the next few sections implicitly rely on them.

2. Picard's method of successive approximations

Picard's method of successive approximations is a method that can be used to prove the existence and uniqueness of solutions to ordinary differential equations by building a sequence of functions that converge uniformly towards the solution of the problem. When applied to the case of a Poincaré map, each approximate function yields an approximation of the Poincaré map by evaluating the functions on the surfaces of section.

This section reviews this method, emphasizing the case of Hamiltonian systems where it is shown that each approximate function generated is symplectic for a restricted class of Hamiltonian, and a modification of Picard's method is also presented to yield energy preserving maps.

2.1. General case

Consider a general system of ordinary differential equations:

$$\dot{\mathbf{X}} = \mathbf{F}(\mathbf{X}, t) \quad (\text{IV.10})$$

The existence and uniqueness of solutions satisfying the initial conditions $\mathbf{X}(t_0) = \mathbf{X}_0$ can be proven if \mathbf{F} is continuous in t and Lipschitz in \mathbf{X} , uniformly in t , and Picard's method can be used to prove this fact.

The method consists of considering the mapping Ψ :

$$\Psi : \mathbf{X}(t) \rightarrow \mathbf{X}_0 + \int_{t_0}^t \mathbf{F}(\mathbf{X}(\tau), \tau) d\tau \quad (\text{IV.11})$$

and showing that it corresponds to a contraction mapping, so that the existence of a unique fixed point (the solution) is guaranteed. Moreover, we know that for any initial condition close to the fixed point, iterates of the map converge uniformly and exponentially towards the fixed point. That is, locally, the sequence of functions:

$$\begin{aligned} \mathbf{X}_{(0)}(t) &= \mathbf{X}_0 \\ \mathbf{X}_{(1)}(t) &= \mathbf{X}_0 + \int_{t_0}^t \mathbf{F}(\mathbf{X}_{(0)}, \tau) d\tau \\ &\dots \\ \mathbf{X}_{(n)}(t) &= \mathbf{X}_0 + \int_{t_0}^t \mathbf{F}(\mathbf{X}_{(n-1)}, \tau) d\tau \\ &\dots \end{aligned}$$

converges uniformly towards the solution of the original problem (IV.10).

More precisely, if \mathbf{F} is bounded by U and is Lipschitz, with constant k , in \mathbf{X} in some region $|t - t_0| \leq T$ and $|\mathbf{X} - \mathbf{X}_0| \leq UT$, then any C^1 function whose graph is contained in that region will converge towards the solution of (IV.10) with initial condition \mathbf{X}_0 . The error between the solution and the n^{th} approximation is given by:

$$|\mathbf{X}(t) - \mathbf{X}_{(n)}(t)| \leq \frac{D}{k} (e^{kh} - 1) \frac{(kh)^n}{n!} \quad (\text{IV.12})$$

where D represents the maximum error of $X_{(0)}$ on the domain $|t - t_0| \leq h$.

Thus, assuming that the n^{th} approximation has been computed, one can compute the change in the state \mathbf{X} between $t_0 - h$ and $t_0 + h$, by evaluating $\mathbf{X}_{(n)}(t)$ at these instants:

$$\Delta \mathbf{X}_{(n)} = \mathbf{X}_{(n)}(t_0 + h) - \mathbf{X}_{(n)}(t_0 - h) = \int_{t_0-h}^{t_0+h} \mathbf{F}(\mathbf{X}_{(n)}(\tau), \tau) d\tau \quad (\text{IV.13})$$

That is, we obtained an approximation of the time $2h$ map of the flow around \mathbf{X}_0 . Also, one can as well consider the time $\pm h$ maps and obtain similar estimates.

2.2. Hamiltonian case

We know that Hamiltonian flows preserve the Hamiltonian function (energy) in the autonomous case, as well as the symplectic structure on the underlying phase space (generally the cotangent bundle of the configuration space). That is, for each time t , the map that associates the initial state \mathbf{z}_0 to the state value at time t is a canonical mapping. Therefore it seems preferable in long term integrations of a Hamiltonian system to prefer either energy preserving or symplectic preserving schemes [†]. Thus, in the case of Picard's method of successive approximations, one can ask if the contracting map Ψ is symplectic or energy preserving.

More precisely, recall that Hamilton's equations can be written as $\dot{\mathbf{z}} = \mathbf{J} \nabla \mathcal{H}(\mathbf{z}, t)$ where $\mathbf{z} = (\mathbf{q}^T, \mathbf{p}^T)$ represents the $2N$ -dimensional state vector and \mathbf{J} is the symplectic matrix. Then Picard's method of successive approximations generates the maps:

$$\Psi_{(i)} : \mathbf{z}_0 \rightarrow \mathbf{z}_0 + \int_{t_0}^t \mathbf{J} \nabla \mathcal{H}(\mathbf{z}_{(i-1)}(\tau), \tau) d\tau \quad (\text{IV.14})$$

where $\mathbf{z}_{(i-1)}$ is the approximate solution at the $(i-1)^{th}$ iteration of the process. Thus, the question is to determine if $\Psi_{(i)}$ is symplectic (t fixed).

First iterate map

The first step consists of checking if $\Psi_{(1)}$ is symplectic. In order to see this, we only need to compute $\mathbf{D}\Psi_{(1)} \mathbf{J} \mathbf{D}\Psi_{(1)}$ and see if it is equal to J .

One can easily compute that $\mathbf{D}\Psi_{(1)} = I + \int_{t_0}^t \mathbf{J} \nabla^2 \mathcal{H}(\mathbf{z}_0, \tau) d\tau$, so that:

$$\mathbf{D}\Psi_{(1)}^T \mathbf{J} \mathbf{D}\Psi_{(1)} = \mathbf{J} + \left(\int_{t_0}^{t_0+t} \nabla^2 \mathcal{H} d\tau \right) \mathbf{J} \left(\int_{t_0}^{t_0+t} \nabla^2 \mathcal{H} d\tau \right) \quad (\text{IV.15})$$

Thus, $\Psi_{(1)}$ is symplectic if [‡] $\left(\int_{t_0}^t \nabla^2 \mathcal{H} d\tau \right) \mathbf{J} \left(\int_{t_0}^t \nabla^2 \mathcal{H} d\tau \right) = 0$.

[†]Preserving both the energy and the symplectic structure has been shown by Z.Ge and J.Marsden to be equivalent to exactly integrating the equations, modulo a reparameterization of time.

[‡]Strictly speaking, one needs only require that $\left(\int_{t_0}^t \nabla^2 \mathcal{H} d\tau \right) \mathbf{J} \left(\int_{t_0}^t \nabla^2 \mathcal{H} d\tau \right) = \lambda \mathbf{J}$ with $\lambda \neq -1$ but we restrict ourselves to the non-scaling case.

In the autonomous case (\mathcal{H} independent of t), the condition simplifies to:

$$\nabla^2 \mathcal{H} \mathbf{J} \nabla^2 \mathcal{H} = 0 \quad (\text{IV.16})$$

and the first step of Picard's method corresponds to an Euler step since the map (IV.14) reduces to $\Psi_{(1)}(\mathbf{z}_0) = \mathbf{z}_0 + (t - t_0) \mathbf{J} \nabla \mathcal{H}(\mathbf{z}_0)$. However, higher order steps differ, in general, from Taylor's series expansions in a similar way as in the non-autonomous case. We restrict ourselves to the autonomous case in this subsection for simplicity.

Expressing the above condition in terms of the conjugate variables \mathbf{q} and \mathbf{p} , one can easily check that it is equivalent to:

$$\begin{cases} \frac{\partial^2 \mathcal{H}}{\partial \mathbf{q}^2} \frac{\partial^2 \mathcal{H}}{\partial \mathbf{p} \partial \mathbf{q}} \text{ symmetric} \\ \frac{\partial^2 \mathcal{H}}{\partial \mathbf{p}^2} \frac{\partial^2 \mathcal{H}}{\partial \mathbf{q}^2} - \left(\frac{\partial^2 \mathcal{H}}{\partial \mathbf{p} \partial \mathbf{q}} \right)^2 = 0 \end{cases} \quad (\text{IV.17})$$

Note that in the case of an integrable system, \mathcal{H} only depends on the action variables \mathbf{p} , and it is clear that the above conditions are satisfied.

For non-integrable systems, one can write \mathcal{H} as an integrable part $\mathcal{H}_0(\mathbf{p})$ that only depends on the action variables, plus a disturbing function $\mathcal{R}(\mathbf{q}, \mathbf{p})$.

$$\mathcal{H} = \mathcal{H}_0(\mathbf{p}) + \mathcal{R}(\mathbf{q}, \mathbf{p}) \quad (\text{IV.18})$$

Then, it can be easily shown that the above conditions are equivalent to :

$$\begin{cases} \frac{\partial^2 \mathcal{R}}{\partial \mathbf{q} \partial \mathbf{p}} \frac{\partial^2 \mathcal{H}_0}{\partial \mathbf{p}^2} = 0 \\ \frac{\partial^2 \mathcal{H}_0}{\partial \mathbf{p}^2} \frac{\partial^2 \mathcal{R}}{\partial \mathbf{q}^2} + \frac{\partial^2 \mathcal{R}}{\partial \mathbf{p}^2} \frac{\partial^2 \mathcal{H}_0}{\partial \mathbf{p}^2} = 0 \end{cases} \quad (\text{IV.19})$$

These conditions are certainly restrictive, but are not restricted to only integrable systems. For example, in the case of a perturbed Kepler problem in a rotating frame, $\mathcal{H}_0 = -\frac{1}{2L} + \mathcal{H}$ in Delaunay's variables, and any disturbing function \mathcal{R} that only depends on G, H, ω and Ω will satisfy the above conditions.

N^{th} iterate map

In the case of higher order approximations, it can be shown that Picard's method leads to symplectic maps for the class of Hamiltonian satisfying the relation:

$$\nabla^2 \mathcal{H}(\mathbf{X}_1) \mathbf{J} \nabla^2 \mathcal{H}(\mathbf{X}_2) = 0 \quad (\text{IV.20})$$

for any \mathbf{X}_1 and \mathbf{X}_2 in the domain under consideration.

Even though the class of Hamiltonian systems satisfying this condition includes all autonomous integrable systems, it seems too unwieldy to be of practical interest, and in particular the Hamiltonian of the Hill problem does not belong to that class. Instead, one can ask if Picard's method preserve the Hamiltonian function.

Energy preserving maps

Away from an equilibrium, $\nabla \mathcal{H} \neq 0$, and one can locally solve for one coordinate (say z_1) in terms of the others.

$$z_1 = \phi(\bar{\mathbf{z}}) \quad (\text{IV.21})$$

where the bar operation consists of removing the first coordinate of its argument. With this reduction, $\mathcal{H}(\phi(\bar{\mathbf{z}}), \bar{\mathbf{z}})$ is constant as $\bar{\mathbf{z}}$ varies. For example, in the case of the Hill problem, one can solve for the Keplerian energy C in terms of the other variables.

The equations of motion for $\bar{\mathbf{z}}$ are given by:

$$\dot{\bar{\mathbf{z}}} = \overline{\mathbf{J} \nabla \mathcal{H}(\phi(\bar{\mathbf{z}}), \bar{\mathbf{z}})} \quad (\text{IV.22})$$

Now, assuming \mathcal{H} to be C^2 (which we have implicitly done so far), it is clear that $\overline{\mathbf{J} \nabla \mathcal{H}(\phi(\bar{\mathbf{z}}), \bar{\mathbf{z}})}$ is C^1 and thus Lipschitz. Picard's method can be applied to this reduced system. The variable z_1 is obtained after each iteration by using (IV.21).

In the case of the first iteration, this process simply reduces to applying Picard's method directly to the full system (since z_0 is constant) and then to correct z_1 so as to preserve the energy. This will be applied in the next section.

3. First step in Hill's problem

In order to apply the previous method to Hill's problem, we use the canonical formulation as given in Chapter III. More precisely, recall that the Keplerian Energy, C , the angular momentum magnitude, G , and the z component of the angular momentum, H , are governed by the differential equations:

$$\dot{C} = \frac{\partial R}{\partial t} \quad ; \quad \dot{G} = \frac{\partial R}{\partial \omega} \quad ; \quad \dot{H} = \frac{\partial R}{\partial \Omega} \quad (\text{IV.23})$$

where the disturbing function, R , is expressed in terms of orbital elements[§]:

$$\begin{aligned} R = & \frac{1}{4} N^2 r^2 [1 + 3 \cos^4(i/2) \{ \cos 2(\omega + \Omega) \cos 2(f - N(t - t_0)) \\ & - \sin 2(\omega + \Omega) \sin 2(f - N(t - t_0)) \} \\ & + 3 \sin^4(i/2) \{ \cos 2(\omega - \Omega) \cos 2(f + N(t - t_0)) \\ & - \sin 2(\omega - \Omega) \sin 2(f + N(t - t_0)) \} \\ & + \frac{3}{2} \sin^2 i \{ \cos 2\Omega \cos 2N(t - t_0) + \sin 2\Omega \sin 2N(t - t_0) \\ & + \cos 2\omega \cos 2f - \sin 2\omega \sin 2f - 1 \}] \end{aligned} \quad (\text{IV.24})$$

Here, t_0 represents any given epoch.

3.1. Estimates for ΔG , ΔH and ΔC

The estimates for ΔG and ΔH , i.e., the changes in G and H from one periapsis passage to the next one (assuming it exists) is obtained by applying the first step of Picard's method to (IV.23). As we have just seen, this consists of performing the quadratures:

$$\int_{t_0}^t \frac{\partial \mathcal{R}}{\partial \omega} d\tau \quad \text{and} \quad \int_{t_0}^t \frac{\partial \mathcal{R}}{\partial \Omega} d\tau$$

with the initial state kept fixed in the integration. This state, given in terms of orbital elements $(a, e, i, \omega, \Omega)$, is chosen at apoapsis since the tidal perturbations are strongest

[§]We use a developed form of \mathcal{R} (as compared to the form given in the previous chapter) since it is better suited for the application to be made.

when farthest from the center of the frame. It can also be verified numerically that these estimates are more accurate when the initial state is taken at apoapsis, as compared to taking it at periapsis.

Then, to obtain the estimates, we evaluate the above integrals at two successive periapsis passages. In the first approximation (and under the restriction pointed out in the first section), this corresponds to integrating over a period defined by the Keplerian approximation, $T = 2\pi a^{-3/2}$, i.e., we set:

$$\Delta G = \int_{t_0-T/2}^{t_0+T/2} \frac{\partial \mathcal{R}}{\partial \omega} d\tau \quad \text{and} \quad \Delta H = \int_{t_0-T/2}^{t_0+T/2} \frac{\partial \mathcal{R}}{\partial \Omega} d\tau$$

where t_0 represents the epoch at apoapsis.

This approach has been applied previously to describe orbital variations due to the attraction of a rotating gravity field [31]. In the case of the Hill problem, the result of the integration can be expressed as:

$$\begin{aligned} \Delta G &= -\frac{3}{2}\tilde{p}^{\frac{7}{2}} \left[\cos^4(i/2) \sin 2(\omega + \Omega) I_2^{-4} \right. \\ &\quad + \sin^4(i/2) \sin 2(\omega - \Omega) I_{-2}^{-4} \\ &\quad \left. + \frac{5\pi}{2} \sin^2 i \sin 2\omega \frac{e^2}{(1-e^2)^{7/2}} \right] \end{aligned} \quad (\text{IV.25})$$

$$\begin{aligned} \Delta H &= -\frac{3}{2}\tilde{p}^{\frac{7}{2}} \left[\cos^4(i/2) \sin 2(\omega + \Omega) I_2^{-4} \right. \\ &\quad - \sin^4(i/2) \sin 2(\omega - \Omega) I_{-2}^{-4} \\ &\quad \left. + \frac{1}{2} \sin^2 i \sin 2\Omega I_0^{-4} \right] \end{aligned} \quad (\text{IV.26})$$

where the integrals I_k^l are defined as:

$$I_k^l = 2 \int_0^\pi (1+e \cos f)^l \cos [kf - 2a^{3/2}(M-\pi)] df \quad (\text{IV.27})$$

These integrals do not have a closed form, but can be evaluated numerically and are related to Hansen coefficients [31]. Figure IV.4-IV.9 show the values of these integrals as contour plots.

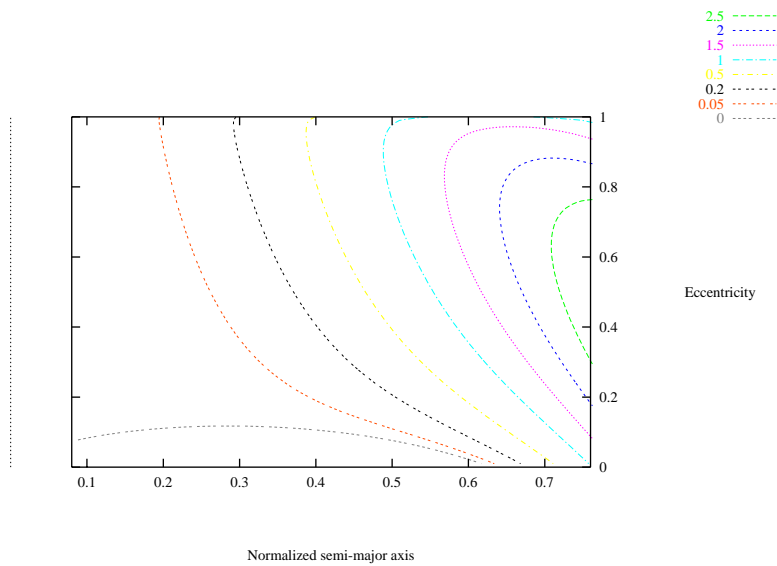


Figure IV.4: Integral $p^{7/2} I_2^{-4}$.

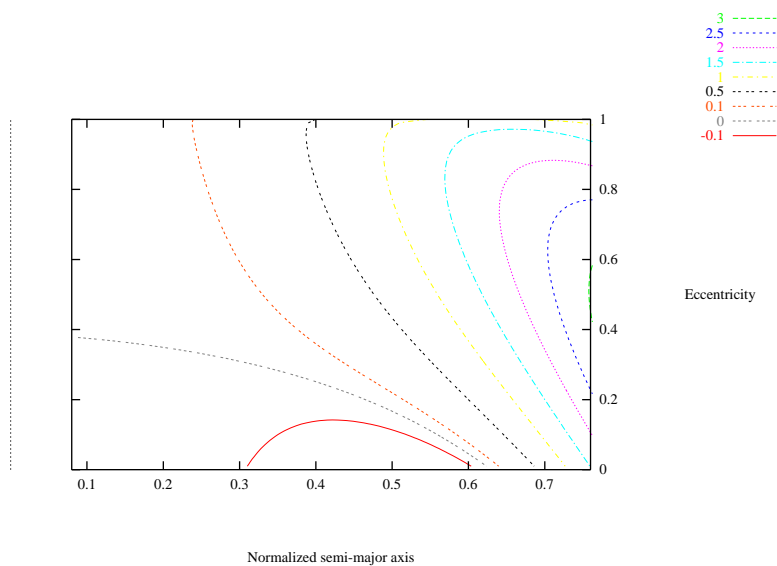


Figure IV.5: Integral $p^{7/2} (I_2^{-4} - I)$.

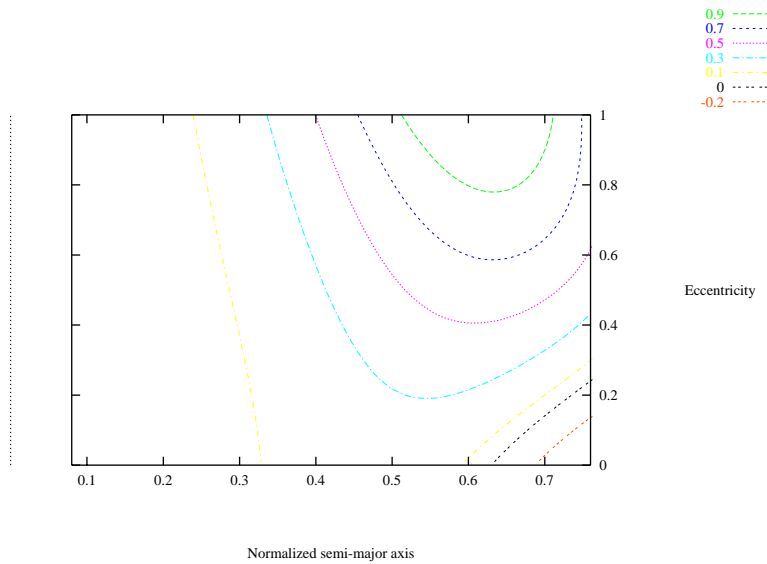


Figure IV.6: Integral $p^{7/2} I_0^{-4}$.

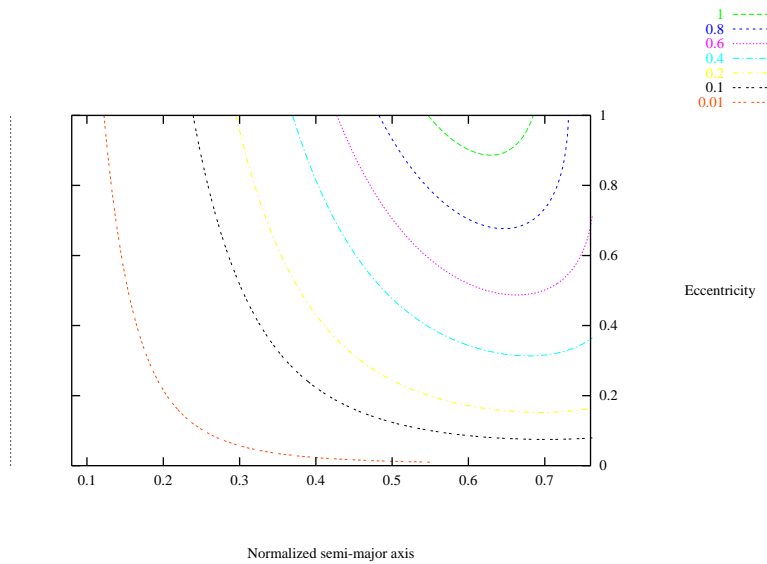


Figure IV.7: Integral $p^{7/2} (I_0^{-4} - I)$.

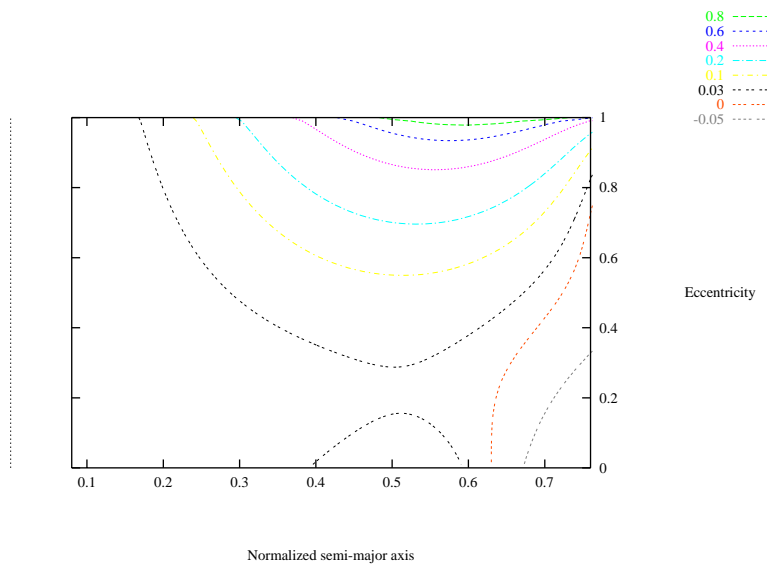


Figure IV.8: Integral $p^{7/2} I_{-2}^{-4}$.

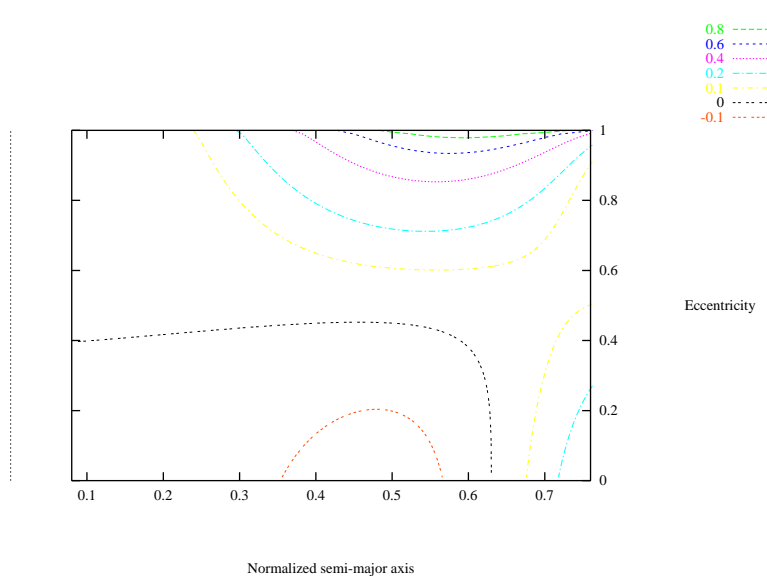


Figure IV.9: Integral $p^{7/2} (I_{-2}^{-4} - I)$.

The estimate for the change in energy, ΔC , is then obtained from the Jacobi integral:

$$\begin{aligned}\Delta C &= C_{(t_0+T/2)} - C_{(t_0-T/2)} \\ &= (J + NH + R)_{(t_0+T/2)} - (J + NH + R)_{(t_0-T/2)} \\ &= N\Delta H - \frac{1}{2}N^2(\Delta r^2 - 3\Delta x^2)\end{aligned}$$

The result of this evaluation is given by:

$$\begin{aligned}\Delta C &= -\frac{3}{2}p^{\frac{7}{2}} [\cos^4(i/2) \sin 2(\omega + \Omega) (I_2^{-4} - I) \\ &\quad - \sin^4(i/2) \sin 2(\omega - \Omega) (I_{-2}^{-4} - I) \\ &\quad + \frac{1}{2} \sin^2 i \sin 2\Omega (I_0^{-4} - I)]\end{aligned}\tag{IV.28}$$

where

$$I = \frac{\sin(2\pi a^{3/2})}{p^{3/2}(1+e)^2}\tag{IV.29}$$

From these results, one can obtain estimates for the change in semi-major axis a , inclination i , eccentricity e and related quantities. For example, $a = -\frac{1}{2C}$ and $T = 2\pi a^{-3/2}$, so that $\Delta a = -\frac{\mu\Delta C}{2C^2}$ and $\Delta T = -2\pi \frac{3}{2}a^{-5/2}\Delta a$ at first order. That is:

$$\frac{\Delta a}{a} = -\frac{\Delta C}{C} \quad \text{and} \quad \frac{\Delta T}{T} = -\frac{3}{2} \frac{\Delta C}{C}$$

Similarly,

$$\frac{\Delta e}{e} = -\frac{1-e^2}{e^2} \left[\frac{1}{2} \frac{\Delta C}{C} + \frac{\Delta G}{G} \right] \quad ; \quad \Delta i = (\cot i) \left[\frac{\Delta G}{G} - \frac{\Delta H}{H} \right]$$

$$\frac{\Delta r_p}{r_p} = \frac{1-e}{2e} \frac{\Delta C}{C} + \frac{1+e}{e} \frac{\Delta G}{G} \quad ; \quad \frac{\Delta r_a}{r_a} = -\frac{1+e}{2e} \frac{\Delta C}{C} - \frac{1-e}{e} \frac{\Delta G}{G}$$

These expressions can also be expressed as a function of the osculating elements using equations (IV.25), (IV.26) and (IV.28). These expressions are reported in Appendix D.

3.2. Check of the accuracy

The validity of the previous approach has been tested using two precise numerical propagations of a trajectory using the DPTRAJ program (Cf. Appendix E). The test case considered here corresponds to an interim orbit for the Europa Orbiter Mission, which is used as

a possible means to lower ΔV in the Europa orbit insertion phase of the mission. The initial conditions are $a = 5386.5$ km, $e = 0.6746$ and $i = 32.0^\circ$ at an epoch 05-MAR-2008. This trajectory impacts the surface of Europa on 12-MAR-2008 after about 12 orbits of the spacecraft around Jupiter.

From the numerical values of the orbital elements at periapsis and apoapsis, the change in energy, angular momentum magnitude and its projection on the z-axis has been computed and compared with the values obtained using the analytical expressions. The previous expressions are then used to calculate the values of the changes in orbital elements.

Table IV.2: Comparison between DPTRAJ and analytical results.

Apoapsis	a (km)	Δa (km)	% error	e	Δe	% error	i (deg)	Δi (deg)	error (deg)
A1	6143.77	-162.88	-0.80	0.648	-0.013	-5.08	38.05	14.94	0.52
A2	5822.98	356.95	-0.15	0.524	-0.233	2.66	42.19	-11.78	0.99
A3	5293.84	-8.30	0.06	0.449	-0.012	0.21	36.42	0.66	-0.51
A4	5738.72	-310.06	-0.68	0.559	0.281	0.30	40.91	6.46	0.20
A5	6058.48	111.50	1.23	0.710	0.003	1.96	31.13	-12.56	-3.04
A6	5441.63	228.99	0.25	0.607	-0.280	5.52	29.37	0.63	0.39
A7	5386.55	-203.49	-0.12	0.593	0.254	-4.04	29.27	-0.62	-0.19
A8	6123.58	-180.46	-0.32	0.683	0.014	-6.35	33.23	14.89	1.26
A9	5800.13	351.44	0.27	0.548	-0.253	-0.32	41.63	-9.86	0.68
A10	5301.54	11.76	-0.03	0.447	-0.026	2.11	35.44	-0.54	0.19
A11	5732.30	-314.47	-0.35	0.532	0.257	0.15	40.17	8.92	-0.29
A12	6096.93	65.31	1.52	0.687	0.045	1.08	34.08	-13.69	-2.11

Table IV.2 shows the numerical value of the change (from periapsis to periapsis) in a , e and i together with the percent error made using the analytical theory where the difference of the changes are normalized by the corresponding quantities at apoapsis. For instance the percentage error in semi-major axis is defined as $100 \frac{\Delta' a - \Delta a}{a}$ where Δ' represent the analytical result, Δ the DPTRAJ result and the value of a is taken at the corresponding

apoapsis.

These results show that the error made using the analytical approach is on the order of a few percent. The expressions derived can hence be used to give a qualitative picture of the dynamics over one orbit in the tidally perturbed environment, but cannot be used as a precise predictive theory. Yet, the results can be used as guidelines in the design of transfer orbits. Some possible applications are discussed in the next sections.

4. Applications

Several qualitative features of the dynamics can be drawn from the analytical estimates. These include the sign of the changes in the orbital elements over one orbit, the mapping of the dynamics as a function of ω and Ω , sufficient conditions to avoid impacting the surface of the primary and variation in the results as functions of a, e, i .

4.1. Sign of the changes

The expressions obtained in the previous section are the linear combinations of defined functions of a, e and i (the integrals I_k^l) scaled by simple trigonometric functions of ω and Ω . This indicates that the signs of the changes will vary as the value of these last two variables change, that is, as the orientation of the trajectory at apoapsis changes with respect to the perturbing body, i.e., Jupiter for the Europa Orbiter.

For example, in the case of zero inclination, the expressions for ΔG , ΔH and ΔC degenerate to:

$$\begin{aligned}\Delta G &= -\frac{3}{2}p^{7/2}I_2^{-4}\sin 2(\omega + \Omega) = \Delta H \\ \Delta C &= -\frac{3}{2}p^{7/2}(I_2^{-4} - I)\sin 2(\omega + \Omega)\end{aligned}$$

resulting in a sinusoidal variation in the changes of these quantities as a function of the longitude of the periapsis ($\omega + \Omega$) in the equatorial plane. The sign of the changes is then completely determined by the quadrant[¶] in which $\omega + \Omega$ falls and the sign of the

[¶]The j^{th} quadrant being defined as $\{\theta : (j-1)\pi/2 \leq \theta < j\pi/2\}$

quantities $p^{7/2} I_2^{-4}$ and $p^{7/2} (I_2^{-4} - I)$. These quantities can be represented as contour plots as a function of the non-dimensionalized semi-major axis and the eccentricity so as to determine their sign (Cf. Figures IV.4 and IV.5). For eccentricities above 0.4, these quantities are positive and the signs of ΔG , ΔH and ΔC are determined by the following rule: the changes are positive in the second and fourth quadrant and negative in the first and third quadrant for $e > 0.4$. A similar analysis applies in the case $i = 180^\circ$.

In the case of non-zero inclination, this degeneracy of the expressions disappears. There exists, however, some symmetry in the expressions since ΔC and ΔH do not include a term depending only on Ω whereas ΔG has no term depending only on ω . This implies that:

$$\begin{aligned}\Delta C(\Omega, \omega) &= -\Delta C(\Omega + \pi/2, \omega) \\ \Delta H(\Omega, \omega) &= -\Delta H(\Omega + \pi/2, \omega) \\ \Delta G(\Omega, \omega) &= -\Delta G(\Omega, \omega + \pi/2)\end{aligned}$$

Thus a shift in ω and Ω of $\pi/2$ can make a maximum of any of the expressions obtained become a minimum and vice versa.

4.2. Dynamics in ω and Ω space

As noticed in the previous subsection, the dynamics are strongly dependent on the argument of periapsis and longitude of the ascending node and can be represented as contour plots in the $\omega + \Omega$, $\omega - \Omega$ plane. Given a , e and i at apoapsis, these plots give a qualitative picture of the discrete dynamics of the changes in orbital elements over one orbit when considered as a function of ω and Ω . Figures IV.10 - IV.19 give some examples of such plots. These figures show that there are regions in the $\omega + \Omega$, $\omega - \Omega$ space such that the changes in a given quantity over one orbit are either positive or negative. These regions indicate how the dynamics of the satellite vary over one orbit, knowing the geometry of the orbit at apoapsis.

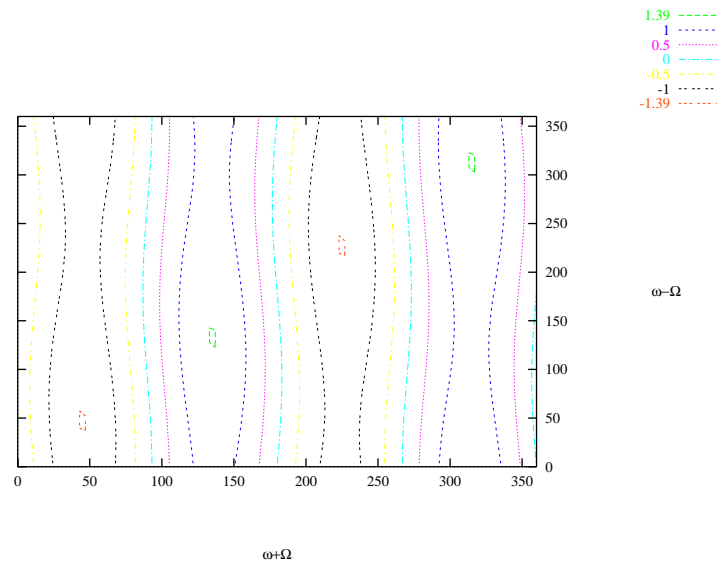


Figure IV.10: $\Delta r_p/r_p$, $a = 6123 \text{ km}$, $e = 0.6839$, $i = 30 \text{ deg}$

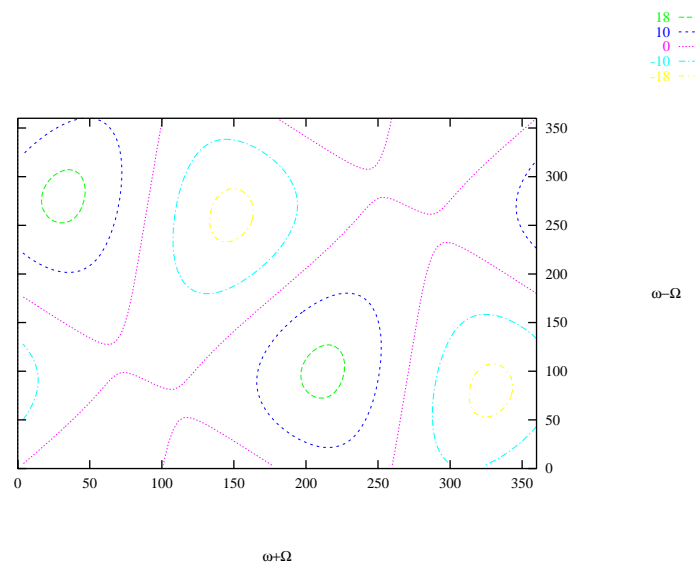


Figure IV.11: Δi , $a = 6123 \text{ km}$, $e = 0.6839$, $i = 30 \text{ deg}$

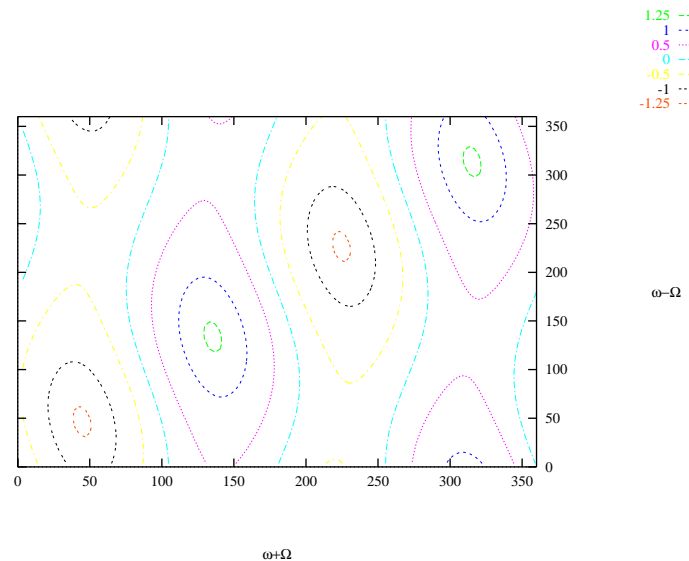


Figure IV.12: $\frac{\Delta r_p}{r_p}$, $a = 6123 \text{ km}$, $e = 0.6839$, $i = 60 \text{ deg}$

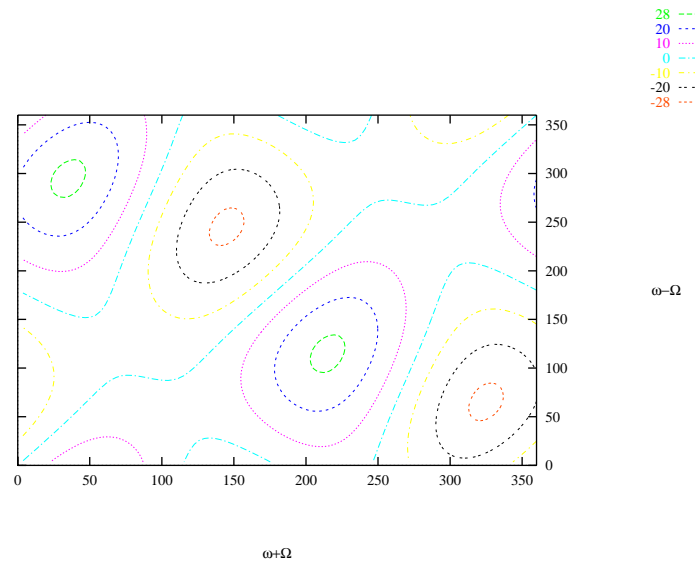


Figure IV.13: Δi , $a = 6123 \text{ km}$, $e = 0.6839$, $i = 60 \text{ deg}$

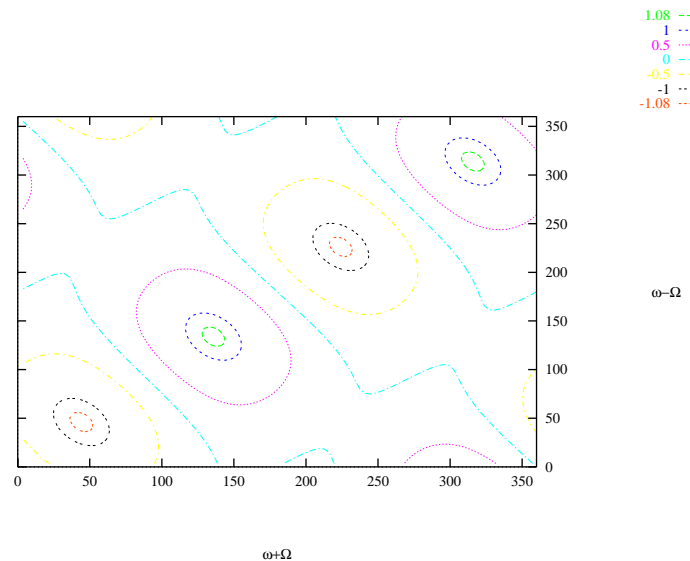


Figure IV.14: $\frac{\Delta r_p}{r_p}$, $a = 6123 \text{ km}$, $e = 0.6839$, $i = 90 \text{ deg}$

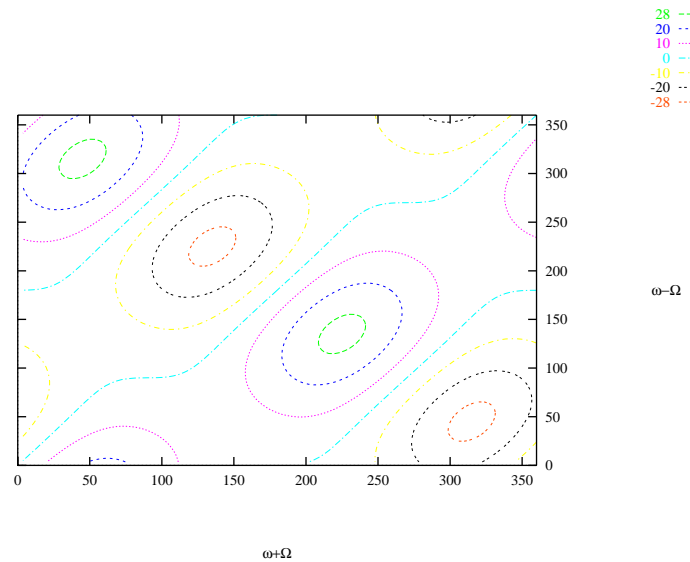


Figure IV.15: Δi , $a = 6123 \text{ km}$, $e = 0.6839$, $i = 90 \text{ deg}$

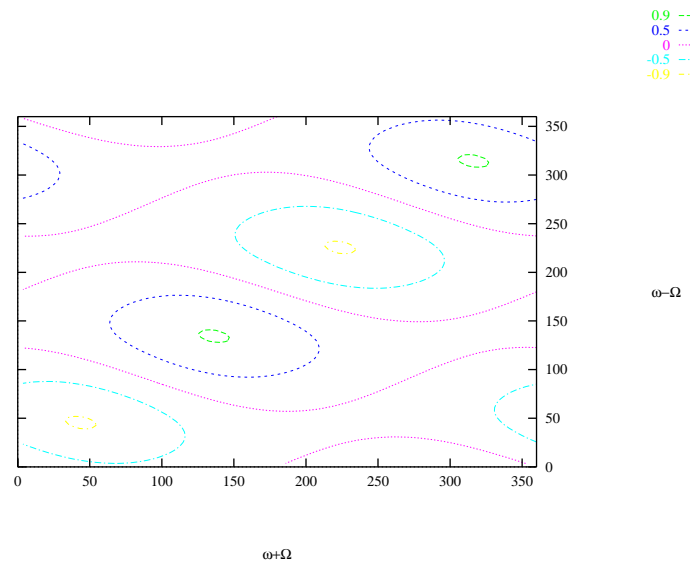


Figure IV.16: $\frac{\Delta r_p}{r_p}$, $a = 6123 \text{ km}$, $e = 0.6839$, $i = 120 \text{ deg}$

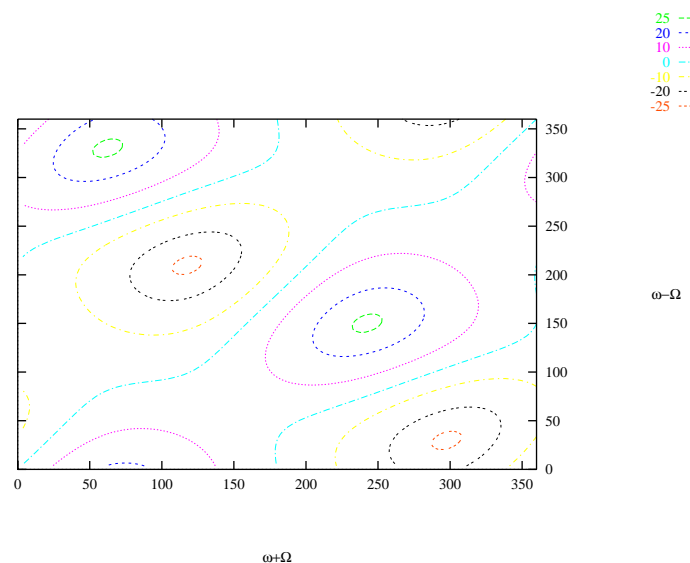


Figure IV.17: Δi , $a = 6123 \text{ km}$, $e = 0.6839$, $i = 120 \text{ deg}$

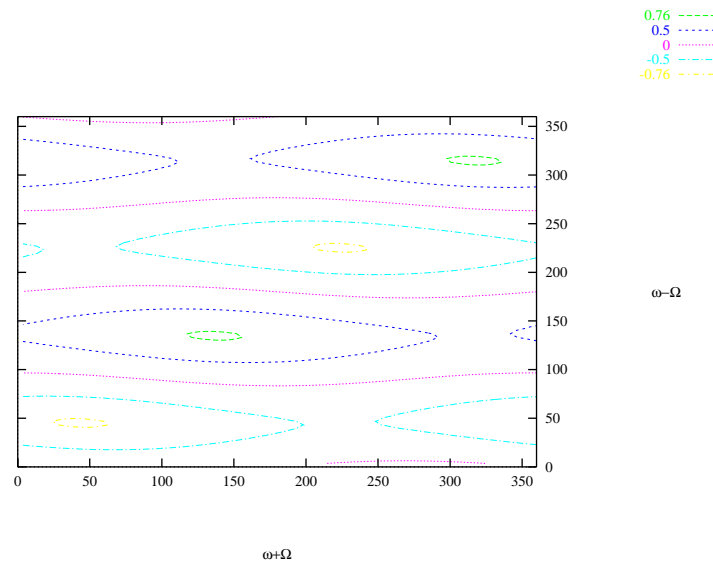


Figure IV.18: $\frac{\Delta r_p}{r_p}$, $a = 6123$ km, $e = 0.6839$, $i = 150$ deg

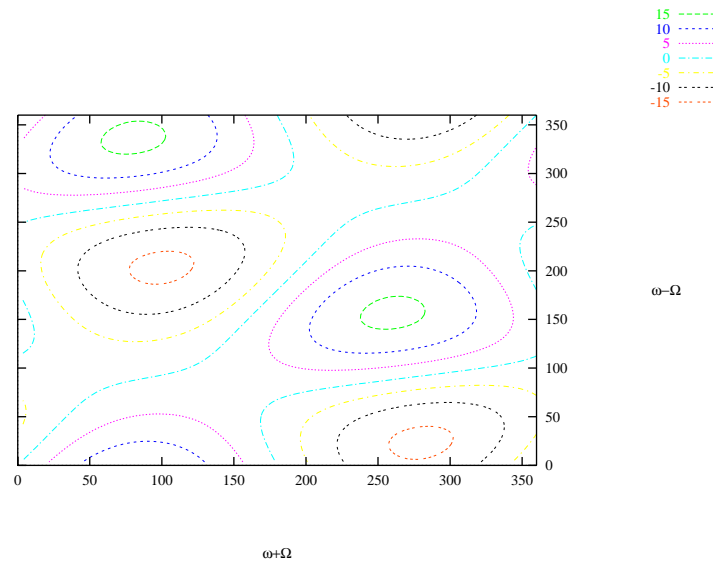


Figure IV.19: Δi , $a = 6123$ km, $e = 0.6839$, $i = 150$ deg

For instance, given the osculating periapsis radius at apoapsis, the regions of impact on the surface of the attracting body are determined by the conditions $\Delta r_p < r_p - R_E$ where r_p is the value of the radius of periapsis at the previous periapsis passage.

Even though this condition cannot be mapped directly onto the contour plots, the regions of strong decrease in periapsis radius over one orbit can be considered as regions of high probability of impact. This leads to a conservative criterion that regions for which an increase in periapsis radius occur ($\Delta r_p > 0$), guarantee that the spacecraft will not impact over one orbit. Note that this result assumes that the previous periapsis radius is above the surface of Europa, and the result is only valid for one orbit taken from periapsis to periapsis.

4.3. Dependence on semi-major axis and eccentricity

The dependence of the dynamics on the semi-major axis and eccentricity is entirely captured by the expressions $p^{7/2} I_2^{-4}$, $p^{7/2} I_{-2}^{-4}$ and $-\frac{15\pi}{4} \frac{p^{7/2} e^2}{(1-e^2)^{7/2}}$ for ΔG , and similar expressions for the other quantities, which are all smooth functions of semi-major axis and eccentricity. As in subsection 4.1, these expressions can be mapped as contour plots (Figures IV.4-IV.5), indicating the strength of their variation with semi-major axis and eccentricity, and the magnitude of the change in orbital elements over one orbit. Indeed, in the estimates obtained, these expressions represent the scaling factor of the trigonometric functions of inclination, longitude of the ascending node and argument of periapsis. Their amplitude give a measure of the maximum that can be achieved by varying only i , ω and Ω .

An important feature of the dynamics is the increase in the amplitude of the changes as apoapsis is raised. This is captured in part by the fact that the values of all the contours get larger as r_a is increased (for eccentricity > 0.4). In particular, changes in inclination of more than 60° can be obtained for a large enough apoapsis. A too large apoapsis radius will result, however, in a direct escape from the primary, as we will see in the next chapters.

4.4. Dependence on inclination

The dependence on inclination of the changes obtained in the previous section is expressed as a combination of trigonometric functions.

Particular cases are given by $i = 0^\circ$ and $i = 180^\circ$, which correspond to equatorial trajectories. In these cases, one can notice that the expression for Δi becomes identically zero, indicating that trajectories which have the equatorial plane as the osculating plane at apoapsis will indeed remain in the equatorial plane. This is in accordance with the invariance of the equatorial plane noted in Chapter III.

Apart from these special cases, the dependence with inclination depends strongly on the precise form of the trigonometric expressions where i enters in the estimates. This is illustrated by a series of contour plots for $\frac{\Delta r_p}{r_p}$ and Δi where only the inclination at apoapsis is varied (Cf. Figures IV.10 - IV.19). The variation of $\frac{\Delta r_p}{r_p}$ is similar to the variation in all the other expressions (such as Δa , Δe , etc.) except for the variations in inclination, Δi .

In the case of $\frac{\Delta r_p}{r_p}$, the dependence passes from a dynamics that depends only on $\omega + \Omega$ at $i = 0^\circ$ to one that depends only on $\omega - \Omega$ at $i = 180^\circ$. This is expected since the definition of the longitude of periapsis degenerates to this dependence in the equatorial plane. This strong variation does not, however, significantly change the position of the maxima and minima.

In the case of Δi , on the other hand, the positions of the extrema vary as we go from $i = 0^\circ$ to $i = 180^\circ$, whereas the zero curve on the diagonal of these plots does not vary much (diagonals correspond to $\Omega = 0^\circ$ [180°]). Indeed, for \tilde{a} small, $\cos 2\tilde{a}(M - \pi) \approx 1$ and $\sin 2\tilde{a}(M - \pi) \approx 0$ so that $I_2^{-4} \approx I_{-2}^{-4} \approx 2 \int_0^\pi (1 + e \cos f)^{-4} \cos 2f df = 5\pi \frac{e^2}{(1-e^2)^{7/2}}$. Then we can show that for $\Omega = 0^\circ$ or 180° ,

$$\Delta i \approx \sin i \sin 2\omega \left\{ \cos^2(i/2) - \sin^2(i/2) - \cos i \right\} \frac{15\pi}{4} \frac{p^3 e^2}{(1-e^2)^{7/2}} = 0$$

Since the relation $I_2^{-4} = I_{-2}^{-4}$ is only an approximation for $a \neq 0$, the diagonal won't correspond exactly to a zero plane change, but will still correspond to a small change in

inclination. This holds as long as a remains small ($a < 0.3$) and the eccentricity is not too high ($e < 0.8$).

All these examples show that the dependence on inclination is strong enough to make the signs of the estimates change over relatively large regions (in the (ω, Ω) space) but still too weak to transform a maximum into a minimum, as opposed to the variations obtained with ω and Ω .

The next two chapters describe two practical applications resulting from these dynamics: plane changes and escape/capture maneuvers in an environment perturbed by a third body.

CHAPTER V

THIRD BODY DRIVEN PLANE CHANGES

This chapter builds on the insights of the two previous chapters by presenting a new class of plane change maneuvers in a 3^{rd} body perturbed environment [40, 39].

As was noted in the introduction of the dissertation, this topic was first motivated by the Europa Orbiter Mission. Indeed, we have seen in Chapter III that low altitude, nearly circular, polar orbits are unstable, with instabilities on the order of weeks for the case of Europa. These polar orbits are interesting scientifically since they allow us to map the high latitude regions of the satellite, a necessary ingredient in some scientific investigations. Placing a spacecraft on such a trajectory requires periodic control maneuvers to avoid an impact with Europa. Such maneuvers are expensive over long time spans, and it seems preferable to transfer the spacecraft into a low inclination, stable orbit to avoid impacts over long intervals of time. Such transfers involve a large plane change maneuver (which is a very expensive maneuver). Minimizing the cost of such a transfer is an important goal.

Also, the topic of plane change maneuvers has its own dynamical interest since it involves, intrinsically, the full 3-dimensional dynamics and a nontrivial comparison with classical strategies. Indeed, as we will review in the first section, the optimal classic strategy for plane changes below $\sim 39^\circ$ is obtained with a one impulse maneuver. This maneuver is still applicable in a 3^{rd} body perturbed environment since it does not involve a transfer trajectory with a large apoapsis radius. Thus, the question of the optimal plane change strategy arises. This question has a beautiful answer found with the help of the Jacobi constant, which allows us to obtain tight bounds on the limits of optimality. This is

derived in Section 3.

Section 2 looks at the third body driven plane changes, without concern about the cost of the transfers. In particular, the problem is formulated as a non-convex optimization problem for which a numerical approach is proposed.

1. Classic vs. third body driven transfers

Classically, the design of orbit transfers is based on the two body problem for the underlying dynamics. In this model, the trajectory of a spacecraft is entirely determined by its five orbital elements: semi-major axis a , eccentricity e , inclination i , longitude of the ascending node Ω and argument of periapsis ω . In this situation, relations between two points on a given orbit are readily obtained and the problem of determining a transfer can be viewed as a geometrical problem of the intersection of conics together with an optimization over all possible impulsive maneuvers. In particular, there is no distinction between the dynamics on the initial, final, and transfer orbits. The time appears as a secondary variable (possibly as a cost function) in the sense that if a transfer is possible at time t_0 , it is also possible at time $t_0 + T$ where T represents the period of motion on the initial orbit. Also, the absolute position of the initial and final orbits relative to a given inertial frame are not generally taken into account in the formulation of the problem, only the relative orientation of the initial orbit with respect to the final one is important. A typical example of transfer is given by the bi-elliptic plane change (or restricted three impulse plane change [7]), where a spacecraft starts in an initial low altitude, circular orbit, a first maneuver transfers it to an ellipse where a second maneuver is performed at apoapsis, changing its orbital plane, and a final maneuver at the next periapsis re-transfers the spacecraft to a low altitude, circular orbit (see Figure V.1).

When perturbations occur, however, this state of affairs changes. Orbital elements are now a function of time and there may be no definite analytical relationship between two points on a given orbit. The situation is not so bad for small perturbations where averaging

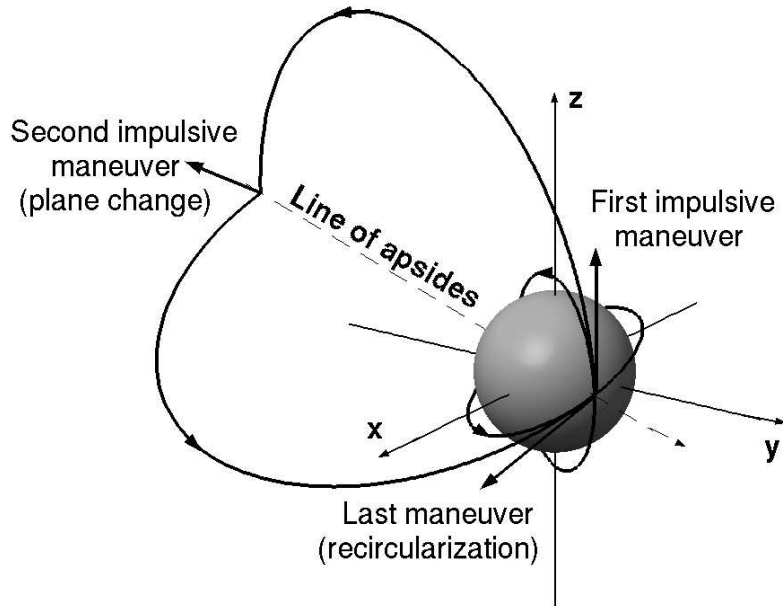


Figure V.1: Geometry of bi-elliptic plane changes

theory gives a good approximation of the secular changes of the orbital elements over one orbit. Since, by assumption, these perturbations are small, variations over one orbit remain small and the two body approximation retains its value and gives useful estimates of the ΔV required for a given maneuver. This is, for example, the case for orbiters moving in a J_2 perturbed gravitational field. Moreover, in this case, the perturbations decrease as the apoapsis of the transfer orbit is raised, justifying again the two body assumption. Still, even in this slightly perturbed environment, ω and Ω are shifted during each orbit and the absolute orientation of the initial and final orbit at a given epoch enters into the problem.

As opposed to the J_2 perturbations, 3^{rd} body forces become more prominent as one gets further from the attracting body and, as we have seen in the previous chapters, the dynamics close to the satellite and on the transfer orbits now have very different characteristics, and the orientation of the initial and final orbits (or equivalently the timing of the maneuvers) is of prime importance. More precisely, assuming that a spacecraft is in a low altitude, circular orbit, and that a ΔV maneuver is performed to place the spacecraft onto an eccentric orbit, performing the maneuver at time t_0 or $t_0 + T$ may result in an impact

or escape from the satellite before the spacecraft has reached the next periapsis. As was noted in Chapter IV, the initial value of ω and Ω now control, in some way, the changes that occur during a transfer orbit, and a careful choice of these variables allows us to use the 3rd body forces to generate the plane change without any cost (see Figure V.2).

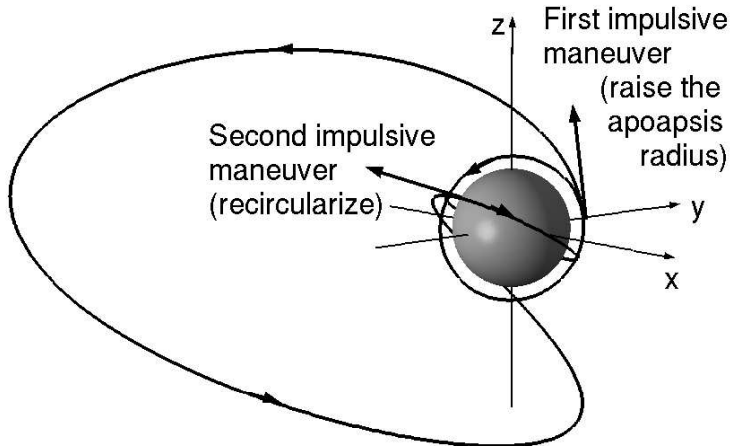


Figure V.2: Geometry of 3rd body driven plane changes

This section reviews the classical strategies used to perform plane change maneuvers and, then, presents the geometry of the 3rd body driven plane changes considered in this work.

1.1. Classical plane change maneuvers

The plane change problem consists of finding a trajectory that transfers a spacecraft from an initial circular orbit of given radius r_0 and inclination i to a final circular orbit with same radius r_0 but with a different inclination, $i + \Delta i$.

Four classical methods are generally considered to solve the plane change problem. Among these methods, the general three impulse maneuver method (as described below) is always fuel optimal over the other maneuvers, but its implementation is somewhat more difficult.

The first method, one impulse plane changes, requires only one impulsive burn to be

performed at one of the nodes of the orbit (i.e., at the crossing with the equatorial plane). This maneuver consists of rotating the velocity vector by the desired amount of the plane change. Thus, its cost is given by:

$$\Delta V_{1-impulse} = 2V_{lc} \sin(\Delta i/2) \quad (\text{V.1})$$

where $V_{lc} = \sqrt{1/r}$ is the local circular velocity speed at the time of the maneuver. This method is easy to implement and is cheaper than bi-elliptic and parabolic maneuvers for plane changes less than 38.9° .

Above this value, bi-elliptic maneuvers become less expensive. These maneuvers consist of first placing the spacecraft on an elliptic trajectory in order to raise the apoapsis radius. When apoapsis is reached, the one impulse plane change is performed so as to obtain the desired plane change. At the next periapsis, the spacecraft is inserted into the final circular orbit. The idea behind this transfer is that V_{lc} decreases with an increase in r so that $\Delta V_{1-impulse}$ decreases with an increase in r , as well. Performing the plane change at apoapsis results in decreased costs. This first and third burn are simply tangent to the path. This method is illustrated in Figure V.1. The cost of these maneuvers is given by:

$$\Delta V = 2V_{lc} \left[\sqrt{\frac{2\rho}{1+\rho}} \left(1 + \frac{\sin(\Delta i/2)}{\rho} \right) - 1 \right] \quad (\text{V.2})$$

where ρ is the ratio of the apoapsis radius of the transfer ellipse to the radius of the initial circular orbit. The optimal choice for this parameter (i.e., the choice which results in the minimization of ΔV for a given Δi) is given by $\rho = 1/(\csc(\Delta i/2) - 2)$.

From this formula, we can easily see that for $\Delta i \rightarrow 60^\circ$, $\rho \rightarrow +\infty$. Thus, starting at $\Delta i = 60^\circ$, plane change are cheaper if we let the spacecraft fly off to ‘infinity’ and perform the plane change at ‘infinity’, where its cost is zero. The cost of the maneuver is, in fact, contained in the first and last burns which correspond to escape and capture maneuvers. From a practical point of view, this result indicates that for large plane change values, the farther the apoapsis of the transfer trajectory is, the cheaper is the maneuver. The cost of

the ideal maneuver is:

$$\Delta V = 2V_{lc} [\sqrt{2} - 1] \quad (\text{V.3})$$

Note that the optimal solution of the general three impulse plane change, which consists of performing plane change maneuvers at each burn of a bi-elliptic transfer, merges with the parabolic result at the same value of $\Delta i = 60^\circ$ as for bi-elliptic transfers. No analytical expression is available for the costs of these transfers as a function of the initial conditions [7].

Thus, we can see from these results, that large plane change maneuvers require significantly raising the apoapsis to perform the transfer and that these maneuvers are very expensive.

As was noted in the introduction of this section, in a 3^{rd} body framework, raising the apoapsis cannot be performed without incurring large changes on all the orbital elements and, among the classical methods discussed above, only the one impulse maneuvers can still be directly applied in such orbital environments.

The next subsection explains a way to take advantage of these dynamics to decrease the cost of plane change maneuvers.

1.2. Third body driven plane changes

The idea of 3^{rd} body driven transfers is to place the spacecraft into a highly eccentric transfer trajectory (to raise the apoapsis radius) so that the large 3^{rd} body forces can perform plane change maneuvers without any ΔV costs at apoapsis. That is, the 3^{rd} body driven plane changes considered here are analogous to bi-elliptic plane changes, with the apoapsis maneuver replaced by the “cost free” action of the third body forces.

More precisely, when the spacecraft moves along an initial, low altitude, circular orbit, we have seen in Chapter III that the mean anomaly, M , and the longitude of the ascending node, Ω , can be approximated by linear functions of time and can be represented as a line

wrapping in the (M, Ω) -torus space (all the other orbital elements remaining fixed during the motion by our approximation of circular motion).

A tangential impulsive maneuver at any point of this initial circular orbit will place the spacecraft at the periapsis of a transfer trajectory, the orbital elements of which are determined using the following correspondences*:

<u>Initial, circular orbit</u>	<u>Transfer trajectory</u>	(V.4)
r_p	\longrightarrow	r_p
ΔV	\longrightarrow	$r_{a(\Delta V)}$
i	\longrightarrow	i
$\Omega = -Nt$	\longrightarrow	Ω
$M = nt$	\longrightarrow	ω

where $n = \sqrt{1/r_p}$ represents the mean motion of the spacecraft on the initial circular orbit. In particular, ω and Ω are directly related to the value of M and Ω of the initial circular orbit and their values vary as we let the spacecraft move along the initial circular orbit.

Now, numerical integration of the flow up to the next periapsis as ω and Ω are varied (r_p , r_a , i being fixed) allows us to map all the possible transfer trajectories from this initial circular orbit and obtain a simple geometric representation of the change in orbital elements over a transfer trajectory. That is, we numerically compute a periapsis Poincaré map with the initial elements taken at periapsis (see Figure V.3).

The existence of $\Delta r_p = 0$ curves indicates that for an appropriate choice of ω and Ω of the transfer trajectory, a zero change in periapsis radius will result at the next periapsis passage. If Δi is non zero for this given value of ω and Ω , a recircularization maneuver at the next periapsis passage will correspond to the completion of a plane change maneuver. Figure V.2 shows a numerically integrated trajectory corresponding to the design of such a third body driven plane change for $\Delta i \simeq 60^\circ$.

* $r_{a(\Delta V)} = \frac{2r_p}{2-(1+\Delta V/V_{i_e})} - r_p$ corresponds to the apoapsis radius obtained from a tangential burn, starting in a circular orbit.

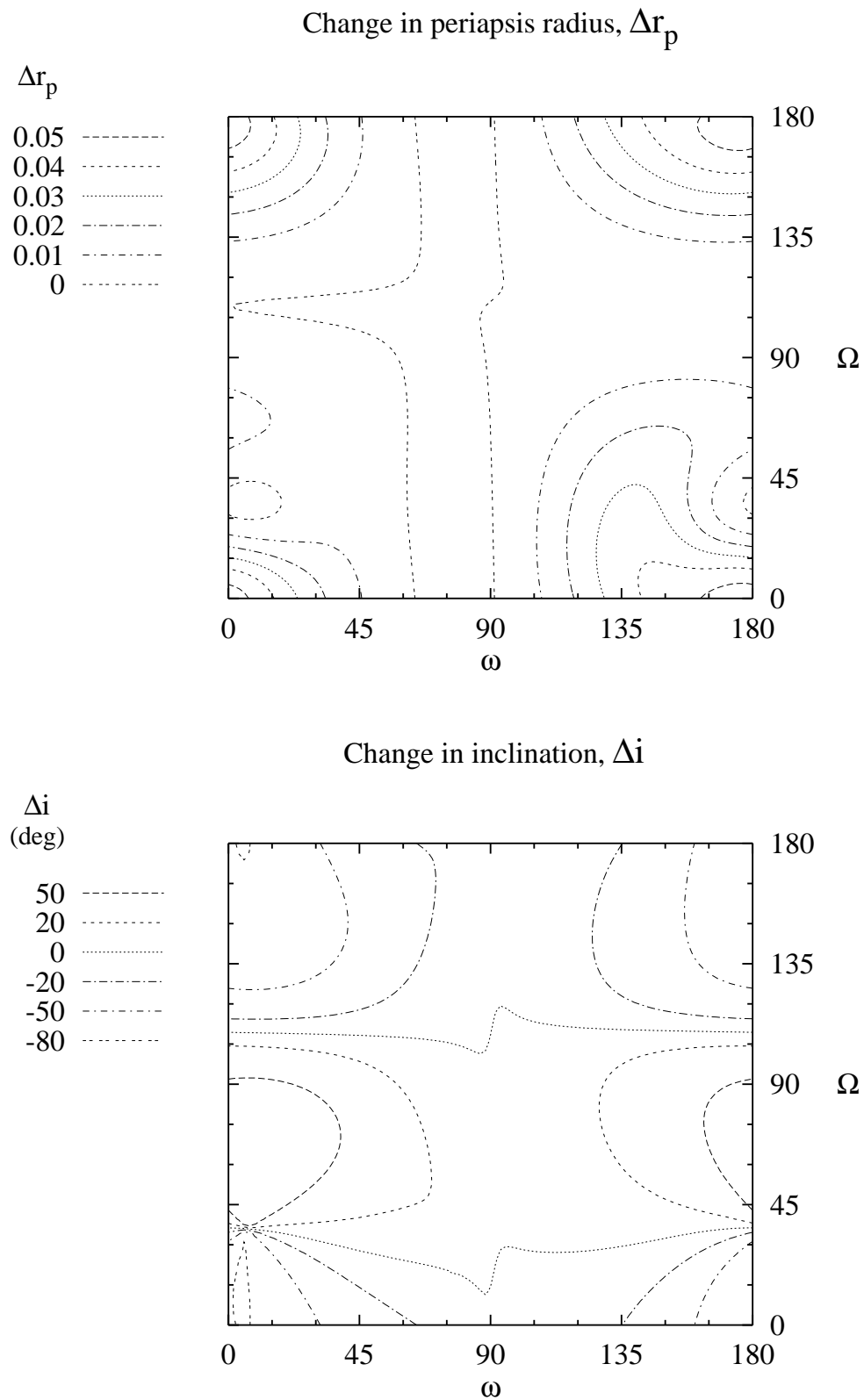


Figure V.3: Example of periapsis Poincaré maps for $r_p = 0.003$, $r_a = 0.5$ and $i = 90^\circ$.

It should be noted that once a choice of ω and Ω of the transfer trajectory has been chosen to meet the desired plane change values, the time of the maneuver is determined by the correspondences given in (V.4). Indeed, recall from Chapter III that, given an epoch, the trajectory of the spacecraft in its initial circular orbit will be represented as a line wrapping in the (ω, Ω) -torus space by the above correspondences. Since the slope of this line is almost surely irrational (i.e. with probability 1), any value of ω and Ω can be approximated to any desired value by waiting long enough. Figure V.4 illustrates this situation.

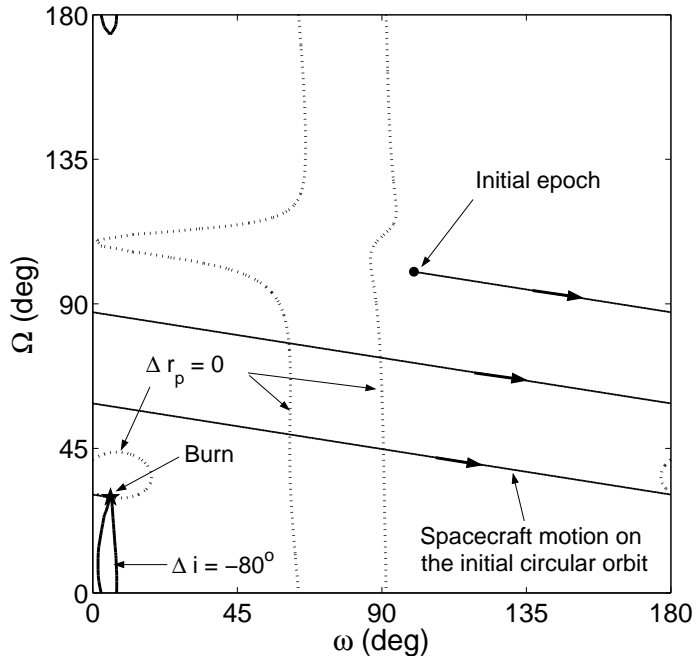


Figure V.4: A geometric view of third body driven plane changes

To determine ω and Ω corresponding to a desired plane change value, the maximum 3^d body driven plane change for given initial conditions (r_p , i and ΔV) can be computed by solving the following optimization problem:

$$\max_{\omega, \Omega} \Delta i_{(\omega, \Omega)} \quad \text{subject to} \quad \Delta r_{p(\omega, \Omega)} = 0 \quad (\text{V.5})$$

Note that in the above optimization problem, Δi and Δr_p are implicitly functions of

r_p , i and ΔV . These first two values are directly determined by the elements of the initial circular orbit, while ΔV has to be adjusted so that the maximum plane change obtained corresponds to the desired value of plane change. A closer look at this process will be given in the next section.

Note also that, because of changes in semi-major axis and eccentricity during the transfer, the magnitude of the recircularizing burn is not, in general, equal to the magnitude of the first maneuver. However, this magnitude can be bounded as we will see also in the next section of this chapter.

Figure V.5 presents a series of numerically integrated transfer trajectories for plane changes ranging from -40° to -60° in the case of an Europa orbiter.

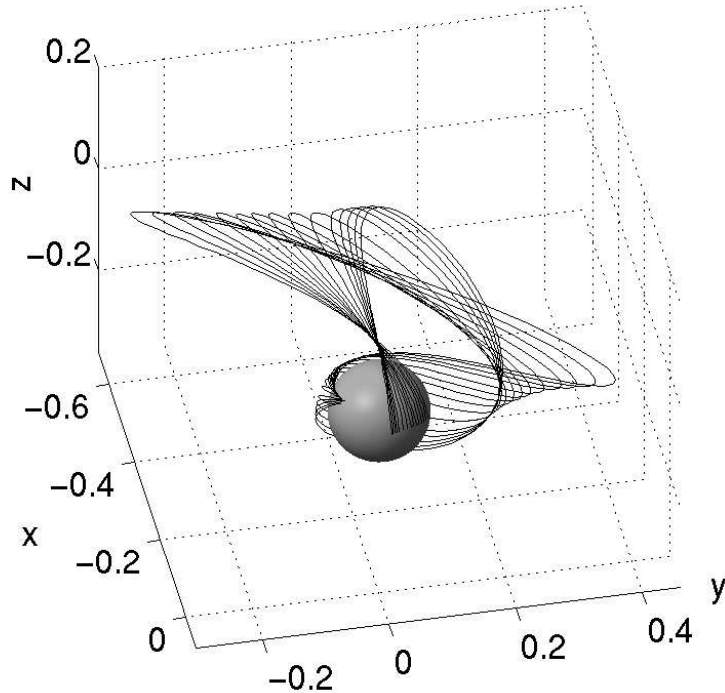


Figure V.5: Series of 3rd body driven plane changes for the Europa case ($r_p = 0.08$, $i = 90^\circ$), plane changes range from -40° to -60° .

It is clearly seen on this figure that the initial values of Ω vary as the desired value of the inclination change is varied. This is to be expected since ω and Ω are used as

control variables and their values are fixed by the amount of plane change to be performed. Moreover, their values at the next periapsis are also fixed, showing the lack of direct control of the longitude of the ascending node on the final orbit. However, since Ω precesses in this environment, phasing methods can be used to achieve specific values of Ω_0 at a given epoch.

2. Fuel unconstrained problem

The above discussion shows that 3rd body driven plane changes can be computed by solving an optimization problem over the Poincaré sections defined by the periapsis conditions. More precisely, we just have seen that the values of ω and Ω that yield a desired plane change are computed by solving the maximum and minimum values of plane change realizable for a given value of initial inclination, periapsis and apoapsis radii (i.e. ΔV). That is, we solve the following non-convex optimization problem:

$$(\omega, \Omega) = \operatorname{Arg} \max_{\omega, \Omega}^* \{\Delta i_{(\omega, \Omega)} | \Delta r_{p(\omega, \Omega)} = 0\} \quad (\text{V.6})$$

This section presents a numerical algorithm to solve this problem, as well as the results of the computation. As it turns out, this problem will allow us to solve a more complex problem formulated in the next section.

2.1. Numerical solution for the maximum and minimum plane change

Even though the above problem can a priori be solved by standard optimization algorithms, the numerical procedure used in this dissertation consists of first searching the Δr_p zero lines on the torus $[0, 180^\circ] \times [0, 180^\circ]$ and then looking for the maximum plane change on these zero lines. This method has the advantage of not necessitating an initial guess while allowing us to keep track of the zero lines.

The search for the $\Delta r_p = 0$ lines is performed by first searching the crossings of the lines with the axes $\omega = 0^\circ$ and $\Omega = 20^\circ$ and then tracking the zero lines from these points.

*Resp. $\operatorname{Arg} \min \{\Delta i | \Delta r_p = 0\}$ for the minimum plane change.

The choice of the search axes has been determined using both physical reasoning and numerical exploration of several contour plots. The point ($\omega = 0^\circ, \Omega = 20^\circ$) represents the approximate values of the argument of periapsis and longitude of the ascending node of the periapsis of the stable manifold associated with the libration point L_1 , and corresponds to the center of sets of periapsis of escaping trajectories (See next Chapter). Neighborhoods of these sets present strong variations in Δr_p and one can think of the lines $\omega = 0^\circ$ and $\Omega = 20^\circ$ as representing two principal directions along which variations in orbital elements are stronger. As a consequence, one can expect that the $\Delta r_p = 0$ lines will meet one or the other axis at some point. This has indeed been observed in the numerical computation of many contour plots.

It is assumed that the number of crossings on one axis does not exceed 10, but in all the cases considered, a maximum of 4 crossings and a minimum of 2 has been found. The search for the crossings is performed by setting a uniform grid on each axis and looking for a change of sign between two consecutive nodes. The step size used is 0.1 degrees, so that two different zero lines are assumed to be separated by at least such a value. This also implies that the escape regions must not lie within 0.1 degrees of a zero line.

Note that these assumptions do not allow us to conclude that the extrema found are global (we may miss a zero line), but it avoids a blind search of the entire (ω, Ω) -space. Also, when such a global search has been performed, the results obtained agreed with the results returned by the previous algorithm.

After this first search, the zero lines are tracked by moving, step by step, along the tangent of these zero lines[†]. Again it is assumed that no escape region lies within 5.7×10^{-3} degrees of these lines, which has always been the case in the domain of phase space considered. However, for large enough apoapsis radius, this may not be the case and the neighborhoods of the escape regions present very strong variations in orbital elements that

[†]The tangent vector to a zero line is given $(\partial \Delta r_p / \partial \Omega, -\partial \Delta r_p / \partial \omega)$. These partial derivatives can be either computed by a finite difference scheme or by computing the state transition matrix of the Hill problem and transforming the results into orbital elements.

cannot be computed with the above assumptions. The maximum step size used to perform this tracking is 1° and a search for the maximum and minimum Δi is then performed over all these points. This means that the determination of the global maximum of plane change is performed to within this limit.

Once the maximum (or minimum) has been found, the accuracy is improved up to 5.7×10^{-3} degrees, that is, the positional accuracy of the local maximum is 5.7×10^{-3} degrees. Note that all integrations performed use a Runge-Kutta-Felhberg integrator of order $7 - 8$, with an accuracy of 10^{-10} per step (see Appendix E).

Figure V.6 gives an example of such a computation for an Europa orbiter. The position of the maximum and minimum of plane change are indicated by small labels.

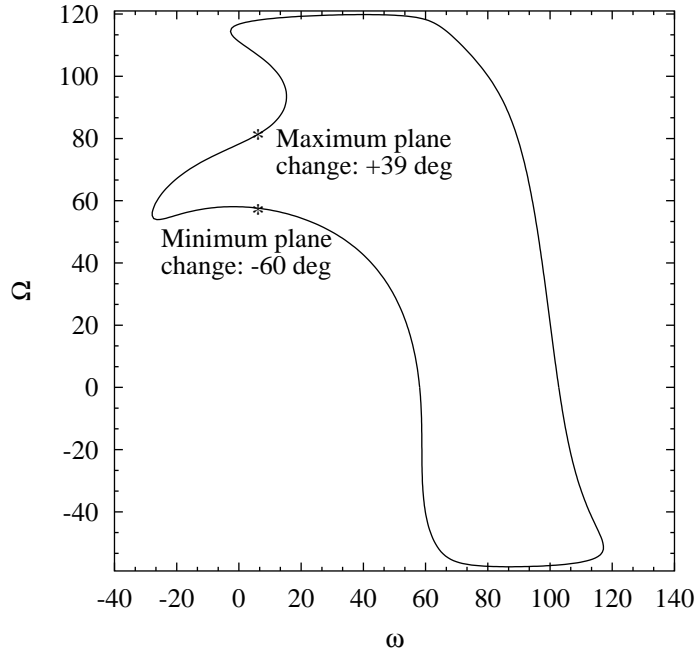


Figure V.6: $\Delta r_p = 0$ lines for $r_p = 0.08$, $r_a = 0.6$ and $i = 90^\circ$

Finally, we should note that the dynamics considered here are smooth (or, at least, continuous), so that when the maximum and minimum plane changes are located on the same Δr_p zero line, all values of plane change between these two extrema are possible. For the case in Figure V.6, we see that plane changes between $+39^\circ$ and -60° are possible

by timing the initial impulsive maneuver. For other cases, such as $\pm 180^\circ$ plane changes indicated in the next subsection, the maximum and minimum plane changes are located on two different, separated zero lines and not all the values of plane change between these extrema are realizable.

2.2. Variations with the initial conditions

Once this computation has been performed for a given set of values of periapsis radius, apoapsis radius, and inclination, the algorithm is repeated to cover a wide range of cases. Figures V.7 to V.11[‡] give the results of such computations when, respectively, the initial inclination, apoapsis radius and periapsis radius are varied. Each plot has been computed with at least 90 points for the independent variable.

Variations with initial inclination

Two distinct behaviors of the variations of the minimum plane change are obtained when inclination varies, according to the initial values of periapsis radius, r_p , and apoapsis radius, r_a .

For the lower values of apoapsis radius (at fixed r_p), the minimum and maximum plane changes obtained for the inclinations of 0° and 180° are zero. In this case, the changes in orbital elements become larger around an inclination of 90° as can be seen on Figure V.7 for the change in inclination.

For higher values of apoapsis radius (or lower values of periapsis radius with fixed r_a), a bifurcation occurs, so that, at the inclinations of 0° and 180° , a maximum and minimum plane change of 180° and -180° , respectively, are obtained, as can be seen in Figures V.8 and V.9[§]. Note that this result is consistent with the invariance of the (x, y) -plane in the Hill problem. A plane change of $\pm 180^\circ$ at an inclination of 0° or 180° corresponds, indeed,

[‡]Tags on these graphs are explained in the next subsection

[§]Only plane changes of -180° are possible with the initial conditions chosen for Figure V.8. Plane changes of 180° are possible for higher apoapsis radii (e.g. $r_a = 0.8$), but some zero lines cannot be computed at such a high value of r_a with the present program.

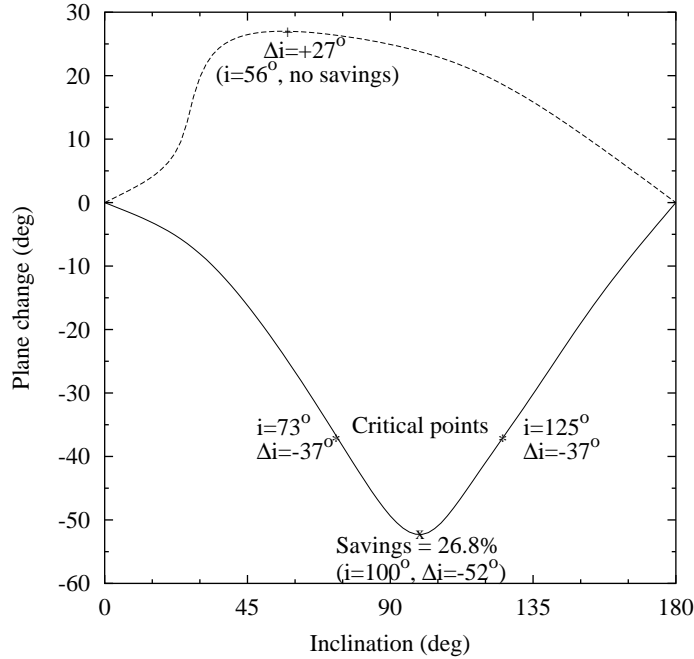


Figure V.7: Extrema values of plane change as a function of inclination ($r_p = 0.08$, $r_a = 0.5$)

to a change in the direction of motion relative to the primary (change from retrograde to direct orbit or vice versa), and does not involve any z -component of the velocity vector. The motion remains planar during such a transfer. Further results on these transfers are given in the next section.

These figures also show that the bifurcations for positive and negative plane changes do not necessarily occur for the same values of periapsis and apoapsis radii. The few numerical explorations performed suggest that the bifurcation for negative plane changes occurs at lower values of apoapsis radius than that for positive plane changes. In fact, as it clearly appears in Figures V.7 to V.11, the dynamics are not symmetric for positive and negative plane changes, even though there are some similarities. It seems that at any value of r_p and r_a , the overall maximum plane change realizable (i.e., over all initial inclinations) is less than the overall negative plane change possible (in absolute value).

In the rest of this subsection, an inclination of 90° has been assumed as a representative

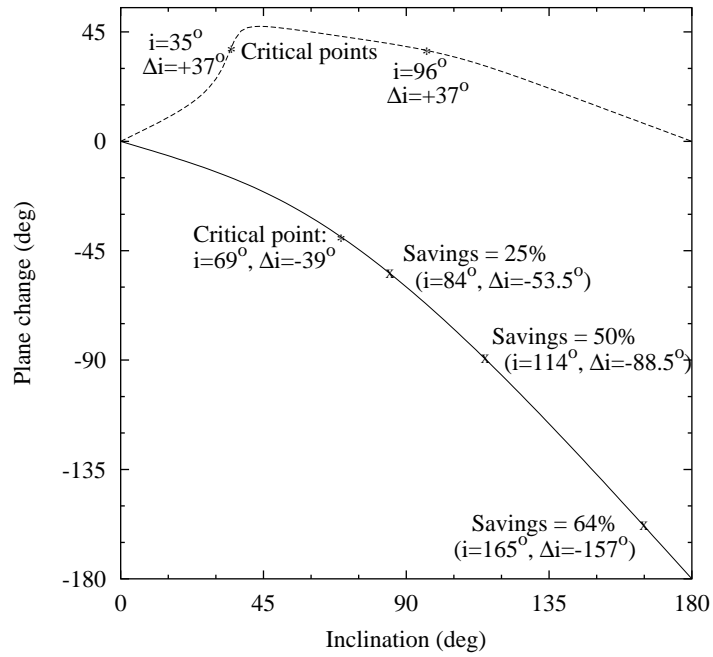


Figure V.8: Extrema values of plane change as a function of inclination ($r_p = 0.08$, $r_a = 0.6$)

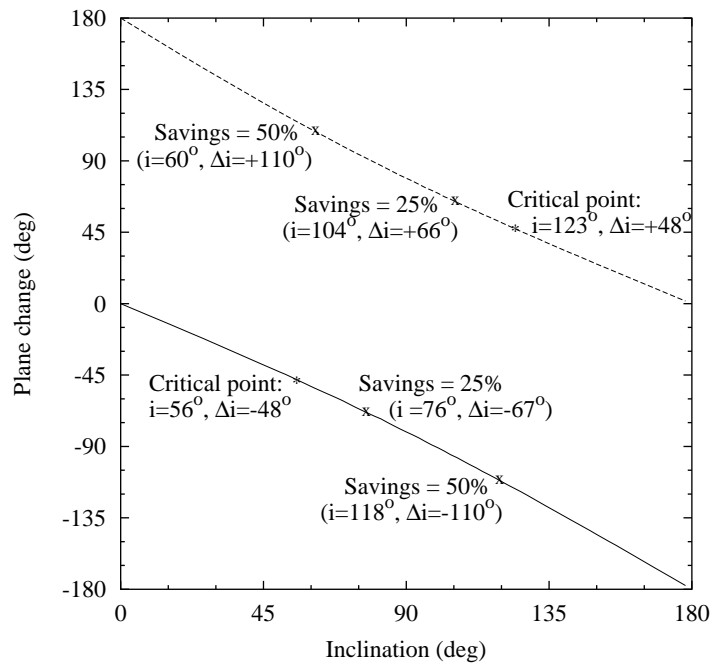


Figure V.9: Extrema values of plane change as a function of inclination ($r_p = 0.003$, $r_a = 0.5$)

initial inclination for the study of the variations of plane change with apoapsis radius and periapsis radius. Such an inclination corresponds, indeed, to the mean inclination over the unstable region for planetary satellite orbiters (see Chapter III), and gives a good representation of the dynamics considered.

Variations with initial apoapsis radius

As the initial apoapsis radius is raised the plane changes obtained become larger, as expected (see Figure V.10). Here again, the dynamics are not symmetric for the maximum and minimum plane change, positive plane changes remaining smaller than the negative plane changes. However, in both cases, large plane changes can be obtained and for initial apoapsis radius larger than 0.7 (with $r_p=0.08$ and $i = 90^\circ$), both positive and negative plane changes allow us to transfer an unstable polar orbiter back to a stable region over a single transfer trajectory. For such values of apoapsis radius, both positive and negative plane changes are, indeed, larger than 50° .

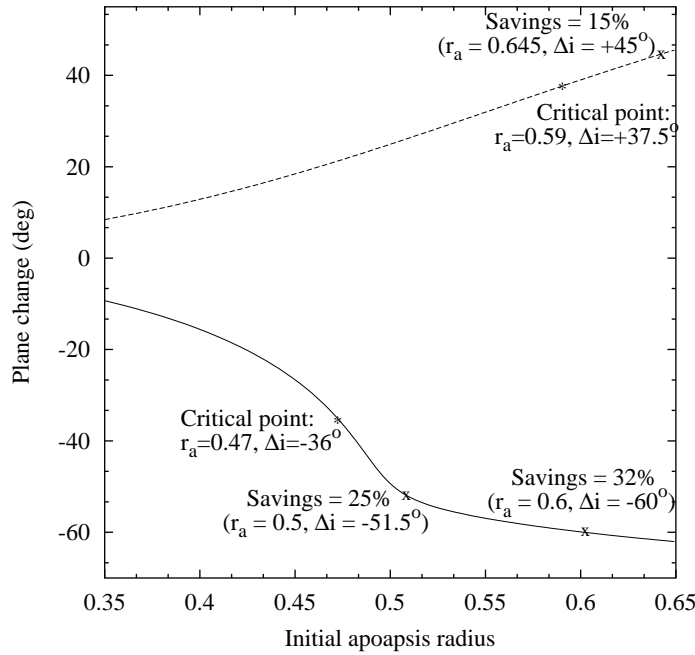


Figure V.10: Extrema values of plane change as a function of apoapsis radius ($r_p = 0.08$, $i = 90^\circ$)

Variations with initial periapsis radius

At fixed apoapsis radius, a decrease in the initial periapsis radius results in the amplification of the 3^{rd} body effects. As a consequence, larger plane changes can be obtained, as shown on Figure V.11. Note that, even though the Hill problem has a similarity property, i.e., it can be made non-dimensional so that each system modeled by the Hill equations of motion can be mapped into one another by a simple scaling, it is not true that the dynamics are similar at different values of the normalized radius. In particular, an increase in r_p with a fixed ratio r_p/r_a does not mean that the plane changes realizable are the same. For instance, at $r_p = 0.08$ and $r_a = 0.4$, the minimum plane change is smaller (in absolute value) than -20° , whereas for $r_p = 0.1$ and $r_a = 0.5$, the minimum plane change achievable is larger than -40° . That is, as the periapsis radius increases with fixed r_p/r_a ratio, the extrema of plane change achievable increase. These dynamics are also not linear in the sense that they do not depend solely on the difference between r_a and r_p , as can be easily checked on the previous graphs.

Finally, it should be noticed that 3^{rd} body driven plane changes of more than 60° (both positive and negative) are possible, hence realizing inclination change values that would classically be performed using parabolic transfers.

2.3. Comparison with classical transfers: first remarks

As we have seen in the first section, of the classical results only the one impulse classic result is still applicable in environments perturbed by a 3^{rd} body and, hence, represents the only classic approach to be compared to 3^{rd} body driven plane changes.

However, because parabolic transfers can indeed be considered as a standard scale to estimate the costs of large plane change maneuvers in preliminary mission analyses, a few comparisons with these transfers are given in the text in order to give an idea of the costs for performing large plane changes in 3^{rd} body perturbed environments.

It should be noted that this scale always corresponds to an overestimate of the costs

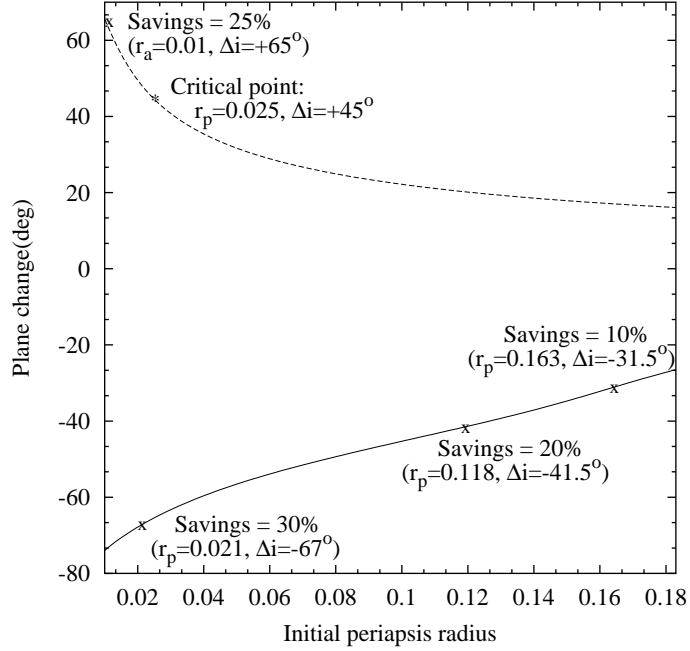


Figure V.11: Extrema values of plane change as a function of periapsis radius ($r_a = 0.5, i = 90^\circ$)

for performing large plane changes in 3^{rd} body perturbed environments. Indeed, parabolic transfers involve the same number of burns as the 3^{rd} body driven plane change maneuvers, but their magnitude is always larger than in the 3^{rd} body driven case.

Numerical results

The ΔV comparisons between the one impulse maneuver (Equation V.1) and 3^{rd} body driven plane changes are given on Figures V.7 to V.11. The tags shown on these figures indicate some values of the savings obtained when using 3^{rd} body driven plane changes. In particular, it is seen that savings larger than 25 percent are obtained for large plane change maneuvers ($\sim 60^\circ$).

The critical points also indicated on these figures show the values of the initial elements and plane change for which the transition of optimality between one impulse maneuvers and 3^{rd} body driven plane changes occurs. That is, for inclination changes larger than the critical values, 3^{rd} body driven plane changes are less costly than one impulse maneuvers.

These critical plane change values depend on the initial conditions of the low altitude, circular orbit (r_p , r_a and i) and seem to increase (in absolute value) as the periapsis radius decreases. For periapsis on the order of the normalized radius of Europa, the critical values for optimality lie close to 38° .

As expected, for plane changes larger than 60° , 3^{rd} body driven maneuvers are less costly than the classic scale of parabolic plane changes. The costs are lower by $\sim 5 - 10\%$ in the case of Figure V.11 and more than 15% in the case of Figure V.10. Also, we should note the large savings made for the case of change of direction of motion (plane changes of -180°), as shown on Figures V.8 and V.9. In this case, savings of more than 15% are obtained when compared to the parabolic transfers and more than 70% as compared to 1-impulse plane changes. In addition, such transfers have the advantage of remaining bounded, and in particular, the transfer time is much smaller than in the parabolic case.

All these results show that the classical optimality of bi-elliptic transfers over one impulse maneuvers for plane changes larger than 39° has an analogue in the case of 3^{rd} body perturbed environments, where bi-elliptic transfers are replaced by the 3^{rd} body driven plane changes defined here. This situation is, however, more complex than in the classical case, since at any given initial conditions, the range of 3^{rd} body driven plane changes realizable is restricted. For example, the equatorial plane is invariant under the flow of the Hill equations, and the only plane changes possible are 0° or $\pm 180^\circ$. One cannot transfer a spacecraft from the equatorial plane to a polar orbit using only the natural dynamics, whereas it is perfectly possible to do this using a one impulse maneuver. The next section looks at this problem by using semi-analytical techniques.

3. Design problem and optimality

The aim of this section is to investigate the optimality of the 3^{rd} body driven plane change maneuvers presented above, by answering the question: given a spacecraft on a circular orbit (with given radius r and inclination i), what is the most cost effective approach to

perform a desired plane change maneuver Δi ?

While the analysis performed in the previous section searched for the global extrema of plane changes that are realizable given some initial conditions [40], the answer to the above question requires a closer look at the range of the possible plane changes realizable using the 3^{rd} body forces. This range does not cover the set of all allowable plane changes, and one impulse maneuvers must still sometimes be used. In the case of 3^{rd} body driven plane changes, analytical estimates and a numerical algorithm are proposed to compare third body driven transfers and direct one impulse maneuvers. It is shown, in particular, that third body driven plane changes are always optimal above a critical value ($\simeq 40^\circ$) that depends on the initial conditions. The resulting criterion for optimality allows us to directly choose the optimal approach for a plane change maneuver, given some initial conditions.

3.1. Approaches to the solution

A natural approach to solve the optimality problem is to compare the ΔV given by the different methods to perform the given plane change, Δi_0 . For one impulse maneuvers, this value is determined by equation (V.1) and for third body driven plane changes, one needs to solve the following optimization problem:

$$\min_{\omega, \Omega, r_a} \Delta V_{(\omega, \Omega, r_a)} \quad \text{subject to} \quad \Delta i_{(\omega, \Omega, r_a)} = \Delta i_0 \quad \text{and} \quad \Delta r_{p(\omega, \Omega, r_a)} = 0 \quad (\text{V.7})$$

Even though such an approach gives a complete solution to the problem, it is not computationally effective and problem (V.7) does not have necessarily a solution for any initial conditions.

Therefore, a better approach consists of first investigating the question of the optimal method to be used without concern for the precise numerical value of the ΔV required. In particular, a first computation must answer the question of the range of third body driven plane changes that are possible. This is discussed in the next subsection by finding the

'local-global' extrema of Δi .

The Jacobi constant can be used to obtain rather sharp estimates for the 3rd body driven ΔV needed to perform a given plane change with given initial conditions r_p , r_a , and i . These estimates result in an upper bound (depending on r_p , r_a , i and Δi) above which 3rd body driven plane changes are shown to be optimal.

However, these constraints do not solve the problem completely and a numerical algorithm must be used to complete the answer. The idea of the algorithm proposed is based on comparing the plane changes obtained via both methods for a given ΔV . This results in reducing the question of the optimal method to solving problem (V.5) instead of (V.7).

3.2. Dynamical restriction on realizable transfers

In the previous section, the solution of (V.5) was solved by finding the global extrema of Δi on the manifolds $\mathcal{Z} = \{(\omega, \Omega) | \Delta r_{p(\omega, \Omega)} = 0\}$. While there is a unique global maximum and minimum for any given value of r_p , r_a and i , their positions in the (ω, Ω) -space may not be on the same connected component of \mathcal{Z} . In such cases, it may happen that the range of 3rd body driven plane changes between the computed extrema may not be connected. This does happen in practice, especially for near equatorial orbits (i near 0° or 180°).

In order to determine the range of possible third body driven plane changes, the extrema of Δi are computed by pairs on each connected component of \mathcal{Z} . Any plane change can then be realized between the two extrema of a given pair.

The connected components of \mathcal{Z} can be computed by first searching along the axis $\omega = 0$ and $\Omega = 0$ and then, by tracking the $\Delta r_p = 0$ lines step by step along their tangents, as in the previous section. Figure V.12 represents an example of manifold \mathcal{Z} with three different connected components with the location of the pair of Δi extrema on these components. In the case shown, the global extrema of plane change are located on the same component and all plane change values between -80.9° and $+79.2^\circ$ are possible.

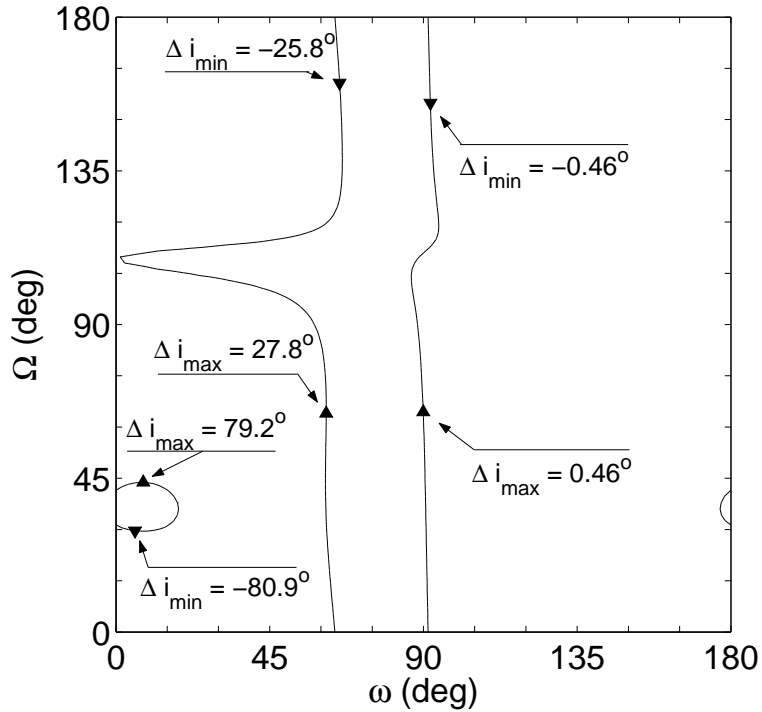


Figure V.12: $\Delta r_p = 0$ line for $r_p = 0.003$, $r_a = 0.5$ and $i = 90^\circ$

Figure V.13 shows the results of the computation of the pairs of Δi extrema for $r_p = 0.003$, at $r_a = 0.4$ and 0.5 as a function of inclination. We can see that near the equatorial plane, a large range of values of plane changes are not realizable using third body driven plane changes and these initial conditions. This is also true for plane change values that correspond to transferring the spacecraft to the equatorial plane. These restrictions are the result of using only the natural dynamics to operate the plane change during the transfer.

From a practical point of view, one needs to impose a limit on the maximal apoapsis radius that can be reached and the range of 3rd driven plane changes realizable corresponds to the range obtained with this maximal apoapsis radius. Such a limit may be imposed by either the limitations of the model (the Hill problem is not representative of the dynamics of a spacecraft far from the primary) or constraints imposed on the maximal time of flight allowed (the larger the apoapsis radius, the longer the time of flight). For $r_p = 0.003$, the realizable range of third body driven plane changes for $r_{a_{max}} = 0.4$ and $r_{a_{max}} = 0.5$ are

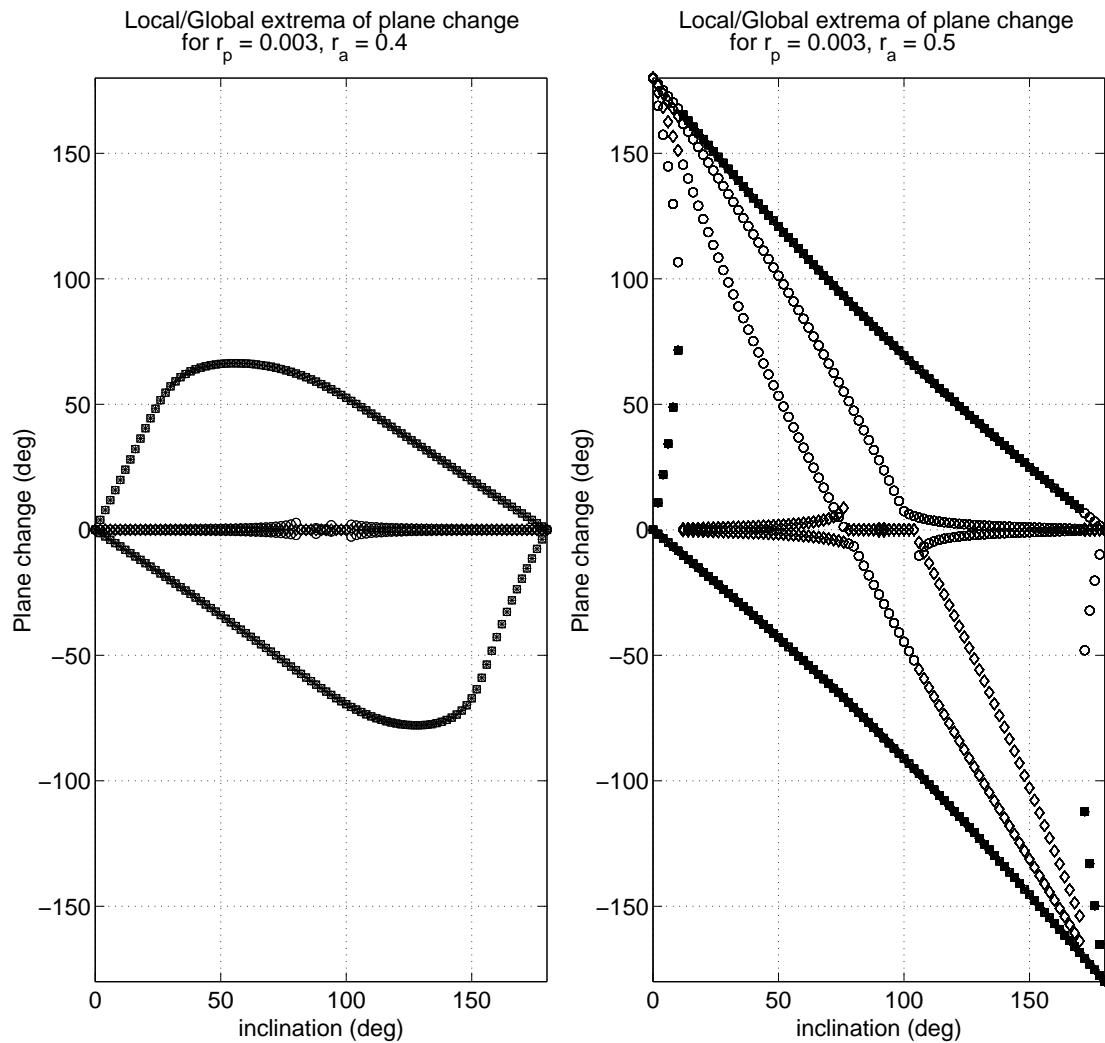


Figure V.13: Local-Global extrema on individual zero lines

given in Figure V.14. These graphs correspond to the envelopes of the results shown in Figure V.13.

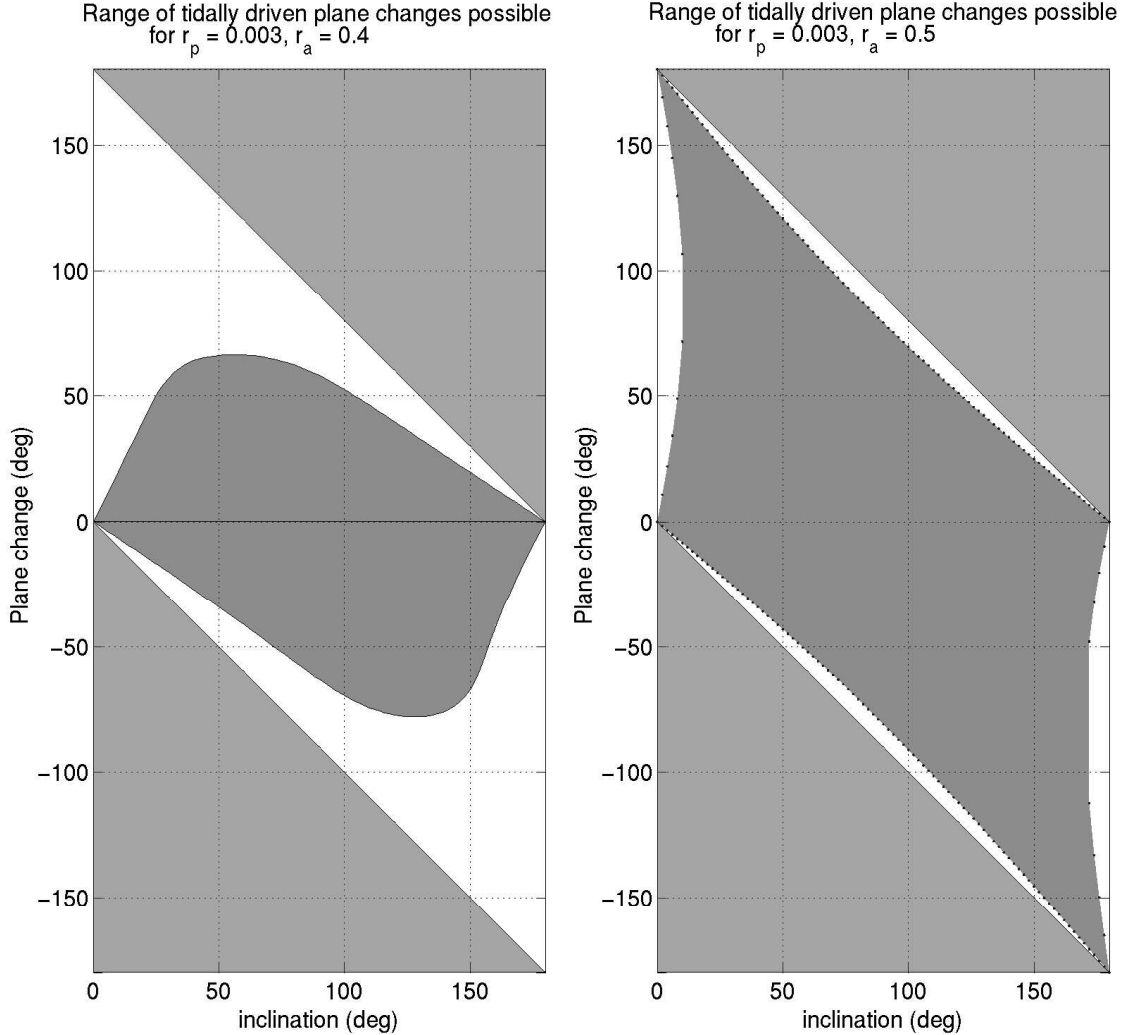


Figure V.14: Range of possible third body driven plane changes

Also, we can see on this figure that the range of realizable 3rd body driven plane change depends on whether $\pm 180^\circ$ plane changes are possible. Thus, in order to obtain large values of realizable plane changes, one need to choose $r_{a_{max}}$ such that $\pm 180^\circ$ plane changes are possible. The limit of existence of such transfers can easily be computed numerically as shown on Figure V.15. It should be noted that the transition between the regions of possible and impossible $\pm 180^\circ$ plane change is not continuous but correspond

to a bifurcation in the planar problem. These plane changes are related to a change of sign in the z component of the angular momentum, and in the limit $r_p \rightarrow 0$, these transfers tend to zero angular momentum trajectories. However, no analytical estimates of the curves presented in Figure V.15 have been obtained yet.

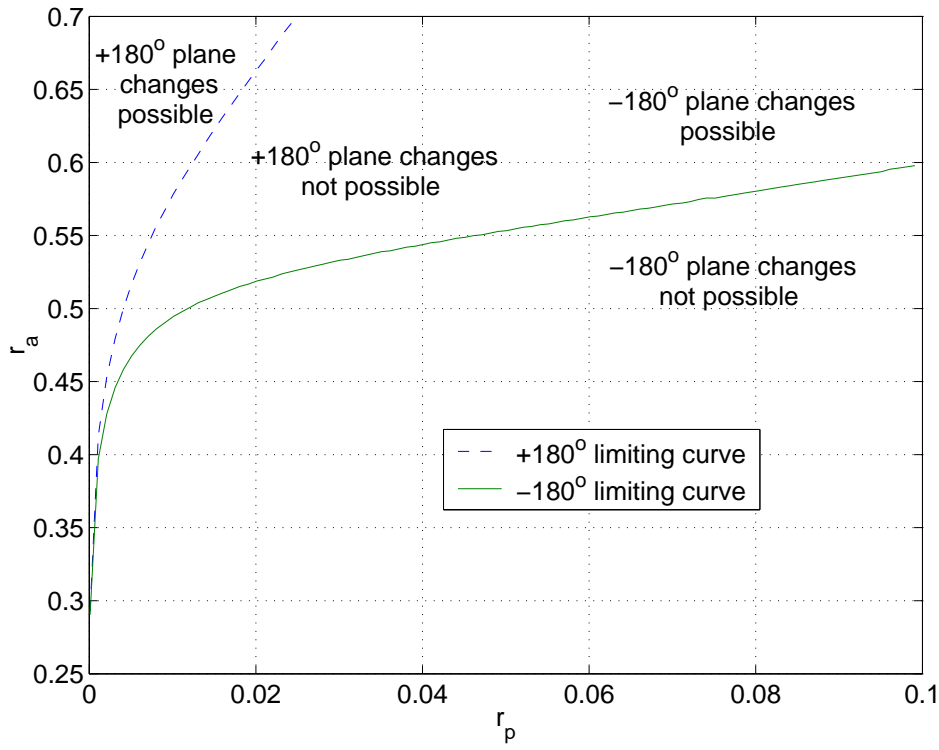


Figure V.15: Limiting curve for the existence of $\pm 180^\circ$ plane changes.

Finally, we note that, in terms of comparison with one impulse plane changes, the above results show that outside the realizable range computed, one impulse plane changes must be used and are, *per force*, optimal.

3.3. Optimal method for performing a desired plane change: an analytical result

In the range of possible 3rd body driven plane changes, the question of the comparison with one impulse maneuvers must still be answered. To do so, an estimate of $\Delta V_{3^{rd} body}(r_p, r_a, i, \Delta i)$

is obtained first, via the Jacobi constant expressed in inertial coordinates:

$$J = \frac{1}{2}V^2 - \frac{1}{r} - G \cos i + \frac{1}{2}r^2 - \frac{3}{2}x^2 \quad (\text{V.8})$$

where r , V and G denote, respectively, the magnitude of the position, velocity and angular momentum vector in inertial space (same origin as in the rotating frame).

Along a transfer trajectory, ω and Ω have been chosen so that $\Delta r_p = 0$. It follows that the terms depending only on r cancel out in the difference of the Jacobi constant taken between the final and initial periapsis passages of the transfer trajectory. Moreover, at periapsis, the angular momentum magnitude is expressed as $G = r_p V$ so that we obtain:

$$\Delta J = J_2 - J_1 = 0 = \frac{1}{2}(V_2^2 - V_1^2) - r_p V_2 \cos(i + \Delta i) + r_p V_1 \cos(i) - \frac{3}{2}(x_2^2 - x_1^2) \quad (\text{V.9})$$

where the subscripts 1 and 2 refer to the initial and final periapsis, respectively.

Now, denoting $c = \frac{3}{2}(x_2^2 - x_1^2)$, we can solve for v_2 (quadratic form in v_2):

$$v_2 = r_p \cos(i + \Delta i) + \sqrt{r_p^2 \cos^2(i + \Delta i) + V_1^2 - 2r_p V_1 \cos(i) + 2c} \quad (\text{V.10})$$

Note, here, that V_1 is expressed in terms of r_p and r_a of the transfer trajectory at the initial periapsis as $V_1 = \alpha V_{lc}$ where $\alpha = \sqrt{\frac{2r_a/r_p}{1+r_a/r_p}}$ only depends on the ratio r_a/r_p . $V_{lc} = \sqrt{\frac{1}{r_p}}$ is the local circular speed in inertial space.

The quantity c in (V.10) depends on ω and Ω and can be bounded as $-\frac{3}{2}r_p^2 \cos^2(i) \leq c \leq \frac{3}{2}r_p^2 \cos^2(i + \Delta i)$, so that we obtain a bound on v_2 as:

$$V_2^- \leq V_2 \leq V_2^+ \quad (\text{V.11})$$

where
$$\begin{cases} V_2^- &= r_p \cos(i + \Delta i) + \sqrt{r_p^2 \cos^2(i + \Delta i) - 3r_p^2 \cos^2(i) + v_1^2 - 2r_p v_1 \cos(i)} \\ V_2^+ &= r_p \cos(i + \Delta i) + \sqrt{4r_p^2 \cos^2(i + \Delta i) + v_1^2 - 2r_p v_1 \cos(i)} \end{cases}$$

It results that $\Delta V_{3^{rd} body}(r_p, r_a, i, \Delta i) = V_1 + V_2 - 2V_{lc}$ is also bounded, $\Delta V^- \leq \Delta V_{3^{rd} body} \leq \Delta V^+$, yielding a bound on the limit of optimality for one impulse plane change maneuvers. Indeed, for any Δi in the realizable range, the minimum $\Delta V_{3^{rd} body}$ to

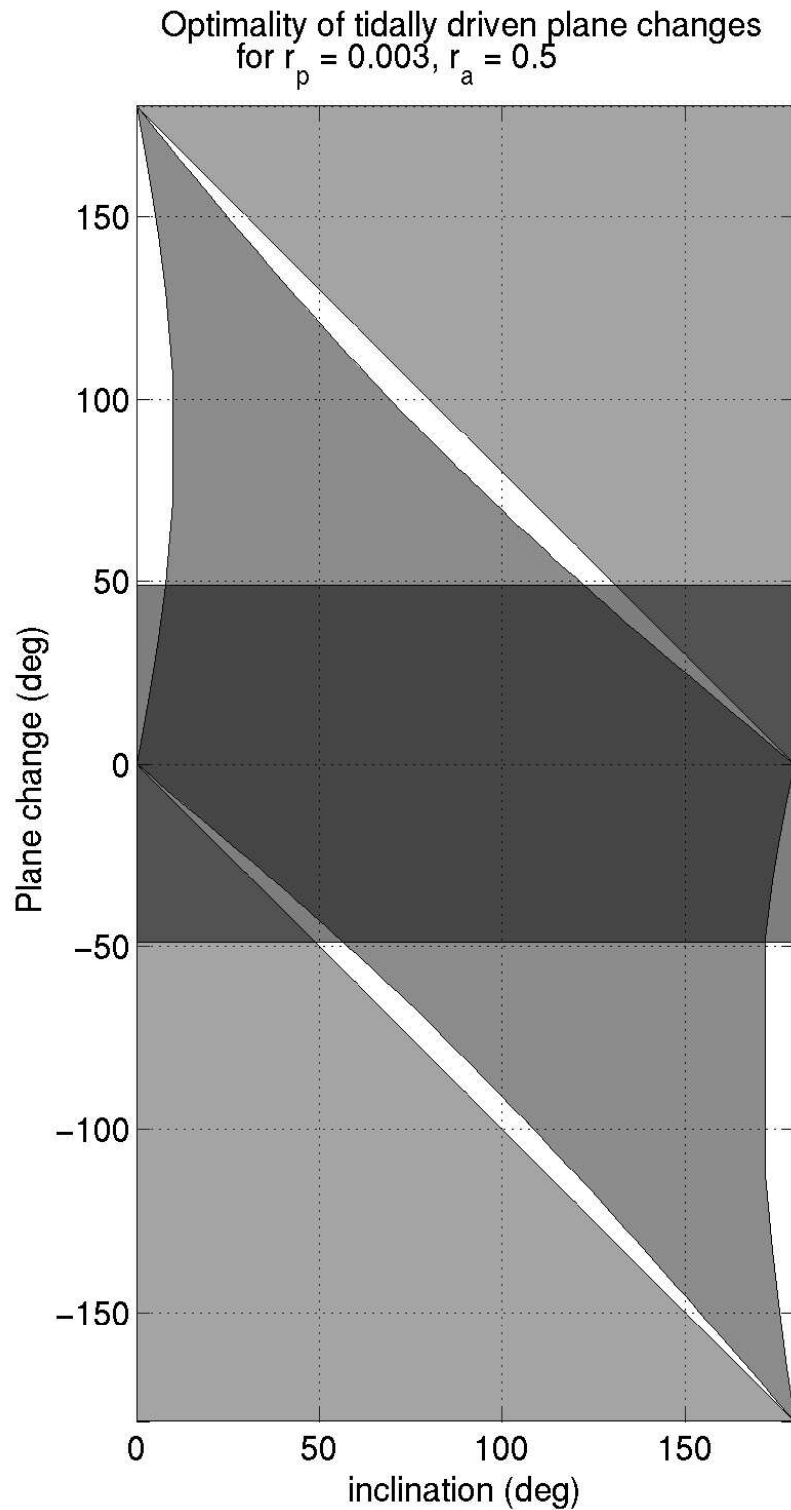


Figure V.16: A bound on the domain of optimality of one impulse maneuvers

perform such plane change satisfies:

$$\Delta V_{3^{rd}body}(\Delta i) \leq \Delta V^+(\Delta i, r_{a_{max}}) \quad (\text{V.12})$$

Therefore, it is clear that third body driven plane changes will be optimal at least when:

$$\Delta V^+(\Delta i, r_{a_{max}}) \leq \Delta V_{1-impulse}(\Delta i) \quad (\text{V.13})$$

Figure V.16 show the resulting regions for $r_p = 0.003$ and $r_a = 0.5$. For plane changes outside the shaded regions, 3^{rd} body driven plane changes are optimal when possible (i.e. in the realizable domain).

It can also be noted that the dependence on i and Δi in ΔV^+ is small and the removal of this dependence in V.13 leads to an explicit upper limit for the optimality of one impulse maneuvers:

$$|\Delta i| \geq 2 \arcsin \left\{ \frac{\alpha}{2} - 1 + \frac{r_p^{3/2}}{2} + \frac{1}{2} \sqrt{(\alpha + r_p^{3/2})^2 + 3r_p^{3/2}} \right\} \quad (\text{V.14})$$

This criterion is a little less precise than the criterion obtained above (relation (V.13)) but allows us to map the upper limit for optimality over a wide range of initial conditions. Figure V.17 shows the contour plots of the equality case in (V.14). At each value of r_p and r_a , third body driven plane changes will be optimal, if realizable, for $|\Delta i|$ greater than the value indicated on the graph. Note that this criterion should be applied to the value $r_{a_{max}}$ chosen, which should lie, for this graph, between 0.3 and 0.7, depending on the maximum transfer time allowed.

Note also that this criterion gives us an upper bound on the cost of 3^{rd} body driven plane changes larger than the criterion value. Indeed, all 3^{rd} body driven plane changes will cost less than $\Delta V^+(r_{a_{max}})$ (where the dependence on i and Δi has been removed, i.e., $\cos(i + \Delta i)$ is taken to be equal to 1 in the expression of ΔV^+). In the case presented, this shows that all 3^{rd} body driven plane changes will cost less than the cost of a one impulse plane change maneuver for $\Delta i \simeq 40^\circ$. More precisely, we obtain:

$$\Delta V_{3^{rd}body} \leq V_{lc} \left(\alpha - 2 + r_p^{3/2} + \sqrt{(\alpha + r_p^{3/2})^2 + 3r_p^{3/2}} \right)$$

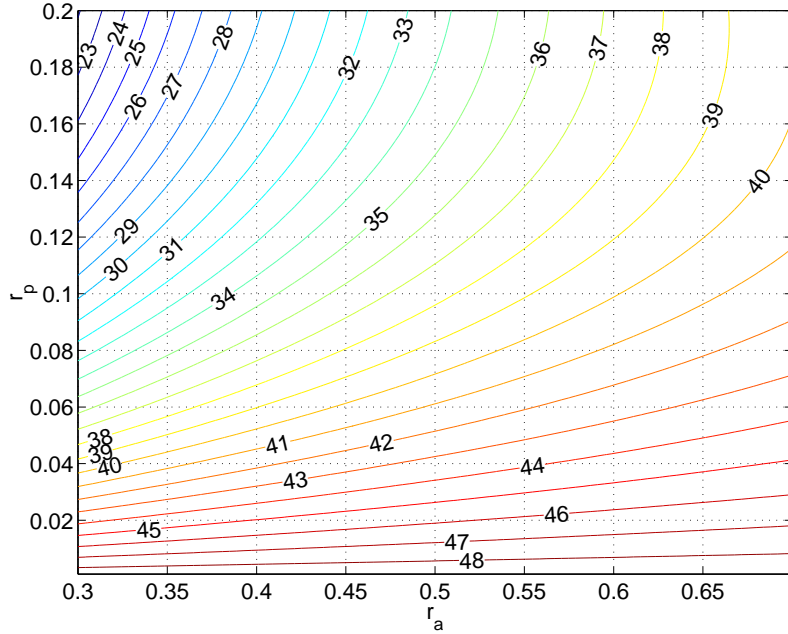


Figure V.17: Analytic estimate of the limit of optimality between one impulse maneuvers and 3rd body driven plane changes.

A contour plot of this upper bound is given in Figure V.18. It gives an idea of the order of magnitude of the savings obtained by the use of the 3rd body forces.

At this point it would seem that a lower bound on when one impulse plane changes are optimal could be obtained via the same method. However, a closing relation, $r_a(\Delta i_{max})$, is missing in order to obtain such a bound. We don't know a priori what apoapsis radius is needed to perform a given plane change and the Jacobi constant estimates do not allow us to obtain a meaningful bound. The restrictions $V_{lc} \leq V_2 \leq V_{escape}$ does not yield any interesting results.

3.4. Optimality criterion: algorithm and numerical results

One can use the above results to devise an algorithm that answers completely the question of optimality below the theoretical upper limit obtained above. Instead of comparing the ΔV 's at fixed Δi , one can compare the Δi 's realized for a fixed ΔV . This is possible because of the 1-1 relation between Δi and $\Delta V_{1-impulse}$ on one hand, and the same monotonic dependence of Δi and ΔV on r_a for 3rd body driven plane changes, on the other

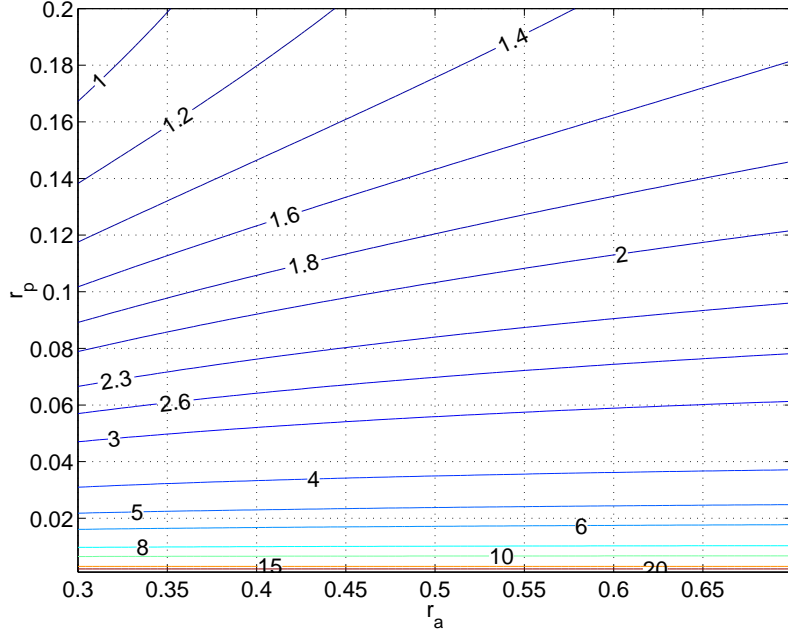


Figure V.18: Analytic upper bound for the cost of 3rd body driven plane changes.

hand.

Given Δi_0 , we have $\Delta V_{1-impulse}$ given by equation (V.1). Then we can solve for r_a in $\Delta V^\pm(r_a) = \Delta V_{1-impulse}$, yielding two solutions r_a^\pm :

$$r_a^\pm = \frac{(\alpha^\pm)^2 r_p}{2 - (\alpha^\pm)^2} ; \quad \alpha^\pm = \frac{A^2 - B^\pm}{2V_{lc}(A - r_p \cos(i))} \quad (\text{V.15})$$

where
$$\left\{ \begin{array}{l} A = \Delta V_{1-impulse} - r_p \cos(i + \Delta i) + 2V_{lc} \\ B^+ = 4r_p^2 \cos^2(i + \Delta i) ; \quad B^- = r_p^2 \cos^2(i + \Delta i) - 3r_p^2 \cos^2(i) \end{array} \right.$$

Now, problem V.5 can be solved numerically with r_a^\pm , resulting in Δi^\pm to be compared with Δi_0 . However, note that, when $\Delta i^+ \leq \Delta i_0 \leq \Delta i^-$, one needs to solve exactly for $\Delta V_{3^{rd}body}$ to decide of the optimality by comparing with $\Delta V_{1-impulse}$. In practice, this case covers only a very thin strip of initial conditions and generally, the above algorithm requires only solving problem (V.5) once or twice per initial conditions to settle the question.

Numerical computations for the case shown in Figure V.16 shows that the theoretical limit (V.13) is within 1° of the numerically computed limit.

Algorithm[¶]:

- Given r_p , i and Δi_0 , solve for $\Delta V_{1-impulse}$ using (V.1).
- Solve for r_a^\pm using the relation $\Delta V^\pm(r_a) = \Delta V_{1-impulse}$.
(Note that $r_a^+ \leq r_a^-$).
- Solve the optimization problem (V.5) with r_p , r_a^\pm , i to obtain Δi^\pm .
(Note that $\Delta i^+ \leq \Delta i^-$).
- compare:
 - If ($\Delta i_0 \geq \Delta i^-$) Then one impulse transfers are optimal
 - If ($\Delta i_0 \leq \Delta i^+$) Then third body driven plane changes are optimal
 - If ($\Delta i^+ \leq \Delta i_0 \leq \Delta i^-$) Then use a dichotomy on r_a to solve exactly for $\Delta V_{3^{rd}body}$

[¶]formulated here for $\Delta i_0 \geq 0$. A similar algorithm can be written for $\Delta i_0 \leq 0$

CHAPTER VI

ESCAPE, CAPTURE AND TRANSIT

This chapter presents a second application of the use of 3^{rd} body forces to effect orbital transfers. As for the previous application, this second application, escape and capture maneuvers, was also motivated by the Europa Orbiter Mission.

While the transfers considered are analyzed using a periapsis Poincaré map, the initial conditions are chosen on a surface of section close to the libration points and the map is then obtained by backward integration. The main difference between the previous chapters (IV and V) is that the existence of a next (or previous) periapsis passage is not guaranteed (since we are working at energies where the zero velocity surface is open, i.e., $J > J_c$). Thus, this approach shows the limits of the approximations of the periapsis Poincaré maps obtained in Chapter IV.

Note that, unlike 3^{rd} body driven plane changes, low energy transit trajectories have been studied by several authors, the first one being Conley [9], who analyzed the flow near the collinear libration points in the planar circular restricted three body problem (PCR3BP). Belbruno [4] pointed out that these nonlinear dynamics can be used to numerically compute ballistic transfers to the moon and gave several ways of finding such transfers. More recent work by Koon et al. [21, 20] gives a more rigorous explanation of these phenomena by applying some techniques from dynamical systems theory to systems of coupled PCR3BP. They obtained a systematic way of designing ballistic lunar transfers and, more generally, trajectories with a predetermined future and past (in terms of transfer from the inner side of the orbit of the primary to the outer side).

In this chapter, we give another view of the geometry of escaping trajectories, focusing on obtaining practical characterizations of the initial conditions of these escaping trajectories at periapsis. Applications of these results are made to the analysis of direct escape maneuvers. In particular, the minimum energy needed to directly escape, starting at a given altitude, is obtained. These results should be useful for mission design and planning.

While the results presented here were first reported in [38], this chapter takes a slightly different point of view by relating these results to the linearized theory at the libration points and the notion of escaping trajectory is slightly sharpened. In [38], escape has been considered from a practical viewpoint where any trajectories crossing the plane $x = \pm r_c$ with an outward velocity (with respect to the primary) was considered to be an escaping trajectory. The aim of the paper was indeed to obtain estimates of the initial costs for escape starting in a low altitude, circular orbit (thus close to the primary) and once near the libration points, a very small ΔV may be used to transfer the spacecraft on a trajectory that will never meet the planetary satellite again.

In this chapter, the set of escaping trajectories that come close to the primary are integrated forward to check that they indeed correspond to escaping trajectories for the Hill problem and can be patched onto the outer restricted three body problem if needed. This does not mean, however, that the spacecraft will not meet the planetary satellite in the framework of the restricted three body problem, but the time of return will at least be much larger than the period of the primary around the disturbing body.

In Section 1, we review the dynamics near the libration points, following a paper by Conley [9], resulting in a classification of the trajectories in this region. The use of a periapsis Poincaré map allows us to extend this local picture up to the neighborhood of the primary by integrating the flow backward, resulting also in a proposed classification of planetary satellites.

Applications of the previous results are then made, in Section 2, to the problem of directly escaping trajectories assuming a spacecraft initially in a low altitude, circular orbit.

It is shown, in particular, that the minimum ΔV to directly escape is obtained for tangential burns and that this minimum decreases as altitude increases. A new optimality criterion is then stated for the class of directly escaping trajectories using one impulsive maneuver, resulting in fuel savings on the order of 130 m/s in the case of Europa (as compared to a two body Keplerian model). Given an initial altitude, the optimal Jacobi constant and the minimum ΔV required to reach escape can be read from some graphs. The time of the maneuver is determined by a condition on the longitude of the ascending node and the argument of periapsis of the transfer trajectory, similar to the previous chapter. Restrictions on the inclination for these transfers to be possible also exist, as the initial orbit must be near-equatorial.

1. Periapsis Poincaré map for escape, capture and transit

We have seen in Chapter III that the linearized dynamics at the libration points is given by a 2-dimensional center manifold and two 1-dimensional invariant manifolds (one stable and one unstable direction) in the planar case. In the spatial problem, the center manifold is 4-dimensional and consists of periodic and quasi-periodic trajectories. This section presents a closer look at these dynamics by first recalling some results from [9] and then extending the local picture obtained with the help of numerical integration methods. The consequences of the results obtained are discussed.

1.1. Taxonomy of trajectories near the libration points

Recall from chapter III that the linearized dynamics around the libration points is given by:

$$\frac{d}{dt} \begin{bmatrix} \mathbf{q} \\ \dot{\mathbf{q}} \end{bmatrix} = \begin{bmatrix} \mathbf{O} & \mathbf{I} \\ \mathbf{A}_1 & \mathbf{A}_2 \end{bmatrix} \begin{bmatrix} \mathbf{q} \\ \dot{\mathbf{q}} \end{bmatrix} ; \quad \mathbf{A}_1 = \begin{bmatrix} 9 & 0 & 0 \\ 0 & -3 & 0 \\ 0 & 0 & -4 \end{bmatrix} ; \quad \mathbf{A}_2 = \begin{bmatrix} 0 & -2 & 0 \\ 2 & 0 & 0 \\ 0 & 0 & 0 \end{bmatrix}$$

and the eigenvalues are denoted $\lambda_1^\pm = \pm\lambda_1$, $\lambda_2^\pm = \pm i\lambda_2$ and $\lambda_3^\pm = \pm i\lambda_3$, where:

$$\lambda_1 = \sqrt{2\sqrt{7} + 1} \quad ; \quad \lambda_2 = \sqrt{2\sqrt{7} - 1} \quad ; \quad \lambda_3 = 2$$

Note that λ_1^+ and λ_2^+ are independent over the reals and that λ_3^+ is independent of λ_1^+ and λ_2^+ over the integers*. These are exactly the assumptions needed to apply Moser's generalization of a theorem of Lyapunov alluded to in Chapter III [29]. This theorem guarantees the existence of an analytic change of variable that allows us to transform the original nonlinear system into the linearized form above. That is, the qualitative picture obtained from the linearized equations is also representative of the nonlinear dynamics.

Now to obtain this linearized picture, one can compute the eigenvectors corresponding to the above eigenvalues. Denoting the corresponding eigenvalue-eigenvector as:

$$\lambda_1^\pm \rightarrow \mathbf{u}_1^\pm \quad ; \quad \lambda_2^\pm \rightarrow \mathbf{u}_2^\pm \quad ; \quad \lambda_3^\pm \rightarrow \mathbf{u}_3^\pm$$

it can easily be checked that the eigenvectors are given by:

$$\mathbf{u}_1^\pm = \begin{bmatrix} 1 \\ \pm\sigma \\ 0 \\ \pm\lambda_1 \\ \sigma\lambda_1 \\ 0 \end{bmatrix} \quad ; \quad \mathbf{u}_2^\pm = \begin{bmatrix} 1 \\ \pm i\tau \\ 0 \\ \pm i\lambda_2 \\ -\tau\lambda_2 \\ 0 \end{bmatrix} \quad ; \quad \mathbf{u}_3^\pm = \begin{bmatrix} 0 \\ 0 \\ 1 \\ 0 \\ 0 \\ \pm i\lambda_3 \end{bmatrix}$$

$$\text{where } \sigma = \frac{\lambda_1^2 - 9}{2\lambda_1} \simeq -0.5399 \quad \text{and} \quad \nu = \frac{\lambda_2^2 - 9}{2\lambda_2} \simeq 3.2080 .$$

Thus, the general form of the solution is:

$$\begin{bmatrix} \mathbf{q} \\ \dot{\mathbf{q}} \end{bmatrix} = \alpha^+ e^{\lambda_1 t} \mathbf{u}_1^+ + \alpha^- e^{-\lambda_1 t} \mathbf{u}_1^- + 2\operatorname{Re} \{ \beta e^{i\lambda_2 t} \mathbf{u}_2^+ \} + 2\operatorname{Re} \{ \gamma e^{i\lambda_3 t} \mathbf{u}_3^+ \} \quad (\text{VI.1})$$

where α^+, α^- are real and β, γ are complex numbers.

The eigenvectors \mathbf{u}_1^\pm span the hyperbolic directions of the dynamics while $\mathbf{u}_{2,3}^\pm$ correspond to the center manifold. In the $(\mathbf{u}_1^+, \mathbf{u}_1^-)$ space, the center manifold projects to a point while the x and y axis projects as shown on Figure VI.1.

*That is, $a\lambda_1^+ + b\lambda_2^+ = 0$ with a and b reals implies that $a = 0$ and $b = 0$, and $k_1\lambda_1^+ + k_2\lambda_2^+ \neq k_3\lambda_3^+$ for any integer k_1, k_2 and k_3 . This is clear since λ_1^+ is real while λ_2^+ is pure imaginary and λ_1^+ is irrational while λ_3^+ is rational. A similar remark holds for λ_1^+, λ_3^+ and λ_2^+ in that order

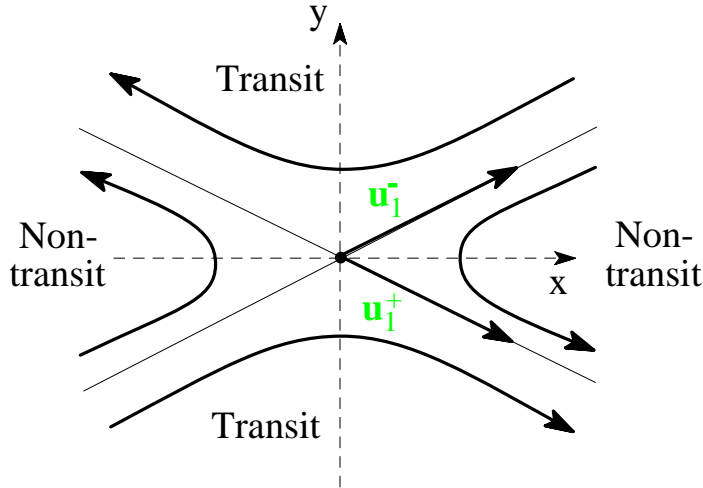


Figure VI.1: Stable and unstable direction of the libration points dynamics

Thus, when, $\alpha_1^+ \alpha_1^- < 0$, the trajectories cross the y axis and go from $-\infty$ to $+\infty$ (or vice versa) in this linearized setting. If $\alpha_1^+ \alpha_1^- > 0$, the trajectories stay on one side of the the y -axis. Thus Conley [9] proposed the following classification:

- $\alpha_1^+ \alpha_1^- < 0$: transit trajectories
- $\alpha_1^+ \alpha_1^- > 0$: non-transit trajectories
- $\alpha_1^+ \alpha_1^- = 0$: asymptotic trajectories

where the last class includes the center manifold as well. This classification was originally derived in the restricted three body problem where transit trajectories go from one region dominated by the gravitational attraction of one body to a region dominated by the second body. In our case, transit trajectories are either escaping trajectories when going from the inner region to the outer region of the Hill's problem, or capture trajectories when going the other way.

Note that it can easily be proven in this linear setting that non-escaping trajectories are bounded by the lines that are tangent to the Lyapunov orbits at their apses. That is, non-transit trajectories coming from the inner region cannot go further than the planes $x = \pm c$ tangent to the apoapsis of the Lyapunov orbits. Thus, as far as this linear picture holds,

if an integrated trajectory crosses the neck from one side of a Lyapunov orbit to the other side (as defined by the above tangent planes), then the trajectory is a transit trajectory. From a practical point of view, we will integrate the trajectories up to a radius $r = 10$ to check escape.

At a given value of J , it can also be shown from (VI.1), that the envelope of the transit trajectories consists of the set of asymptotic trajectories. This set forms, moreover, a ‘tube’ that separates the phase space. In the planar problem, these tubes project onto some strips (resp., solid cylinders in the spatial problem) in position space and any initial condition outside these tubes corresponds to a non-transit trajectory, no matter what the direction of the velocity is. Inside the strips, transit and non-transit trajectories are distinguished by a condition on the velocity direction.

In the case of escaping trajectories at L_2 , the tubes are formed by the inner branch of the stable manifold associated with the center manifold, W^s , and the outer branch of the unstable manifold, W^u . Llibre et al. [22] have shown that for low values of J (i.e., such that the above linear picture holds), W^u extends to infinity in the planar Hill problem. That is, in the framework of the Hill problem, once an escape trajectory crossed the neck region, it never comes back close to the primary, i.e., it is really an escape trajectory. However, in the framework of the restricted problem, the spacecraft can return close to the neck region after one or several loops around the disturbing body and encounter the primary again.

In view of these results, a trajectory can be considered as escaping as soon as it crosses the neck region and numerical integration only needs to be performed up to that point. However, since an estimate of the value of the Jacobi constant for which the linear picture can be used is not available, we will numerically integrate escaping trajectories up to $r = 10$ to ensure escape.

Concerning capture trajectories, we defined them as trajectories that come from the outer regions, cross one of the neck and then have at least one of their periapsis passages close to the primary (i.e. inside the first curve $w(r) = 0$ of chapter IV). Thus, in view

of the S_1 symmetry of the Hill problem (time-reversal reflection about the (y, z) -plane), we see that the symmetric of an escape trajectory is a capture one and vice versa. It is therefore sufficient to analyze escaping trajectories to obtain a complete characterization of transit trajectories.

Finally, we should note that while the above picture has first been obtained by Conley in the planar case[†], the three dimensional case has been obtained by Appleyard [1] and a more recent presentation is given in [11].

1.2. Numerical integration of escaping trajectories

In view of the preceding results, the envelope of the escaping trajectories can simply be obtained by computing W^s . This computation is, however, subtle and a more direct numerical scheme is proposed to analyze escaping trajectories. This scheme is closely tied with the results presented in [38] and consists of integrating the outward flow of the neck regions close to the libration points, back to the previous periapsis passages[‡]. Because of the symmetries S_3 and S_4 (see Chapter III), we only need to integrate the outward flow near L_2 and at those points having a positive z coordinate.

From the linearized results, it would seem that a good choice of surface of section in the neck regions would be a sphere or plane, normal to the x -axis and located just above the apoapsis of the Lyapunov orbits (as viewed from the primary). This choice requires, however, to compute the Lyapunov orbit and the precise value at which the surface must be located is not clear for large values of J . It should be taken far enough to ensure that non-transit trajectories from the inside regions do not cross the surface, yet not too far since the number of points used to integrate the flow increases with the area of the surface

[†]One should be careful in reading Conley's paper because of an error in the linearization (the J matrix should really be $-J$). This error does not change the results except for a global reversal of time. Thus, the direction of the Lyapunov orbit is clockwise and not counter-clockwise.

[‡]The 'fbw' is integrated by randomly sampling the phase space region corresponding to the initial conditions and using an integration subroutine to propagate in time this discrete set of points. The difficulty with this approach lies in the large number of sampling points that may be required to obtain a sufficient accuracy for computing, for example, the boundary of the phase space region considered.

of section[§].

Thus, instead of performing such a choice, we define the first surface of section, Σ_1 , as the minimum area section of the zero velocity surface which is reached, as we have seen in Chapter III, at $r = r_c$. Moreover, we impose that $\dot{r} > 0$ to ensure that the flow is going outward. The second surface of section, Σ_2 , is defined by the periapsis condition. Then, the flow is integrated backward from Σ_1 to the first intersection with Σ_2 , and, in order to distinguish between escape and capture trajectories are taken into account, a forward integration is performed up to $r = 10$. That is, if a trajectory returns close to the primary before reaching $r = 10$, it is considered to be captured.

The surface Σ_1 is parameterized by longitude, ϕ , and latitude, λ , for the position space and the velocity angles are denoted by δ and ν . The magnitude of the velocity is obtained via the Jacobi constant J , i.e., $v = \sqrt{2(J + \frac{1}{r}) + r^2 g(\phi, \lambda)}$. Thus, with this parameterization, the Cartesian coordinates of the points on Σ_1 are given by:

$$\begin{aligned} x &= r_c \cos \phi \cos \lambda & ; \quad \dot{x} &= v \cos \delta \cos \nu \\ y &= r_c \sin \phi \cos \lambda & ; \quad \dot{y} &= v \sin \delta \cos \nu \\ z &= r_c \sin \lambda & ; \quad \dot{z} &= v \sin \nu \end{aligned}$$

where ϕ, λ are chosen so that $g(\phi, \lambda)r_c^3 + 2Jr_c + 2 > 0$ and δ, ν range in the interval $(-\pi/2, \pi/2)$.

In the computations performed, all these angles have been chosen randomly so that the initial surface of section is sampled “uniformly”. The computations made involved as least 100×100 points in the planar problem and 300×300 points in the spatial problem. The Jacobi constant has been varied from $J_c + 10^{-9}$ to $J_c + 0.11$.

On Σ_2 , we either used the coordinates (x, y, z) or (r_p, ω, Ω) to locate a periapsis passage and the inclination has been used to determine the direction of the velocity vector.

Note that in the planar problem the Poincaré map defined is only 2-dimensional and can be directly represented in position space. In this case, λ and ν are set to zero on Σ_1

[§]One cannot take the plane tangent to the Lyapunov orbits since for large J the results of the linearized theory are deformed and the amount of the deformation is not known from the linearized results.

and, on Σ_2 , ω and Ω degenerate into $\tilde{\omega} = \omega + \Omega$ and the inclination is, of course, zero. Figure VI.2 illustrates this situation.

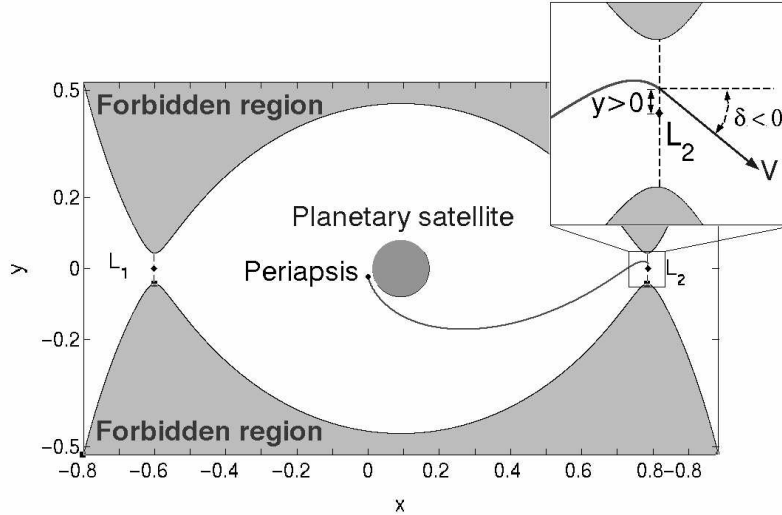


Figure VI.2: Geometry of the Poincaré map

1.3. Results

Figure VI.3 gives an example of a Poincaré map for $J = -2.16$, together with two close-ups where the distinction between non-escaping and escaping trajectories is exhibited. As appears immediately on this Figure, the image of the Poincaré map is divided into two disjoint sets denoted Σ_2^a and Σ_2^b . The first one, Σ_2^a , oval shaped, is close to the primary and confined to a small region of altitude and longitude of periapsis. It corresponds to trajectories that come from the neighborhood of the primary. The second set, Σ_2^b , is confined close to L_2 and corresponds to a medley of periapsis passages of all trajectory types in the neck regions. The results obtained in Chapter IV on the limiting curves between periapsis and apoapsis regions clearly indicates that this separation is not a numerical illusion, i.e., Σ_2^a and Σ_2^b consists of two disjoint sets of points. This shows that the roots (3) and (4) of $w(r)$ (see the diagram of Chapter IV, Section 1) can be considered as the non-linear boundaries of the neck regions for low enough energies.

In the sequel, we will focus almost exclusively on the first region, Σ_2^a . It is, indeed, the most important set to be considered for the practical application of these computations to the problem of direct escape from a planetary satellite. The main information coming from the set Σ_2^b is a measure of the extent to which the neck region extends.

We can also see from Figure VI.3 that the non-escaping trajectories coming from the vicinity of the primary surround the set of escaping trajectories, Σ_2^a . From the linearized results, we know that the boundary of Σ_2^a should be the stable manifold associated with the Lyapunov orbit at L_2 . As we can see, the set of non-escaping trajectories computed (i.e., the non-escaping trajectories that reach Σ_1 with an outward velocity) is rather small and the distance between this set and Σ_2^a will decrease forward in time under the influence of W^s . Thus, in the neck region, a small ΔV will be sufficient to transfer a non-escaping particle that cross Σ_1 onto an escaping trajectory, thus supporting the pragmatic viewpoint adopted in [38].

The above remarks made for the planar Poincaré map shown in Figure VI.3 remain valid for the results obtained in the spatial problem. It is found that the set of points obtained is divided into two disjoint sets Σ_2^a and Σ_2^b , whose intersections with the (x, y) -plane match the image of the Poincaré map in the planar case. The three dimensional picture of Σ_2^a looks like the set of points obtained from the planar Σ_2^a , by rotating it along its diameter (the line connecting the points of extremal radius on this set). Restrictions on inclination for Σ_2^a are given in Figure VI.11 and will be discussed in the next section.

Note, however, that, unlike the planar case, the projection of the set of non-escaping points onto position space includes all the points in the projection of Σ_2^a . Indeed, W^s is four dimensional in the spatial problem and the separation between escape and non-escape also involves the inclination of the velocity vector. Thus, at a given position, small values of inclination may correspond to a escaping trajectory, while larger values will correspond to non-escaping trajectories.

As J varies, the size and shape of Σ_2^a varies. Figure VI.4 shows a series of Poincaré

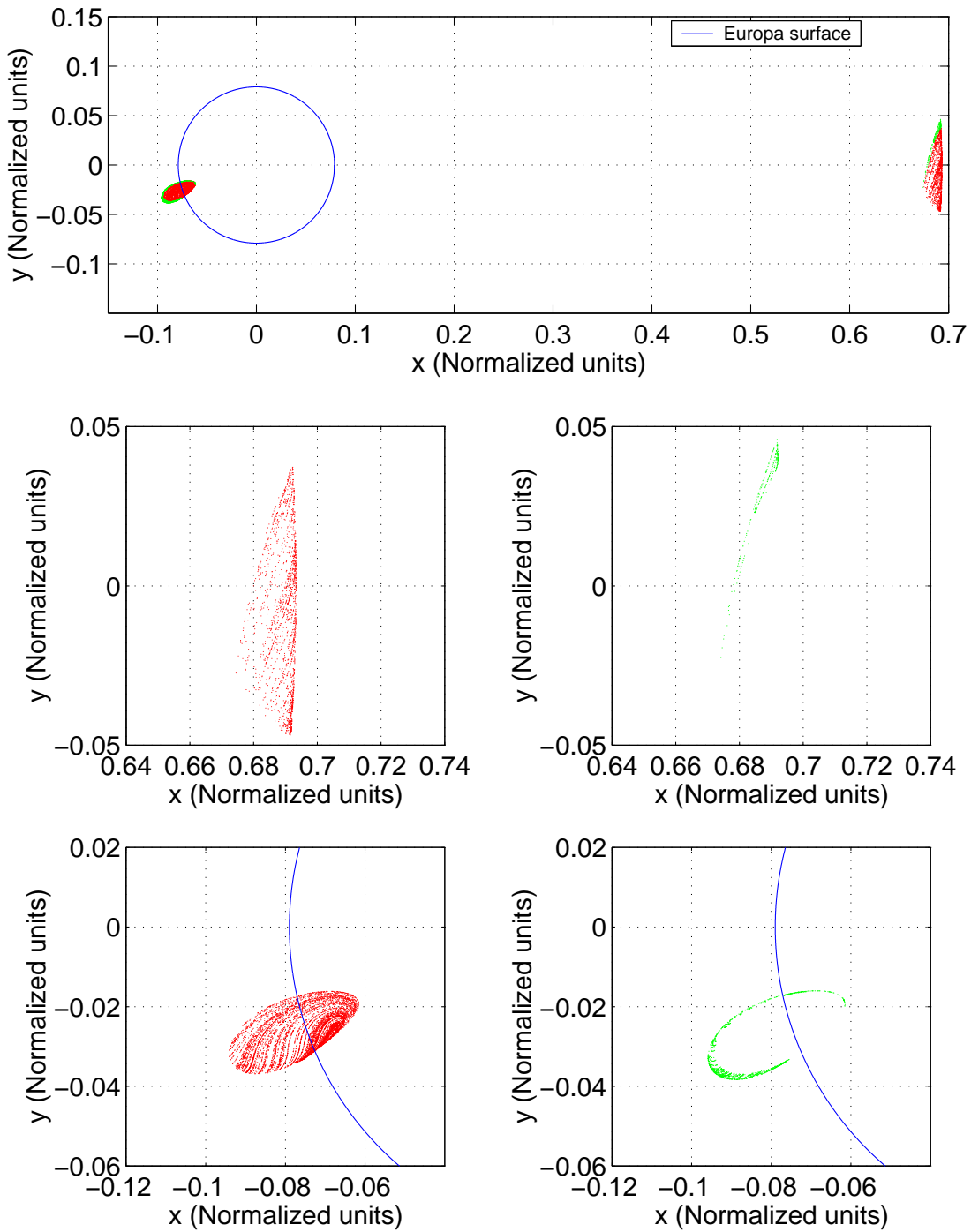


Figure VI.3: Example of a 2D Poincaré map for $J = -2.16$. Full results (top) and close-ups (Left: escaping trajectories. Right: non-escaping trajectories).

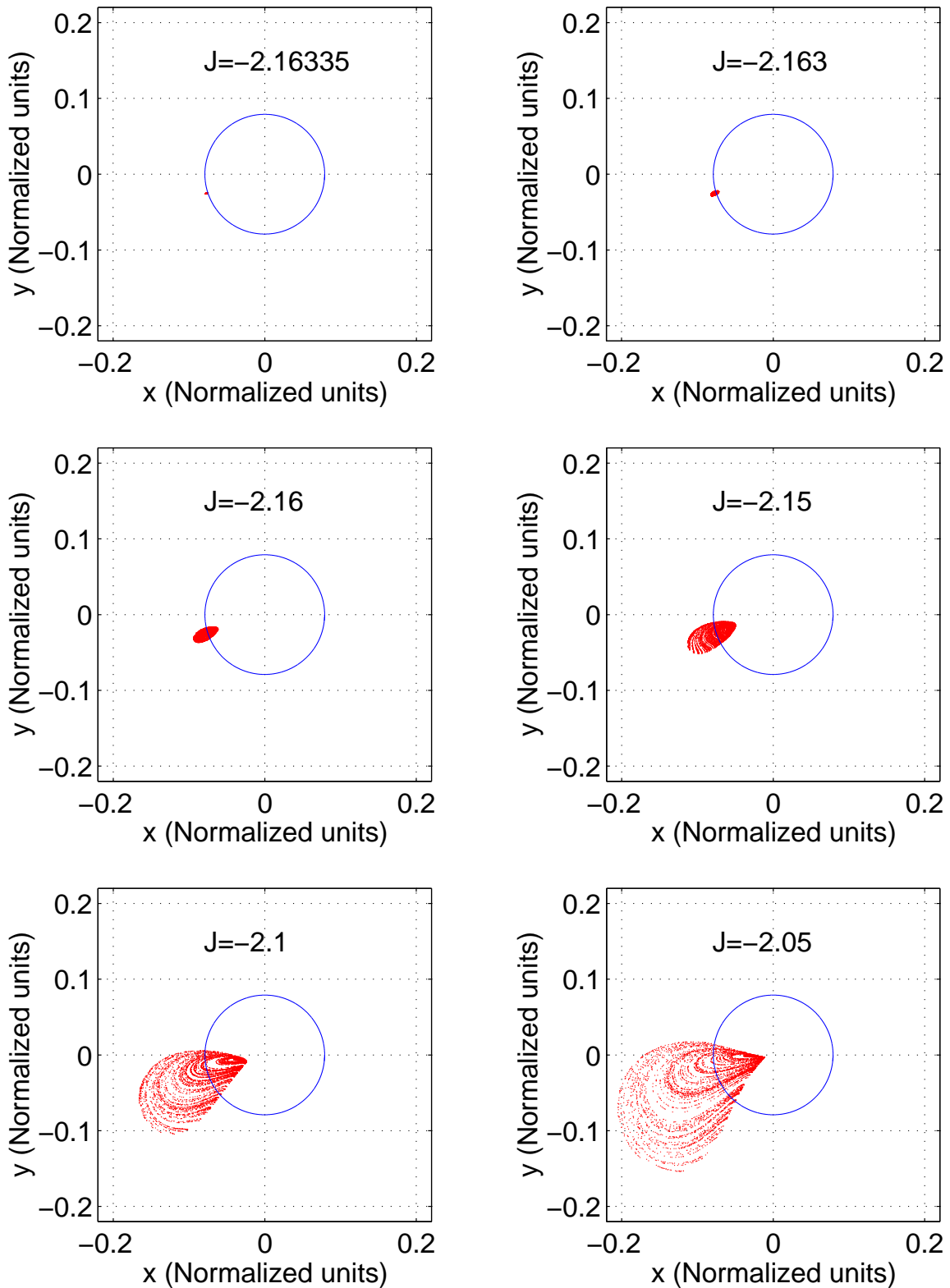


Figure VI.4: Series of Poincaré maps (Σ_2^a) at several values of the Jacobi constant with the surface of Europa.

maps at different values of the Jacobi constant[¶]. One can see that, while Σ_2^a increases with J , it remains rather confined to a small region close to the primary. However, for $J \geq -2.1225$, the boundary of Σ_2^a , denoted $\partial\Sigma_2^a$ crosses the (x, z) -plane. Since $\partial\Sigma_2^a$ corresponds to points on W^s , we can deduce that the points of intersection with the (x, z) -plane correspond to homoclinic trajectories. Indeed, recall that by the S_2 symmetry, escaping trajectories through L_2 are transformed into capture trajectories that transit through the L_2 neck regions. This symmetry leaves the (x, z) -plane invariant and, thus, the points of intersection of $\partial\Sigma_2^a$ and the (x, z) -plane also belong to the boundary of the set of capture trajectories, $\partial(S_1(\Sigma_2^a))$, which are in the unstable manifold associated with the Lyapunov orbit at L_2 . That is, these points are homoclinic points which have only one periapsis passage close to the primary.

The existence of such trajectories is not new. However, the use of the periapsis map allows us to see the intersection of W^s and W^u directly in position space for the planar problem. In particular, it shows that for $J \leq -2.1225$, homoclinic trajectories must have at least two periapsis passages close to the primary, and homoclinic trajectories having just one such periapsis must, *per force*, be symmetric.

The same remarks holds for the intersection of Σ_2^a with the (y, z) -plane and heteroclinic connections (i.e., trajectories that asymptotic to both the Lyapunov orbits at L_1 and L_2), respectively, if such intersections occur. Indeed, the reflection about the (y, z) -plane (S_1 symmetry), transforms escaping trajectories through L_2 into capture trajectories that transit through L_1 . However, at the values of Jacobi constant considered, no such intersection has been found, so that no “direct” heteroclinic connection exist.

Further backward iterations of the periapsis map allows us to verify that heteroclinic trajectories indeed exist, as was first proven in [21] in the case of the planar circular restricted three body problem.

In order to further characterize the sets $\Sigma_2^1(J)$, the extrema of radius, longitude of

[¶]Escaping trajectories only. The reader is referred to [38] for an analog series that includes non-escaping trajectories as well.

periapsis, eccentricity and inclination have been computed as a function of J , as shown on Figures VI.6 and VI.7. Note that all these quantities have been computed on both the escaping and the non-escaping trajectories, allowing us to estimate the thickness of the surrounding set of non-escaping trajectories. Also, it has been found that, within the accuracy of the discretization, all these extrema are reached at some point in the equatorial plane in the case of the spatial problem.

These graphs allow us to obtain the characterizations of all transit trajectories, i.e. escape and capture trajectories through both L_1 and L_2 , by applying the symmetries discussed above and in Chapter III. This is illustrated in Figure VI.5. In particular, the only change in these graphs will be some shifts in Ω .

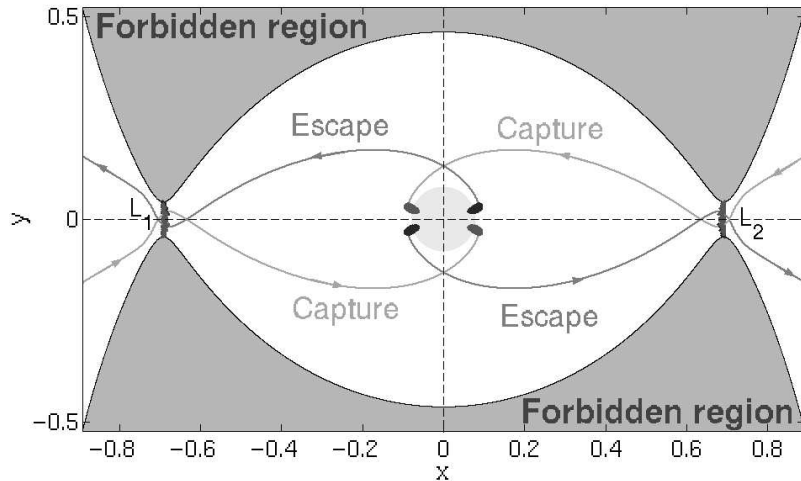


Figure VI.5: Poincaré maps for escape and capture (case of Europa $J = -2.16$)

Finally, we note that as J tends to J_c , Σ_2^a reduces to a point corresponding to the first periapsis passage of the stable manifold associated with the libration point L_2 . In this connection, we notice that planetary satellites having this periapsis below their physical surface will have all the first periapsis of low energy capture impact the satellite, and direct escape from the surface of the primary is possible. These facts may be of interest in the formation process of proto-planets and for the analysis of the insertion maneuvers

of spacecraft around these satellites. In particular, this shows that very low energy capture trajectories are not viable options for insertion around these celestial bodies and low energy capture maneuvers would have to be designed carefully (since at *any* value of J a large set of capture trajectories will impact). In [38], we proposed to refer such planetary satellites as being of type 1, the other planetary satellites being referred to as type 2 (i.e., having the periapsis of the stable manifold associated with $L_{1,2}$ above their physical surface. Table 1 in Appendix B gives the type of many planetary satellites in the solar system. For example, Miranda is of type 1 (periapsis below the surface), Europa, Titan and Triton are of type 2 (periapsis above the surface). Note however, that Europa is rather exceptional: the periapsis of the stable (and unstable) manifold associated with L_2 (or L_1) lies only 40km above the surface of Europa^{||}.

^{||} Periapsis radius of the stable manifold $r_{L_2} \simeq 0.081$. Normalized radius of Europa $\simeq 0.079$.

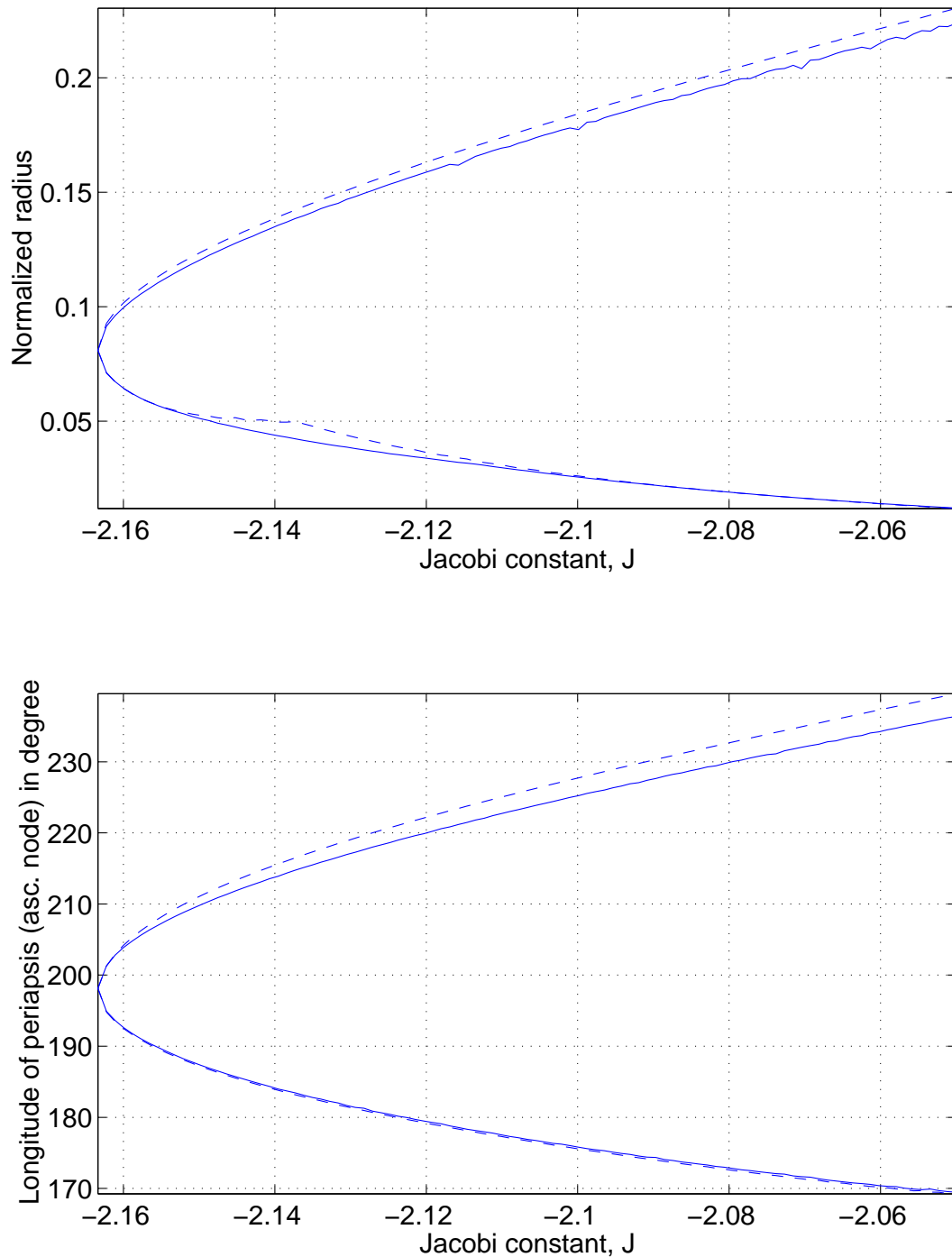


Figure VI.6: Extrema of radius and longitude of periapsis on Σ_2^a as a function of J (solid line: escape trajectories; dashed line: capture trajectories)

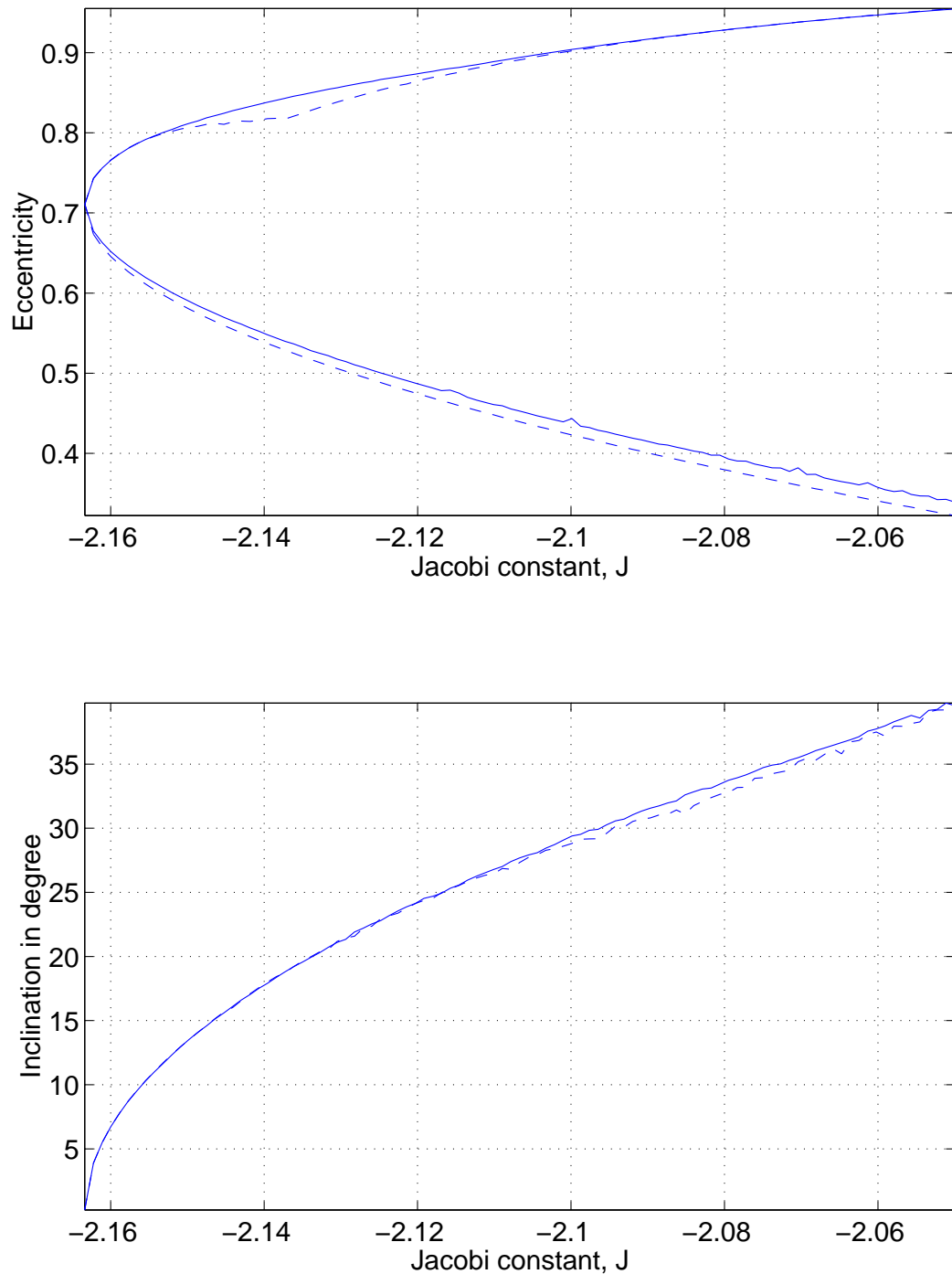


Figure VI.7: Extrema of eccentricity and inclination on Σ_2^a as a function of J (solid line: escape trajectories; dashed line: capture trajectories)

2. Application to escape and capture maneuvers

As discussed in Chapter III, for low altitudes and relatively short time spans, quasi-circular orbits can be approximated by a Keplerian circular motion in a rotating frame. Assuming a spacecraft in such an orbit, one can investigate what the minimum ΔV needed to escape the planetary satellite is. This section investigates the case of one impulse, direct escape maneuvers.

This question can be viewed from two different points of view. The first one asks if there is a particular altitude for which the ΔV to escape is minimal among all direct escape maneuvers starting in low altitude circular orbits. The second assumes the spacecraft is in a low altitude, circular orbit and asks what the minimal ΔV to escape from this given orbit is. With this last problem, one must investigate all the possible techniques to escape starting in a low altitude, circular orbit to obtain an optimal escape criterion. The first problem is then answered as a consequence of this criterion and the method used to derive it.

After proving that tangential burns are optimal for escape maneuvers, different strategies for performing the maneuver are evaluated, leading to an optimal criterion in the planar case. Then, the 3 dimensional case is considered. All this analysis uses the computations explained in the previous section.

2.1. Tangential burns are optimal

When in a circular orbit, the ΔV needed to place a spacecraft into an arbitrary trajectory crossing the circular orbit can be expressed as:

$$\Delta V = \sqrt{V_i^2 + V_{lc}^2 - 2V_i V_{lc} \cos \gamma} \quad (\text{VI.2})$$

where γ is the flight path angle, $V_{lc} = \sqrt{\frac{1}{r}}$ is the local circular speed at a given radius r in inertial space, and $V_i = \sqrt{v^2 + x^2 + y^2 + 2rv \cos \theta}$ is the inertial velocity on the arbitrary trajectory. Here $v = \sqrt{2(J + 1/r) + 3x^2 - z^2}$ has been obtained from the Jacobi constant

and θ represents the inclination in the rotating frame.

Figure VI.8 shows the numerical computation of ΔV along the stable manifold associated with the libration point L_2 . As it appears clearly, ΔV achieves a minimum at periapsis and the value of this minimum is, remarkably, equal to one.

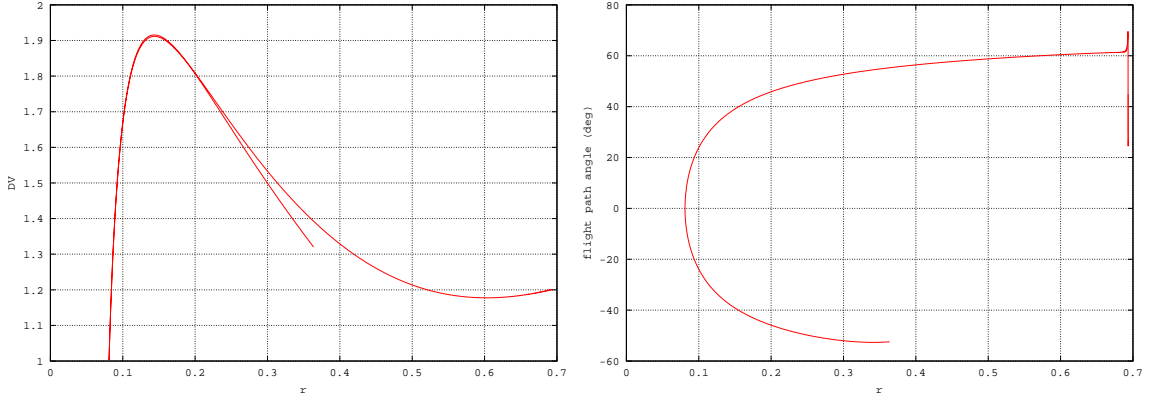


Figure VI.8: ΔV as computed along the stable manifold associated with L_2

In the planar case, heuristic argument can be used to show that ΔV reaches its minima at the periapsis passages of the trajectory considered. Indeed, near periapsis, the motion is very fast and the change in orbital elements are small. Thus, as a first approximation, one can consider the motion to be represented by a Keplerian motion in a rotating frame. That is, we let $r = \frac{p}{1+e \cos f}$ and $\cos \gamma = \frac{p}{r\sqrt{1+e^2+2e \cos f}}$, where $p = a(1 - e^2)$ denotes the semi-latus rectum and f is the true anomaly.

In this approximation, it can be checked that:

$$\frac{d\Delta V}{df} = A(f) \frac{\sin f}{2\Delta V}$$

where

$$\begin{aligned} A(f) &= \frac{er^2}{pv}(V_i - V_{lc} \cos \gamma) \left\{ 2v - \frac{1}{r^2} + \frac{6x^2}{r} \right\} \\ &\quad - \frac{e\sqrt{r}}{p}(V_{lc} - V_i \cos \gamma) \\ &\quad - 2er^2 V_i V_{lc} \left(2 \cos^2 \gamma - \frac{r}{p} \right) \cos \gamma \end{aligned}$$

Therefore, at periapsis, $\sin f = 0$ and $\frac{d\Delta V}{df} = 0$. Furthermore, one can compute $\frac{d^2\Delta V}{df^2}$:

$$\frac{d^2\Delta V}{df^2} = \frac{\cos f}{2\Delta V} A + \sin f \left(\frac{1}{2\Delta V} \frac{\partial A}{\partial f} + A \frac{\partial}{\partial f} \frac{1}{2\Delta V} \right)$$

so that, at periapsis, $\frac{d^2\Delta V}{df^2} = \frac{A(0)}{2\Delta V}$

$$A(0) = \frac{e}{pv} (V_i - V_{lc})(2r^2v^2 + 6r^2x^2v + v\sqrt{r} - 1) - 2V_iV_{lc}(2 - \frac{1}{1+e})r^2e$$

Now, observe that, for $J_c \leq J < 0$ and $r < \frac{1}{|J_c|} \simeq 0.462$, $V_{lc} < \alpha V_{lc} < v < \beta V_{lc}$ where $\alpha = \sqrt{2 - 2|J_c|}$ and $\beta = \sqrt{2 + 3r^3}$. Thus under these restrictions and the assumption that $e > 0.3$, $A(0)$ is bounded by below as:

$$A(0) > 0.15 \frac{(\alpha + 1)V_{lc} + r}{\beta rv} (2r^2\alpha^2V_{lc}^2 + \alpha V_{lc} - 1) - 4\{(\beta + 1)V_{lc} + r\}r^2$$

This rough estimate shows that for $r < 0.245$, ΔV achieves its minimum at periapsis (This value of r is sufficient for our purpose since we have seen that the existence of quasi-circular motion restricts us to radii below ~ 0.2 .

In the three dimensional case, the above argument yields more complicated relations between f , ω and Ω at the minimum of ΔV . However, the results indicate that, even though this relation is not exactly reached at periapsis, when $\omega = 0$, the minimum is nearly reached at periapsis (in this case, the only non-zero term in $\frac{d\Delta V}{df}$ depends only on $\sin \Omega$ and is less than $6\frac{r^2}{v} < 0.13$ with the above restrictions).

All these results indicate that the cost of a direct escape maneuver on a *given* escaping trajectory will be cheaper if performed at the periapsis of this trajectory. This fact justifies *a posteriori* the use of the Poincaré maps considered in the previous section to obtain practical optimal criterion for escape.

2.2. Direct escape in the planar problem

In the previous section we showed that along an escaping trajectory the minimum ΔV to escape is reached at periapsis with a tangential burn. Since $\frac{\partial \Delta V}{\partial J} = \frac{1}{v} > 0$ it also shows that this ΔV is the true optimal value if the altitude of the initial circular orbit is exactly equal

to the periapsis radius r_{L_2} of the stable manifold of L_2 . However, for arbitrary r this case is not met in general. Two strategies for escape are then possible. The first one consists of considering a larger value of J so that the Poincaré map reaches the given radius (i.e., $r \in \Sigma_2^a(J > J_{L_2})$). Then, a tangential burn is applied at the periapsis of an escaping trajectory. We indeed saw in the subsection VI.1.3 that the range of altitudes reached by Σ_2^a increases as J increases. The second strategy, only applicable for $r \geq r_{L_2}$, consists of performing a non-tangential burn to place the spacecraft on the stable manifold of L_2 . For $r < r_{L_2}$, only the first strategy is applicable in the case of single impulse, direct escape maneuvers. Figure VI.9 illustrates the geometry of these two strategies.

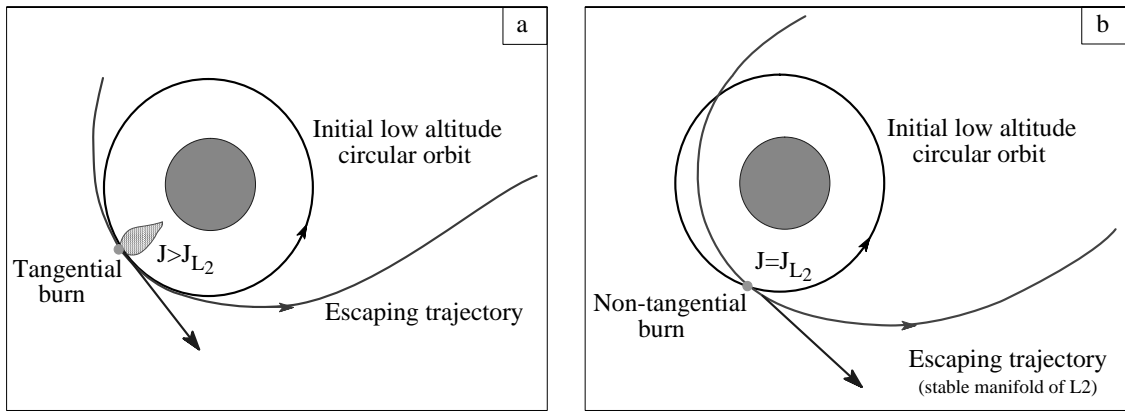


Figure VI.9: Strategies to escape. (a) First strategy: increase J and perform a tangential burn. (b) Second strategy: non-tangential burn to place the spacecraft into the stable manifold associated with L_1 or L_2 .

Let's for now assume $r > r_{L_2}$ and compare these strategies. To do so, we compute the minimum ΔV possible using the first strategy, the ΔV corresponding to the second approach being greater than or equal to 1.

Minimum ΔV as a function of J

For $J > J_{L_2}$, Σ_2^a is not reduced to a single point and on this set, ΔV is a function of radius r and longitude of periapsis $\tilde{\omega}$. We can show that for $r < 0.35$, $\frac{\partial \Delta V}{\partial r} < 0$ and that the minimum ΔV is reached on the boundary of the Poincaré map at a point close to (but not

equal to) the maximal radius point in the Poincaré map. Denoting $\Delta V_{min}(J)$ this minimal value at a given J , we can numerically compute this value at several values of the Jacobi constant. The altitude r at which ΔV_{min} is reached increases with J so that we can also compute $\Delta V_{min}(r)$, which is more convenient from a practical point of view. Figure VI.10 gives the results of such a computation.

We clearly see that ΔV_{min} decreases as a function of r . This result allows us to choose the first strategy as being optimal. Indeed, for $J_0 > J_{L_2}$, $\Delta V_{min} \leq \Delta V(r, \tilde{\omega}, J_0)$ where $(r, \tilde{\omega}) \in \Sigma_2^a(J_0)$. Now $\Delta V(r, \tilde{\omega}, J_0) \leq \Delta V_{traj}(r, \tilde{\omega}, J_0)$ where ΔV_{traj} corresponds to the ΔV calculated at any point of an escape trajectory having $(r, \tilde{\omega}, J_0)$ as periapsis (by the optimality of tangential burns). Therefore, $\Delta V_{min}(J_0) \leq \Delta V_{traj}(r, \tilde{\omega}, J_0)$ for any $r, \tilde{\omega}$ in the Poincaré map at a given Jacobi constant J . By the fact that ΔV_{min} decreases as J increases, we see that this inequality is, in fact, satisfied for any $(r, \tilde{\omega}) \in \Sigma_2^a(J \leq J_0)$. In particular, $\Delta V_{min}(J_0) \leq \Delta V_{traj}(J_{L_2})$, i.e., the first strategy for escape is more optimal than the second strategy.

For $J \geq J_0$, no optimality of $\Delta V_{min}(J_0)$ has been proven**. In the case of non-optimality, this result is, thus, only sufficient.

Optimal criterion

For $r < r_{L_2}$, the strategy to escape is similar to the case $r \geq r_{L_2}$. However, in this case, the minimum ΔV to escape does not correspond to the minimum ΔV taken over the set Σ_2^a . It is reached at a point near (but not exactly at) r_{min} . From a practical point of view, r_{min} is considered as an optimal solution in this case.

When applying a tangential burn at a given point, the elements of the transfer trajectory are fixed at periapsis. Therefore, at the time of the maneuver, $\tilde{\omega}$ is equal to the polar angle (which is approximated by Nt in a circular orbit), which allows us to characterize the placement of the maneuver in terms of $\tilde{\omega}$. Using this remark and the results of the previous

**i.e., it may happen that $\Delta V(J, r, \tilde{\omega}(J))$ (as taken on the boundary of Σ_2^a) is slightly less than $\Delta V_{min}(J_0, r, \tilde{\omega}(J_0))$ for J slightly greater than J_0 . Settling this question depends on evaluating $\frac{\partial \tilde{\omega}}{\partial J}$ at a fixed r on the boundary of Σ_2^a , which is a difficult quantity to compute.

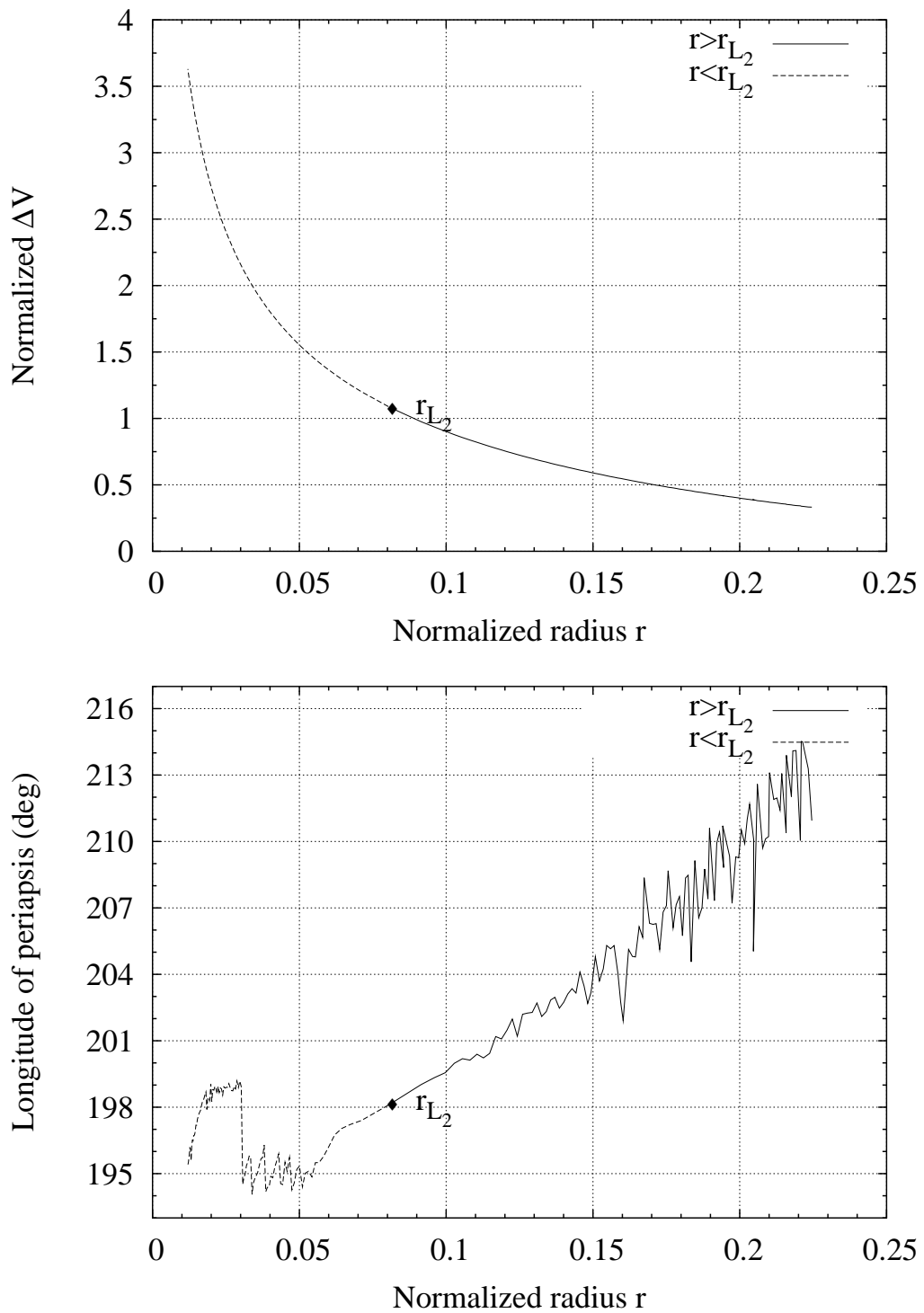


Figure VI.10: Optimal ΔV and longitude of periapsis for escape

sections, we obtain the following escape criterion^{††}:

*Starting in a low altitude, circular orbit, at a given radius r , fuel optimal direct escape maneuvers are obtained using an impulsive thrust, tangential to the path, whose magnitude and placement are determined, respectively, by $\Delta V(r)$ and $\tilde{\omega}(r)$, as given in Figure VI.10**.

We should note that, even though this criterion may be optimal, in practice one would better use a larger value of ΔV to achieve escape since the optimal point lie on the boundary of Σ_2^a , which is in W^s . That is, the spacecraft is transferred on trajectory that is caught in the neck regions for, ideally, an infinite amount of time. This point of optimality is thus very sensitive to the initial conditions. Applying a ΔV larger than this value (at the same longitude of periapsis), results in increasing J so that $\Sigma_2^a(J) \supset \Sigma_2^a(J_{opt})$ and the point of the maneuver lies now inside Σ_2^a , i.e., the transfer trajectory escapes. This result also indicates that increasing ΔV results in a certain robustness of escape relative to errors in the initial thrust. In fact, since the optimal point is not isolated, small errors in thrust direction correspond to placing the spacecraft on an escaping trajectory with periapsis near the optimal value.

Finally, besides quantitatively determining fuel optimal direct escape maneuvers, Figure VI.10 shows that the answer to the first initial question is negative: there is no optimal value of r such that ΔV is minimal among all directly escaping transfers for low circular orbits. In fact, one can show that there is a minimum for $r > 0.44$ (corresponding to $\frac{\partial \Delta V}{\partial r} = 0$), but the assumption for a spacecraft to be in a circular orbit at this radius is not valid anymore and the definition of ΔV is less meaningful. Applying our previous results to the available planetary satellites (whose normalized radius are covered by the range of

^{††}Note that, as compared to the results reported in [38], the difference in ΔV cannot be seen at the resolution of the graphs given. The only main difference lie in a small difference in the optimal longitude of the periapsis.

*Because of the limited sampling of the phase space in the numerical procedure, the results for the longitude of periapsis present some noise for large values of J . This appears clearly on this plot, even though the computations have been performed with 300×300 points in this case.

Jacobi constant considered), we can compute the minimal ΔV to escape from these planetary satellites starting in a circular orbit at a low altitude ($h \simeq 0$). The savings compared to a Keplerian escape maneuver (parabolic trajectory) are also computed and summarized in Table VI.1. Note that savings on the order of $130m/s$ in the case of Europa are obtained.

Table VI.1: Minimum ΔV to escape the surface of some planetary satellites

Planet	Satellite	Non-dimensional ΔV	ΔV scale factor (m/s)	ΔV to escape (m/s)	Keplerian ΔV to escape (m/s)	Savings when comp. to Kepler. (m/s)
Earth	Moon	2.79	235.4	656.8	695.7	38.9
Mars	II Deimos	0.44	1.9	0.8	1.9	1.1
Jupiter	I Io	0.76	624.7	474.8	748.7	273.9
	II Europa	1.12	402.9	451.2	590.9	139.7
	III Ganymede	1.44	464.9	669.5	802.8	133.3
	IV Callisto	2.04	315.0	642.6	716.0	73.4
	X Lysithea	2.75	1.1	3.0	3.3	0.3
Saturn	II Enceladus	0.38	64.0	24.3	58.2	33.9
	III Thethys	0.52	123.8	64.4	126.3	61.9
	IV Dione	0.75	123.1	92.3	146.6	54.3
	V Rhea	1.00	139.0	139.0	193.5	54.5
	VI Titan	2.02	345.3	697.5	775.6	78.13
	VII Hyperion	2.08	15.7	32.7	36.3	3.6
Uranus	I Ariel	0.75	137.5	103.1	163.5	60.4
	II Umbriel	0.96	111.0	106.6	151.1	44.5
	III Titania	1.53	125.2	191.6	225.8	34.2
	IV Oberon	1.92	102.7	197.2	212.5	15.3
	V Miranda	0.37	62.0	22.9	57.5	34.6
Neptune	I Triton	1.42	260.8	370.3	426.3	56.0
Pluto	I Charon	1.58	135.8	214.6	252.4	37.8

2.3. Direct escape in the spatial problem

As noticed in the first section, the extrema of r and i over Σ_2^a are reached at some point in the equatorial plane ($z = 0$). This is also true for ΔV , for which the minimal value is reached at $r \simeq r_{max}$. The previous optimal criterion is therefore still valid in 3 dimensional space. However in this case, one can ask what is the minimum ΔV to escape starting in a non-zero inclination initial orbit.

Variations in inclination

As J varies, the ranges of inclination reached by the Poincaré maps increase, reaching rather large values for relatively large values of J (see Figure VI.7).

The radius where the maximal inclination is reached decreases with J . However, it is still true that at any fixed r , the maximum in inclination increases with J . Figure VI.11 gives the envelope curve of a series of Poincaré maps at several values of Jacobi constant, projected onto the (r, i) space.

By projecting the data points representing Σ_2^a on the (z, i) plane, it is observed that, to within the accuracy of the discretization, all these extrema are reached at some point of the equatorial plane.

Strategy to escape starting in a non-zero inclined orbit

The above remark, and the results discussed on the optimality of tangential burns show that tangential maneuvers are optimal when compared to non-tangential ones at the points where the inclination achieves some extrema. This leads us to choose the same approach to the problem as in the planar case (see subsection “Strategies to escape”).

Starting from a non-zero inclination, low altitude, circular orbit (determined by the radius r and the inclination i), the strategy to escape consists of increasing J so that the maximal inclination reached by the Poincaré map at the given radius r equals the initial inclination i . Then, a tangential maneuver is applied at this point of maximal inclination (at fixed radius r). Since we know that this maximum is reached in the equatorial plane

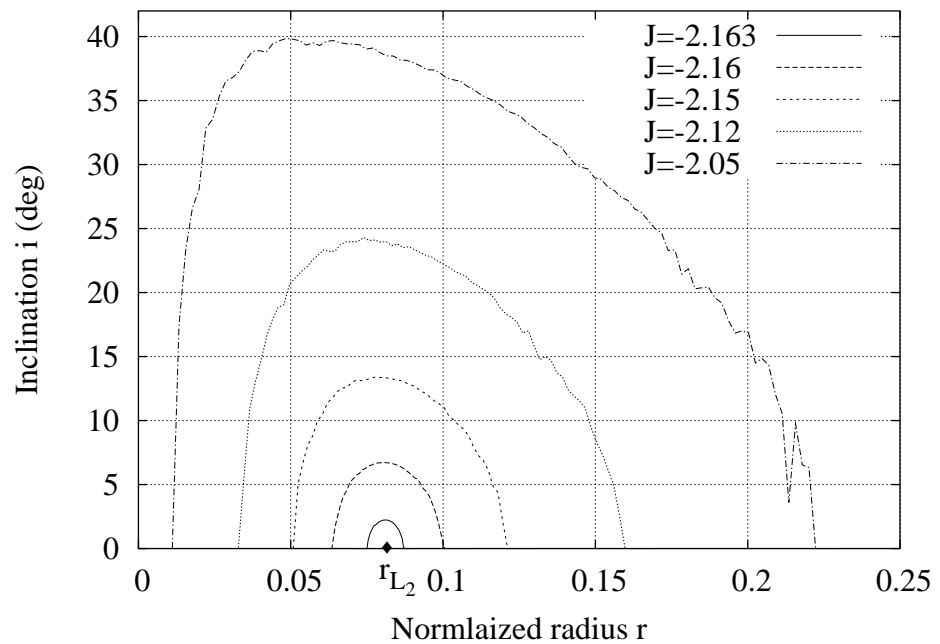


Figure VI.11: Envelopes of the projections of a few Poincaré maps (Σ_2^g) onto the (r, i) space

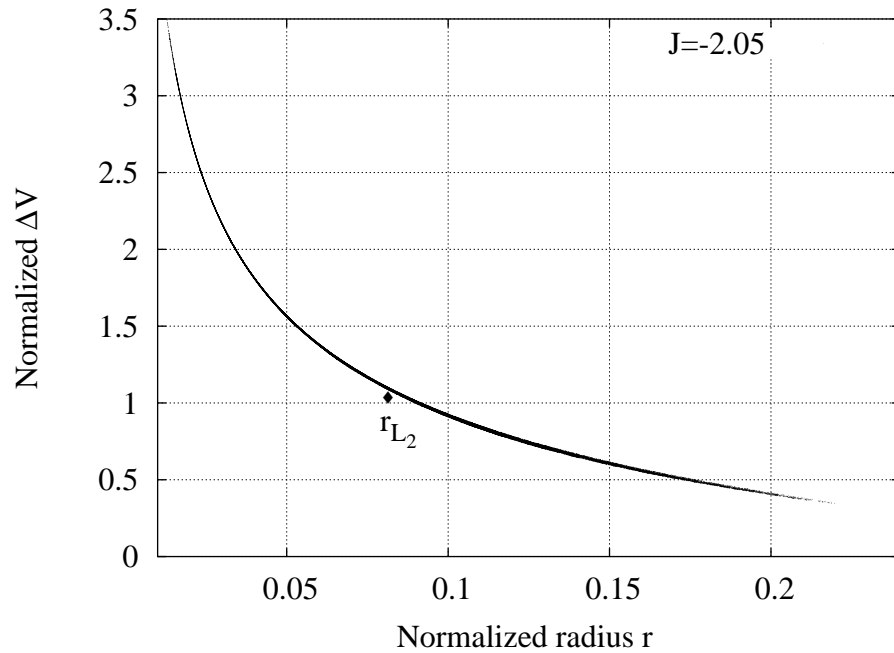


Figure VI.12: Projection of a Poincaré map onto the $(r, \Delta V)$ space

($z = 0$), we have the condition $\omega = 0^\circ$ at the time of the maneuver. The longitude of the ascending node at such point is restricted to lie in the range $[\Omega_{min}, \Omega_{max}]$, as determined by Figure VI.6.

Next arises the question of the optimality of such an approach, for which no definite result is given in this paper. However, a hint at the near optimality of such an approach is given in Figure VI.12, which presents the projection of a Poincaré map onto the $(r, \Delta V)$ space. We can see on this graph that, at any fixed radius r and Jacobi constant J , the variations of ΔV over the cross-section of the Poincaré map is very small (less than 0.05). In fact, as J decreases, the thickness of the cross-sections decreases as well, so that for all the values of J considered in this paper, the variations of ΔV over a Poincaré map at a fixed radius r are less than 0.05. Moreover, since, as J increases, ΔV increases at any fixed point, it can be concluded that, in the case of non-optimality of the previous approach, the value obtained is very close to the true optimum.

Thus, this ΔV may be sufficient from a practical point of view. For example, less than 5% error on the total ΔV costs in the case of Europa are due to the small variations of ΔV across Σ_2^a at fixed radius r .

CHAPTER VII

FUTURE DIRECTIONS

This chapter concludes the dissertation by summarizing the results obtained and discussing some thoughts on possible research directions.

1. Summary of the results obtained

As we have seen in the previous chapters, the central theme of this dissertation lies in the idea of periapsis Poincaré maps (which capture the notion of orbital dynamics) and the use of 3^{rd} body perturbations to help achieve orbital control objectives at reduced costs.

1.1. Periapsis Poincaré maps

The investigation of the concept of periapsis lead us to very simple but interesting results that are a beautiful generalization of the two body problem dynamics. We have seen indeed that for each value of the Jacobi constant, the position space is partitioned into exclusively periapsis and apoapsis regions by pairs of surfaces defined as the zero loci of a six degree polynomial ($w(r) = 0$). These pairs of surfaces are delimited by a “mean” surface ($f(r) = 0$) which is a scaled version of the surface of zero velocity. In the Kepler problem, this mean surface is represented by the set of circular orbits (at a given values of energy) and the surfaces $w(r) = 0$ collapse into this mean surface. This situation is very similar to the analogy between the zero velocity surfaces in the Hill problem and the Kepler problem.

We have seen that a direct application of these curves is that the tori of quasi-periodic

motion predicted by the KAM theory must lie close to these curves, giving us an idea of the variations of these tori with the Jacobi constant. These results also indicate that retrograde motion seems more stable than the direct case , a fact also observed in the stability of periodic orbits [12].

Periapsis Poincaré maps also appear as a natural arena to analyze orbital transfers and, in particular, are well suited to check the non-impact condition for transfer trajectories.

The use of Picard's method of successive approximations allows us to derive approximate expressions for these maps, yielding a first qualitative idea of the short term dynamics in the Hill problem, notably, the ‘quadrant rule’ of the planar problem that has been observed by several authors has been generalized to the spatial problem.

These estimates also show that 3^{rd} body forces can be controlled by the longitude of the ascending node and the argument of periapsis of a transfer trajectory, thus opening the way for the use of these forces in orbital control purposes.

Thus, it appears that the concept of periapsis is very useful in many orbit transfers and the features of the periapsis Poincaré maps should be investigated in connection with other problems in astrodynamics.

1.2. Third body driven transfers

A new way of performing plane changes in an orbital environment perturbed by a 3^{rd} body has been investigated both for its own interest, and as an example of a 3^{rd} body driven maneuver.

These 3^{rd} body driven plane changes are performed using two impulsive maneuvers and a timing of the first burn, resulting in transfers analogous to the bi-elliptic plane changes, but with the apoapsis maneuver suppressed. It has been shown that these transfers can improve the classical one impulse results by lowering the required ΔV for plane change values larger than $\simeq 39^\circ$. Savings on the order of 25% have been obtained for large plane changes ($\sim 60^\circ$) and the possibility of a reversal of the direction of motion has been

shown to exist using such an approach.

Besides these results, the analysis performed shows that interesting information can be obtained with the help of the Jacobi constant, yielding in our case an analytical estimate of the limit of optimality between 3^{rd} body driven plane changes and one impulse maneuvers and a significant simplification of the numerical algorithm used to solve the design problem. This method may be applicable to other problems of astrodynamics.

1.3. Escape and Capture maneuvers

Escaping and capture trajectories in the Hill three body problem have been investigated using a Poincaré map. This map allows us to characterize the set of periapses before escape (or, after capture) by some bounds on radius, longitude of periapsis and inclination.

These results show, in particular, that very low energy capture trajectories cannot be performed for all planetary satellites since the capture trajectories would impact the surface of the primary before reaching periapsis.

These results have also been applied to the problem of determining the minimum ΔV needed to escape from a planetary satellite, starting in a low altitude, circular orbit. An optimal criterion has been given in the planar case and a practical approach has been given in the three dimensional case. It is shown that the resulting cost for escape decreases as the initial altitude increases. The cost to escape in the vicinity of a planetary satellite is on the order of the ΔV scale factor, $(\mu N)^{1/3}$, and represents significant savings as compared to a parabolic escape.

2. Possible future research directions

In this section we outline some possible directions of research that emerge from the preceding work. Two main lines of investigation can be envisioned, one related to the periapsis Poincaré maps (tools of investigation) and the other would be more focused on the applications to orbital transfers.

2.1. Periapsis Poincaré maps

The idea of periapsis limiting curves can be applied to the restricted three body problem or other astrodynamical problems such as the asteroid or binary asteroid problems. As we have seen, while involving rather simple calculations, these curves can yield information on the qualitative behavior of quasi-circular motion and may be used to corroborate results obtained by other means.

A second path of research would be to develop computer algebra techniques to deal with higher order estimates of the periapsis Poincaré maps. These techniques would allow us to apply the method of periapsis Poincaré maps to other astrodynamical systems and yield more accurate information on the dynamics than first order estimates. This would lead to a software tool that could be used to analyze multiple loop transfers or optimization problem with path constraints, such as a non-impact condition.

2.2. Further transfers

The limitations encountered on the range of 3^{rd} body driven plane changes due to the sole use of the natural dynamics can be removed by performing plane changes at the first and last burn. With the addition of an apoapsis maneuver, these transfers would generalize the classic full three impulse plane change to the case of 3^{rd} body perturbed environments, improving the savings obtained here. This approach would unconditionally improve on the classical results and may appear as the optimal method over all the possible impulsive transfers in such environments.

Other orbital objectives could also be analyzed in the 3^{rd} body perturbed environments, the most direct extension of these results presented being the case of simultaneous radius change and plane change maneuvers. Instead of computing the zero lines of Δr_p , one has to compute the lines $\Delta r_p = \alpha$ where α represents the amount of desired radius change. Though larger savings may be possible in such cases, the order of magnitude of the savings obtained for the case $\Delta r_p = 0$ should be attainable since these zero lines correspond to

a change of sign of the function $\Delta r_p(\omega, \Omega)$, so that performing the first maneuver a little ahead or after the values considered in this dissertation should yield a positive or negative net change in periapsis radius while keeping the values of plane change realized with the zero periapsis change. This may be of interest for safety issues where a decrease in periapsis radius is generally not desirable.

Third body driven transfer ideas could also be used in conjunction with other transfer techniques used in interplanetary mission. For example, as the 3^{rd} body driven maneuvers involve raising the apoapsis radius to a significant distance from the central body, third body effects together with fly-bys of other celestial bodies in the vicinity of the primary, e.g., the Moon in the Earth environment, could be used to perform cheaper transfers. Another example would be to use the control of ω and Ω in conjunction with aerocapture techniques to decrease the energy of a spacecraft upon arrival at Mars faster than with the sole use of the aerocapture technique, thus shortening the travel time from Earth to Mars.

Finally, escape and capture maneuvers should be investigated further. Notably, results in the spatial problem should be obtained and multiple loop transfers (i.e., escape after N revolution around the primary) should be investigated. These transfers involve interesting dynamics that mix transit through both libration points L_1 and L_2 . Moreover these transfers could be connected with the previous ideas on third body driven transfers to obtain path constrained transits. That is, one could envision design of capture trajectories that reach a desired inclination after N revolutions around the primary, only with the use of natural dynamics or with a minimum amount of impulsive control, much in the same spirit as some of the results reported in [11].

APPENDIX A

SYMPLECTIC TRANSFORMS, JACOBI COORDINATES AND KEPLER PROBLEM

This appendix reviews the basics facts about symplectic transformations, the Jacobi coordinates and the Kepler problem.

1. Symplectic transformations with multipliers

Symplectic transformations were defined classically as transformations that leave the form of Hamilton's equations invariant. As such, there are no restrictions on the form of the Hamiltonian, provided that the transformed variables satisfy Hamilton's equations with the new Hamiltonian. With this definition, it has been shown by Wintner [43] that a transformation $\psi : (\mathbf{q}, \mathbf{p}) \rightarrow (\mathbf{Q}, \mathbf{P})$ is symplectic if and only if:

$$\mathbf{D}\psi^T \mathbf{J} \mathbf{D}\psi = \mu^{-1} \mathbf{J} \quad (\text{A.1})$$

where $\mathbf{J} = \begin{bmatrix} \mathbf{O} & \mathbf{I} \\ -\mathbf{I} & \mathbf{O} \end{bmatrix}$ is the symplectic matrix and μ is non-zero and is called the multiplier of the transformation (\mathbf{I} and \mathbf{O} are the identity and zero elements of the $\mathbb{R}^{n \times n}$, respectively). In this case the original Hamiltonian $\mathcal{H}(\mathbf{q}, \mathbf{p})$ is transformed into the new Hamiltonian $\mathcal{K}(\mathbf{Q}, \mathbf{P}) = \mu \mathcal{H}(\psi^{-1}(\mathbf{Q}, \mathbf{P}))$.

These transformations are also called symplectic transformations with multiplier μ , to reserve the appellation symplectic transformation to the case where $\mu = 1$.

These transformations with multiplier allow us to scale the variables 'canonically' in Hamiltonian systems. For example, if $\mathbf{q} = (q_1, \dots, q_n)$ and $\mathbf{p} = (p_1, \dots, p_n)$, then the

transformation:

$$Q_i = \epsilon^{-\alpha_i} q_i \quad ; \quad P_i = \epsilon^{-\beta+\alpha_i} p_i$$

is symplectic with multiplier $\epsilon^{-\beta}$.

2. Application to the Kepler problem

When in a frame with origin at the center of mass of the frame, the two body problem reduces to the Kepler problem. That is, the Kepler problem represents the relative motion of two point mass particles interacting gravitationally. Expressed in a rotating frame, this problem is given by the Hamiltonian:

$$\mathcal{H}_{Kepler} = \frac{|\mathbf{p}|^2}{2M_1} - \mathbf{q}^T \boldsymbol{\Omega} \mathbf{p} - \frac{Gm_1 m_2}{|\mathbf{q}|}$$

where $M_1 = \frac{m_1 m_2}{m_1 + m_2}$ is sometimes called the reduced mass of the system. In fact, Kepler's problem depends only on one parameter, the total mass of the system. The following symplectic transformation with multiplier M_1 makes this fact apparent:

$$\mathbf{q} \rightarrow \mathbf{q} \quad ; \quad \mathbf{p} \rightarrow \frac{\mathbf{p}}{M_1} \quad ; \quad \mathcal{H}_{Kepler} \rightarrow \frac{|\mathbf{p}|^2}{2} - \mathbf{q}^T \boldsymbol{\Omega} \mathbf{p} - \frac{\mu}{|\mathbf{q}|}$$

where $\mu = G(m_1 + m_2)$ is the gravitational parameter of the system.

In this form, we see also that Kepler's problem can be interpreted as the motion of a unit mass in a central gravitational field (fixed center) of strength μ . This interpretation leads to the restricted two body problem when one of the masses is much smaller than the other one. For example, in the case of $\frac{m_2}{m_1} \ll 1$, $\mu = Gm_1 + \mathcal{O}(\frac{m_2}{m_1})$. Even though these two problems represent two different situations, they are represented by the same set of equations and the restricted two body problem is generally referred to as the Kepler problem, as well.

Now observe that the equations of motion are given by:

$$\begin{cases} \dot{\mathbf{q}} = \mathbf{p} + \boldsymbol{\Omega} \mathbf{q} \\ \dot{\mathbf{p}} = -\boldsymbol{\Omega} \mathbf{p} - \frac{\mu}{|\mathbf{q}|^3} \mathbf{q} \end{cases}$$

Thus $\dot{\mathbf{q}} = 0$ and $\dot{\mathbf{p}} = 0$ when \mathbf{q} and \mathbf{p} are constant (say, \mathbf{q}_0 and \mathbf{p}_0 , respectively) and we obtain the following relations:

$$\begin{cases} \mathbf{p}_0 = -\Omega \mathbf{q}_0 \\ \Omega \mathbf{p}_0 = -\frac{\mu}{|\mathbf{q}_0|^3} \mathbf{q}_0 \end{cases}$$

These solutions represent relative equilibria of the Kepler problem and correspond to circular orbits in the inertial space.

For these solutions, the angular velocity is related to the orbit radius. Indeed, from the above relations we obtain:

$$\Omega \Omega \mathbf{q}_0 = \frac{\mu}{|\mathbf{q}_0|^3} \mathbf{q}_0$$

and, denoting ω the angular speed of the frame:

$$\omega^2 = \frac{\mu}{|\mathbf{q}|^3}$$

In order to investigate the motion close to a relative equilibrium, one can look at small perturbations from these solutions. That is, we let:

$$\begin{aligned} \mathbf{q} &= \mathbf{q}_0 - \boldsymbol{\xi} \\ \mathbf{p} &= -\Omega \mathbf{p}_0 - \boldsymbol{\eta} \end{aligned}$$

This transformation is symplectic, and, applying Taylor's expansion theorem to the Hamiltonian, one obtains:

$$\begin{aligned} \mathcal{H}_{Kepler} &= \mathcal{H}_{Kepler}(\mathbf{q}_0, \mathbf{p}_0) + [\nabla \mathcal{H}_{Kepler}(\mathbf{q}_0, \mathbf{p}_0)]^T \begin{bmatrix} \boldsymbol{\xi} \\ \boldsymbol{\eta} \end{bmatrix} \\ &\quad + \frac{1}{2} \left[\begin{bmatrix} \boldsymbol{\xi} & \boldsymbol{\eta} \end{bmatrix}^T \nabla^2 \mathcal{H}_{Kepler}(\mathbf{q}_0, \mathbf{p}_0) \begin{bmatrix} \boldsymbol{\xi} \\ \boldsymbol{\eta} \end{bmatrix} \right] + \dots \end{aligned}$$

Since $(\mathbf{q}_0, \mathbf{p}_0)$ is a relative equilibrium, $\nabla \mathcal{H}_{Kepler}(\mathbf{q}_0, \mathbf{p}_0) = \mathbf{0}$. Also, the constant term is generally dropped since it does not change the equations of motion. The Hessian

$\nabla^2 \mathcal{H}_{Kepler}$ is given by:

$$\nabla^2 \mathcal{H}_{Kepler}(\mathbf{q}_0, \mathbf{p}_0) = \begin{bmatrix} \omega^2 \left(\mathbf{I} - 3 \frac{\mathbf{q}_0 \otimes \mathbf{q}_0}{|\mathbf{q}_0|^2} \right) & -\boldsymbol{\Omega} \\ \boldsymbol{\Omega} & \mathbf{I} \end{bmatrix}$$

and the higher order terms only involve the terms $\frac{\partial^n \mathcal{H}_{Kepler}}{\partial \mathbf{q}^n}(\boldsymbol{\xi}, \dots \boldsymbol{\xi})$ ($n \geq 3$), and these terms scale with \mathbf{q} as $\frac{\mu}{|\mathbf{q}|^{2n-1}}$. That is, if we let $\mathbf{q}_0 = \epsilon^{-1} \mathbf{a}$, $\frac{\partial^n \mathcal{H}_{Kepler}}{\partial \mathbf{q}^n}(\boldsymbol{\xi}, \dots \boldsymbol{\xi})$ scales as $\epsilon^{2(n-2)}$ since the term $\frac{\mu}{|\mathbf{q}_0|^3} = \omega^2$ is fixed. Thus, we find that

$$\mathcal{H}_{kepler} = \frac{1}{2} \begin{bmatrix} \boldsymbol{\xi} & \boldsymbol{\eta} \end{bmatrix}^T \nabla^2 \mathcal{H}_{Kepler}(\mathbf{q}_0, \mathbf{p}_0) \begin{bmatrix} \boldsymbol{\xi} \\ \boldsymbol{\eta} \end{bmatrix} + \mathcal{O}(\epsilon^2)$$

3. Symplectic completion

A simple but useful operation related to symplectic transformations is the process of symplectic completion, that is the extension of a point transformation on configuration space into a symplectic transformation in phase space. This process was first analyzed by Matthieu and are also referred to as Matthieu transforms.

Let $\mathbf{Q} = \mathbf{Q}(\mathbf{q})$ be a point transformation on configuration space (any smooth manifold). Then one can complete this transformation into a symplectic transformation with multiplier μ by transforming the corresponding momenta \mathbf{p} according to $\mathbf{P} = \mathbf{P}(\mathbf{p})$ such that:

$$\mathbf{D}\mathbf{P} = \mu^{-1} \mathbf{D}\mathbf{Q}^{-T} \quad (\text{A.2})$$

Indeed, let ψ denote the transformation from the (\mathbf{q}, \mathbf{p}) to the (\mathbf{Q}, \mathbf{P}) variables. That is, $(\mathbf{Q}, \mathbf{P}) = \psi(\mathbf{q}, \mathbf{p})$. Then:

$$\mathbf{D}\psi = \begin{bmatrix} \mathbf{D}\mathbf{Q} & \mathbf{O} \\ \mathbf{O} & \mathbf{D}\mathbf{P} \end{bmatrix}$$

so that

$$\mathbf{D}\psi^T \mathbf{J} \mathbf{D}\psi = \begin{bmatrix} \mathbf{O} & \mathbf{D}\mathbf{Q}^T \mathbf{D}\mathbf{P} \\ -\mathbf{D}\mathbf{P}^T \mathbf{D}\mathbf{Q} & \mathbf{O} \end{bmatrix}$$

and, upon imposing the relation (1), one arrives at (2).

In the particular case of a linear transformation $\mathbf{Q} = \mathbf{A}\mathbf{q}$ where $\mathbf{A} \in \mathbb{R}^{n \times n}$ is non-singular, one obtain a symplectic transformation with multiplier μ by transforming the momenta according to $\mathbf{P} = \mu^{-1} \mathbf{A}^{-T} \mathbf{p}$. Similarly, the symplectic completion of $\mathbf{P} = \mathbf{A}\mathbf{p}$ is $\mathbf{Q} = \mu^{-1} \mathbf{a}^{-T} \mathbf{q}$.

4. Application to the Jacobi coordinates

In Chapter II, we defined the Jacobi coordinates from the \mathbf{Q} variables the the \mathbf{u} variables by choosing \mathbf{u}_0 to represents the position of the center of mass of the three particles, \mathbf{u}_1 to represents the relative position of the second particle with respect to the first particle and \mathbf{u}_3 to be the position of the third particle with respect to the center of mass of the first two particles, as is illustrated in Figure II.1. That is, we made the point transformation $\mathbf{u} = \mathbf{A}\mathbf{Q}$, where:

$$\mathbf{A} = \begin{bmatrix} \frac{m_1}{m} & \frac{m_2}{m} & \frac{m_3}{m} \\ -1 & 1 & 0 \\ -\frac{m_1}{m_1+m_2} & -\frac{m_2}{m_1+m_2} & 1 \end{bmatrix}$$

where $m = m_1 + m_2 + m_3$.

Then we immediately obtain the conjugate momenta $\mathbf{v} = \mathbf{A}^{-T} \mathbf{P}$ so that transformation is $(\mathbf{u}, \mathbf{v}) = (\mathbf{u}(\mathbf{Q}), \mathbf{v}(\mathbf{P}))$ is symplectic. \mathbf{A}^{-T} can easily be computed as:

$$\mathbf{A}^{-T} = \begin{bmatrix} 1 & 1 & 1 \\ -\frac{m_2}{m_1+m_2} & \frac{m_1}{m_1+m_2} & 0 \\ -\frac{m_1}{m} & -\frac{m_2}{m} & \frac{m_1+m_2}{m} \end{bmatrix}$$

and we readily obtain the formulas given Chapter II (equations (II.6)-(II.6)).

APPENDIX B

SCALING TO PLANETARY SATELLITES

The following table (1) give the length and time scales of all the planetary satellites in the solar system whose mass, orbital period and radius are known [35].

The length and time scales, $l = \left(\frac{\mu}{N^2}\right)^{1/3}$ and $\tau = \frac{1}{N}$ are the unit length and time scales used to normalize the Hill equations in Chapter II. The type has been defined in Chapter VI. A planetary satellite is of type 1 if the first periapsis of the stable manifold of the libration points L_1 and L_2 are below the physical surface of the satellite. It is of type 2 otherwise.

Table B.1: Length and time scales of the solar system planetary satellites

Planet	Satellite	μ (km^3/s^2)	N (1/s)	l (km)	τ (hr)	Radius (km)	Normalized radius	Type
Earth	Moon	4.903E+03	2.662E-06	88454.7	104.36	1738	0.0196	2
Mars	I Phobos	6.4E-04	2.280E-04	23.1	1.22	11	0.4859	1
	II Deimos	1.3E-04	5.760E-05	33.8	4.82	6	0.1881	1
Jupiter	I Io	5.930E+03	4.111E-05	15196.3	6.76	1815	0.1194	1
	II Europa	3.193E+03	2.048E-05	19672.6	13.56	1569	0.0797	2
	III Ganymede	9.883E+03	1.016E-05	45733.4	27.33	2631	0.0575	2
	IV Callisto	7.171E+03	4.357E-06	72283.6	63.75	2400	0.0332	2
	V Amalthea	4.814E-01	1.460E-04	282.7	1.90	98	0.3454	1
	VI Himalia	6.335E-01	2.902E-07	19592.3	957.09	93	0.0047	2
	VII Elara	5.068E-02	2.801E-07	8645.0	991.80	38	0.0044	2
	VIII Pasiphae	1.267E-02	9.894E-08	10897.8	2807.49	25	0.0023	2
	IX Sinope	5.070E-03	9.594E-08	8196.2	2895.35	18	0.0022	2
	X Lysithea	5.070E-03	2.805E-07	4008.2	990.15	81	0.0202	2
	XI Carme	6.330E-03	1.051E-07	8308.9	2643.25	20	0.0024	2
	XII Ananke	2.530E-03	1.152E-07	5756.7	2410.24	15	0.0026	2
	XIII Leda	3.800E-04	3.046E-07	1600.0	911.84	8	0.0050	2
	XIV Thebe	5.068E-02	1.078E-04	163.4	2.58	50	0.3060	1
	XV Adrastea	1.270E-03	2.438E-04	27.7	1.14	10	0.3606	1
	XVI Metis	6.330E-03	2.467E-04	47.0	1.13	20	0.4251	1
Saturn	I Mimas	3.035E+00	7.717E-05	798.8	3.60	196	0.2453	1
	II Enceladus	4.931E+00	5.307E-05	1205.2	5.23	250	0.2074	1
	III Thethys	4.931E+01	3.852E-05	3215.0	7.21	530	0.1648	1
	IV Dione	7.018E+01	2.657E-05	4632.3	10.45	560	0.1208	1
	V Rhea	1.669E+02	1.610E-05	8636.0	17.26	765	0.0885	1
	VI Titan	9.028E+03	4.561E-06	75714.8	60.91	2575	0.0340	2
	VII Hyperion	1.138E+00	3.418E-06	4601.2	81.27	148	0.0322	2
	VIII Lapetus	1.252E+02	9.167E-07	53010.4	303.02	730	0.0137	2
	IX Phoebe	2.655E-02	1.321E-07	11501.6	2102.68	110	0.0095	2
Uranus	I Ariel	9.017E+01	2.885E-05	4766.7	9.63	579	0.1214	1
	II Umbriel	7.803E+01	1.755E-05	6328.1	15.83	586	0.0926	1
	III Titania	2.347E+02	8.353E-06	14982.5	33.25	790	0.0527	2
	IV Oberon	2.006E+02	5.402E-06	19014.2	51.43	762	0.0400	2
	V Miranda	4.624E+00	5.145E-05	1204.4	5.40	240	0.1992	1
Neptune	I Triton	1.433E+03	1.237E-05	21075.1	22.45	1353	0.0642	2
	II Nereid	1.372E+00	2.019E-07	32280.8	1375.62	170	0.0052	2
Pluto	I Charon	2.202E+02	1.139E-05	11931.7	24.40	593	0.0497	2

APPENDIX C

REDUCED CUBIC EQUATIONS

This appendix reviews the basic results about reduced cubic equations and applies these results to the zero velocity surfaces defined in Chapter III. The book by Conkwright [8] has been used as a reference for the cubic equation.

1. Basic results

A reduced cubic equation is an equation of the form:

$$z^3 + 3Hz + G = 0 \quad (\text{C.1})$$

where the variable z is a priori a complex number and we restrict ourselves to the case of H and G real.

In this case, Descartes' rule in conjunction with the sign of the discriminant, allows us to determine the number of positive and negative roots of the equation. More precisely, Descartes' rule consists of counting the numbers of change of sign between the coefficients. Then, it follows that the number of positive roots differs from this number by an even integer. For example, if H is negative and G is positive, there is two change of signs and thus the equation (3) has zero or two positive roots. If G and H are both positive, this rule ensures that there is exactly one positive root. By applying Descartes' rule to the equation obtained by replacing z by $-z$, one can obtain some informations about the number of negative roots.

The discriminant rule consists of computing the discriminant of the reduced cubic equation:

$$D = -27(G^2 + 4H^3) \quad (\text{C.2})$$

and then applying the following result:

- if $D < 0$, then equation (3) admits exactly one real root.
- if $D = 0$, then equation (3) admits a double root.
- if $D > 0$, then equation (3) admits three distinct real roots.

When Descartes' rule informed us that the equation (3) has 0 or 2 positive roots, the discriminant can tell us which number to choose. If $D < 0$ then there is zero positive root, whereas if $D > 0$ then the equations admits exactly two positive roots. This last statement is not a direct consequence of the discriminant rule but follows from the specific form of the reduced cubic equation. Indeed, when $D > 0$, the three roots of (3) are given by:

$$z_k = 2\sqrt{-H} \cos\left(\frac{\phi + 2k\pi}{3}\right), \quad k = 0, 1, 2 \quad (\text{C.3})$$

where $\cos \phi = -\frac{G}{2\sqrt{-H^3}}$, $0 \leq \phi \leq \pi$.

From this form of the solution, it is clear that when the reduced cubic has three distinct real roots, at least one of them is negative. Thus the result follows.

When $D = 0$, $G^2 = -H^3$ so that $\cos \phi = \pm 1$ depending on the sign of G . The roots are given in this case by:

$$-2\epsilon\sqrt{-H} ; \quad \epsilon\sqrt{-H} ; \quad \epsilon\sqrt{-H}$$

where ϵ represents the sign of G .

When $D < 0$, the only real root is given by Cardan's formula:

$$z = \left[\frac{-G + \sqrt{G^2 + 4H^3}}{2} \right]^{1/3} + \left[\frac{-G - \sqrt{G^2 + 4H^3}}{2} \right]^{1/3} \quad (\text{C.4})$$

When G and H are function of a parameter (as in the case of the defining equation of the zero velocity surfaces), the roots of (3) are also continuous functions of the parameter. For example, if $D > 0$, and (3) has exactly two positive roots and if a change in the parameter results in setting $D = 0$, then the two positive roots collapse at $\sqrt{-H}$. If further change in the parameter results in $D < 0$, then we know that the only real root will be negative. Moreover, in this case, the two positive roots (when $D > 0$) are separated by the collapse value so that one root will increase towards $\sqrt{-H}$ while the other root will decrease towards this value. This situation occurs when J goes from $J < J_c$ to $J > J_c$, starting first on the x-axis. For $J < J_c$, $D > 0$ and the two positive roots correspond to the two components of \mathcal{Z} and the value of $r = \sqrt{-\frac{2J}{3}}$ separates these components. When $J = J_c$, the roots collapse at $r = r_c = \sqrt{-\frac{2J_c}{3}}$. For $J > J_c$, there are no longer any positive roots and the zero velocity surface is now open.

2. Application to the zero velocity surfaces

Recall that the zero velocity surface, \mathcal{Z} , is defined as the zero loci of the reduced cubic equation:

$$r^3 + 3Hr + G = 0$$

where $H = \frac{2J}{3g(\phi, \lambda)}$, $G = \frac{2}{g(\phi, \lambda)}$ and $g(\phi, \lambda) = 3\cos^2\phi\cos^2\lambda - \sin^2\lambda$ and is non-zero (In the case $g = 0$, the above cubic equation reduces to $r = -\frac{1}{J}$ for $J < 0$ and has no real positive solutions for $J \geq 0$).

From (4), we see that $D = -\frac{27 \times 4}{g^2} \left\{ 1 + \frac{1}{g} \left(\frac{2J}{3} \right)^3 \right\}$, and the sign of D is determined by the sign of $1 + \frac{1}{g} \left(\frac{2J}{3} \right)^3$.

Now, applying the above results (Descarte's and discriminant rules), we obtain the characterization of the roots presented in Table 2.

In order to check the critical points of the roots, r , of (3) with ϕ and λ , we first note that r depends on ϕ and λ only through g , so that these critical points are obtained when $\frac{\partial r}{\partial g} = 0$ (when defined).

Table C.1: Roots of the reduced cubic equation defining \mathcal{Z} .

$g \cdot J$	$-\infty$	J_c	0	$+\infty$
$g < 0$	$D > 0$		$g < -\left(\frac{2J}{3}\right)^3$ Single real positive root	
	Single real positive root		$g < -\left(\frac{2J}{3}\right)^3$ Double root, $D = 0$	
	Formula (6)		$g < -\left(\frac{2J}{3}\right)^3$ No real positive root	
$g = 0$	$r = -\frac{1}{J}$			
$g > 0$	Two distinct real positive roots	$D < 0$	$g < \left(\frac{2 J }{3}\right)^3$ Two real positive roots	No real positive root
		$D = 0$	$g = \left(\frac{2 J }{3}\right)^3$ Double root, $D = 0$	
	Formula (5)	$g > \left(\frac{2 J }{3}\right)^3$ No real positive root		

Now, observe that for all g between -1 and 3 , $gr^3(g) + 2Jr(g) + 2 = 0$, so that taking the partial derivative with g , on obtains:

$$r^3 + (3gr^2 + 2J)\frac{\partial r}{\partial g} = 0$$

Thus, for $g \leq 0$ and $J \leq 0$, we see that $\frac{\partial r}{\partial g} < 0$. Moreover, since the proposition $\frac{\partial r}{\partial g} = 0$ for some g implies $r^3 = 0$ and we know that $r(g)$ is at least C^1 , we deduce that in the range of values of g considered, $\frac{\partial r}{\partial g} < 0$, except, perhaps, at the boundary points -1 and -3 . Thus, the minimum of r is reached at $g = -1$, that is on the z -axis, when $J \leq 0$. In the planar problem, g only varies between 0 and 3 so that the minimum is reached at $g = 0$, which corresponds to the intersection of \mathcal{Z} with the y -axis at $r = -\frac{1}{J}$ ($J < 0$).

For $J > 0$, by continuity of $\frac{\partial r}{\partial g}$ with respect to g , we see that in the region where $r(g)$ exists, $\frac{\partial r}{\partial g} < 0$, thus showing again that the minimum radius is reached on the z -axis.

APPENDIX D

CHANGES IN ELEMENTS

$$\begin{aligned} \frac{\Delta a}{a} = & \cos^4(i/2) \sin 2(\omega + \Omega) \left\{ \frac{3p^{9/2}}{1-e^2} (I_2^{-4} - I) \right\} \\ & + \sin^4(i/2) \sin 2(\omega - \Omega) \left\{ \frac{3p^{9/2}}{1-e^2} (I_{-2}^{-4} - I) \right\} \\ & + \sin^2(i) \sin(2\Omega) \left\{ \frac{3}{2} \frac{p^{9/2}}{1-e^2} (I_0^{-4} - I) \right\} \end{aligned}$$

$$\begin{aligned} \frac{\Delta e}{e} = & \cos^4(i/2) \sin 2(\omega + \Omega) \left\{ -\frac{3}{2} \frac{p^{9/2}}{e^2} (I_2^{-4} - I) + \frac{3}{2} \frac{1-e^2}{e^2} p^3 I_2^{-4} \right\} \\ & + \sin^4(i/2) \sin 2(\omega - \Omega) \left\{ -\frac{3}{2} \frac{p^{9/2}}{e^2} (I_{-2}^{-4} - I) + \frac{3}{2} \frac{1-e^2}{e^2} p^3 I_{-2}^{-4} \right\} \\ & + \sin^2(i) \sin(2\Omega) \left\{ -\frac{3}{4} \frac{p^{9/2}}{e^2} (I_0^{-4} - I) \right\} \\ & + \sin^2(i) \sin(2\omega) \left\{ \frac{15\pi}{4} \frac{p^3}{(1-e^2)^{5/2}} \right\} \end{aligned}$$

$$\frac{\Delta r_p}{r_p} = \cos^4(i/2) \sin 2(\omega + \Omega) \left\{ \frac{3}{2} \frac{p^{9/2}}{(1+e)e} (I_2^{-4} - I) - \frac{p^3(1+e)}{e} I_2^{-4} \right\}$$

$$- \sin^4(i/2) \sin 2(\omega - \Omega) \left\{ \frac{3}{2} \frac{p^{9/2}}{(1+e)e} (I_{-2}^{-4} - I) - \frac{p^3(1+e)}{e} I_{-2}^{-4} \right\}$$

$$+ \sin^2 i \sin 2\Omega \left\{ \frac{3}{4} \frac{p^{9/2}}{(1+e)e} (I_0^{-4} - I) \right\}$$

$$- \sin^2 i \sin 2\omega \left\{ \frac{5\pi}{2} \frac{p^3(1+e)e}{(1-e)^{7/2}} \right\}$$

$$\frac{\Delta r_a}{r_a} = \cos^4(i/2) \sin 2(\omega + \Omega) \left\{ \frac{3}{2} \frac{p^{9/2}}{e(1-e)} (I_2^{-4} - I) + \frac{3}{2} \frac{1-e}{e} p^3 I_2^{-4} \right\}$$

$$- \sin^4(i/2) \sin 2(\omega - \Omega) \left\{ \frac{3}{2} \frac{p^{9/2}}{e(1-e)} (I_{-2}^{-4} - I) - \frac{3}{2} \frac{1-e}{e} p^3 I_{-2}^{-4} \right\}$$

$$+ \sin^2(i) \sin(2\Omega) \left\{ -\frac{3}{2} \frac{p^{9/2}}{1-e} (I_0^{-4} - I) \right\}$$

$$+ \sin^2(i) \sin(2\omega) \left\{ \frac{15\pi}{4} p^3 \frac{e}{(1-e^2)^3(1-e)} \right\}$$

$$\Delta i = \sin(i) \cos^2(i/2) \sin 2(\omega + \Omega) \left\{ \frac{3}{4} p^3 I_2^{-4} \right\}$$

$$+ \sin(i) \sin^2(i/2) \sin 2(\omega - \Omega) \left\{ -\frac{3}{4} p^3 I_{-2}^{-4} \right\}$$

$$+ \sin(2i) \sin(2\omega) \left\{ -\frac{15\pi}{8} \frac{p^3 e^2}{(1-e^2)^{7/2}} \right\}$$

$$+ \sin(i) \sin(2\Omega) \left\{ -\frac{3}{4} p^3 I_0^{-4} \right\}$$

APPENDIX E

NUMERICAL INTEGRATION

Throughout this work, a Runge-Kutta-Felhberg type integrator of order 8(7) has been used for the numerical integrations, with accuracy of 10^{-10} per step. That is, an embedded 7th order Runge-Kutta method is used in an 8th order scheme to estimate the truncation error made at each step and correct the time step in order to meet the desired accuracy.

The results presented in Table IV.2 have been obtained from the data of an integrated trajectory with DPTRAJ, communicated by M.D. Guman. The following paragraph, also due to M.D. Guman, briefly presents this integration.

DPTRAJ is a high accuracy trajectory computation program developed at the Jet Propulsion Laboratory for use in the navigation and design of space missions [10]. It is an accurate and general spacecraft trajectory program due to its ability to model all relevant force perturbations found in the solar system to high levels of precision. In order to simulate the “real” orbit dynamics of the Europa orbiter we use this program with a complete suite of force models. In the runs made for this analysis these force models included gravitational perturbations from the Sun and planets, the Galilean satellites (Io, Ganymede, Callisto, and Europa of course), J_2 and J_4 for Jupiter and the Europa gravity field up to 2nd degree and order. Also incorporated are the non-gravitational perturbations of the Europa atmosphere and solar radiation pressure.

Bibliography

- [1] D.F. Appleyard. *Invariant Sets near the Collinear Lagrangian Points of the Nonlinear Restricted Three-Body Problem*. PhD thesis, University of Wisconsin, 1970.
- [2] V.I. Arnol'd. *Dynamical systems III*. Encyclopedia of Mathematical Sciences. Springer-Verlag, 1988.
- [3] V.I. Arnol'd. Small denominators and problems of stability of motion in classical and celestial mechanics. *Russian Mathematical Surveys (published by the London Mathematical Society)*, 18(6), Nov-Dec. 1963.
- [4] E.A. Belbruno. Sun-perturbed Earth-to-Moon Transfers with Ballistic Capture. *Journal of Guidance, Control and Dynamics*, 16(4), July-August 1993.
- [5] J.V. Breakwell and L.M. Perko. Matched asymptotic expansions, patched conics and the computation of interplanetary trajectories. In *Proceedings of the AIAA/ION Astrodynamics Specialists Conference*, pages 291–300, 1965.
- [6] B. Chavineau. *Dynamique à long terme des astéroïdes binaires. Bilan des observations et approche théoriques*. Ph.D. thesis. Université de Nice, 1990.
- [7] V.A. Chobotov, editor. *Orbital Mechanics*. AIAA Education Series. American Institute of Aeronautics and Astronautics, 3rd edition edition, 2002.
- [8] N.B. Conkwright. *Introduction to the Theory of Equations*. Blaisdell Publishing Company, New York, Toront, London, 1965.

- [9] C.C. Conley. Low energy transit orbits in the restricted three-body problem. *SIAM Journal of Applied Mathematics*, 16(4):732–746, July 1968.
- [10] J.E. Ekelund. *DPTRAJ-ODP User's Reference Manual, volume 1*. Jet Propulsion Laboratory internal memo JPL 642-3405-DPTRAJ-ODP, 1996.
- [11] G. Gomez, W.S. Koon, M.W. Lo, J.E. Marsden, J. Masdemont, and S.D. Ross. Invariant manifolds, the spatial three-body problem and space mission design. In *Astrodynamic Specialist Meeting*, pages AAS 01–31, Quebec City, Canada, August 2001.
- [12] M. Hénon. Numerical exploration of the restricted problem.v. hill's case: Periodic orbits and their stability. *Astronomy and Astrophysics*, 1:223–238, 1969.
- [13] M. Hénon. *Generating families in the restricted three-body problem*. Lectures Notes in Physics. New series m. Springer-Verlag, 1997.
- [14] M. Hénon. New families of periodic orbits in hill's problem of three bodies. *Celestial Mechanics and Dynamical Astronomy*, 85(3):223–246, March 2003.
- [15] M. Hénon and J.M. Petit. Series Expansions for Encounter-type Solutions of Hill's Problem. *Celestial Mechanics and Dynamical Astronomy*, 38:67–100, 1986.
- [16] M. Hénon and J.M. Petit. Satellite encounters. *Icarus*, 66(3):536–555, June 1986.
- [17] J. Henrard and J.F. Navarro. Spiral structures and chaotic scattering in coorbital satellites. *Celestial Mechanics and Dynamical Astronomy*, 79:297–314, 2001.
- [18] G.W. Hill. Researches in the Lunar Theory. *American Journal of Mathematics*, 1:5–26, 1878.
- [19] Kaula. *Application of Satellite to geodesy*. Dover Science Books, New York, 1960.

- [20] W.S. Koon, M.W. Lo, J.E. Marsden, and S.D. Ross. Low energy transfer to the moon. *Celestial Mechanics and Dynamical Astronomy*, 81:63–73, 2001.
- [21] W.S. Koon, M.W. Lo, J.E. Marsden, and S.D. Ross. Heteroclinic connections between periodic orbits and resonance transitions in celestial mechanics. *Chaos*, 10(2):427–469, June 2000.
- [22] J. Llibre, R. Martínez, and C. Simó. Transversality of the invariant manifolds associated to the lyapunov family of periodic orbits near l_2 in the restricted three-body problem. *Journal of Differential Equations*, 58:104–156, 1985.
- [23] M.W. Lo, B.G. Williams, W.E. Bollman, D.S. Han, Y.S. Hahn, J.L. Bell, E.A. Hirst, R.A. Corwin, P.E. Hong, K.C. Howell, B. Barden, and R. Wilson. Genesis mission design. *Journal of the Astronautical Sciences*, 49(1):169–184, January–March 2001.
- [24] K.R. Meyer. Periodic solutions of the n-body problem. *Journal of Differential Equations*, 39:2–38, 1981.
- [25] K.R. Meyer. Scaling hamiltonian systems. *SIAM Journal of Mathematical Analysis*, 15(5), September 1984.
- [26] K.R. Meyer and G.R. Hall. *Introduction to Hamiltonian Dynamical Systems and the N-body Problem*, volume 90 of *Applied Mathematical Sciences*. Springer-Verlag, 1991.
- [27] K.R. Meyer and D.S. Schmidt. Hill’s lunar equations and the three-body problem. *Journal of Differential Equations*, 44:263–272, 1982.
- [28] O. Montenbruck and E. Gill. *Satellite Orbits: models, methods, and applications*. Springer, 2000.
- [29] J. Moser. On the generalization of a theorem of a.lyapunov. *Communications on Pure and Applied Mathematics*, XI:257–271, 1958.

- [30] D.J. Scheeres. The restricted Hill four-body problem with applications to the Earth-Moon-Sun system. *Celestial Mechanics and Dynamical Astronomy*, 70:75–98, 1998.
- [31] D.J. Scheeres. Changes in rotational angular momentum due to gravitational interactions between two finite bodies. *Celestial Mechanics and Dynamical Astronomy*, 81(1-2):39–44, 2001.
- [32] D.J. Scheeres, M.D. Guman, and B.F. Villac. Stability analysis of planetary satellite orbiters: Application to the Europa orbiter. *Journal of Guidance, Control and Dynamics*, 24(4), July-August 2001.
- [33] D.J. Scheeres and F. Marzari. Spacecraft dynamics in the vicinity of a comet. *Journal of Astronautical Sciences*, 50(1):35–52, January-March 2002.
- [34] Scottish Universities Summer School in Physics, editor. *The restless Universe: applications of gravitational n-body dynamics to planetary, stellar and galactic systems*. Copublished by Scottish Universities Summer School in Physics & Institute of Physics Pub., 2001.
- [35] K.P. Seidelmann. *Explanatory supplement of the Astronomical almanac*. Mill Valley Calif.: University Science Books, 1992.
- [36] C. Simó and T.J. Stuchi. Central stable/unstable manifolds and the destruction of kam tori in the planar hill problem. *Physica D*, 140:1–32, 2000.
- [37] V. Szebehely. *Theory of Orbits*. Academic Press, New York, 1967.
- [38] B.F. Villac and D.J. Scheeres. Escaping trajectories in the hill three body problem and applications. *Journal of Guidance, Control and Dynamics*, 26(2):224–232, 2002.
- [39] B.F. Villac and D.J. Scheeres. Optimality of tidally driven plane changes. In *Proceedings of the New trends in Astrodynamics conference*, 2003.

- [40] B.F. Villac and D.J. Scheeres. A new class of optimal plane change maneuvers. *Journal of Guidance, Control and Dynamics*, in press.
- [41] B.F. Villac, D.J. Scheeres, L.A. D'Amario, and M.D. Guman. The effect of tidal forces in orbit transfers. In *Proceedings of the AAS/AIAA Spaceflight Mechanics Meeting at Santa Barbara, CA*, pages 2049–2070, 2001.
- [42] S. Wiggins. *Introduction to Applied Nonlinear Dynamical Systems and chaos*. Springer-Verlag, 1990.
- [43] A. Wintner. *Analytical Foundations of Celestial Mechanics*. Princeton University Press, 1941.